Quantifying ice-shelf basal melt and ice-stream dynamics using high-resolution DEM and GPS time series

David E. Shean

A dissertation

submitted in partial fulfillment of the

requirements for the degree of

Doctor of Philosophy

University of Washington

2016

Reading Committee:

Ian R. Joughin, Chair

Benjamin E. Smith

Howard Conway

Program Authorized to Offer Degree:

Earth and Space Sciences

University of Washington

Abstract

Quantifying ice-shelf basal melt and ice-stream dynamics using high-resolution DEM and GPS time series

David E. Shean

Chair of the Supervisory Committee:
Dr. Ian R. Joughin
Applied Physics Laboratory

This dissertation describes methods to generate high-resolution digital elevation models (DEMs) of the Earth's ice sheets, and combines these observations with *in situ* GPS measurements to study basal melting beneath the Pine Island Glacier ice shelf, Antarctica. Pine Island Glacier (PIG) is currently losing mass at a rate of ~40 Gt/yr and contributing ~0.1 mm/yr to global sea level rise. This mass loss has been attributed to rapid retreat, speedup, thinning, and increased discharge in recent decades, due to ocean forcing and/or internal instability.

The automated, open source NASA Ames Stereo Pipeline (ASP) was adapted to generate digital elevation models (DEMs) and orthoimages from very-high-resolution (VHR) commercial imagery. I outline a processing workflow for ~0.5 m ground sample distance (GSD) DigitalGlobe WorldView-1/2/3 stereo image data. Output DEM products are posted at ~2 m with direct geolocation accuracy of <5.0 m CE90/LE90. An automated co-registration workflow reduces absolute vertical and horizontal error to <0.5 m, with observed standard deviation of ~0.1-0.5 m for overlapping, co-registered DEMs.

I processed all available 2010-2015 WorldView/GeoEye DEMs over the PIG ice shelf, and integrated with other available 2002-2015 DEM/altimetry data. I analyzed Eulerian elevation change (dh/dt) over grounding zones and upstream ice, and developed novel Lagrangian elevation change (Dh/Dt) methodology for elevation measurements over floating ice. I combined these results with an annual mass budget analysis to quantify the spatial and temporal evolution of ice shelf baasal melt. This analysis reveals the complex spatial/temporal evolution and interconnection of grounding zones, sub-shelf cavity geometry, basal melt rates, and upstream dynamics over grounded ice.

Rapid PIG grounding line retreat ended between ~2008-2009, followed by the ephemeral regrounding of ~2-3 deep keels as a positive ice shelf thickness anomaly advected over a seabed ridge. Thinning upstream of the grounding line decreased from ~5-10 m/yr in 2008-2010 to ~0 m/yr by 2012-2014, with a small grounding line advance from 2012-2015.

Mean 2008-2015 basal melt rates were ~80-90 Gt/yr for the full shelf, with ~200-250 m/yr melt rates within large channels near the grounding line, ~10-30 m/yr over the main shelf, and ~0-10 m/yr over the North and South shelves, with the notable exception of ~50-100 m/yr near the grounding line of a fast-flowing tributary on the South shelf.

I processed 2008-2010 and 2012-2014 GPS records for the PIG shelf and analyzed multi-path antenna heights, horizontal velocities, strain rates, cm-accuracy surface elevation and Lagrangian Dh/Dt elevation change. These data provide validation for the corrected stereo DEMs, with sampled DEM error of ~0.7 m. The GPS antenna height records document a relative surface increase of ~0.7-1.0 m/yr, which is consistent with estimated RACMO2.3 surface mass balance (SMB) and firn compaction rates from the IMAU-FDM dynamic firn model over the PIG shelf. Observed surface Dh/Dt is highly linear for all GPS records, with trends of -1 to -4 m/yr and <0.4 m residuals. Similar Dh/Dt estimates with reduced variability are obtained after removing expected downward GPS pole base velocity from GPS antenna Dh/Dt. Basal melt rates derived from GPS Dh/Dt are ~10 to 40 m/yr for the outer PIG shelf and ~4 m/yr for the South shelf. These estimates show good agreement with contemporaneous *in situ* measurements and stereo DEM records.

Melt rates were highest for the 2008-2010 period, with a ~20-30% decrease by 2010-2012, followed by a gradual increase from 2010-2012 to 2013-2015. Melt rates vary significantly across ~km-scale ice shelf thickness variations, with focused melting in basal channels near the grounding

line and keels over the outer shelf. The DEM and GPS records also document higher melt rates within and near transverse surface depressions/rifts associated with longitudinal extension. I suggest that these ~km-scale features alter sub-shelf circulation, leading to positive feedbacks that can influence regrounding and upstream ice dynamics.

A positive linear relationship between melt rate and depth is observed, with increasing melt rate magnitude and increasing variability at depth. The slope and spread of this linear relationship varies over time. Existing piecewise melt rate parameterizations in prognostic ice flow models provide reasonable approximations for this relationship, but fail to capture km-scale variability.

The DEM and GPS Dh/Dt melt products do not show the ~50% decrease in melt rates between 2010 and 2012 inferred from hydrographic observations in Pine Island Bay, with no significant melt rate variability associated with observed ~2012 ocean cooling in mooring records. This suggests that PIG melt rates are not directly correlated with observed ocean heat content near the shelf front, and that during the 2008-2015 period, observed ice shelf melt and upstream dynamics were more sensitive to grounding evolution, channel-scale circulation, and internal instability than oceanographic forcing. These findings have important implications for flow modeling efforts used for projections of 21st-century sea level rise.

TABLE OF CONTENTS

LIST OF FIGURES

LIST OF TABLES

ACKNOWLEDGEMENTS

I wanted to start with a quote about how an effort like this is never done, but I didn't have time to find the right one. Instead I found this one:

"We'd be fools not to ride this strange torpedo all the way out to the end."

-Raoul Duke

That more or less summarizes my experience at the University of Washington, thus far at least.

I thought that I understood glaciers in 2004 after looking at many grayscale images of Mars. I even read a few textbooks and some journal articles about glaciers on planet Earth. I learned from some fantastic teachers and some fantastic scientists. I spent some time living on a glacier in a very special part of Antarctica. By the time I did that again, I came to the humbling realization that glaciers were far more complicated than I ever imagined.

I naively returned to grad school in 2011, thinking it would be a breeze. I sought new challenges, and I found plenty. I am a different (hopefully better) scientist now, and I suppose a different (hopefully better) person in many ways. I can say that I've again learned from some fantastic teachers and some fantastic scientists. I spent some time living on a glacier in a very special part of Greenland. By the time I did that again, I was even more humbled, but I also had some new ideas about complicated glaciers. Many of those ideas were nonsense, some have lingering file folders, and some even have proper documentation. This dissertation contains a few projects that started brewing around that time.

Many people have supported me over the years and helped me get to this point. I need to start with my advisor Ian Joughin, who in August 2011, suggested that I take a look at some high-resolution images of Greenland. Turns out that was a good idea, and I quickly learned that Ian's ideas are usually good ones.

I am constantly impressed by Ian. He identifies and approaches scientific problems as an engineer, tackling complex, challening questions in a frighteningly efficient and rigorous manner. He regularly publishes seminal high-profile articles and has plenty of academic accolades, medals, society memberships, etc. I'm perhaps more impressed, however, by the fact that he also

maintains his own servers, writes in C, and goes home at 4:30 every afternoon. I try not to think about how valuable an hour of his time is when I knock on his door, and I am grateful for the countless hours he has spent with me over the years. I am truly honored that he has tried to instill some of his knowledge and wisdom in me.

Ben Smith has effectively been a co-advisor for this effort. I am always amazed by Ben's technical abilities, but also his seemingly innate understanding of how glaciers, instruments, and numbers work. I rarely have to explain things to Ben, but he has always taken the time to explain concepts and algorithms to me, no matter how rudimentary, until they stick.

I consider myself very lucky to have learned from this pair. They are world-class scientists, but also patient, modest, and just generally good guys. Whether they like it or not, they are role models at this stage in my career, and I look forward to working with them for years to come.

Pierre Dutrieux provided invaluable feedback for the PIG work, and took the time to help me fine-tune the final methodology and interpretion, often staying at the office way too late during animated discussions. Pierre's combined understanding of PIG oceanography and glaciology is unparalleled in my opinion, and he helped lay the foundation for much of the work contained in this dissertation. I sometimes wish that my results matched the impressive ocean observations he has compiled over the years, but it's potentially more exciting to now figure out why they do not. We have plenty of work to do, my friend.

Twit Conway willingly accepted the invitation to join my committee, and has provided excellent feedback (both scientific and much-needed positive support) along the way.

Thanks to Zack Moratto, Oleg Alexandrov, and all past/present ASP developers for building and maintaining an incredible set of tools, and for teaching me many, many things in the process. Another big thanks to Claire Porter, Paul Morin and others at the PGC, for tasking, managing, and delivering the huge volume of image data used for this work.

As with most other UW glaciology grads of my generation, Ed Waddington taught me many secrets of glacier physics, and how to think about ice in a numerical way. He is a fantastic teacher, with seemingly endless patience, and it was a pleasure being his TA.

Thanks to Knut Christianson, for letting me crash on his couch when he was in my situation several years ago, and for eagerly providing the PIG GPS data, which significantly improved this work.

Others in the UW Glaciology group have shared their infectious enthusiasm, and taught me many things over the years – thanks to Bernard Hallet, Steve Warren, Dale Winebrenner, Michelle Koutnik, and T.J. Fudge, among others.

To my ATG 208B officemates and good friends, Max Stevens, Kristin Poinar, Emily Newsom, David Lilien and Laura Kehrl – thanks for years of laughter, support, and general distraction from the madness of grad school. The same goes for many other past/present ESS grads - Perry Spector, Adam Campbell, Regina Cairns, Kate Allstadt, Trevor Hillebrand, Sarah Schanz, and Shelley Chestler, to name a few. To all of the past/present Thunderfjords – we had big fun over the years, and even won a few softball games along the way. Thanks also to my wonderful housemates, especially Louisa and Emily, and many "real-world" friends in Seattle and abroad who supported me over the years.

I learned many tricks from the Cascadia Users of Geospatial Open Source (CUGOS), where I always found a shared passion for geospatial data. On that note, a huge thank you to the countless developers across the planet who poured countless hours into the tools that enabled this work (Python, GDAL/OGR, NumPy/SciPy, Matplotlib, iPython, among many others). You don't need the shoulders of giants when you have a giant pyramid of open-source software developers.

I would like to formally acknowledge NASA Cryosphere program manager Tom Wagner, for pointing me in the right direction 5 years ago, and providing support over the past decade. For the record, in early 2014, Tom presciently suggested that the remote sensing observations were the key to understanding the oceans beneath Antarctica's ice shelves.

I would also like to formally acknowledge the UW Student Technology Fee (STF) program, which provided funding to purchase equipment that greatly enhanced my educational experience and research capabilities as a UW grad student. Thanks to Devin Bedard, Jon Beyeler, Keith Hodson, Tait Russell, Perry Spector, Max Stevens, and many other UW students for all of their help with STF proposals/projects over the years.

I should also acknowledge a few big names from my early career. Joe Fahle taught me how to build a proper data processing workflow, and introduced me to ASP. Mike Malin always pushed my scientific and technical thinking, and offered one piece of advice as I left for UW – “you’re going to feel like a kid in candy store, stay focused.” I didn't necessarily follow this advice, but he was absolutely right. Dave Marchant oversaw my first forays into Antarctic glaciology, and

taught me how to do polar research. Finally, a special thank you to Jim Head, who saw potential in a wavering computer engineering student, got me hooked on planets, spacecraft, and ice, and taught me the art of giving a great talk.

To Ellie, who has made the past few years of my life so much better, and provided ongoing support and love as this effort consumed my time and energy in the final months. I look forward to all of the things that don't involve a dissertation.

Finally, to my family, who has supported me longer than anybody else on Earth, and welcomed me back to the terrestrial community with open arms.

Chapter 1. INTRODUCTION

Over the past few decades, remote sensing observations, field observations, and modeling efforts have confirmed that the Earth's ice sheets and glaciers are losing mass (Figure 1-1), potentially at an accelerating rate [*Shepherd et al.*, 2012; *Vaughan et al.*, 2014]. The mechanisms responsible for this mass loss include changes in ice dynamics (e.g. increased discharge due to retreat, acceleration, and thinning of outlet glaciers) and surface/basal mass balance. Understanding the nature, causes, and evolution of this mass loss is critical for constraining projections of corresponding contributions to sea-level rise (Figure 1-2).

This dissertation leverages multiple remote sensing datasets, field observations, and model output to investigate ice sheet mass loss and associated processes. The common link between these investigations is repeat high-resolution digital elevation models (DEMs) derived from commercial stereo satellite imagery.

1.1 ORGANIZATION OF THE DISSERTATION

This introductory chapter offers a brief overview of relevant background information. Each chapter contains a detailed introduction, with a thorough literature review included in Chapter 3.

The second chapter is a manuscript entitled "**An automated, open-source pipeline for mass production of digital elevation models (DEMs) from very high-resolution commercial stereo satellite imagery**," which was published in the ISPRS Journal of Photogrammetry and Remote Sensing [*Shean et al.*, 2016a]. This provides detailed documentation of modifications to the NASA Ames Stereo Pipeline, and an automated workflow to generate high-resolution DEMs from high-resolution commercial stereo satellite imagery. It also describes methodology for DEM co-registration and includes multiple accuracy analysis case studies.

The third chapter is a manuscript entitled "**Basal melting of the Pine Island Glacier Ice Shelf, West Antarctica from a 2008-2015 high-resolution DEM record**" to be submitted in summer 2016, likely split as a long-format and a short-format article. This paper presents observations of timing, spatial distribution, and magnitude of ice shelf melt and upstream ice dynamics for the Pine Island Glacier (PIG) from 2008-2015. The methodology includes a detailed description of

novel Lagrangian Dh/Dt melt rate analysis and mosaicking routines used to integrate hundreds of high-resolution DEM sources.

The fourth chapter is a manuscript entitled "**In situ GPS records of surface mass balance, strain rates, and basal melt rates for Pine Island Glacier, Antarctica**," to be submitted in summer 2016. This includes analysis of cm-accuracy surface elevation change for several GPS receivers on the PIG shelf with continuous temporal coverage. These results provide important constraints for surface mass balance and firn compaction, while also validating DEM time series and basal melt rate estimates.

1.2 ADDITIONAL WORK

An additional manuscript, entitled "**Seasonal and interannual evolution of Jakobshavn Isbrae, Greenland from a high-resolution DEM and Velocity time series**," was not included in this dissertation due to time constraints. This analysis integrated >200 high-resolution DEMs from various sources to document the 2003-2015 seasonal and interannual elevation change and calving behavior for Jakobshavn Isbrae – Greenland's largest and most dynamic outlet glacier. This work was presented during invited talks at the 2015 AGU fall meeting and 2014 IGARRS meeting [*Shean et al.*, 2014], and will be finalized for publication in 2016.

I have also been involved with several additional research projects during the course of my PhD, making significant contributions to the following manuscripts as a coauthor:

- Observations of seasonal and diurnal glacier velocities at Mount Rainier, Washington, using terrestrial radar interferometry [*Allstadt et al.*, 2015]
- Short-term grounding line variability and subglacial lake drainage on Pine Island Glacier, Antarctica [*Joughin et al.*, 2016]
- Sensitivity of Pine Island Glacier to observed ocean forcing [*Christianson et al.*, 2016]
- Seasonal to multiyear variability in ice-front position, glacier speed, and surface elevation at Helheim and Kangerdlugssuaq Glaciers, SE Greenland, from 2008-2016 [*Kehrl et al.*, 2016]

with minor contributions to several additional publications in recent years [*Joughin et al.*, 2014a; *Pope et al.*, 2015; *Stevens et al.*, 2015].

1.3 ICE SHELF BACKGROUND

Ice shelves form when grounded ice encounters a body of water and begins to float (Figure 1-3). For the ice sheets, this grounding "zone" transition occurs where ice streams and outlet glaciers meet the ocean, thin via longitudinal stretching, and achieve hydrostatic equilibrium with the surrounding water [*Brunt et al.*, 2010; *Rignot et al.*, 2011a]. Beyond the grounding line, drag along shear margins, fjord walls, and/or pinning points provides critical buttressing support for inland ice stability [e.g., *Dupont*, 2005]. Thinning, front retreat, and/or complete loss of ice shelves decreases this buttressing effect, inducing upstream acceleration, thinning, and increased discharge of grounded ice – a process that was well-documented following the 2002 loss of Larsen B ice shelf [*Rignot et al.*, 2004; *Scambos*, 2004]. While the floating portions of the ice shelves are in hydrostatic equilibrium with the ocean, this increased discharge from grounded ice can provide a significant contribution to sea level rise.

Unlike the Greenland ice sheet, which loses ~50% of its mass via surface melting and ~50% via outlet glacier discharge, the Antarctic ice sheet loses mass almost exclusively through ice shelf basal melting and iceberg calving (Figure 1-3). Recent inventories suggest that basal melting constitutes ~55% of Antarctic mass loss while calving is responsible for the remaining ~45% [*Depoorter et al.*, 2013; *Rignot et al.*, 2013]. Hydrographic observations suggest that enhanced atmospheric and ocean circulation has led to increased transport of warm circumpolar deep water (CDW) onto the continental shelf since the ~1990s [*Jenkins et al.*, 2010], where it is funneled toward the grounding line of vulnerable ice shelves in West Antarctica (Figure 1-4).

Previous studies have suggested that important connections exist between ocean circulation, ice shelf melting, and inland ice dynamics for the Amundsen Sea sector of West Antarctica [e.g., *Pritchard et al.*, 2012]. However, "the fact that such warm water masses have no surface expression in the vicinity of the ice sheets makes them impossible (thus far) to detect via remote sensing, greatly complicating the task of monitoring water-mass changes" [*Joughin et al.*, 2012]. This dissertation attempts to do just that – leverage a growing archive of high-resolution remote sensing observations to constrain ocean properties and circulation as part of a larger effort to evaluate their importance for ice shelf basal melt and ice sheet mass loss.

1.4 HIGH-RESOLUTION STEREO DEMS

High-resolution DEMs from commercial stereo imagery can resolve sub-meter vertical elevation change for large, spatially-continuous regions of the ice sheets, while also providing unprecedented detail in glaciologically important locations (e.g. grounding zones, shear margins). Repeat DEMs provide a consistent set of observations to study ongoing ice sheet change in the post-ICESat-1 era (2009-present). These satellite observations complement airborne remote sensing observations from NASA's Operation IceBridge (OIB) mission (2009-present), and I make use of OIB data throughout the dissertation.

The archive of available high-resolution commercial stereo imagery over the ice sheets has grown significantly in recent years (Figure 1-5). During my PhD, I processed stereo DEMs for the entire West Antarctic coastline, excluding the Ross and Ronne-Filchner ice shelves (Figure 1-6). This dataset provides near-continuous 2010-2015 coverage for the Amundsen Sea Embayment, with excellent repeat coverage over Pine Island Glacier (PIG). This dense coverage, combined with extensive existing literature, large dynamic signals, and the availability of airborne control data, make PIG an ideal candidate to develop and validate these methods.

FIGURES

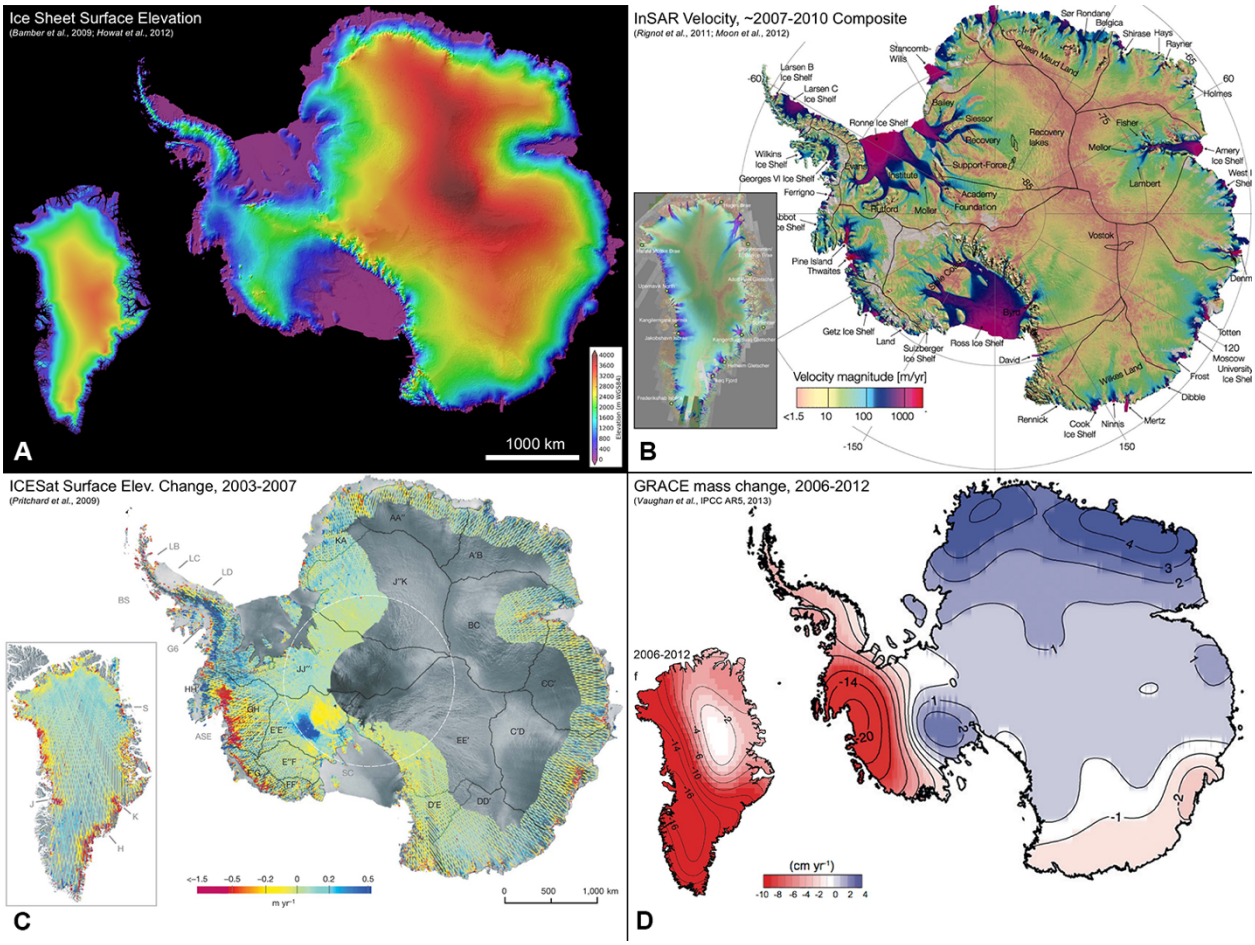

Figure 1-1: Remote sensing observations of the Greenland and Antarctic ice sheets. A) Surface elevation [*Fretwell et al.*, 2013; *Howat et al.*, 2014a], B) Surface velocity [*Rignot et al.*, 2011b; *Moon et al.*, 2012], C) Elevation change [*Pritchard et al.*, 2009], D) Mass change [*Vaughan et al.*, 2014]. Note significant thinning and mass loss over the Amundsen Sea Embayment (ASE) in West Antarctica.

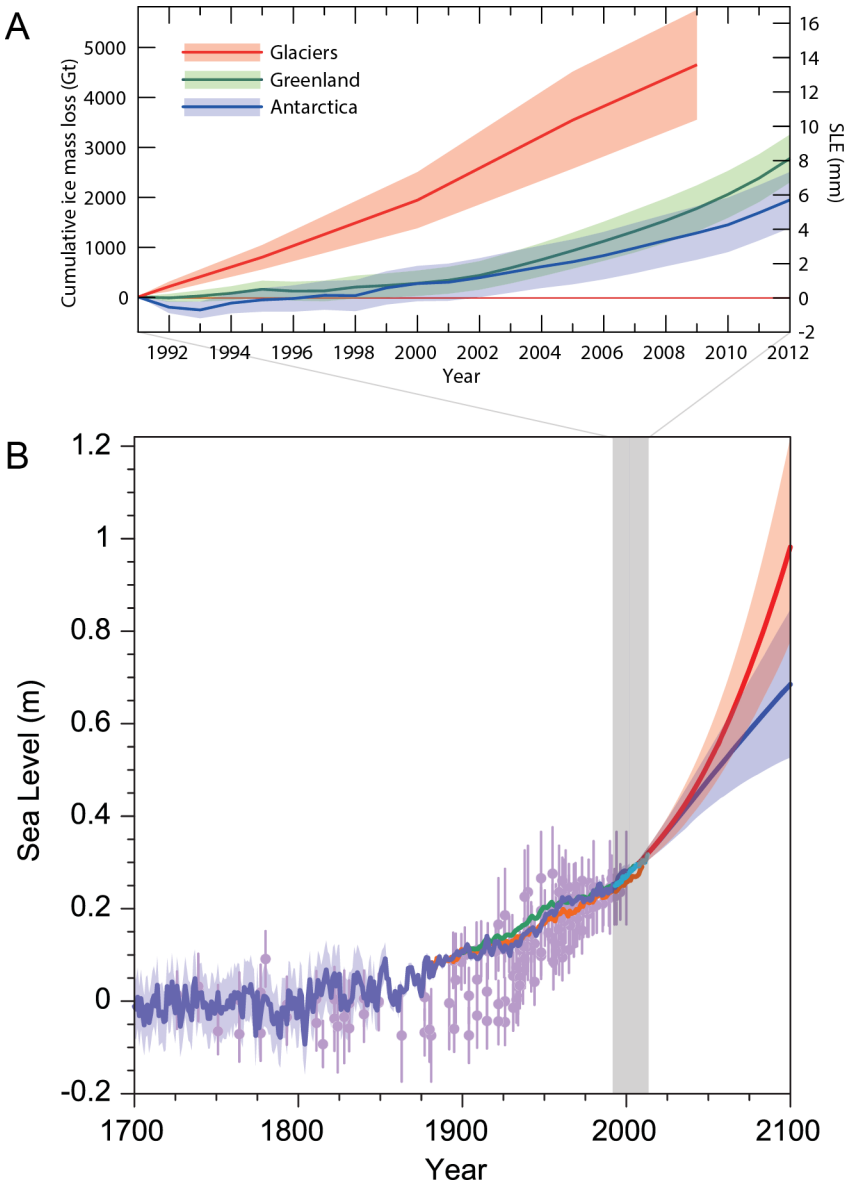

Figure 1-2: Recent ice sheet mass loss and sea level rise contribution. A) Observed mass loss and corresponding sea level rise contribution for Greenland, Antarctica, and all other glaciers. B) Historical sea level rise (relative to pre-industrial values) from tide gauge data, satellite altimetry data (cyan), and model predictions for RCP2.6 (blue) and RCP8.5 (red). Adapted from [*Church et al.*, 2013].

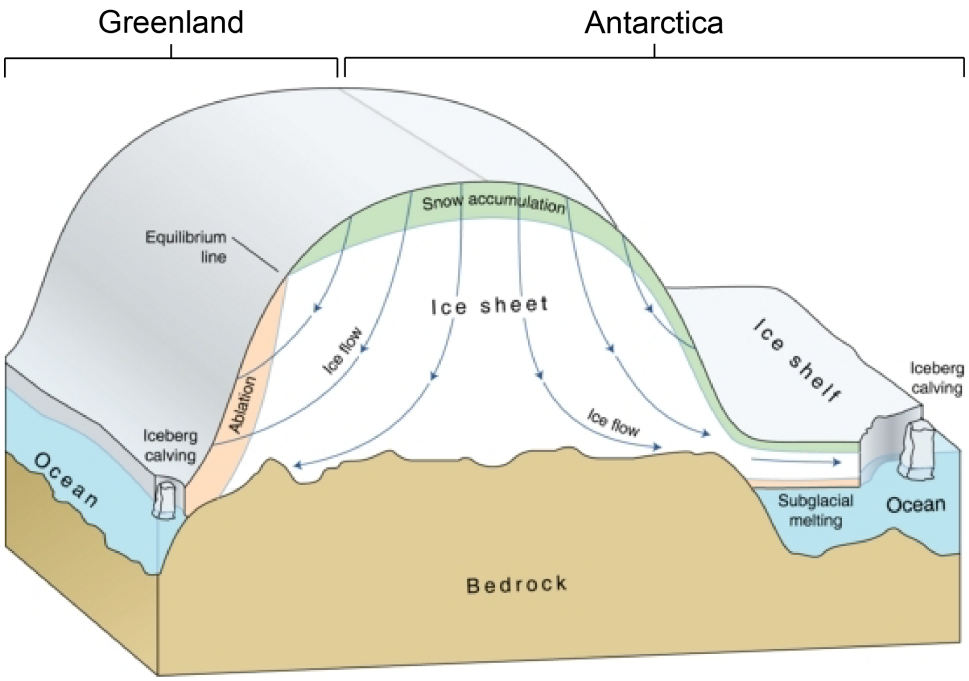

Figure 1-3: Processes responsible for ice sheet mass balance of the Greenland and Antarctic ice sheets. Basal melting of ice shelves is the dominant process responsible for mass loss in Antarctica. Adapted from http://www.climate.be/textbook/chapter3_node15.xml.

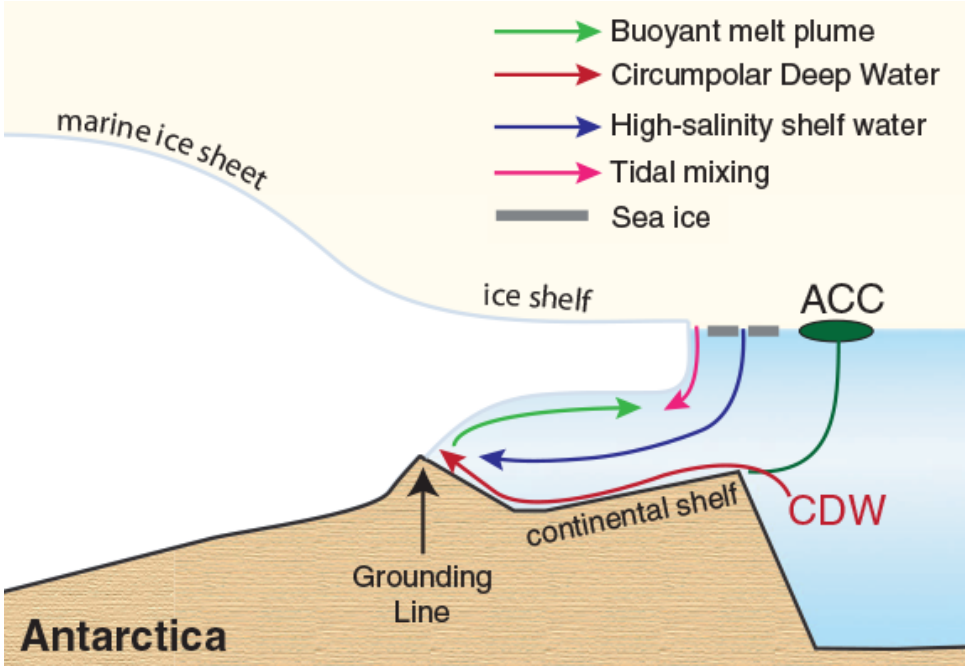

Figure 1-4: Simplified ocean circulation pathways beneath an ice shelf with marine ice sheet geometry. The circumpolar deep water (CDW) pathway is the most relevant for ice shelves in

the Amundsen Sea Embayment of West Antarctica, including the Pine Island Glacier. Adapted from [*Joughin et al.*, 2012].

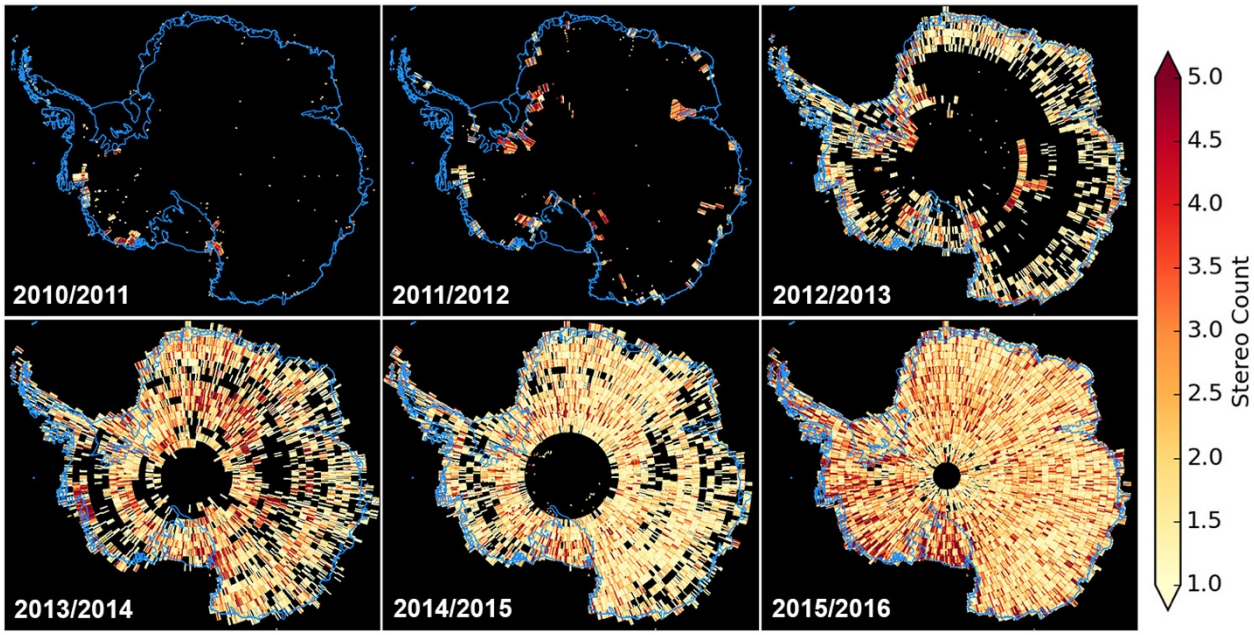

Figure 1-5: Annual DigitalGlobe along-track stereo coverage with cloud cover <75%.

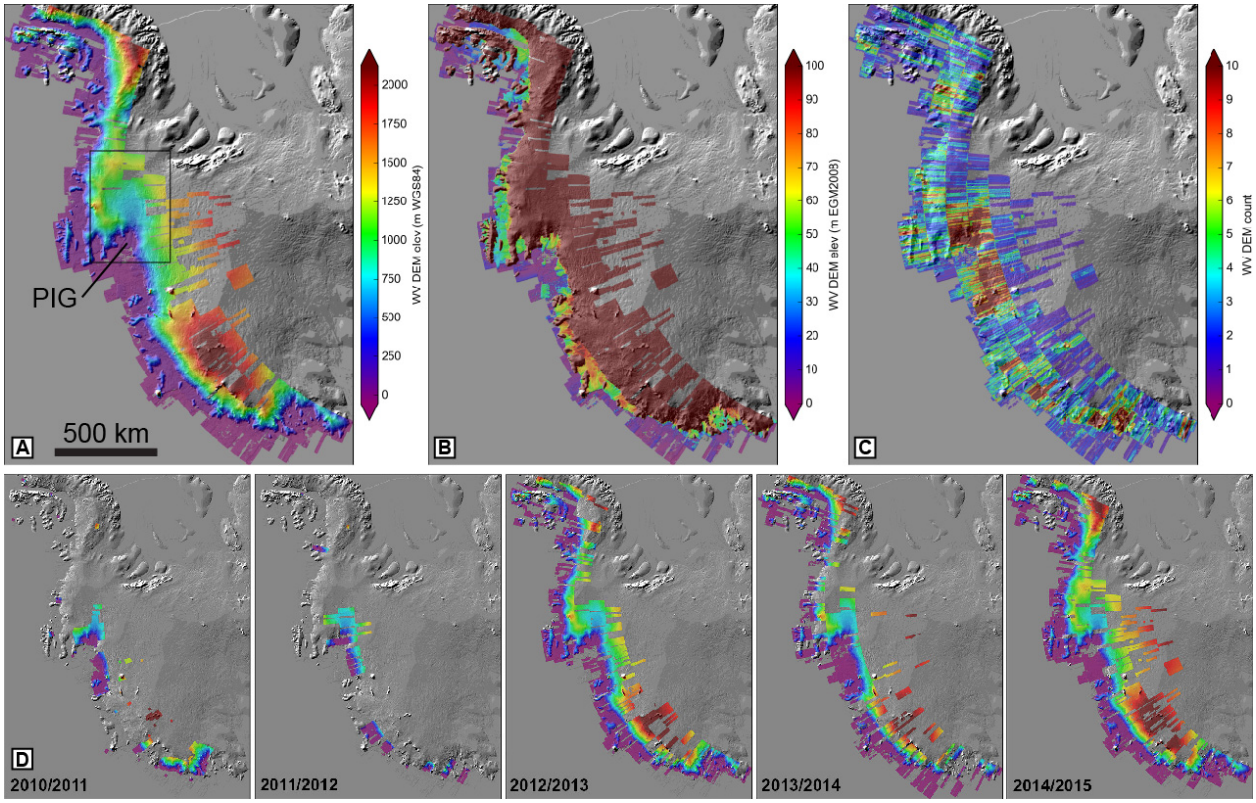

Figure 1-6: Cumulative and annual DEM mosaics for West Antarctica. A) Cumulative mosaic of ~3000 WorldView/GeoEye stereo DEMs from 2010-2015, overlaid on Bedmap2 shaded relief. B) DEM mosaic adjusted to EGM2008 geoid and stretched to show surface elevation over floating ice shelves. C) Total count of DEMs for the 2010-2015 time period. D) Annual DEM mosaics with same color scale as in A. Total cumulative 2-m DEM coverage is 4.11 million km^2.

Chapter 2. AN AUTOMATED, OPEN-SOURCE PIPELINE FOR MASS PRODUCTION OF DIGITAL ELEVATION MODELS (DEMS) FROM VERY-HIGH-RESOLUTION COMMERCIAL STEREO SATELLITE IMAGERY

ABSTRACT

We adapted the automated, open source NASA Ames Stereo Pipeline (ASP) to generate digital elevation models (DEMs) and orthoimages from very-high-resolution (VHR) commercial imagery of the Earth. These modifications include support for rigorous and rational polynomial coefficient (RPC) sensor models, sensor geometry correction, bundle adjustment, point cloud co-registration, and significant improvements to the ASP code base. We outline a processing workflow for ~0.5 m ground sample distance (GSD) DigitalGlobe WorldView-1 and WorldView-2 along-track stereo image data, with an overview of ASP capabilities, an evaluation of ASP correlator options, benchmark test results, and two case studies of DEM accuracy. Output DEM products are posted at ~2 m with direct geolocation accuracy of <5.0 m CE90/LE90. An automated iterative closest-point (ICP) co-registration tool reduces absolute vertical and horizontal error to <0.5 m where appropriate ground-control data are available, with observed standard deviation of ~0.1-0.5 m for overlapping, co-registered DEMs (n=14,17). While ASP can be used to process individual stereo pairs on a local workstation, the methods presented here were developed for large-scale batch processing in a high-performance computing environment. We are leveraging these resources to produce dense time series and regional mosaics for the Earth's polar regions.

2.1 INTRODUCTION

The archive of very high-resolution (<1 m) satellite optical imagery for Earth has grown exponentially in the past decade. Commercial vendors can collect on-demand, sub-meter imagery anywhere on the planet from multiple platforms, with revisit times of less than a day at higher latitudes. Resampled (0.25 m minimum GSD as of June 2014, formerly 0.5 m) image products are now available to United States federal employees and federally-funded civilian researchers through the NextView license — a partnership between the National Geospatial-Intelligence Agency (NGA), commercial vendors, and federal agencies supporting scientific research [*Neigh et al.*, 2013]. Access to these data is enabling exciting new research across many disciplines, including wildlife ecology, forestry, geology, volcanology, and cryospheric sciences.

In 2009, the Polar Geospatial Center at the University of Minnesota initiated a campaign to obtain commercial imagery for the Earth's polar regions, specifically Antarctica, Greenland, and Alaska. This effort has grown significantly, with millions of scenes, many acquired as stereo pairs, now available for polar research and logistical applications. This growing catalog contains multiple years of cloud-free observations (Figure 2-1), including hundreds of repeat observations for many high-priority science targets (e.g. Jakobshavn Isbrae, Greenland [*Shean et al.*, 2014]).

2.1.1 *Instrument Description*

DigitalGlobe currently offers high-resolution optical imagery from six spacecraft. The high inclination and relatively short period of these polar-orbiting satellites is ideal for repeat high-latitude data collection, where competition for commercial tasking is limited. Here, we focus our discussion on the WorldView-1 and WorldView-2 platforms, which constitute the bulk of the archived commercial stereo imagery from 2009-2015.

WorldView-1 and WorldView-2 share a similar pushbroom linescan camera with 11-bit dynamic range and 8–64 line time-delayed integration (TDI). The WorldView-1 focal plane includes 50 panchromatic (450–800 nm) charge-coupled devices (CCDs, also known as Detector Sub-Arrays [DSAs]) with 8-micron pixel size, arranged in two adjacent rows [see Figure 1 of *Updike and Comp*, 2010]. This provides an effective swath width of 35840 pixels, corresponding to ~17.6 km at ~0.5 m GSD for nadir acquisitions. WorldView-2 has a similar panchromatic array, with ~16.4 km swath width and ~0.46 m nadir GSD.

Numerous high-resolution satellite platforms are capable of acquiring stereo imagery [e.g., *Deilami and Hashim*, 2011]. However, only sub-meter GSD images resolve small-scale surface features (e.g., sastrugi, crevasses) that are not apparent at lower resolution (e.g. ~15–30 m GSD Landsat imagery). This high-frequency texture enables precise image correlation for feature tracking and/or surface reconstruction.

The WorldView-1 and WorldView-2 spacecraft acquire images at off-nadir angles from 0° to >45°, with the ability to acquire two or more images of the same target (>90% overlap) in a single orbital pass, forming an along-track stereo pair with typical convergence angles of ~30°–60°. The relatively short time interval (~60–90 seconds) between acquisitions of subsequent along-track images almost always ensures repeat observation of an effectively identical scene with similar illumination. In addition, sensor position/attitude errors for along-track stereo pairs are correlated, which generally improves relative accuracy [*Dolloff and Theiss*, 2012].

While the analysis presented here focuses on along-track stereo pairs, it also is possible to form across-track or "coincident" stereo pairs from two images acquired on different orbits, as long as they have appropriate convergence angle, solar illumination, and time separation [e.g., *Becker et al.*, 2015]. The maximum allowable time separation depends on surface displacement rates and/or textural change rates (e.g. snow accumulation or melt rates). An interval of a few hours is generally appropriate for fast-flowing outlet glaciers, whereas the threshold for a static desert landscape might be several years.

2.1.2 *Data Description*

Nearly all WorldView data available from the NGA archives are Level 1B (L1B) products — seamless, geometrically- and radiometrically-corrected mosaics of sub-images from DSAs in the focal plane array. Images are typically delivered in the National Imagery Transfer Format (NITF), which consists of a comprehensive header and compressed JPEG2000 subdatasets.

The L1B images are often split in the along-track direction and delivered as a set of overlapping, ~30K-line (~14 km) subscenes, rather than a single long image strip (Figure 2-2). Stereo L1B images are often delivered in larger tiled row/column subscenes (R1C1, R1C2, etc.). Adjacent subscenes are prepared with at least 1.8 km (~3600 lines) of overlap, and all subscenes include a right and bottom border of "empty" pixels with DN values of ~1–3.

All DigitalGlobe L1B products have associated XML metadata files that include two sensor models to transform interior sensor coordinates to exterior world coordinates for higher-level image processing. The first is a generalized, industry-standard model involving rational polynomial coefficients [e.g., *Grodechi and Dial*, 2003] for ratios of 20-term, 3rd-degree, two-variable polynomials relating image coordinates (row, column) to geodetic coordinates (latitude, longitude, height). The second is a synthetic, linearized (1-D), rigorous sensor model that relates image line number to time in ephemeris/attitude tables. In practice, the rigorous model is more computationally expensive but more accurate than the RPC model, especially for scenes with significant topographic relief. The Ames Stereo Pipeline supports both models, with a default hybrid approach for optimized performance and quality — initial processing steps are performed with the RPC model, and final triangulation with the rigorous model.

The horizontal geolocation accuracy specification (direct sensor orientation, <30° off nadir, excluding terrain effects) for WorldView-1 and WorldView-2 L1B products is 5.0 m CE90 (90% of circular error, ~1.6-sigma) and 2.3 m root-mean-square error (RMSE) [*DigitalGlobe,* 2014]. A study involving 979 WorldView-1 images and 4412 WorldView-2 images provided observed horizontal accuracy estimates of 4.0 m and 3.5 m CE90, respectively [*DigitalGlobe*, 2014]. Independent studies estimate <2–3 m horizontal RMSE without ground control, and ~1 m RMSE after zero-order RPC correction with only 1–2 ground control points (GCPs) [*Cheng and Chaapel*, 2008].

The vertical accuracy specification for WorldView-1 and WorldView-2 L1B products (<30° off nadir, excluding terrain effects) is 5.0 m LE90 (90% of linear error) [*DigitalGlobe,* 2014], with observed vertical accuracy for WorldView-1 (181 stereo pairs) and WorldView-2 (160 stereo pairs) estimated at 3.7 m and 3.6 m LE90 [*DigitalGlobe*, 2014], respectively. An independent analysis of 50 WorldView-1 stereo pairs found 90% of measured errors for individual stereo pairs to be <3.4 m horizontal and <4.5 m vertical at 101 reference points [*Dolloff and Settergren*, 2010]. We refer the reader to Aguilar et al. [2013, 2014] for a review of other relevant case studies.

2.2 DATA PROCESSING

Many commercial, GUI-based software packages are capable of processing DigitalGlobe stereo image data. While sophisticated and proven, these options can be prohibitively expensive, especially for non-academic users. In addition, these options are less amenable to batch

processing, as they require a trained operator to perform manual tasks (e.g. picking tie points) between "black box" processing steps. Our approach leverages mature, open-source, command-line software to process these data, which enables fully-automated processing of thousands of images in a high-performance computing environment.

The NASA Ames Stereo Pipeline (ASP) [*Broxton and Edwards*, 2008; *Broxton et al.*, 2009; *Moratto et al.*, 2010] was developed by the Intelligent Robotics Group (IRG) at the NASA Ames Research Center with sensor models for NASA planetary missions available from the open source USGS Integrated Software for Imagers and Spectrometers (ISIS) [*Anderson*, 2008]. The planetary community has used ASP for numerous mapping applications [*Broxton et al.*, 2009; e.g., *Beyer et al.*, 2010; *Shean et al.*, 2011; *Re et al.*, 2012; *Watters et al.*, 2015; *Fassett*, 2016].

The ASP code is written in C++, and leverages many 3rd-party open-source libraries. Several core algorithms are implemented in the NASA Vision Workbench (VW) library — an image-processing and computer-vision library designed to efficiently work with extremely large images. This efficiency is accomplished using lazy evaluation and a thread-safe caching system for parallel processing of image blocks (default 256x256 pixels). As a result, most ASP utilities are multi-threaded with limited memory usage.

In 2012, we began integrating support for rigorous DigitalGlobe sensor models and generic RPC models into the existing ASP codebase. As a result of these efforts, many new tools and improvements have been implemented in ASP/VW. The methods presented here outline our preferred mass-production workflow for WorldView-1/2 along-track stereo imagery. The pipeline has been tuned for L1B imagery of the Antarctic and Greenland ice sheets, and test cases in Washington State and Alaska. The terrestrial Cryosphere community has embraced these tools, with several recent publications leveraging ASP-derived DEMs for scientific investigations [e.g., *Pope et al.*, 2015; *Stevens et al.*, 2015; *Willis et al.*, 2015]. The information presented here is based on the October 2014 release of ASP v2.4.2.

Official documentation and precompiled ASP binaries for Linux and Mac OS X are available from the IRG website. The documentation contains detailed background information, sample commands, and recommended parameters for all supported sensors. The latest development source code is available in a public GitHub repository (NeoGeographyToolkit/StereoPipeline and visionworkbench/visionworkbench) under an Apache 2 license.

2.3 METHODS: ASP PROCESSING WORKFLOW

The ASP workflow consists of several modular, command-line utilities (Figure 2-2). This design involves the creation of intermediate files, which increases storage requirements, but allows the user to resume interrupted processing or bypass time-consuming steps when reprocessing. The primary processing steps (utilities) include image preprocessing (stereo_pprc), integer image correlation (stereo_corr), sub-pixel disparity refinement (stereo_rfne), disparity filtering (stereo_fltr), stereo triangulation (stereo_tri), and gridded DEM generation (point2dem). Python scripts (stereo, parallel_stereo) offer wrappers to run the full pipeline with a single command.

2.3.1 *Input Image Preparation*

ASP currently supports stereo processing for two input images, which are referred to as "left" (reference or "master") and "right" (source or "slave") images. All processing is performed in the original coordinate system of the "left" image.

2.3.1.1 L1B Correction

As mentioned earlier, each WorldView-1 and WorldView-2 L1B product is derived from many separate Level 0 (L0) sub-images acquired by individual CCDs (DSAs) in the focal-plane array. These sensors are organized in two rows that are physically offset by ~0.5–1.0 cm (actual dimensions are proprietary). This geometry requires both optical distortion and along-track parallax corrections to derive the rigorous sensor model distributed with the data, which models the 2-D sensor array as a single "synthetic" 1-D line of pixels. The requisite corrections depend on acquisition parameters (i.e., TDI, image scan direction) and product resampling.

DigitalGlobe does not distribute raw L0 data products from individual DSAs and does not disclose the details of the L1B mosaic generation (e.g., seam locations, optical distortion parameters). To the naked eye, the L1B products appear seamless. Sub-pixel disparity maps derived from L1B products, however, consistently reveal sub-pixel offsets of ~0.1–0.5 pixels at DSA boundaries, with largest offsets for low TDI settings. These offsets create systematic DEM artifacts with alternating +/- errors of approximately ~0.1–0.5 m (Figure 2-3). Similar artifacts are observed for other sensors with CCD arrays [e.g., SPOT5, *Leprince et al.*, 2008].

Using a large sample (~1500) of WorldView-1 and WorldView-2 along-track stereo pairs, we derived corrections to remove these offsets from L1B images. The corrections involve DSA

boundary locations (initial sample number and period in pixels) and x and y offsets that minimize the total sub-pixel disparity variance for each combination of spacecraft, TDI setting, and scan direction.

The ASP wv_correct utility applies this correction to input L1B images. We apply the correction to individual subscenes before mosaicking to avoid complications that can arise from differences in subscene resampling (see Section 7.7). While this correction may not be necessary for most applications involving qualitative image analysis, it is essential for production of precise displacement maps (e.g., feature tracking to derive surface velocities), and DEM difference maps with subtle elevation change signals.

2.3.1.2 Subscene Processing

As mentioned earlier, L1B images longer than ~30K lines typically are delivered as multiple subscenes with unique sensor model parameters. Two processing approaches can be used to generate full orthoimages/DEMs from these split products: piecemeal and mosaicked.

The first step of the piecemeal approach involves identifying valid, overlapping "left" and "right" subscene combinations. This is nontrivial, as the subscene boundaries are not coincident, and often a single "left" subscene will need to be processed with two or more "right" subscenes. This yields many possible subscene pair combinations, often with redundant overlap. To overcome this issue, we compute intersection area for all possible overlapping "left" and "right" subscenes, then process only those with overlap area above some threshold (e.g., ~30 km^2). This is more efficient than a brute force approach to batch process all possible combinations, but can result in small residual gaps in coverage. The piecemeal approach generates output products for all subscene pairs, which must be mosaicked to reconstruct the full L1B image extent. Seamless results can be obtained by coregistering subscene point clouds (Section 5) before DEM generation (Section 3.6).

Our preferred methodology combines the individual L1B subscenes before stereo processing. The ASP dg_mosaic utility can mosaic multiple input L1B subscenes from the same parent image (with common DigitalGlobe catalog ID) to produce a single output image with combined xml metadata, including updated sensor models. While the output mosaics often have large file sizes and image dimensions (e.g., ~36000 x 220000 pixels for 1° geocell images), mosaicking eliminates the need to process redundant image data where individual subscenes overlap, and ASP's tile-based

processing can efficiently handle these large images. We find that a nodata threshold value of ~5 successfully eliminates the empty (but nonzero) border from input subscenes.

The dg_mosaic utility generates a new RPC model for the mosaicked L1B product, which can be used for subsequent orthorectification. It should be noted, however, that RPC accuracy decreases with increasing image size, since a polynomial of the same degree is used to characterize a much larger geographic extent. Thus, the piecemeal approach may provide improved results if the RPC sensor model is used during triangulation. Such a limitation does not apply when using the rigorous sensor model for triangulation, which is the ASP default for DigitalGlobe imagery.

2.3.1.3 Bundle Adjustment

An optional bundle adjustment tool (bundle_adjust) can update sensor ephemeris/attitude information for two or more input images. Interest points are identified and matched for all input images, and valid matches are forward-projected to triangulate 3D points using the rigorous or RPC sensor model. The user also can provide known ground control point coordinates and corresponding image pixel locations. The 3D point locations and sensor positions/orientations are optimized using one of several solvers and robust cost functions to minimize reprojection error. The updated ephemeris/attitude information can then be used during triangulation of dense matching results.

Considering the inherent geolocation accuracy of WorldView-1 and WorldView-2, and limited observed triangulation error variance (e.g., Figure 2-3), we typically bypass this step. We have found that automated co-registration of triangulated point clouds or final DEM products using a rigid-body transformation (see Section 5) can accomplish similar results, with reduced processing time and no need for manual identification of control points in input images. However, bundle adjustment before stereo reconstruction can be essential for other sensors (e.g., early planetary orbiters).

2.3.1.4 Input Orthorectification

ASP currently supports two types of input images: 1) L1B images in original sensor coordinates (image line, sample) and 2) orthorectified images in real-world, projected coordinates (e.g. UTM, polar stereographic).

The unmodified L1B images preserve original image GSD, do not require existing knowledge about surface topography, and are not susceptible to distortion caused by geolocation error and/or

errors in the DEM used for orthorectification. During ASP preprocessing, interest point matching is used to align the "right" image to the "left" image via a simple transformation to reduce disparity offsets. Currently supported transformations include generalized projective (Homography) and affine epipolar (AffineEpipolar). These alignment options generally work well, but may fail for scenes with significant nonplanar relief (e.g. a large, isolated stratovolcano) or limited image contrast/texture.

When an existing DEM covering the extent of input images is available, the left and right L1B images can be aligned via multithreaded orthorectification. This process removes most of the terrain disparity signal, and the subsequent stereo processing effectively uses residual feature offsets to refine the existing DEM. Our mass-production workflow utilizes the RPC sensor model to orthorectify mosaicked images, with an appropriate projection automatically determined by input image latitude.

The optimum orthoimage resolution depends on the frequency content of the source images and the application-specific requirements for output products. Our workflow uses the minimum GSD (highest resolution, smallest off-nadir angle) of the two input images to preserve as much high-frequency texture as possible. We have found, however, that a subsampled orthoimage resolution of ~1.0 m GSD often produces comparable results with significantly reduced data volume and processing time for WorldView imagery. For typical meter-scale ice-sheet texture, correlation success decreases substantially for subsampled input image resolutions >2.0 m GSD.

Our workflow pre-computes orthoimage extent using the intersection of corner coordinates listed in the "left" and "right" xml metadata. We also smooth the input DEM used for orthorectificaion to avoid introducing artifacts and distortion. We have successfully processed WorldView-1/2 imagery using the USGS National Elevation Dataset DEM [*Gesch et al.*, 2002], Greenland Ice Mapping Project (GIMP) DEM [*Howat et al.*, 2014b], BEDMAP2 Antarctic Surface DEM [*Fretwell et al.*, 2013], and various gridded airborne LiDAR DEMs.

2.3.2 *Correlation*

Correlation in ASP is performed by a generalized image correlator that attempts to match a "reference" image chip (default 21x21 pixels) from the "left" image with similar "source" chips extracted from a specified 2-D search window in the "right" image. The correlation is computed using an efficient caching scheme in the spatial domain rather than the frequency domain to allow

correlation with missing data. Multiple cost metrics are available, but the default normalized cross-correlation offers the best results for most applications. To improve match confidence, the correlation is computed both forward (L–>R chip matching) and reverse (R–>L) with a configurable difference threshold (default 2 pixels).

The correlator produces dense disparity maps, where an integer disparity (x and y pixel offsets for matched chips) is computed for each valid pixel in the input image. Correlator performance is closely tied to the search window dimensions — runtime is proportional to the number of pixels in the image times the number of offsets in the search window. This scheme is efficient for small search ranges and scenes with limited relief, but can require long runtimes if significant offsets remain following initial image alignment, or if the DEM used to orthorectify the input images contains significant errors. To overcome this issue, ASP uses a Gaussian pyramid approach, iteratively performing the correlation on subsampled versions of the input images, and using the low-resolution disparities to seed finer-resolution correlation. Over ice-sheet surfaces, however, images subsampled to resolutions coarser than ~2–8 m can appear nearly featureless, potentially causing this hierarchical search scheme to fail.

Search window dimensions can be defined globally (constant over the entire input image), or locally (spatially-variable). The latter is accomplished by initially seeding the correlator with a low-resolution map of the optimal x and y search window offsets and search window dimensions (Figure 2-2). Proper seeding can effectively limit the local search window size to only a few pixels for all pyramid levels and all locations in the input image, offering significant correlator performance improvement. The low-resolution search window maps also include a mask defining regions to be correlated, which prevents time-consuming searches over regions lacking sufficient texture (e.g., clouds and open water).

Depending on input frequency content, our workflow seeds the correlation using one of two methods: 1) dense correlation of subsampled input images (seed-mode 1), or 2) sparse, local disparities computed from full-resolution input images (seed-mode 3). The former performs well for input images with substantial low-frequency texture (e.g. scenes with significant relief and/or well-distributed albedo differences in the subsampled images), while the latter is necessary for input images with limited low-frequency contrast/texture (e.g., ice-sheet interior). Regardless of seeding method, a tile timeout option is leveraged to prevent problematic blocks from slowing overall progress.

2.3.3 *Sub-pixel Refinement*

The ASP integer correlation step generates dense grids of discrete integer disparity offsets. This is a relatively crude estimate, and more precise disparity maps, potentially up to ~0.1 pixel resolution, can be generated via sub-pixel refinement [e.g., *Heid and Kääb*, 2012]. Three sub-pixel refinement algorithms are available in ASP [*Broxton et al.*, 2009]: parabolic (subpixel-mode 1), affine adaptive Bayes expectation-maximization (subpixel-mode 2), and affine adaptive (subpixel-mode 3).

With parabolic refinement, a 2-D parabola is fit to correlation cost scores within a 3x3 window around each valid pixel in the integer disparity map, and new sub-pixel disparity values are estimated at the parabola minimum. This approach is very efficient, but can suffer from "pixel-locking" artifacts in the output DEM [e.g., *Shimizu and Okutomi*, 2002]. For highest-quality results, ASP offers a more robust sub-pixel refinement — affine adaptive with Bayesian expectation-maximization [*Nefian et al.*, 2009]. This "BayesEM" sub-pixel refinement computes a 2-D affine transformation to match the "right" and "left" image chips within a Bayesian expectation-maximum framework, offering improved results for images distorted by steep topography and noise. Additionally, ASP now includes an affine adaptive refinement option [e.g., *Stein et al.*, 2006] without the computationally-intensive BayesEM framework, offering a compromise between output quality and processing time.

The choice of sub-pixel refinement approach is application-specific. BayesEM provides superior results for scientific analyses of small-scale topographic features with steep slopes (e.g. moraines, crevasses). Parabolic refinement should be adequate for applications that require DEM products with high accuracy but relatively coarse resolution over surfaces with limited relief. In practice, we begin with parabolic sub-pixel refinement, and preserve the integer disparity maps (D.tif) for later reprocessing with BayesEM if desired. It is also possible to limit refinement to a user-specified sub-region, which can significantly reduce runtimes.

2.3.3.1 Sub-pixel Refinement Comparison

We performed systematic tests to evaluate the performance and output quality of available ASP refinement methods. The first involved 12 WorldView-1/2 stereo pairs over volcanoes in the Pacific Northwest, with input image dimensions of ~36000x36000 pixels. Wall time for BayesEM refinement was ~41–114 times greater than for Parabolic refinement on a dedicated computing

node (dual 8-core 2.60GHz Intel Xeon E5-2670, 16 ASP threads). A second test was performed for a ~13000x13000 pixel section from two stereo pairs acquired over supraglacial lakes on the Greenland ice sheet (Figure 2-4). All refinement options were run using 12 ASP threads on a server with eight 4-core 2.27GHz Intel Xeon X7560 processors. Results are summarized in Table 2-1 and Figure 2-5.

Comparison of output DEMs produced with different refinement algorithms and posting (Figure 2-5) shows variation in morphologic detail, especially over steep slopes and regions with increased roughness. These tests show that the BayesEM and affine adaptive refinement offer superior results over parabolic refinement, but at the expense of a ~50–150x and ~10-30x increase in CPU time, respectively. We observe limited differences amongst refinement methods for smooth surfaces, especially for >8-32 m posting. We also note that reducing output DEM posting by a factor of ~8x eliminates most parabolic refinement artifacts and fills small data gaps. See Section 3.6 for further discussion of output product generation.

2.3.4 *Filtering*

Regardless of sub-pixel refinement approach, it is inevitable that the output disparity map will include spurious matches that lead to artifacts ("blunders") in the triangulated point cloud and gridded DEM products. The ASP workflow includes filtering algorithms to remove these problematic disparity values before triangulation. We have found that the erosion of small, isolated clusters (~32-1024 pixels) surrounded by missing data removes many problematic disparity values, with minor loss of detail. A subsequent mean difference to neighbors (filter-mode 1, default) or thresholding (filter-mode 2) can help remove residual outliers, with additional filtering options available during DEM generation (section 3.6).

2.3.5 *Triangulation*

Triangulation combines spacecraft ephemeris/attitude information with a sensor model and known image disparity offsets to generate a 3D point cloud. The ASP triangulation routine computes 3D coordinates (in a Cartesian Earth-Centered Earth-Fixed [ECEF] coordinate system) for the closest intersection of forward-projected rays originating from the physical locations (i.e., sensor orbital position) of all matched pixels. For the rigorous DG sensor model, this is accomplished by querying the ephemeris/attitude tables and interpolating camera pose at linetimes corresponding

to “left” and “right” matched pixel location in the refined, filtered disparity map. If the input images were initially orthorectified using a low-resolution DEM (Section 3.1.4), an inverse transformation (using the same external DEM from the orthorectification step) is applied to determine original L1B image coordinates of the disparities, which are then triangulated as described above.

The output is a 4-band raster point cloud file format (PC.tif). For every successfully-matched pixel in the input “left” image, band 1 contains the triangulated ECEF x-coordinate, band 2 the y-coordinate, and band 3 the z-coordinate (Figure 2-2). Band 4 provides a triangulation error metric (distance, in meters, between the two rays at closest intersection) that can be used to evaluate the quality of the disparity matches, the sensor model, and ephemeris/attitude data.

2.3.6 *Output Product Generation*

The ASP point2dem utility converts an input point cloud (native PC.tif format, CSV, or LAS) to a gridded DEM. Multiple filters are available for outlier removal, including a triangulation error filter (percentile or absolute threshold) and threshold filter that removes outliers relative to the median of a rolling window. We have found the default percentile triangulation error filter (3 * value at 75^{th} percentile) to be effective at removing common blunders for WorldView-1/2, eliminating the need for the threshold median filter. After filtering, a final elevation value is calculated for each output grid cell using a Gaussian weighted average of points within a specified radius (default, one cell width). Output elevation values are computed relative to the WGS84 ellipsoid and the ASP dem_geoid utility can be used to apply a geoid correction (e.g., EGM96, EGM2008) to obtain orthometric heights.

Since the along-track WorldView stereo products only involve two images, steep slopes within an acquisition-dependent aspect range are susceptible to occlusion. The point2dem utility includes optional gap-filling routines that can improve the aesthetics of output DEM and orthoimage products. Our production workflow does not use these options, however, as we wish to limit scientific analysis to elevation values derived from triangulated points.

The default point2dem output posting is similar to the “left” image resolution. Adjacent points are not necessarily independent, however, with the degree of spatial correlation dependent on input image texture content and correlator chip size. Figure 2-5 shows that native (~0.5 m) DEM posting does not offer any improvement over the “4x” (~2 m) posting. Thus, we reduce output DEM

posting by a factor of at least ~4, which results in artifact mitigation, noise reduction, and reduced output file size.

2.4 BENCHMARK TESTS

We deployed ASP on the NASA Pleiades Supercomputer, and performed benchmarking and profiling tests for the workflow outlined in Section 3. Figure 2-6A shows a breakdown of runtimes for 149 WorldView-1/2 stereo pairs (typical dimensions ~36000x220000 pixels) over West Antarctica, processed using 12 ASP threads on Pleiades Westmere nodes (dual 6-core 2.93 GHz Intel Xeon X5670). These tests show that the correlation and refinement steps require the longest wall time with greatest spread due to input image variability (e.g., image quality, surface texture, clouds) and problematic tile issues discussed below.

Figure 2-6 also shows the results of a benchmarking test (on a Pleiades Bridge node, 8 quad-core 2.27 GHz Xeon X7560 processors) with variable number of cores/threads (1–32) for the clipped ~13000x13000-pixel images shown in Figure 2-4A. Additional cores/threads significantly reduce runtime, with diminishing performance improvements beyond ~8–10 cores/threads.

Several ASP processing steps (e.g., orthorectification, correlation, refinement) can efficiently utilize all available CPU resources for extended periods of time. However, some stages are limited by the speed at which data can be read from or written to the disk, and some steps cannot be parallelized (e.g. computing global statistics during preprocessing). Also, problematic (often featureless) tiles can delay further processing and cause temporary drops in CPU utilization due to a sequential tile-writing requirement for the tif file format. This can be mitigated with the tile timeout option, tuned VW tile cache parameters, and/or a wrapper that splits input images for parallel processing (parallel_stereo).

2.5 DEM CO-REGISTRATION WITH CONTROL DATA

While the <5.0 m geolocation accuracy of the L1B WorldView-1/2 products is impressive, it is insufficient for many precise geodetic applications. We now consider approaches to further improve horizontal and vertical accuracy of DEM products.

Traditional photogrammetric workflows involve manual identification of tie points and control points in input imagery that are used to improve accuracy during bundle adjustment. Unfortunately, this approach does not scale for extremely large datasets, and it assumes either

near-simultaneous image acquisition or a static surface — a situation that does not hold for WorldView data of the Earth's dynamic ice sheets. Numerous alternative approaches have been developed to remove offsets between overlapping gridded DEMs [e.g., *Berthier et al.*, 2007; *Nuth and Kääb*, 2011; *Noh and Howat*, 2014]. Here, we present a generalized, automated co-registration workflow for the ice sheets that relies on accurate, temporally- and spatially-coincident control data (i.e., GPS, airborne/terrestrial LiDAR point clouds, existing gridded DEMs).

The ASP pc_align utility automatically co-registers an input "source" file (point cloud or gridded DEM) to available "reference" control data. This is accomplished using a point-to-plane or point-to-point iterative closest point (ICP) algorithm [*Pomerleau et al.*, 2013] that iteratively improves the transformation required to minimize offsets. The default point-to-plane algorithm works best for control data with adequate spatial distribution over surfaces with sufficiently-variable slope and aspect. Alternatively, the point-to-point ICP algorithm can offers superior co-registration results for smooth, planar surfaces like those over the ice sheet interior. The ICP output is a 3-D transformation (3 translation and 9 rotation terms) in the ECEF coordinate system, which can optionally be limited to a 3-parameter translation without rotation. The utility optionally applies this transformation to export a corrected 4-band ASP point cloud.

We have found that a simple translation (i.e. removal of constant horizontal and vertical bias) is almost always sufficient to correct WorldView-1 or WorldView-2 PC/DEM products. Based on this finding, it follows that only a small number of control points are required for co-registration [e.g., *Cheng and Chaapel*, 2008]. We have also observed, however, that a limited number of the larger DEM products (e.g., ~17x110 km geocell pairs) display an along-track, planar tilt of ~1–3 m (~0.5–1.0x10^{-3} degrees) and/or an occasional ~1 m cross-track tilt. For these situations, control data should be well distributed throughout the scene to constrain an appropriate rotation correction.

2.5.1 *Ice Sheet Control Points*

We have compiled a comprehensive database of available control data for Antarctica and Greenland (Table 2-2). The primary sources include NASA ICESat-1 Geoscience Laser Altimeter System (GLAS) data [*Zwally et al.,* 2002; *Schutz et al.,* 2005], NASA Airborne Topographic Mapper (ATM, [*Krabill et al.*, 2002; *Martin et al.*, 2012]) and Land, Vegetation, and Ice Sensor (LVIS, [*Blair et al.*, 1999; *Hofton et al.*, 2008]) airborne LiDAR data, all available from the National Snow and Ice Data Center. These data are typically collected as annual or seasonal

campaigns spanning relatively short time windows (weeks–months), with data acquisition for a particular site typically occurring over ~1–3 days.

We filter the dense L1B (qfit format) ATM data to remove unwanted returns (e.g., crevasse floors). Median elevation values are computed for 10-meter grid cells after removing outliers (20–80th percentile pass for rolling 20-meter window). For each of these points, a plane is fit to all points within a 50 m radius, and the point is preserved if it falls <10 m from this plane. Additional filters for GLAS data remove points with low uncorrected reflectivity (reflctUC < 0.025) and high waveform misfit (iceSVar > 0.04 mV).

Our automated workflow queries the filtered control point database for an input DEM extent and extracts independent surface velocity data [*Joughin et al.*, 2010a; *Rignot et al.*, 2011b] for the same extent. For each valid control point within this extent, an estimated displacement ($\|\mathbf{v}\| \cdot dt$) is computed from the sampled 2-D velocity vector $\mathbf{v}$ and the time offset dt between the control point timestamp and DEM timestamp (Figure 2-7). The point is discarded if the estimated displacement exceeds some threshold (e.g., 5.0 m), or the time offset exceeds a fixed threshold (e.g., 120 days). The remaining points tend to be clustered over static surfaces (e.g. exposed bedrock) and "dynamic control surfaces" (e.g., low-velocity ice with limited surface slope and roughness).

An absolute elevation filter (e.g., >10 m above sea level) and ice-shelf mask removes points over floating ice, while an absolute elevation difference filter (e.g., $|z_{DEM} - z_{GCP}| < 30$ m) excludes outliers. Site-specific filtering parameters are set according to local control point availability and prior knowledge of local ice sheet dynamics. If a sufficient number of control points with sufficient spatial distribution remain, they are used to correct the DEM and estimate accuracy.

Looking forward, the NASA ICESat-2 mission [*Abdalati et al.*, 2010] is slated for launch in 2017. The multi-beam laser altimetry data will offer near-contemporaneous, global control data with ~10 cm accuracy for all subsequent WorldView stereo DEMs. These data will eliminate the need for complex control point filtering algorithms and provide robust accuracy estimates for DEMs over dynamic surfaces, regardless of static control surface availability.

2.6 Accuracy analysis

We now present two case studies to estimate relative and absolute horizontal/vertical accuracy for WorldView-1 and WorldView-2 DEMs generated using ASP. Each involves a different setting, with variable surface conditions and control data availability.

2.6.1 *Summit, Greenland Case Study*

We obtained all available 2010–2013 WorldView stereo image pairs with <75% cloud-cover for Summit, Greenland, where the National Science Foundation maintains Summit Station (Figure 2-7, Figure 2-8). This location is just west of the ice-sheet divide and has extremely low surface slopes (<0.2°), surface velocities (~3-5 m/yr, Figure 2-7B), and annual accumulation rates (~0.2 meters water equivalent per year). Recent studies of accumulation rates, firn compaction rates, and ice dynamics near Summit show that surface elevations remained effectively constant from ~2010–2013 (R.L. Hawley, personal communication, 2015). These characteristics make Summit an ideal calibration site for satellite observations of the Greenland ice sheet [e.g., *Siegfried et al.*, 2011].

We processed WorldView-1 (n=3) and WorldView-2 (n=11) stereo pairs using the workflow outlined in Section 3, with seed-mode 3, parabolic refinement, and ~2 m output DEM posting. A total of 3.73×10^6 control points spanning 1999–2014 were extracted for the area covered by these DEMs (Figure 2-7B). The control points were filtered with a maximum time offset *dt* of 1.5 years and a maximum $\|\mathbf{v}\| \cdot dt$ displacement of 10 m. Final control point samples included 8.4×10^4 to 3.3×10^5 points, with >2–5 non-parallel flightlines available for each DEM (Figure 2-7C). A random sample of 10^5 points was used for co-registration, with 75% of these points considered inliers during ICP. The points not used for co-registration can serve as independent check points, although their spatial distribution is nearly identical along flightlines, and we compute final error estimates using all original filtered control points for each DEM.

Co-registration was performed with point-to-point ICP, a maximum displacement setting of 20 m, and final transformation limited to a translation (no rotation). The high-density DEMs (~0.25 pts/m^2) were set as the "reference" for co-registration, with low-density control points (~0.01 pts/m^2) as the moveable "source." The DEMs were then corrected using the inverse of the final ICP solution. These ECEF translation vectors were converted to a local stereographic projection (Figure 2-9A) and the resulting horizontal and vertical offsets were used to compute CE90 and LE90 for the 14 DEM sample using standard formulas [*Federal Geographic Data Committee*, 1998]:

$$RMSE_{j=\{x,y,z\}} = \sqrt{\frac{1}{n}\sum_{i=1}^{n} \Delta j_i{}^2} \tag{2.1}$$

$$CE90 = 2.146 \cdot (RMSE_x + RMSE_y)/2 \quad (2.2)$$

$$LE90 = 1.6449 \cdot RMSE_z \quad (2.3)$$

Additionally, errors $\Delta z_i = (z_{GCP_i} - z_{DEM_i})$ and absolute errors $|\Delta z_i|$ at all control points were computed for each DEM, both before and after the transformation. These errors rarely display normal distributions and outliers can skew traditional accuracy measures (e.g., RMSE, standard deviation), so robust statistics [e.g., *Höhle and Höhle*, 2009] were computed to further characterize ASP/WV uncertainty. For each DEM, the median (50th percentile), 16th and 84th percentile of signed errors was computed (Figure 2-9B), as was the normalized median absolute deviation (NMAD):

$$m_{\Delta z} = median(\Delta z_i) \quad (2.4)$$

$$NMAD = 1.4826 \cdot median(|\Delta z_i - m_{\Delta z}|) \quad (2.5)$$

which provides a robust estimate of standard deviation.

2.6.1.1 Absolute Vertical Accuracy

The observed 5.22 m LE90 for uncorrected DEMs slightly exceeds the 5.0 m CE90/LE90 specification published by DigitalGlobe (Table 2-3), although 6 of these pairs contain at least one image acquired at off-nadir angles >30° (Figure 2-9C). One DEM (April 4, 2013) acquired with a combination of relatively high off-nadir angles (37.7°, 26.1°) and low convergence angle (33°) displayed vertical bias of +8.83 m (Figure 2-9C). We note that if this DEM is excluded, LE90 drops to 3.61 m (Table 2-3) for the remaining 13 DEMs acquired with more favorable geometry.

The sample of Summit DEMs shows an apparent vertical bias of +2.1 m, with uncorrected WorldView DEMs higher than control points (Figure 2-9A-B, Table 2-3). There are many possible factors that could contribute to such a bias (e.g., sensor model error, preferred acquisition geometry for a particular geographic location, a small systematic error in the ASP code). Fortunately, we have run enough test cases to confirm that this +2 to +3 m vertical bias appears systematic, suggesting it is related to an error in the ASP/WorldView workflow and can be systematically removed from uncorrected DEM products before co-registration and accuracy analysis. Removing this bias reduces LE90 to 3.91 m (Table 2-3).

Figure 2-9B shows that ICP co-registration successfully removes vertical bias for all Summit DEMs (Table 2-3). The NMAD values remain the same, as horizontal corrections are small, with

limited potential for improvement over near-planar surfaces with limited slope/aspect variance. After co-registration, both RMSE and NMAD are ~0.2 m for all DEMs (Table 2-3).

2.6.1.2 Relative Vertical Accuracy

We now consider residual errors in the co-registered Summit DEMs. The standard deviation of elevation values computed for every pixel in a "stack" (n=14) of overlapping DEMs ranges from 0.1 to >0.5 m (Figure 2-10B), with a mean value of 0.19 m. If we assume that residual translation offsets are negligible and the surface is not changing over time, then these values provide a measure of relative DEM accuracy. Residual error is related to "jitter" artifacts, DSA boundary artifacts, pixel-locking artifacts, "blunders" due to spurious disparities, and other sources of measurement noise.

Qualitatively, the map of standard deviation displays several characteristics that warrant discussion. The first involves primarily along-track undulations that we attribute to independent spacecraft "jitter" artifacts in each DEM (Figure 2-10B). The orientation of these artifacts is variable, as the available DEMs include both ascending and descending acquisitions, and artifact amplitude appears dampened over areas with higher sample count. Section 7.6 offers further discussion of these artifacts.

Standard deviation values appear to increase near the lateral margins of some input DEMs (Figure 2-10B). This likely involves increased error in the sensor geometry and/or optical distortion correction near the edges of the sensor, especially for certain TDI/scan-direction combinations. This variability also affected the derivation of L1B corrections applied by the wv_correct utility (Section 3.1.1), which could compound observed error near lateral DEM margins.

2.6.2 *Tracy Glacier Region, Greenland Case Study*

The Summit analysis involved smaller DEMs over near-planar surfaces with extremely low slopes and surface velocities, effectively offering a "best case" scenario for DEM accuracy evaluation. The following analysis includes larger DEMs over an area near the Greenland coast with variable relief, slope, and aspect.

We obtained all available 2012-2013 WorldView stereo image pairs with cloud-cover <75% in a 1°-latitude geocell near Tracy Glacier in Northwest Greenland (Figure 2-11). This location covers several outlet glaciers, fjords, small ice caps, and exposed bedrock. We processed 17 overlapping

~17–110 km WorldView-1 (n=9) and WorldView-2 (n=8) stereo pairs using the same methodology described in the Summit case study.

A total of 4.4×10^7 filtered database control points spanning 1999–2014 were available for co-registration (Figure 2-12B). For this analysis, we limited control data to static bedrock surfaces. A "RockMask" of ice-free surfaces was generated from the 90 m Greenland Ice Mapping Project (GIMP) IceMask and OceanMask datasets [*Howat et al.*, 2014b]. The extent of this mask was further reduced with three 1-pixel erosion iterations to avoid pixels near ice margins and shorelines. After applying this RockMask and clipping to individual DEM extents, the total number of control points per DEM ranged from $\sim 8.5 \times 10^5$ to $\sim 1.5 \times 10^6$, with broad spatial distribution over bedrock surfaces (Figure 2-12B).

We expect some surface elevation variability due to snow accumulation on bedrock surfaces during control point and/or DEM acquisition. Snow depth measurements at Thule airport varied from 0 to ~0.5 m from 2012–2013 [*Czimczik*, 2014]. Additionally, valleys tend to accumulate windblown snow and can preserve snow longer into the melt season. Thus, we might expect increased elevation variance near steep valley walls. To mitigate these effects, we did not apply a time offset filter — final control data included all available points from 1999–2014, with acquisition during different times of year (Figure 2-12C). This approach, combined with the 25% outlier removal during ICP, should limit the influence of points acquired when seasonal snow was present on bedrock surfaces.

2.6.2.1 Results

As with Summit, the ICP co-registration successfully removes vertical bias for all input DEMs (Figure 2-13, Table 2-3). In addition, horizontal corrections reduce the Δz_i error spread for all DEMs (Figure 2-13B), with sample (n=17) average NMAD of 0.44 m after co-registration (Table 2-3). Standard deviation of elevation values in the stack of overlapping DEMs range from ~0.1–0.5 m over flat bedrock, ~1–2 m over ice-covered lakes, and >2–5 m over dynamic outlet glaciers (Figure 2-11C). The latter provides a sample of the seasonal and interannual ice thickness change signals motivating much of this work.

2.6.2.2 Slope-dependent Accuracy

The mean of standard deviation values for the stack of co-registered DEMs is 0.46 m over bedrock (Figure 2-14B). An analysis of stack standard deviation values that fall within 1.0° slope bins

shows an apparent linear relationship between DEM error and surface slope (Figure 2-14C). The bin median for slopes up to ~35° is <1.0 m, although the spread within each bin increases with increasing slope. Bin median values of ~0.2-0.4 m are observed for <10° slopes, which should be representative of most ice sheet surfaces. These results are consistent with a similar error vs. slope analysis for photogrammetrically-derived DEMs over mountainous terrain [*Müller et al.*, 2014]. We note that the input DEMs for this test were generated with ASP's Parabolic sub-pixel refinement, which can introduce "step" artifacts over steep slopes (Figure 2-5). Reprocessing with BayesEM refinement would likely decrease observed error over steeper slopes, which would decrease the slope of the linear fit in Figure 2-14C.

2.7 Limitations and Discussion

Along-track stereo WorldView imagery offers an exciting, high-resolution dataset for Earth science applications. As with any remote sensing technology, however, these data and methods are subject to several limitations, which we now address.

2.7.1 *Atmosphere*

First and foremost, these are optical data, and successful image correlation requires a clear view of the surface. Opaque clouds in the scene cause DEM data gaps, but we have found that partial atmospheric obfuscation (e.g. thin clouds, smoke, haze, etc.) has essentially no impact on output DEM quality, as long as sufficient surface texture is visible through the clouds to allow correlation. Unlike commercial photogrammetric software options (e.g. SOCET SET), ASP does not currently include corrections for atmospheric refraction, as it was originally developed for NASA planetary orbiters around airless (or nearly airless) bodies. However, this effect should be negligible for WorldView-1/2 altitude and typical off-nadir angle range.

2.7.2 *Water*

We have found that it is possible to correlate bathymetric surfaces in shallow (~1–5 m), clear water (e.g., surface meltwater lakes on the Greenland ice sheet, Figure 2-4). Accurate triangulation of subaqueous surfaces, however, requires a localized refraction correction — functionality that has not yet been implemented in ASP v2.4. Without this correction, shallow subaqueous surfaces will

have an apparent positive vertical offset, with magnitude dependent on water depth and pair geometry.

Deep open water will almost always fail to correlate, especially when surface waves or sun glint are present. The primary exception involves floating surface features such as sea ice or flotsam, which can provide acceptable correlation results (e.g., Figure 2-4). One must use caution during interpretation, however, as these floating features may experience significant (>0.1–5.0 px) displacements due to waves or surface winds/currents over the ~60–90 second interval between along-track image acquisition. If ignored, these displacements will produce anomalous topographic signals, sometimes 10's to 100's of meters depending on displacement magnitude and pair geometry. While this situation is not ideal for surface reconstruction, it may be valuable for other applications, as it is possible to measure these relatively rapid displacements through feature-tracking [e.g., *Kääb and Leprince*, 2014].

2.7.3 *Vegetation*

Samples of WorldView-1/2 stereo data over glaciers in the Pacific Northwest with nearby forests and meadows confirm that correlation success is typically near-perfect over exposed rock and ice, with increased noise and data gaps over vegetated surfaces. Stereo geometry and vegetation characteristics (e.g., density, height, shape, and spacing) will affect correlation success. For sparse, low-lying vegetation (e.g. winter brush), it often is possible to image the underlying ground surface, ultimately providing a digital terrain model (DTM) of surface elevations. For dense vegetation, successful correlation is still possible, but the resulting digital surface model (DSM) will include vegetation/canopy . While undesirable for many geoscience applications, these measurements have value for forestry and other biomass inventory applications, especially when existing bare-earth DTM data are available.

2.7.4 *Image Saturation and Shadows*

The 11-bit WorldView-1 and WorldView-2 sensors offer excellent dynamic range and image contrast. With appropriate sensor TDI/gain settings during acquisition, high signal-to-noise ratios are possible for both high (e.g., snow, ice) and low (e.g., basaltic rock) albedo surfaces in the same scene. The same is also true for scenes with significant relief, where both illuminated slopes and shadows contain sufficient contrast for successful correlation. While continuous DEMs can be

produced for these scenes (excluding occluded areas), we have noted artifacts along some shadow edges (e.g., Figure 2-8) due to the pixel-locking phenomenon discussed in Section 3.3.

Many early and late season images at high latitudes have very high solar incidence angles (>80° from nadir). If sensor TDI/gain settings are not properly set, partial saturation of extremely bright or dark regions can occur. While this often produces substantial gaps in disparity maps, we have found that successful correlation is still possible for saturated regions when limited surface texture is visible.

2.7.5 *DSA Boundary Artifacts*

As described earlier, the sub-pixel DSA offsets in the L1B mosaics can produce alternating ±0.1–0.5 m vertical errors in output DEMs (Figure 2-3). The wv_correct utility mitigates these artifacts, but corrected images will inevitably contain residual linear artifacts, especially near image margins (Figure 2-3, Figure 2-10B). These artifacts are highlighted when differencing WorldView DEMs over surfaces with little or no elevation change. In some cases, an empirical correction for the full scene can be derived from along-track statistics over these surfaces [e.g., *Nuth and Kääb*, 2011], although this becomes more challenging for scenes with significant relief due to distortion of initially linear artifacts.

2.7.6 *Jitter Artifacts*

In section 6.1, we identified along-track elevation errors with magnitude of ~0.1–0.5 m (Figure 2-10B) due to "jitter" — slight variations in spacecraft orientation that are not captured by the 50 Hz attitude tables provided with the L1B rigorous sensor model. Comparable artifacts and corrections [e.g., *Mattson et al.*, 2009] are well documented for the High Resolution Imaging Science Experiment (HiRISE) camera aboard the NASA Mars Reconnaissance Orbiter [*McEwen et al.*, 2007], which shares a similar heritage with WorldView-1/2. In theory, similar corrections could be derived for WorldView-2 using the physically offset panchromatic and multispectral sensors. Unfortunately, unlike HiRISE, the raw L0 image data from individual WorldView-2 DSAs are not available for additional processing. As with the L1B DSA artifacts, these "jitter" artifacts are most apparent in DEM difference products, and custom corrections can potentially be derived for some applications [e.g., *Berthier et al.*, 2007; *Nuth and Kääb*, 2011].

2.7.7 *Resampled Subscene Artifacts*

Prior to June 2014, federal license restrictions required commercial image vendors to downsample L1B data to ≥0.5 m GSD for civilian customers. Due to evolving off-nadir angles for longer image acquisitions, many WorldView-2 products contain some full-resolution subscenes with collected/product GSD of >0.5 m and some subscenes with collected GSD <0.5 m and resampled product GSD of 0.5 m. This selective resampling also affects the rigorous sensor model parameters (e.g., synthetic detector pixel size). The dg_mosaic utility handles these cases by scaling all input subscenes to generate a seamless image with uniform sensor model parameters. We have noticed, however, that some output DEMs derived from these images can display residual artifacts and elevation offsets along subscene boundaries. In some cases, an along-track tilt of ~1 m is observed for each individual subscene, creating a sawtooth profile along the full DEM. Despite multiple efforts to develop a dg_mosaic workaround, we have found that it is often simpler to reorder these problematic catalog IDs, or to generate DEMs using the piecemeal processing workflow described in section 3.1.2.

2.8 Additional Sensors and Future Work

While this work focuses on WorldView-1 and WorldView-2 data, the DigitalGlobe archive contains VHR stereo pairs acquired by the IKONOS, QuickBird-2, and GeoEye-1 sensors, with data acquisition beginning in ~1999. Although the resolution and quality of ephemeris/attitude information for IKONOS and QuickBird-2 is inferior to WorldView-1/2 and GeoEye-1, the methodology and tools described here can also be used to generate high-quality DEMs from these data. In addition, WorldView-3 now offers improved resolution (~0.31 m nadir GSD) on top of the existing WorldView-2 stereo acquisition capabilities and accuracy specifications.

The updated ASP tools can process commercial VHR image products from other vendors (e.g., Airbus DS, SkyBox) that include standardized RPC sensor models. The ASP source code also includes several sensor templates (e.g., linescan, framing, pinhole) that can be adapted to support additional rigorous sensor models.

The ASP codebase is presently under active development, and will continue to evolve in the coming years, especially as the terrestrial developer/user community continues to grow. Proposed future work includes improved multi-view stereo and Structure from Motion support, integration

of more sophisticated correlation algorithms, and various performance improvements. Finally, our ongoing research efforts continue to leverage ASP and WorldView DEMs to study outlet glaciers in Greenland, ice streams/shelves in Antarctica, and glaciers/snowpack in the Pacific Northwest.

ACKNOWLEDGEMENTS

We gratefully acknowledge funding from the NASA Cryosphere program for ASP development. D. Shean was supported by a NASA NESSF fellowship (NNX12AN36H). B. Smith (NNX09AE47G) and I. Joughin (NNX08AL98A) acknowledge support from NASA. Support for the Polar Geospatial Center was provided by the National Science Foundation (ANT-1043681). We would like to thank Milan Karspeck and Chris Comp at DigitalGlobe for initial guidance on L1B corrections. Comments from two anonymous reviewers helped improve the manuscript. Resources supporting this work were provided by the NASA High-End Computing (HEC) Program through the NASA Advanced Supercomputing (NAS) Division at Ames Research Center.

TABLES

Refinement Method	July 28, 2009 pair Wall time (s)	June 17, 2011 pair Wall time (s)	Avg. ratio to Parabolic
None	46	47	0.4
Parabolic	110	110	-
Affine	2573	2737	23.4
BayesEM	16556	16231	150.5

Table 2-1: Runtime comparison for ASP refinement methods. The time for "None" offers an estimate of baseline disk input/output requirement. Integer correlation wall times for the July 28, 2009 and June 17, 2011 pairs were 154 and 141 seconds, respectively.

Instrument (data product)	Instrument type	Observation Period	Shot diameter (m), swath width	Shot Density	Horizontal Accuracy (m)	Vertical Accuracy (m)
GLAS (L2, GLA12)	Satellite laser altimeter	2003-2009	~65 m shot	172 m along-track	~6-20	~0.1-0.5
ATM (L1B)	Conical-scanning airborne LiDAR	1993-present	30-45° swath	1 pt/10 m^2	~0.75	<0.1
LVIS (L2)	Swath-scanning airborne LiDAR	2009-present	~10-25 m shot, 12° swath	1 pt/400 m^2	<2	<0.1

Table 2-2: Elevation control sources for the Earth's ice sheets.

	Summit		Tracy
Sample size	14	13 (outlier removed)	17
Mean vertical offset (m)	+2.10	+1.58	+2.52
CE90 (m)	0.57	0.58	3.61
LE90 (m)	5.22/3.91	3.61/2.51	5.04/2.86
RMSE before co-reg (m)	2.40	1.90	2.83
RMSE after co-reg (m)	0.20	0.21	0.96
NMAD before co-reg (m)	0.20	0.20	0.48
NMAD after co-reg (m)	0.20	0.20	0.44

Table 2-3: Co-registration results and error analysis for Summit and Tracy sites. LE90 values are computed before/after removing mean vertical offset (see text for discussion). The Summit n=13 values are computed after removing April 4, 2013 DEM with poor acquisition geometry. The final four rows provide an average of the specified metric for all DEMs in the sample.

FIGURES

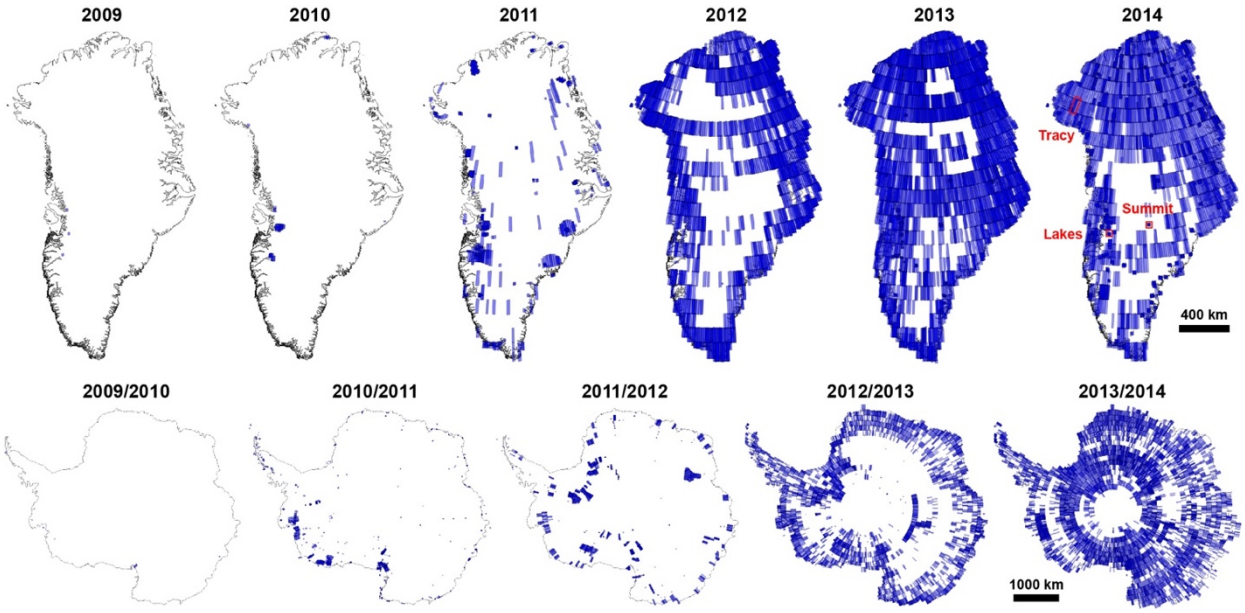

Figure 2-1: Annual DigitalGlobe stereo coverage for Greenland and Antarctica. Cloud cover <75%) for Greenland (top row) and Antarctica (bottom row) in DigitalGlobe archive. Labels (Tracy, Summit, Lakes) and outlines on 2014 Greenland map indicate case study site locations.

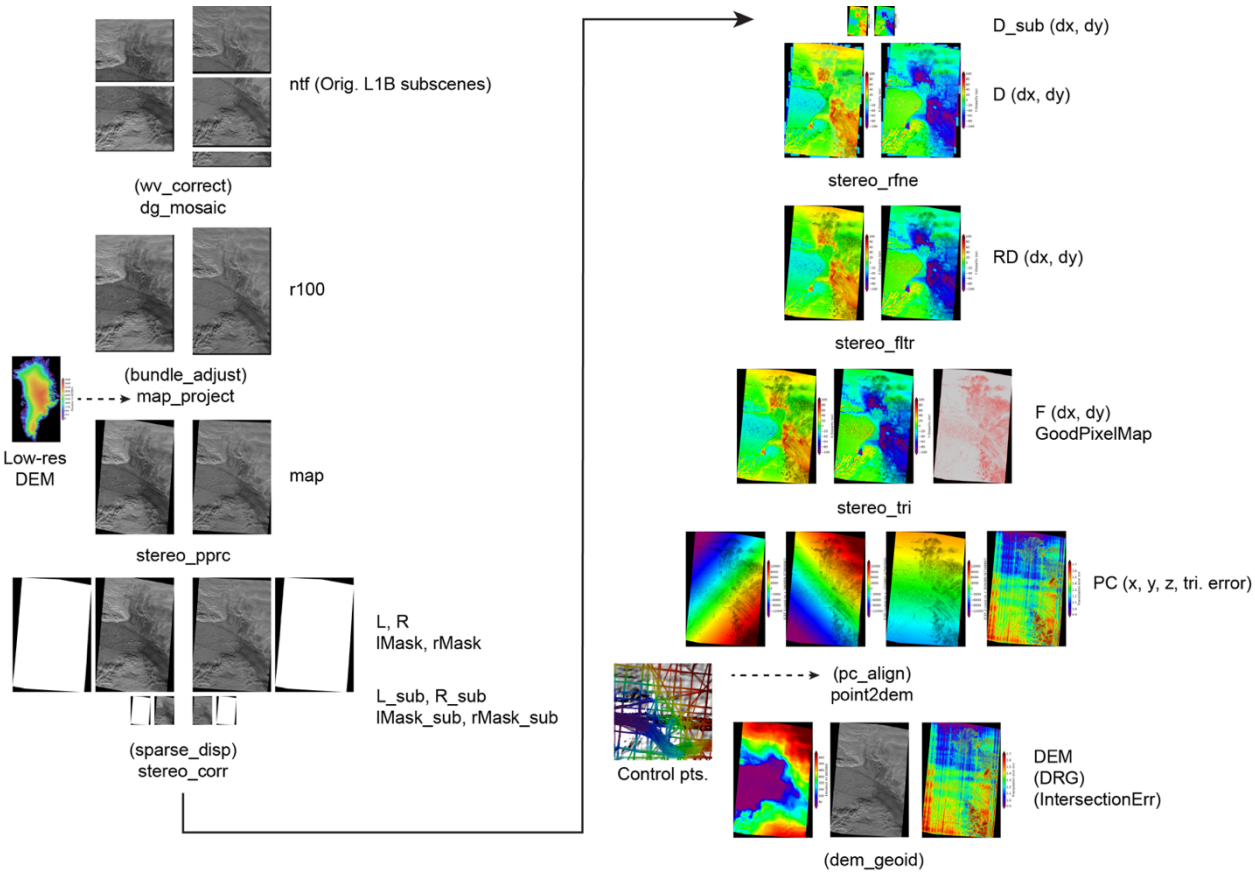

Figure 2-2: ASP v2.4 workflow for WorldView imagery. Commands are listed in line with thumbnails with optional commands in parenthesis; default product extensions are listed to the right of each step, with product type listed for each band (e.g. RD band 1 = x disparity, band 2 = y disparity). Dashed arrows indicate external data input (i.e., low-res DEM for orthorectification, control points for co-registration).

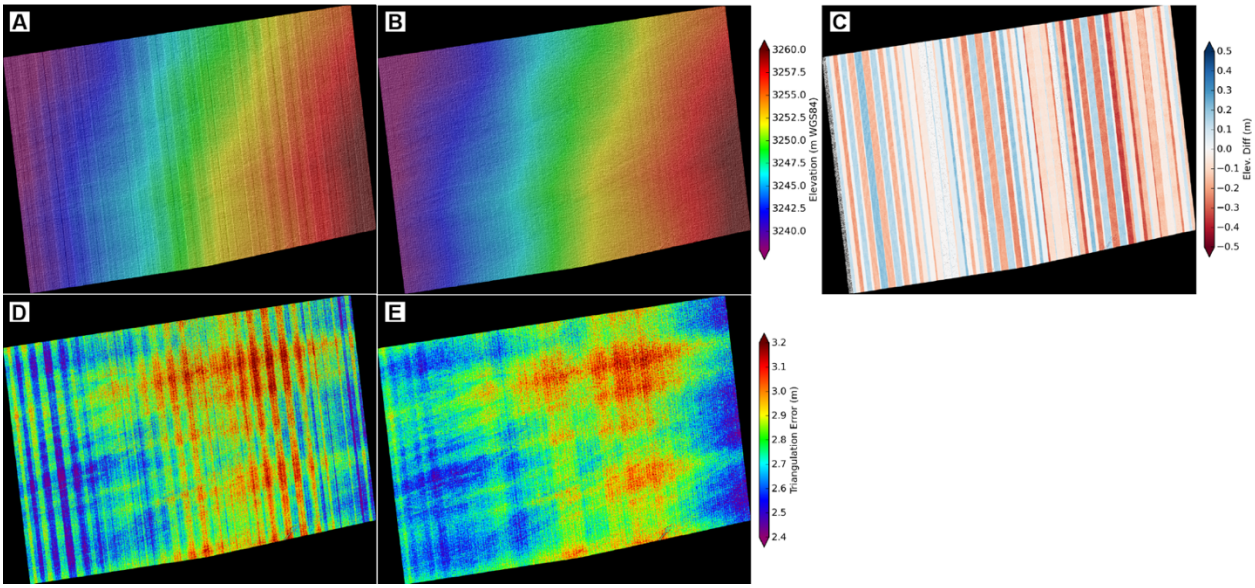

Figure 2-3: WorldView L1B correction for CCD artifacts. DEMs derived from A) uncorrected, and B) corrected WorldView-2 L1B input images near Summit station on July 13, 2011. C) Elevation difference map showing magnitude of artifacts. D+E) Triangulation error maps for DEMs in A and B. For color versions of all figures, please refer to online version.

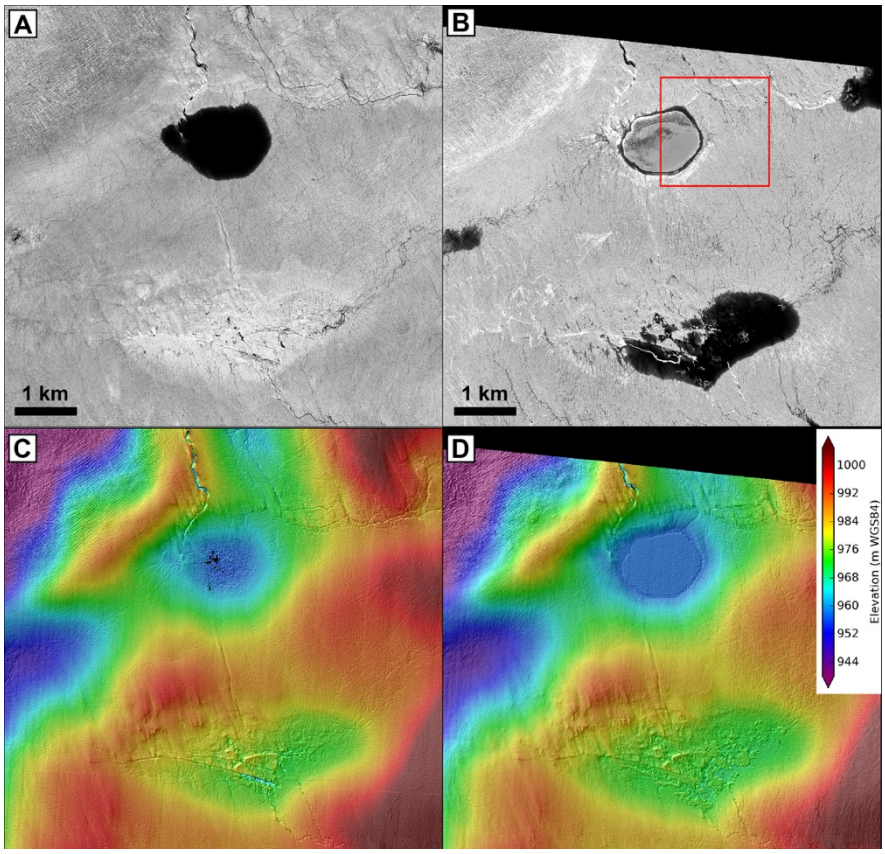

Figure 2-4: WorldView-1 orthoimages and DEMs of lakes site in West Greenland. A+C) July 28, 2009 and B+D) July 17, 2011. Note variable lake levels and lake ice cover, with successful correlation/triangulation of shallow supgraglacial lake bathymmtery and floating ice on lake surface. Outline in panel B shows extent of Figure 2-5. Images © 2015 DigitalGlobe, Inc.

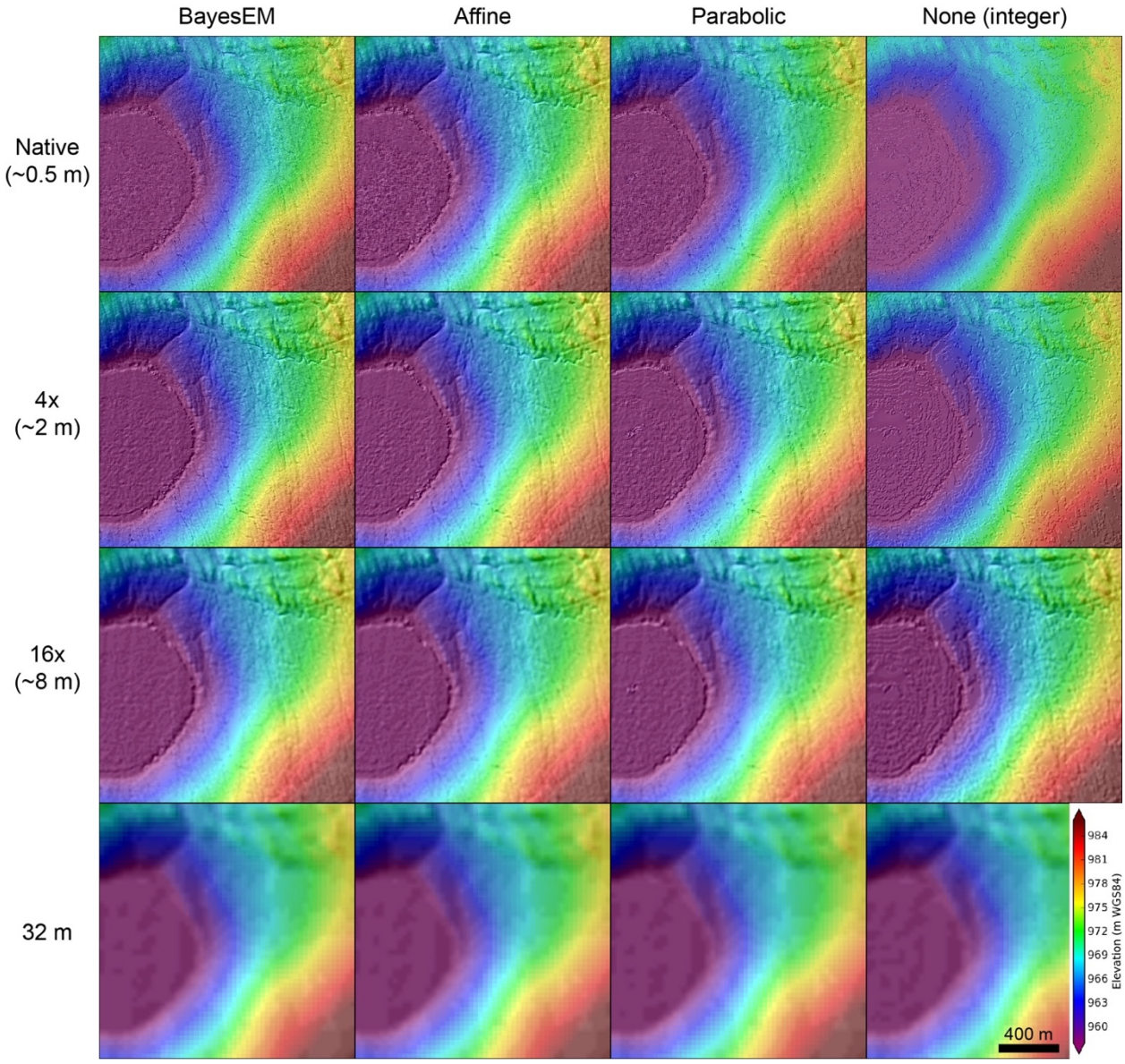

Figure 2-5: Comparison of ASP refinement and DEM posting. Sub-pixel refinement methods (columns) and output DEM posting (rows) for 1.7x1.7 km section of the July 17, 2011 DEM over ice-covered supraglacial lake and stream channels (see Figure 2-4 for context).

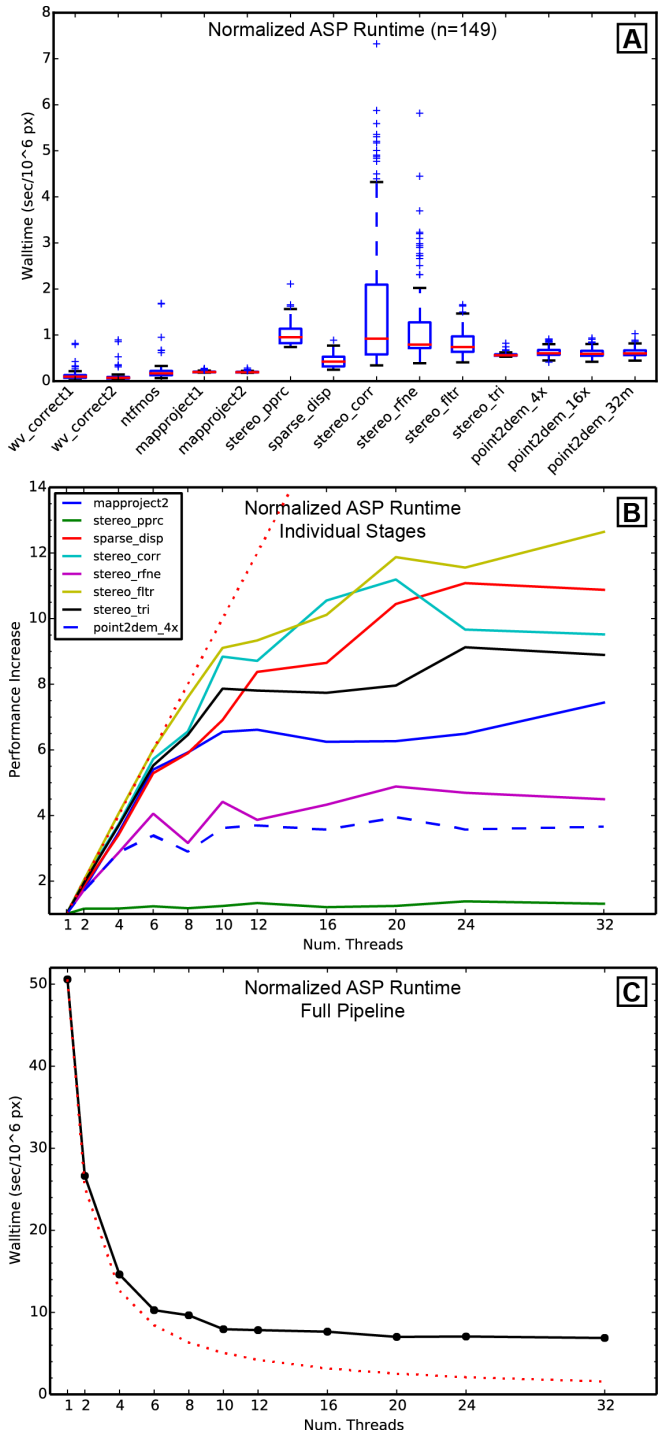

Figure 2-6: ASP benchmark test results. A) Area-normalized runtime of individual ASP stages for 149 pairs with variable dimensions/quality. Box and whisker plot shows median runtime, inner quartile (box) and 1.5*IQR whiskers (ticks) with fliers as crosses. B) Area-normalized performance increase (multiplicative factor relative to single-threaded case) vs. number of ASP threads (set to number of physical CPU cores) for each ASP stage on clipped

July 28, 2009 input images (Figure 2-4A). Dotted line is idealized linear relationship. Each thread count test was run once on shared hardware resources, which explains some of the variability. C) Area-normalized performance vs. number of ASP threads when running full pipeline on clipped July 28, 2009 input images. Dotted line is idealized 1/n relationship.

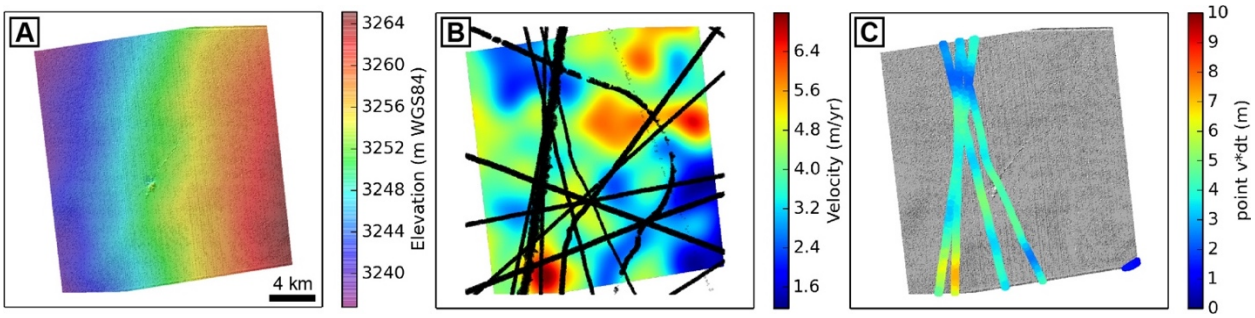

Figure 2-7: Summit control point filtering. A) Summit DEM from April 9, 2013. B) Surface velocity map [*Joughin et al.*, 2010a] with all ~3.7x10^6 available ground control points from 1999-2014 (black). Magnitude of spatial variation is within measurement noise for this location. C) Culled ground control points (~3.3x10^5) with colors indicating expected displacement ($\|\mathbf{v}\| \cdot \boldsymbol{dt}$) for time offset *dt* between DEM and control point acquisition.

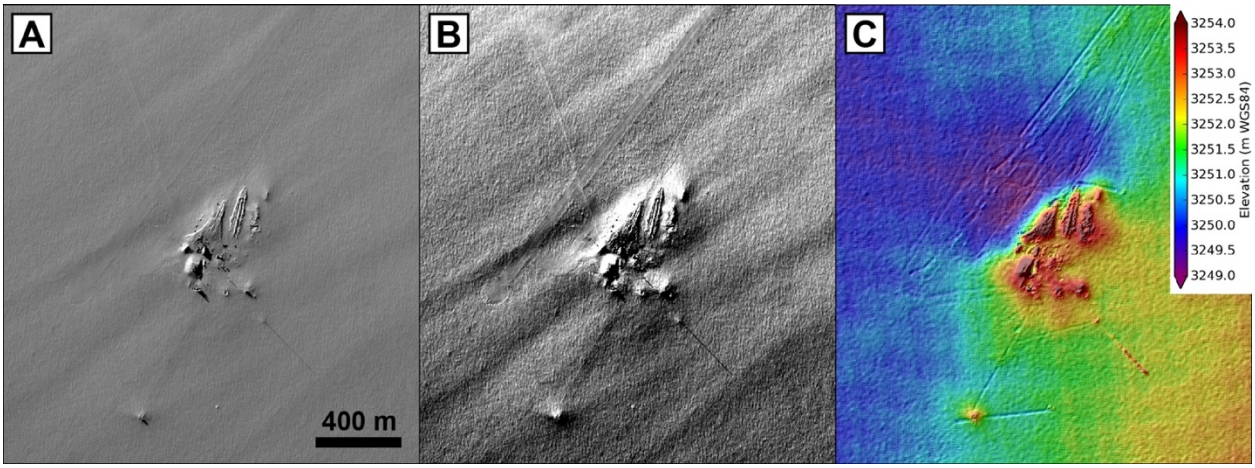

Figure 2-8: WorldView-1 image/DEM of Summit Station, Greenland on July 14, 2013 with A) 0.1-99.9% stretch and B) 2-98% stretch. Note presence of meter-scale texture (sastrugi). C) DEM generated with BayesEM refinement and posted at ~2 m. Note color ramp range of 5 m vertical meters, and the presence of a broad depression to the northwest of the station. Linear artifacts are the result of residual pixel locking on snowmobile tracks, runway margins, and tower shadow. Images © 2015 DigitalGlobe, Inc.

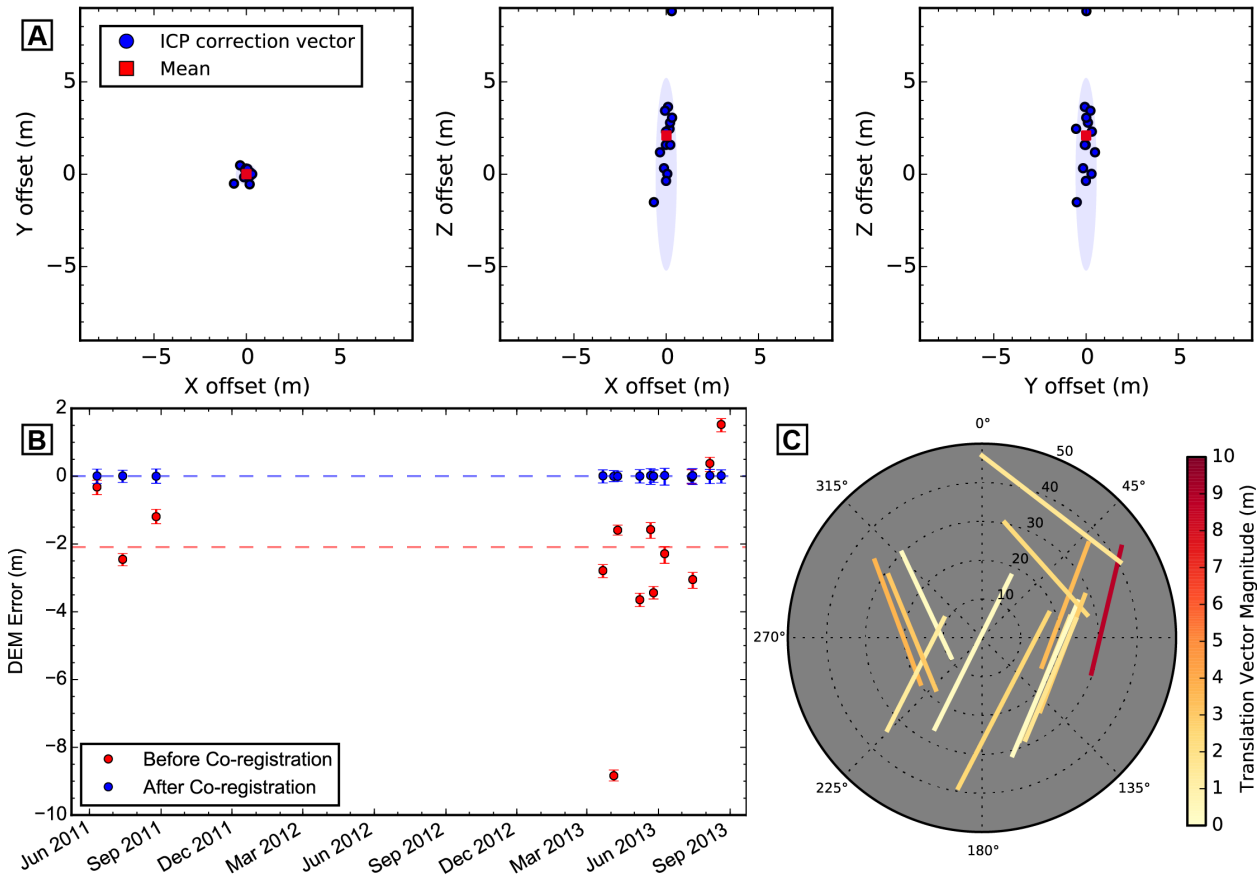

Figure 2-9: Summit ICP co-registration results. A) Components of ICP translation vectors required to correct each Summit station DEM to filtered control point data. Mean vertical offset for all 14 DEMs is +2.1 (DEMs 2.1 m above control data). Shaded ellipses show CE90 and LE90. Note presence of April 4, 2013 outlier with significant z translation of 8.8 m. B) Median of error ($\Delta \boldsymbol{z_i} = \boldsymbol{z_{GCP_i}} - \boldsymbol{z_{DEM_i}}$) sampled at all (~8.4x10^4–3.3x10^5) control points, before and after ICP co-registration. Error bars show 16th–84th percentile spread (robust estimate of ±1-sigma) and dashed horizontal lines show mean of n=14 sample. C) Stereopair baseline geometry for Summit DEMs. The endpoints of each line represent the spacecraft azimuth and elevation of the two stereo images comprising the pair. Color represents the magnitude of the ICP translation vector required to co-register the DEM with the control data. Note relatively short baseline and high off-nadir angles of outlier.

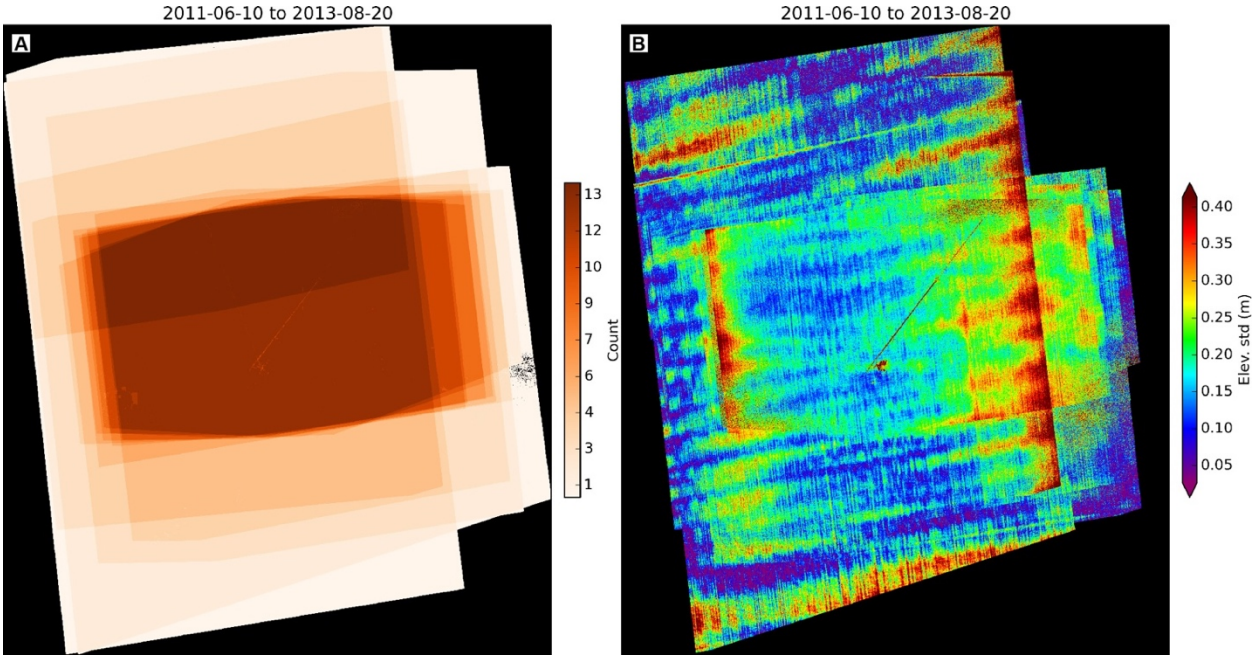

Figure 2-10: Relative DEM accuracy for Summit test case. Maps of A) pixel count, and B) standard deviation for stack of co-registered Summit DEMs (n=14).

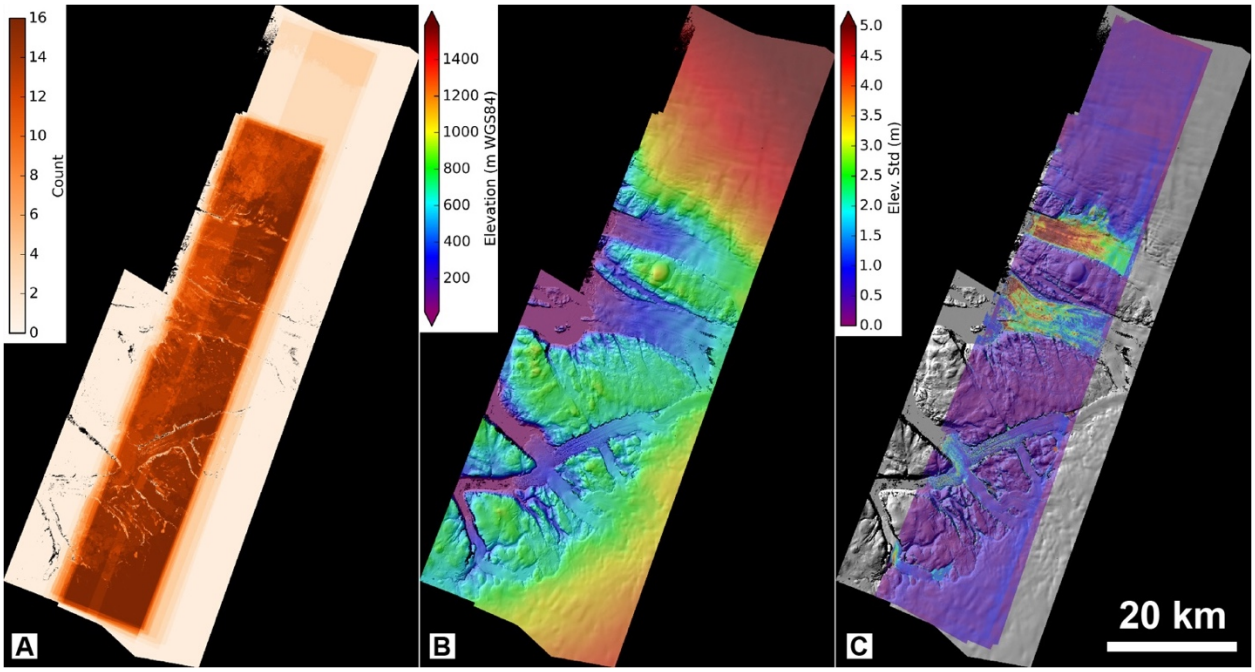

Figure 2-11: Tracy Glacier geocell DEMs. Maps of A) pixel count, B) median elevation, and C) standard deviation for stack of co-registered Tracy Glacier geocell DEMs (n=17). Note high standard deviation over dynamic outlet glaciers. See Figure 2-14 for further analysis of error over bedrock.

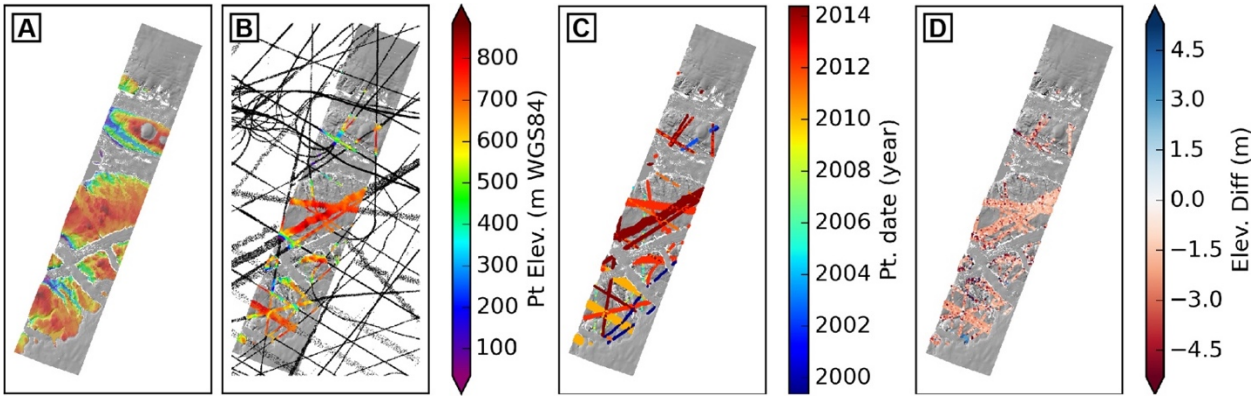

Figure 2-12: Tracy Glacier geocell control point filtering for April 25, 2013 DEM. A) Shaded relief map with colored elevation values over bedrock surfaces. B) All available ~4.4x10^{7} control points (black) and 1.3x10^{6} filtered points over bedrock (color). C) Filtered point timestamps (min = 5/10/1999; max = 5/20/2014). D) Elevation difference between control points and DEM before co-registration.

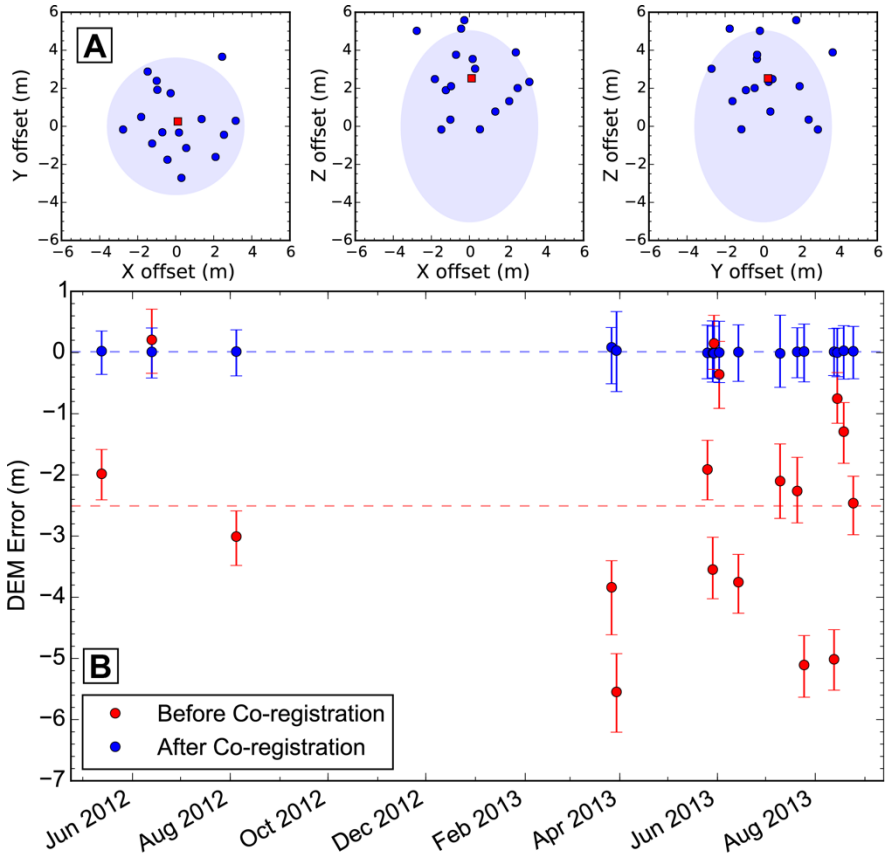

Figure 2-13: Tracy Glacier co-registration results. A) ICP translation vector components, and B) Median error (with 16th–84th percentile spread) for Tracy Glacier DEMs. See Figure 2-9 caption for details.

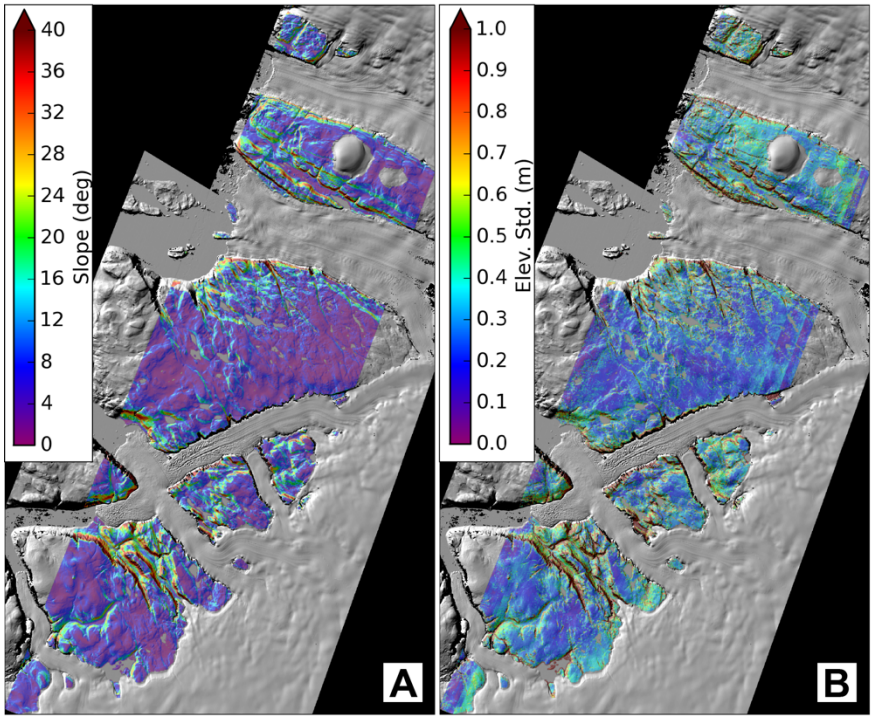

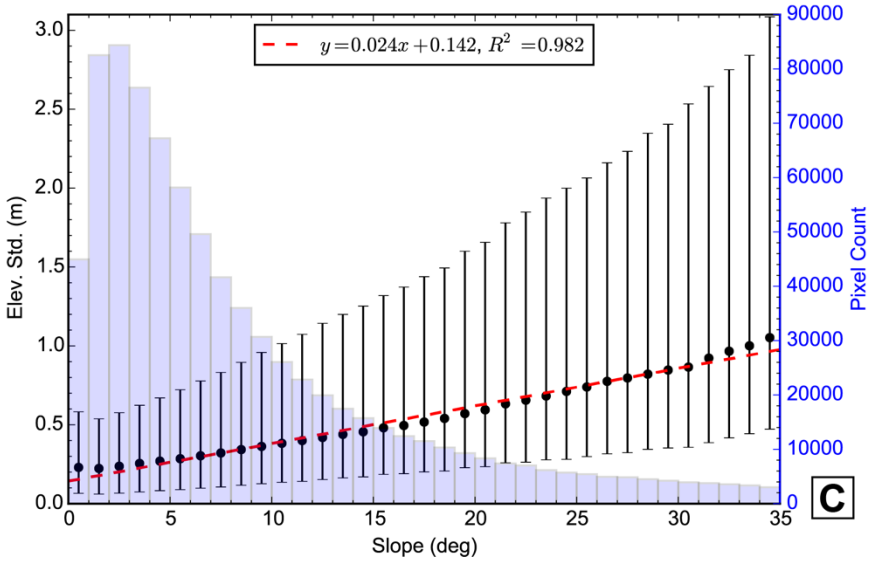

Figure 2-14: Tracy Glacier relative accuracy and slope-dependent error analysis. Analysis of Tracy Glacier DEM stack (n=17) over bedrock (~827 km^2). A) Surface slope computed from median elevation (Figure 2-11B), B) standard deviation, and C) standard deviation vs. surface slope. Points represent median (with 16th–84th percentile spread) of all standard deviation values

that fall within each 1.0° slope bin. Shaded bars show bin pixel counts (right axis). Dashed line shows linear fit to median values within each bin.

Chapter 3. BASAL MELTING OF THE PINE ISLAND GLACIER ICE SHELF, WEST ANTARCTICA FROM A 2008-2015 HIGH-RESOLUTION DEM RECORD

ABSTRACT

Pine Island Glacier (PIG) is currently losing mass (~40 Gt/yr) and contributing ~0.1 mm/yr to global sea level rise. This mass loss has been attributed to rapid retreat, speedup, thinning, and increased discharge from the mid-1990s to ~2012 due to ocean forcing and/or internal instability. We generated a new high-resolution DEM record from WorldView/GeoEye satellite stereo imagery, and integrated with available 2002-2015 DEM/altimetry data over the PIG ice shelf. We developed novel Lagrangian Dh/Dt methodology and combined with annual mass budget analysis to estimate the spatial and temporal evolution of basal melt. This analysis reveals the complex spatial/temporal evolution and interconnection of grounding zones, sub-shelf cavity geometry, basal melt rates, and upstream dynamics over grounded ice.

We document significant main shelf grounding line retreat between 2008-2009, and the ephemeral regrounding of ~2-3 deep keels as a positive ice thickness anomaly advects over a seabed ridge. Thinning upstream of the grounding line decreased from ~5-10 m/yr in 2008-2010 to ~0 m/yr by ~2012-2014, with a small grounding line advance from 2012-2015.

Mean 2008-2015 basal melt rates were ~80-90 Gt/yr for the full shelf, with ~200-250 m/yr melt rates within large channels near the grounding line, ~10-30 m/yr over the main shelf, and ~0-10 m/yr over the North and South shelves, with notable exception of ~50-100 m/yr near the grounding line of a fast-flowing tributary on the South shelf. The DEM Dh/Dt melt rates show excellent agreement with, and provide spatial/temporal context for *in situ* melt rate observations.

Melt rates were highest for the 2008-2010 period, with a ~20-30% decrease by 2010-2012, followed by a gradual increase from 2010-2012 to 2013-2015. Melt rates vary significantly across ~km-scale ice shelf thickness variations, with focused melting in basal channels near the grounding line and keels over the outer shelf. We suggest that these features alter sub-shelf circulation, leading to positive feedbacks that can influence regrounding and upstream ice dynamics.

We observe a positive linear relationship between melt rate and depth, with increasing melt rate magnitude and increasing variability at depth. The slope and spread of this linear relationship

varies over time. Existing piecewise melt rate parameterizations in prognostic ice flow models provide reasonable approximations for this relationship, but fail to capture km-scale variability. The Dh/Dt melt products do not show the inferred ~50% decrease in melt rates between 2010 and 2012 from hydrographic observations in Pine Island Bay [*Dutrieux et al.*, 2014b], and we do not observe significant melt rate variability associated with observed ~2012 ocean cooling in mooring records [*Christianson et al.*, 2016]. This suggests that PIG melt rates are not directly correlated with observed ocean heat content in Pine Island Bay, and that during the 2008-2015 period, observed ice shelf melt and upstream dynamics were more sensitive to grounding evolution, channel-scale circulation, and internal instabilities than oceanographic forcing. These findings have important implications for diagnostic/prognostic flow modeling efforts used for projections of 21st-century sea level rise.

3.1 INTRODUCTION

The Amundsen Sea sector of the West Antarctic ice sheet (WAIS) has experienced significant acceleration, thinning, and grounding line retreat since at least the 1970s [*Joughin et al.*, 2003; *Mouginot et al.*, 2014; *Rignot et al.*, 2014]. During this period, regional mass loss increased, potentially at an accelerating rate, with present day estimates of ~100-120 Gt/yr [*Medley et al.*, 2014; *Sutterley et al.*, 2014; *Velicogna et al.*, 2014]. These changes appear to be linked to warming [*Jacobs et al.*, 2011; *Schmidtko et al.*, 2014] and increased transport [*Thoma et al.*, 2008; *Steig et al.*, 2012] of the dense, relatively warm (~0.5-1.2°C, up to +2-4°C above *in situ* freezing point [*Rignot and Jacobs*, 2002; *Jacobs et al.*, 2012]) Circumpolar Deep Water (CDW) onto the continental shelf [*Jacobs et al.*, 1996; *Shepherd et al.*, 2004; *Pritchard et al.*, 2012; *Dutrieux et al.*, 2014b], where it is funneled along deep troughs toward the vulnerable grounding lines of large ice streams with reverse bed slopes [*Jenkins et al.*, 2010]. Marine ice sheet grounding lines on reverse bed slopes are inherently unstable [*Weertman*, 1974; *Schoof*, 2007], and this focused melting can trigger further grounding line retreat, acceleration, and dynamic thinning [*Joughin and Alley*, 2011]. Approximately 75% of the WAIS is grounded below sea level, raising concerns about large-scale collapse due to this instability, which could lead to ~3.3 m of global sea level rise [*Bamber et al.*, 2009].

Ice flow modeling efforts have attempted to understand the nature and timescales of the glaciological response to this ocean forcing [*Joughin et al.*, 2010b, 2014b; *Favier et al.*, 2014; *Seroussi et al.*, 2014]. Model sensitivity analyses for the Pine Island Glacier (PIG) and Thwaites Glacier demonstrate that basal melt rates are the dominant factor for initiating and maintaining dynamic retreat, with other factors (e.g., calving, shear margin strength, surface mass balance) displaying secondary importance. Results from prognostic models using estimates of present-day melt rates suggest that irreversible marine ice sheet collapse may already be underway for WAIS [*Joughin et al.*, 2014b] – a finding that has been corroborated by recent observations of retreat [*Rignot et al.*, 2014]. However, this collapse only occurred for a subset of the modeled melt scenarios, and the onset/pace of retreat varied significantly.

The spatial distribution of basal melt is an important factor for ice stream stability [*Rignot and Jacobs*, 2002]. In general, melt rates are expected to increase with depth in the water column due suppression of the freezing point with increasing pressure. At PIG, the presence of dense, warm

water at depth enhances this relationship. Focused melt near the grounding line can increase local thickness gradients, resulting in greater driving stress and speedup [*Rignot and Jacobs*, 2002; *Joughin et al.*, 2012]. Simulations with the same total shelf melt, but enhanced melt near the grounding line (rather than distributed over shallower portions of the shelf) resulted in significant retreat at an accelerated pace [*Walker et al.*, 2008]. Prognostic ice flow models use different approaches to estimate the spatial distribution of sub-shelf melting, with some models using empirically-derived piecewise linear melt rate vs. depth relationships [*Joughin et al.*, 2010b, 2014b; *Favier et al.*, 2014], and others using a fixed melt rate distribution from ocean circulation model output [*Seroussi et al.*, 2014].

Over the past ~30 years, numerous observational studies have attempted to estimate Antarctic ice shelf melt rates (e.g., Table S2 of [*Rignot et al.*, 2013]). The scope of these efforts ranges from continent-wide remote-sensing inventories [*Shepherd et al.*, 2010; *Pritchard et al.*, 2012; *Depoorter et al.*, 2013; *Rignot et al.*, 2013] to detailed analysis of individual shelves [e.g., *Joughin and Padman*, 2003; *Dutrieux et al.*, 2013; *Moholdt et al.*, 2014]. Various methods were used for these assessments, including mass budget ("input-output" flux gate) methods [*Depoorter et al.*, 2013; *Rignot et al.*, 2013], satellite laser altimetry [*Pritchard et al.*, 2012], satellite radar altimetry [*Shepherd et al.*, 2004; *Paolo et al.*, 2015], field observations with phase-sensitive radar [*Jenkins et al.*, 2006; *Stanton et al.*, 2013; *Dutrieux et al.*, 2014a; *Langley et al.*, 2014b; *Marsh et al.*, 2015], *in situ* sub-shelf oceanographic observations from boreholes [*Stanton et al.*, 2013; *Kobs et al.*, 2014] and autonomous submersible [*Jenkins et al.*, 2010; *Dutrieux et al.*, 2014b], traditional mooring or ship-based oceanographic observations beyond the ice shelf margins [*Jacobs et al.*, 1996, 2011; *Jenkins et al.*, 1997; *Kim et al.*, 2016], and ocean circulation modeling [*Payne et al.*, 2007; *Schodlok et al.*, 2012; *Dutrieux et al.*, 2014b].

Each of these methods has advantages and disadvantages, with variable logistical costs, spatial coverage/resolution, temporal coverage/resolution, and measurement uncertainty. Many methods require multiple input datasets, and available data often span different time periods. For example, most previous mass budget analyses combine elevation change rates derived from ~2003-2008 ICESat-1 altimetry – a time period characterized by significant change and imbalance – with velocities from a single year. Elevation data from satellite laser/radar altimetry are further limited by large footprints and/or sparse (~10-20 km) repeat track spacing, with increased uncertainty over surfaces displaying non-negligible slopes or roughness.

The following approach uses high-resolution observations of ice shelf elevation to evaluate the role of ocean forcing on sub-shelf melt, and better understand connections with observed changes in upstream ice stream behavior.

3.2 PINE ISLAND GLACIER

Pine Island Glacier (PIG, Figure 3-1) has a relatively long history of observation and numerical modeling. It has received significant attention due to the ~30 km grounding line retreat along its centerline [*Rignot et al.*, 2014] (~8 km average [*Joughin et al.*, 2016]), ~75% increase in surface velocity [*Mouginot et al.*, 2014], and >100 m of thinning [*Bindschadler*, 2002; *Pritchard et al.*, 2009] since the 1970s, with accelerated retreat beginning in the 1990s due to increased ocean heat content, circulation, and basal melt [*Jacobs et al.*, 2011].

Total discharge across the main PIG grounding line increased from ~73 Gt/yr in the mid-1990s to ~114 Gt/yr in 2009, with a corresponding increase from ~10 to ~12 Gt/yr across the South shelf [e.g., "Wedge" catchment in *Medley et al.*, 2014]. Retreat, speedup and thinning peaked between 2009-2010, followed by an observed ~2-3% velocity decrease over the main shelf from ~2012-2013 [*Mouginot et al.*, 2014; *Christianson et al.*, 2016], and return to ~2009 velocities by early 2015. This glacier accounts for nearly ~20% (~120-130 Gt/yr) of present-day WAIS discharge and nearly ~40% (40 to 50 Gt/yr) of recent ASE mass loss [*Rignot*, 2008; *Medley et al.*, 2014]. This ice loss corresponds to a sea-level rise contribution of ~0.10-0.15 mm/yr – a significant portion of the present-day Antarctic ice sheet contribution of ~0.26 mm/yr [*Church et al.*, 2013; *Rietbroek et al.*, 2016].

A detailed understanding of the processes (e.g., ocean forcing, marine ice sheet instability) responsible for these observed changes, and their relative importance over time, is critical for future projections of PIG dynamics, mass loss, and contributions to global sea-level rise.

3.2.1 *Geographic setting*

The main PIG shelf is ~25 km wide and nearly 100 km long (Figure 3-2), with ice thickness of ~1-1.5 km near the main grounding line, and ~300-400 m near the calving front. Surface velocities over the main shelf are currently ~4 km/yr (~11 m/day) (Figure 3-1). Two large shelves are present on the north and south side of the main shelf, separated from the main shelf by ~2-4 km wide shear

margins (Figure 3-2). We define three primary regions over the PIG shelf (Figure 3-2C) – the "main shelf," "North shelf," and "South shelf."

Total shelf area in recent decades varied between ~5500-6000 km^2, due to changes in the grounding line and calving front position. The full PIG catchment (Figure 3-1) covers ~1.8-2.0x10^5 km^2 with surface mass balance estimates of ~68+/-6 Gt/yr [*Medley et al.*, 2014].

The surface of the PIG shelf is characterized by a series of longitudinal ridges/troughs near the centerline, with transverse ridges/troughs toward the lateral margins that correspond to basal keels/channels [*Vaughan et al.*, 2012] (Figure 3-2A).

The sub-shelf bathymmetry is characterized by a large transverse seabed ridge with relief of ~400 m above adjacent seafloor (Figure 3-2B). This ridge has been the site of intermittent grounding since the 1970s, and it affects circulation within the cavity, effectively blocking some of the deep warm CDW [*De Rydt et al.*, 2014; *Dutrieux et al.*, 2014b]. We further subdivide the main shelf into "inner" and "outer" regions relative to the transverse seabed ridge.

The "ice plain" [e.g., *Thomas et al.*, 2004] mentioned throughout the text describes a region over the inner shelf with relatively smooth, gently-sloping bed (Figure 3-2B). The "ice plain" was lightly grounded and experienced significant retreat from ~1990s to ~2008, with average rates of ~1 km/yr [*Park et al.*, 2013; *Rignot et al.*, 2014]. The DEM record presented here begins near the end of this progressive retreat, when only a few isolated spots appear lightly grounded over the "ice plain."

3.2.2 *Oceanography*

Westerly surface winds near the continental shelf edge drive northward Ekman transport of surface water away from the continent. This draws deep, relatively warm CDW up onto the continental shelf where it flows toward Pine Island Bay along two broad bathymetric channels carved by previous glacial advances [e.g., *Jakobsson et al.*, 2012; *Kirshner et al.*, 2012].

The circulation pathway beneath the PIG ice shelf is less certain, but should generally be clockwise in nature, with CDW inflow at depth along the north side of the outer cavity, and outflow of relatively fresh meltwater along the south side of the outer cavity [*Dutrieux et al.*, 2014b]. Deep, inflowing water encountering the large transverse seabed ridge is likely diverted to the south, flowing alongside the ridge within the outer cavity and moving toward the South cavity. Water at intermediate depth is expected to overflow the seabed ridge, creating a sharp density front and a

northward jet at the ridge crest. Eventually, these waters continue down local bathymetric slopes within the inner cavity toward the grounding line. Once in the inner cavity, the dense CDW reaches the grounding line [*Jenkins et al.*, 2010], with expected cyclonic (clockwise) circulation along the grounding line, and buoyant meltwater outflow along the centerline and south side of the shelf. The temporal evolution of this general circulation pattern, and exchange between the inner, outer, and South shelf ocean cavities will depend on a number of factors, including cavity geometry defined by the ice shelf base and grounding line evolution.

Ice shelf melt is expected to be a function of the friction velocity and thermal driving at the ice-ocean interface [*Holland et al.*, 2008]. These parameters are determined from ocean current and temperature gradients across the boundary layer between the lower mixed ocean and the ice-ocean interface. The efficiency of heat exchange across the this boundary layer and the associated melting should be highly variable across the shelf, leading to higher melt rates over steep basal base slopes near the grounding line [*Little et al.*, 2009]

Hydrographic observations along the main shelf calving front in Pine Island Bay show a decrease in ocean heat content and an inferred ~50% decrease in melt between January 2010 and January 2012 [*Dutrieux et al.*, 2014b]. A similar ~30-40% decrease in glacial meltwater fraction was also inferred near the Dotson and Getz ice shelves from 2011 to 2012 [*Kim et al.*, 2016], suggesting that these ocean changes occurred on a regional scale. Mooring observations show a temperature decrease of ~1.25°C at depths of ~450-770 m in January 2012 [*Christianson et al.*, 2016].

3.2.3 *Previous melt rate estimates*

Recent inventories partition the ~2003-2008 PIG mass loss as ~65% (~95-101 Gt/yr) basal melt and ~35% (~50-62 Gt/yr) calving [*Depoorter et al.*, 2013; *Rignot et al.*, 2013], confirming the importance of basal melt for this system. Table S2 of Rignot et al. [2013] provides a comprehensive review of past melt rate assessments for PIG.

It is well established that relatively high basal melt rates (>100 m/yr) are found near the main shelf grounding line, with reduced melt rates over the outer shelf [*Payne et al.*, 2007; *Bindschadler et al.*, 2011; *Dutrieux et al.*, 2013]. However, little is known about the temporal variability of PIG melt rates. A recent study by Bindschadler et al. [2011] concluded that a transverse channels/keels formed annually near the grounding line due to seasonal CDW intrusion [e.g., *Thoma et al.*, 2008].

Simulations by Sergienko [2013] showed that similar features may form spontaneously due to meltwater plume flow.

3.3 DATA AND METHODS

We present high-resolution surface elevation observations to investigate the spatial and temporal evolution of PIG between 2008-2015. The following section includes details of input data sources and relevant processing methodology.

3.3.1 *Elevation data*

3.3.1.1 Along-track commercial stereo DEMs

We generated DEMs from high-resolution commercial stereo satellite imagery (DigitalGlobe WorldView-1, WorldView-2, WorldView-3, and GeoEye-1) using the methodology described in Shean et al. [2016a]. A total of ~3000 along-track stereo images with cloud cover <75% from October 2010 to May 2015 were processed for the WAIS coastline. Image dimensions are typically ~13–17 km wide and 111 km long, with ~0.3–0.5 m ground sample distance (GSD).

Full resolution, Level 1B images were orthorectified at the minimum pair GSD using a smoothed version (3x3 pixel Gaussian) of the Bedmap2 surface DEM [*Fretwell et al.*, 2013]. Specific ASP processing settings [see *Shean et al.*, 2016a] include 'seed-mode 3' (sparse_disp utility) to initialize the correlation, a 2-level pyramid limit for correlation, a correlation timeout of 360 seconds, parabolic sub-pixel refinement and erosion of isolated disparity clusters of <1024 pixels. We focus our analysis for a ~260x240 km region with dense WorldView/GeoEye DEM coverage (n=288) covering the PIG shelf and lower trunk (Figure 3-3).

3.3.1.2 Cross-track commercial stereo DEMs

We also generate "cross-track" DEMs from independent, "coincident mono" images that have appropriate geometry for stereo reconstruction. We identified candidate pairs in the DigitalGlobe archive based on the criteria in Table 3-1, and generated an additional 24 DEMs from images acquired between October 2011 and January 2012.

Some of these candidate pairs were acquired on the same orbit, while others were acquired on different orbits or by different spacecraft (e.g., WorldView-1 and WorldView-2). Final time

offsets between the images ranged from 0.007 to 1.6 days. The DEMs were processed as described in [*Shean et al.*, 2016d].

These cross-track DEMs have larger errors due to residual horizontal displacement errors (i.e., errors due to ice flow between image acquisitions), non-ideal stereo geometry (e.g., smaller convergence angles) and the fact that errors in ephemeris data are independent (as opposed to highly correlated for along-track pairs). In practice, this can result in increased DEM vertical/horizontal bias and increased relative error (e.g., more extreme DEM "tilt").

Despite this increased error, we include these cross-track DEMs in our analysis to cover critical areas near the PIG grounding line, and to increase overall sample count over the shelf during the 2011/2012 season. We correct the cross-track DEMs using the same techniques as described for along-track stereo DEMs, which significantly reduces these errors.

3.3.1.3 SPIRIT DEMs

We obtained all available SPIRIT (SPOT 5 stereoscopic survey of Polar Ice: Reference Images and Topographies, [*Korona et al.*, 2009]) DEMs for PIG. A total of six 40-m posting DEMs cover some portion of the PIG shelf between January 5, 2008 and January 18, 2010. Unlike the WorldView imagery, the ~5 m GSD SPOT-5 images are unable to resolve meter-scale ice sheet texture, so that stereo image correlation often fails for flat, effectively featureless slopes, leading to gaps in the output DEM. The km-scale ridge/trough morphology, ~100–1000 m wind-sculpted surface features, and rifts on the main PIG shelf, however, provide sufficient texture for correlation. Compared to the WorldView DEMs, the SPIRIT DEMs display increased noise and artifacts, but cover a much larger area.

Elevation values in the SPIRIT DEMs are represented as whole integers, with horizontal and vertical accuracy estimates of <10 m [*Bouillon et al.*, 2006; *Korona et al.*, 2009]. We used the DEM V1 products (correlation parameters tuned for gentle slopes), applied the bundled "CC" mask to preserve correlation scores between 50-100% (masking most interpolated areas), reprojected to polar stereographic (EPSG:3031), and removed the EGM96 geoid offset to obtain elevations relative to the WGS84 ellipsoid. We filtered the resulting products to remove isolated pixels, mask elevations <20 m above the geoid, and remove any pixels with absolute elevation difference >30 m from the median of 2010-2015 WorldView DEMs.

3.3.1.4 Altimetry

We assembled all available NASA Airborne Topographic Mapper (ATM, [*Krabill et al.*, 2002; *Martin et al.*, 2012]) and Land, Vegetation, and Ice Sensor (LVIS, [*Blair et al.*, 1999; *Hofton et al.*, 2008]) airborne LiDAR data for use in our study area. NASA's Operation IceBridge (OIB) mission has collected airborne altimetry data annually during one or more PIG campaigns from 2009/2010 to 2014/2015, except for the 2013/2014 season. These data typically were collected during April-May campaigns, with data acquisition flights for a particular site typically occurring over ~1–3 days.

We processed all points as described in [*Shean et al.*, 2016a], and produced gridded 32-m and 256-m DEMs for each campaign using the ASP point2dem utility (weighted mean within radius of 1 grid cell). A total of 25 ATM flights and 7 LVIS flights crossed the study area between 2009-2015, with data collection for individual flights typically lasting <4 hours. The high-altitude LVIS surveys on October 20, 2009 and October 10, 2011 cover a significant portion of the main shelf, while other LVIS/ATM flights generally consist of a few sparse flightlines distributed across the shelf.

We also include available 2003-2009 NASA ICESat-1 Geoscience Laser Altimeter System (GLAS, [*Zwally et al.*, 2002; *Schutz et al.*, 2005]) satellite altimetry data. These data were clustered by ~33-day campaign and gridded as described above, providing 18 additional sparse DEMs. While intercomparison of these sparse data over rough surfaces or steep slopes can be problematic, we include them in our analysis to extend the observational record back to 2003.

3.3.2 *DEM co-registration and correction*

Adjacent WorldView/GeoEye stereo DEMs are often acquired weeks or months apart during a particular season, resulting in horizontal and vertical offsets for overlapping areas in fast-flowing regions. Generally, this temporal sampling is not a problem for smaller targets covered by a single WorldView image footprint (e.g., Greenland outlet glacier termini). Larger targets like the PIG shelf, however, can require >10 DEMs for complete coverage, so that more sophisticated co-registration is necessary. The following sections describe a tiered co-registration and correction workflow used to improve both absolute and relative DEM accuracy over the PIG study area.

3.3.2.1 Co-registration with altimetry

Where possible, a point-to-point iterative closest point (ICP) algorithm was used to co-register DEMs to filtered altimetry data as described in Shean et al. [2016a] from the sources described in Section 3.3.1.4. All control points have vertical accuracy of ~0.1 m.

The altimetry database was queried for each DEM extent and the returned points were filtered to preserve those over static (e.g., nunataks) and "dynamic" control surfaces. The latter include slow-moving ice with limited slopes/roughness, and were refined using a maximum expected displacement (product of measured surface velocity and time offset between the point and DEM timestamp) threshold of 10 m and maximum DEM–point time offset of 1 year. Control points were excluded over floating portions of the PIG shelf.

3.3.2.1.1 WorldView/GeoEye DEM co-registration

The majority of WorldView/GeoEye DEMs had 10^6–10^8 filtered points available for co-registration, with DEM–point time offsets of only a few months. The results of the initial co-registration are summarized in Figure 3-4 and Table 3-2. The ICP co-registration provided translation corrections for 368 DEMs over the PIG catchment and 248 of the 288 DEMs over the shelf and lower catchment study area. Figure 3-3 shows a significant improvement in the multiple quality metrics following co-registration. Uncorrected DEMs had an initial mean vertical bias of +3.11 m above the altimetry data (Figure 3-4), and we apply a -3.11 m vertical correction to the 40 uncorrected DEMs.

3.3.2.1.2 SPIRIT DEM co-registration

The filtered SPIRIT DEMs were co-registered with the ICP routine described in Section 3.3.2.1, and the results are shown in Figure 3-5. In addition to the filtered airborne data, a large sample of near-contemporaneous ICESat-1 GLAS data were available for co-registration of the 2008-2009 DEMs. After co-registration we estimate that the lower-resolution SPIRIT DEM products have <3-4 m absolute vertical accuracy (1-sigma). One of the DEMs (January 3, 2009) produced large residual offsets between control point and DEM elevation, so we performed a secondary round of vertical co-registration (-3.1 m) to minimize offsets between the DEM and 2010-2015 WorldView DEM median elevation over flat, smooth surfaces surfaces near the main shelf.

3.3.2.2 Elevation correction for ocean and atmospheric variability

After co-registration, we corrected all elevation data over the floating portions of the PIG shelf to remove the effects of ocean tides, atmospheric pressure (Inverse Barometer Effect (IBE), [e.g., *Padman et al.*, 2003]) and mean dynamic topography.

We compute tidal amplitude Δh_t using the CATS2008A inverse barotropic tide model, an updated version of the model described in Padman et al. [2002]. The inverse barometer effect magnitude Δh_{IBE} is computed from 6-hour interval ERA-Interim mean sea level pressure reanalysis data [*Dee et al.*, 2011]. We remove the 2002-2016 median (985.21 hPa), and scale residuals by ~1 cm/hPa to obtain the approximate inverse barometer correction. Tidal amplitude for DEM timestamps ranges from -0.75 to +1.04 m ($\sigma = 0.33$ m), while the inverse barometer effect amplitude ranges from -0.3 to 0.35 m ($\sigma = 0.11$ m). These high-frequency (~hourly–daily) corrections show excellent agreement with observed surface elevation records from GPS receivers on the PIG shelf [*Shean et al.*, 2016c].

The mean dynamic topography (Δh_{MDT}) correction removes residual offsets between the geoid and mean sea level due to ocean circulation. Estimates for mean dynamic topography near ASE are approximately -1.2 m [*Andersen and Knudsen*, 2009].

The final corrected ice surface elevation above sea level is calculated as:

$$h = h_e - \Delta h_g - \alpha(\Delta h_{MDT} + \Delta h_t + \Delta h_{IBE}) \quad (3.1)$$

Where h_e is measured elevation above the WGS84 ellipsoid, and Δh_g is the EGM2008 geoid offset [*Pavlis et al.*, 2012] (approximately -27.6 to -24.4 m across PIG shelf). The coefficient α increases linearly with distance *l* beyond the grounding line:

$$\alpha(l) = \begin{cases} 0, & l \leq 0 \\ 0.33l, & 0 < l \leq 3\ km \\ 1, & l > 3\ km \end{cases} \quad (3.2)$$

ensuring a smooth transition from floating to grounded ice for these corrections. The grounding line was defined with a single composite polygon derived from DInSAR [*Rignot et al.*, 2014; *Joughin et al.*, 2016] and high-resolution DEM data, with an approximate timestamp of 2011.

After correction using Equation 3.1, surface elevation from airborne laser altimetry approaches 0 m above sea level over open water. We neglect elevation change due to long-term sea level rise (<0.003 m/yr) and glacial isostatic adjustment (GIA, elastic response is approximately +0.02–0.03 cm/yr for ASE [*Groh et al.*, 2012; *Gunter et al.*, 2014]).

3.3.2.3 WorldView/GeoEye DEM "tilt" correction

As identified in Shean et al. [2016a], a subset (~5-10%) of the WorldView/GeoEye DEMs appear to have a slight along-track and/or cross-track "tilt" of ~1-3 m over ~111 km. For many of these cases, the control point spatial distribution is insufficient to constrain an ICP rotation correction. Initial attempts with bootstrapped corrections and least-squares minimization for adjacent DEMs with ~1-2 km of overlap failed due to overfitting and propagation of increased error near DEM edges (where most intersections occur).

To correct these problematic DEMs, we identify "dynamic control surfaces" within the full set of overlapping DEMs, and simultaneously solve for interannual dh/dt and planar corrections to remove individual DEM tilt over these surfaces. In principle, this is similar to the SERAC method used for altimetry over the Greenland ice sheet [*Schenk and Csatho*, 2012; *Csatho et al.*, 2014].

Fortunately, the WorldView DEM record (November 16, 2010 to April 6, 2015) postdates the period of rapid dynamic change at PIG that ended in ~2009. Surface velocities and SMB display limited variability from 2010-2015, suggesting that elevation change rates over grounded ice should also remain relatively constant. We manually mask the main shelf and fast-flowing trunk within ~30 km of the grounding line, and then use the criteria listed in Table 3-3 to identify dynamic control surfaces (Figure 3-3) over grounded ice with limited linear trend and variance about this trend.

Over these surfaces, we assume that the elevation at any particular DEM pixel i at location (x_i, y_i) at time j is given by:

$$h_{i,j} = (a_i + b_i t_j) + (c_j x_i + d_j y_i + e_j) \quad (3.3)$$

where b_i and a_i represent the slope and offset of a linear fit to elevations at pixel i, and coefficients c_j, d_j and e_j define a planar correction for all i within a DEM at time j.

We solve for these coefficients using least squares minimization with regularization and a smoothness constraint to penalize large spatial gradients. Filtered altimetry data are included with increased weight over the stereo DEMs, and DEMs with along-track length <40 km are limited to a vertical offset correction (e_j), with no tilt correction. Tilt tolerances are increased for cross-track DEMs (Section 3.3.1.2) and vertical offset tolerances are increased for input DEMs that were not initially co-registered using ICP. Tilt tolerance is limited in the cross-track direction, as most of the observed tilt is along-track. Figure 3-3 and Table 3-4 summarize the results of these corrections.

3.3.2.4 Output elevation data

We prepared a resampled "stack" of all co-registered, corrected DEMs over the full shelf using a 256-m grid. Additional stacks were prepared over high-priority areas (inner shelf, GPS validation sites) with increased grid resolution of 64-m and 32-m.

3.3.3 *DEM accuracy*

As discussed in [*Shean et al.*, 2016a], the uncorrected along-track commercial stereo DEM vertical/horizontal accuracy is ~5.0 m CE90/LE90. After systematic artifact removal and co-registration, vertical accuracy can be as low as ~0.2-0.4 m over slopes <10° when adequate control data are available. We conservatively estimate final DEM accuracy of ~1 m after co-registration and least-squares "tilt" correction. We expect increased uncertainty for 2013/2014 DEMs due to reduced availability of altimetry data for initial ICP co-registration. The least-squares correction, however, leverages altimetry data and corrected WorldView/GeoEye DEMs in adjacent years, which should reduce 2013/2014 uncertainty.

Several factors can reduce the effectiveness of DEM co-registration with altimetry. The primary issues for PIG include sparse control data with limited slope/aspect variance for a particular DEM, and large DEM–point time offsets (~1-12 months). Over these timescales, surface processes (e.g., accumulation/ablation, wind redistribution of snow) can potentially lead to surface elevation changes of ~1 m, and advection of small-scale surface features can lead to horizontal co-registration errors.

We used a network of five 2012-2014 GPS sites on the outer shelf [*Christianson et al.*, 2016; *Shean et al.*, 2016c] as independent check points for WorldView DEMs. Corrected DEM elevations show good agreement (~0.7 m RMSE) with cm-accuracy surface elevations derived from multi-path reflector height records [*Larson et al.*, 2015] at each site [*Shean et al.*, 2016c]. Unfortunately, no valid SPIRIT DEM pixels are available over 2008-2010 GPS sites [*Shean et al.*, 2016c].

The upcoming ICESat-2 mission [*Abdalati et al.*, 2010] will acquire ~0.1-cm-accuracy control points over multiple tracks for individual DEM footprints within days-weeks of stereo image acquisition. The availability of these contemporaneous control data should constrain full translation+rotation ICP DEM co-registration. This will effectively eliminate the need for the

control point filtering and least-squares correction, and should improve absolute vertical DEM accuracy to ~0.5 m.

3.3.4 *Annual DEM mosaics*

We generated mosaics for all available elevation data in a given year (~September–April, typically ~October–March), and assign a nominal January 1 timestamp (Figure 3-6). Mosaic elevation values were computed using a weighted average approach that favors pixels near the center of individual input DEMs, where data quality is best. The resulting mosaics appear seamless, but can also smooth advecting features in the along-flow direction for periods with variable temporal sampling (e.g. DEMs with identical footprint in October and March).

To obtain full-shelf coverage while also preserving relative elevations within individual DEMs, additional mosaics were generated for each ~October-March period without averaging or edge blending. We used a "reverse" ordering scheme for input DEM timestamps, so that the last DEMs from each season were mosaicked on top.

We also generate WorldView DEM mosaics when complete shelf-wide coverage is available over a relatively short time span (e.g., October–December 2012, Figure 3-2). Input DEM products were manually selected and ordered to minimize feature offsets.

3.3.5 *Surface velocity*

Surface velocity data are necessary to constrain horizontal advection of surface topography and aide interpretation of observed elevation change. In an effort to generate self-consistent velocity and DEM products, we initially tried estimating velocity using feature tracking with normalized cross-correlation of two DEMs, similar to the approach described by Dutrieux et al. [2013]. However, this approach is susceptible to spurious correlations and data gaps over flat, featureless areas, especially for low-resolution inputs (e.g., 40-m SPIRIT DEMs). This technique also fails due to decreased coherence over longer time intervals (>1-2 years), related to surface processes, anisotropic deformation, and the anisotropic basal melt signals we are attempting to measure. For these reasons, we use gridded velocity products from independent data sources for our study period. While not as precise as direct sub-pixel correlation of input DEMs/images, this approach enables reconstruction of particle paths for arbitrary elevation data, including sparse altimetry.

We used 22 surface velocity mosaics [*Joughin*, 2002] derived from TerraSAR-X/TanDEM-X, ALOS and Landsat-8 (LS8) data (Figure 3-1). The 500 m/px ALOS and LS8 products cover the entire PIG shelf for late 2006, 2007, 2008, 2010, 2013, 2014, and 2015, while the 100 m/px TSX/TDM products are available every ~3–6 months over the main shelf from 2009-2015. The individual mosaics are derived from images spanning a period of ~11-189 days, with most products spanning <88 days.

We used these mosaics to derive a spatially and temporally continuous velocity time series for the full PIG shelf. This was accomplished using piecewise linear interpolation via 3D (*x,y,t*) Delaunay Triangulation, with increased weighting in the time dimension. Linear barycentric interpolation was then used to extract spatially continuous velocity grids with 512-m resolution for a regular time interval of 122 days from January 1, 2008 to June 1, 2016.

The interpolated velocity products were smoothed in the time dimension with a 610-day, 2nd-order Savitzy-Golay filter, and then in the spatial dimension with a 2.5-km rolling median filter to remove artifacts and horizontal offsets in the mosaics. A secondary interpolation with a high-resolution timestep (e.g., ~5-20 day) and increased spatial resolution (e.g., 32–256 m) was performed for use during the Lagrangian Dh/Dt analysis, with a final 1.28 km Gaussian smoothing filter (~0.17 km sigma) applied in the spatial dimension to reduce any residual interpolation artifacts. The melt rate calculations described in Section 3.3.9 require estimates of the velocity divergence, which we calculate from these interpolated, smoothed velocity products as:

$$\nabla \cdot \mathbf{u} = \frac{du_x}{dx} + \frac{du_y}{dy} \tag{3.4}$$

for each high-resolution time step using a central difference approach.

3.3.6 *Bed topography*

We evaluated five different beds for PIG (Figure 3-7), including Bedmap2 [*Fretwell et al.*, 2013], an aerogravity inversion constrained by Autosub bathymetric data [*De Rydt et al.*, 2014], an aerogravity/Autosub inversion constrained by active source seismic surveys [*Muto et al.*, 2016], a mass-conserving bed embedded in Bedmap2 [*Morlighem et al.*, 2011], and the CReSIS L3 gridded Multichannel Coherent Radar Depth Sounder (MCoRDS) ice thickness product using 2009-2010 airborne radio echo sounding. These beds vary in extent/resolution, with significant (>100-300 m) discrepancies in places, especially over the inner cavity.

We produced a new combined bed dataset using aerogravity/Autosub data, existing open-water bathymetry, and all available quality-controlled CReSIS MCoRDS and British Antarctic Survey (BAS) Polarimetric Airborne Survey Instrument (PASIN) ice thickness measurements collected over grounded ice. We fit a smooth surface to these data using an inversion procedure that preferentially minimizes bed curvature in the along-flow direction, while matching the bed elevation at data points to within the estimated data errors [see methods of *Medley et al.*, 2014]. While some local "peaks" over the longitudinal seabed ridge may be too high, this bed appears most consistent with observed grounding line evolution [*Joughin et al.*, 2016].

3.3.7 *Surface mass balance (SMB)*

The Regional Atmospheric Climate Model (RACMO) v2.3 [*Van Meijgaard et al.*, 2008; *Ettema et al.*, 2009; *Lenaerts et al.*, 2012; *Van Wessem et al.*, 2014] provides continent-wide estimates of surface mass balance for a 27-km grid. We use monthly average SMB products from January 1979 to December 2013, and repeat the observed 2013-2014 SMB signal for calculations spanning 2014-2015. The RACMO SMB data were interpolated over the study area to generate gridded products with the same extent and spatial sampling as the DEM and velocity products.

3.3.8 *Elevation change*

We consider elevation change for PIG using both Eulerian dh/dt (measured for a fixed reference grid) and Lagrangian Dh/Dt (measured for a grid moving with the surface) descriptions. These two approaches are complementary and provide distinct information over grounded and floating ice.

3.3.8.1 Theory

Assuming incompressibility, constant ice density (ρ_i), and column-average velocity $\mathbf{u}$, the Eulerian description of mass conservation for a column of ice with thickness H (after removing firn air content d) can be expressed as:

$$\frac{\partial H}{\partial t} = -\nabla \cdot (H\mathbf{u}) + \dot{a} - \dot{b} \tag{3.5}$$

where $\dot{a}$ is surface accumulation rate (meters ice equivalent for specified time interval dt) and $\dot{b}$ is basal melt rate (defined as positive for melt). The flux divergence, $\nabla \cdot (H\mathbf{u})$, can be expanded as:

$$\nabla \cdot (H\mathbf{u}) = H(\nabla \cdot \mathbf{u}) + \mathbf{u} \cdot (\nabla H) \tag{3.6}$$

where $\nabla \cdot \mathbf{u}$ is the velocity divergence (positive for extension) and ∇H is the thickness gradient. The relationship between Lagrangian and Eulerian thickness change is provided by the material derivative definition:

$$\frac{DH}{Dt} = \frac{\partial H}{\partial t} + \mathbf{u} \cdot (\nabla \mathrm{H}) \tag{3.7}$$

Equations 3.5, 3.6, and 3.7 can be combined to obtain Lagrangian thickness change for the column:

$$\frac{DH}{Dt} = -H(\nabla \cdot \mathbf{u}) + \dot{a} - \dot{b} \tag{3.8}$$

Over grounded ice, we can assume that bed elevation remains constant, and substitute Eulerian surface elevation change *dh/dt* for Eulerian thickness change *dH/dt*. This does not hold for floating ice. If we assume hydrostatic equilibrium, however, we can estimate freeboard ice thickness from observed surface elevation. We remove firn air content from observed surface elevation (*h* in Equation 3.1) to obtain ice-equivalent freeboard surface elevation h_f:

$$h_f = h - d \tag{3.9}$$

and then compute ice-equivalent freeboard thickness:

$$H \approx h_f \left(\frac{\rho_w}{\rho_w - \rho_i}\right) \tag{3.10}$$

assuming a constant density for sea water (ρ_w) and ice (ρ_i), which can be substituted into Equation 3.8:

$$\frac{Dh_f}{Dt} = -h_f(\nabla \cdot \mathbf{u}) + \left(\dot{a} - \dot{b}\right)\left(\frac{\rho_w - \rho_i}{\rho_w}\right) \tag{3.11}$$

to provide a mass conservation expression for Lagrangian surface elevation change.

3.3.8.2 Eulerian dh/dt

We generated Eulerian dh/dt products with a 1-year and 2-year interval from the annual DEM mosaics described in Section 3.3.4 (Figure 3-8). The two time intervals provide continuous records of elevation change for variable DEM mosaic coverage.

3.3.8.3 Eulerian DEM anomaly maps

We computed average 2008-2015 elevation from the annual mosaics and smoothed with a 5.1 km Gaussian (0.83 km sigma) kernel to characterize long-wavelength shelf topography. This

smoothed reference was then subtracted from annual mosaics to produce surface elevation "anomaly" maps for each year (Figure 3-8).

3.3.8.4 Eulerian long-term interannual trend

To characterize long-term (~5-10 year) elevation change over the PIG shelf, we computed interannual trend for the 2003-2010 and 2010-2015 periods (Figure 3-9). This was accomplished using a linear fit to surface elevation for each grid cell with 3 or more observations that spanned at least 1 year. Most cells have >6 valid samples over ~4-5 years. No smoothness constraint was imposed – all fits were computed independently, although adjacent elevation values are highly correlated.

3.3.9 *Basal melt rate*

Both Eulerian and Lagrangian frameworks can be used to estimate basal melt rate. The Lagrangian description tracks elevation change for the same column of ice as it advects downstream, eliminating potential aliasing due to advection of high-frequency surface gradients (i.e., ice shelf ridges/troughs). Early studies employed a Lagrangian analysis to derive estimates for ice shelf melt rates using *in situ* observations [e.g., *Jenkins et al.*, 2006], and more recent studies have demonstrated this same approach can be used with remote sensing data [*Dutrieux et al.*, 2013; *Moholdt et al.*, 2014].

If velocity divergence and surface accumulation are known, it is possible to rearrange Equation 3.11 to solve for the component of observed elevation change due to basal melt:

$$\dot{b} = -\left(\frac{Dh_f}{Dt} + h_f(\nabla \cdot \mathbf{u})\right)\left(\frac{\rho_w}{\rho_w - \rho_i}\right) + \dot{a} \qquad (3.12)$$

3.3.9.1 Lagrangian Dh/Dt melt rate implementation

Past studies of Lagrangian Dh/Dt melt rates used single pairs of elevation observations [*Dutrieux et al.*, 2013] or a series of sparse point data [*Moholdt et al.*, 2014] for a single time period. Our approach uses hundreds of independent, spatially continuous DEM observations over the PIG shelf, with variable spatial and temporal coverage. This provides thousands of DEM(t_1)-DEM(t_2) combinations for Lagrangian Dh/Dt melt rate computation, with the flexibility to vary the relative t_1-t_2 time offset. Most of the DEM data are acquired annually from ~October-March, so we

compute Dh/Dt for DEM-pair time intervals of ~1 (0.5-1.5) year and ~2 (1.5-2.5) years, with center timestamp of $t_1+(t_2-t_1)/2$. Longer time intervals offer improved signal to noise, but the observed Dh/Dt values are integrated across a longer path, which effectively decreases spatial resolution of inferred melt rate products.

For each DEM(t_1), all valid pixels ("particles") over the shelf are propagated along flow paths computed from the time-variable velocity fields, and local velocity divergence is sampled at each time step along each path (Figure 3-10). An appropriate time step (~10-20 days for 256-m grid) is automatically determined based on the grid cell size and maximum velocities in the scene. If enough particles (>10 km^2) intersect another DEM at time t_2, and the t_1-t_2 offset is within the specified range, then DEM(t_2) elevations are sampled at appropriate particle locations and Dh/Dt is computed. This observed Dh/Dt is used to estimate surface elevation h at each time step, and local $h(\nabla \cdot \mathbf{u})$ values are integrated along each path. This novel approach should accurately capture time-variable thinning/thickening due to local velocity divergence experienced along each path, rather than sampling velocity divergence from single, fixed velocity grid. With estimates for Dh/Dt and $h(\nabla \cdot \mathbf{u})$ we use Equation 3.12 to estimate basal melt for each path.

3.3.9.2 Melt rate path distribution

For longer time intervals (~2 years) and high advection rates (~4 km/yr), path lengths (~8 km) can greatly exceed the input DEM grid cell size (~256 m), which brings about the important question of where to place melt rate estimates in a global Eulerian coordinate system (e.g., EPSG:3031).

We consider two end members for the spatial distribution of sub-shelf melt rates. The first assumes that the spatial variability is highly correlated with local shelf thickness, so that local melt rates advect with features on the shelf (e.g., once formed, a transverse channel will continue to experience high melt rates as it advects downstream). The second assumes a fixed (both horizontally and vertically) sub-shelf melt rate field for a given time period, so that shelf thickness variations (i.e., keels and channels) are exposed to different melt rates as they advect through this field. In reality, melt likely occurs due to some combination of these two end members – melt rates may be locally enhanced due to ice shelf thickness variations, but the magnitude of this enhancement will vary based on the location of these variations against a "fixed" background melt field.

We developed Lagrangian Dh/Dt frameworks for both end members: 1) an "initial pixel" approach, where path melt rate values are assigned to initial DEM(t_1) pixel locations, and 2) an "along-flow distribution" approach, where path melt rates are evenly-distributed over each path, and statistics are computed using all paths that pass through cells of a fixed Eulerian grid (Figure 3-10). The first approach is relatively straightforward, and was used in earlier work [e.g., *Dutrieux et al.*, 2013]. The second is more complex, but potentially more realistic, and we offer the following detailed description.

The path history of all valid particles for a particular DEM(t_1)-DEM(t_2) combination is reduced to identify a unique set of occupied Eulerian grid cells, and cumulative particle counts are computed for each cell. This count is spatially variable – only one particle will pass through a cell on the upstream edge of the domain, while ~10-100 particles could pass through a cell in the center of the domain during the t_1-t_2 interval. For each path, time-averaged Dh/Dt, $h(\nabla \cdot \mathbf{u})$, and corresponding basal melt rate $\dot{b}$ for the path are distributed along encountered cells. We then compute the mean and standard deviation of these values for all paths crossing each cell (Figure 3-10). This approach significantly reduces noise (e.g., suppressing anomalous Dh/Dt for a path that beings or ends over a DEM artifact) and provides metrics to evaluate variance and uncertainty in derived melt rates. However, longer time intervals can result in "smeared" melt rate estimates in the along-flow direction, which reduces the ability to resolve local spatial variability, especially for features with transverse orientation (e.g. transverse channels/keels, rifts).

A complementary "along-flow distribution" approach uses least-squares minimization with regularization and smoothness constraint to solve for the Eulerian melt rate within each cell (rather than computing mean melt rate from all paths crossing each cell). A linear equation is defined for each path, equating total observed path Dh/Dt with the amount of time spent in each cell along the path, yielding an overdetermined system to solve for melt rate at all cells. While this approach is potentially more appropriate for resolving small-scale variations in melt without along-flow "smearing," it assumes that the melt field remains fixed during the ~1 or ~2-year time interval. Edge effects and anomalous Dh/Dt values related to DEM artifacts can also introduce unphysical melt/freeze-on signals that introduce errors in the final solution. For these reasons, we used the mean "along-flow distribution" melt rate products for further analysis.

3.3.9.3 Melt rate composites

Thus far, we have only considered melt rates for a single DEM(t_1) and DEM(t_2) pair, which represents only one of many potential valid pairs that can be formed for a particular DEM(t_1). The DEM(t_1) particles are propagated and the process is repeated for other viable DEM combinations until the maximum t_1-t_2 time interval (~1 year or ~2 years) is reached, typically yielding ~2-40 products for each DEM(t_1). The entire process is then repeated for all possible DEM(t_1), yielding 1000s of individual DEM(t_1)-DEM(t_2) products.

The individual DEM(t_1)-DEM(t_2) melt rate products may have relatively high uncertainty and/or limited spatial extent, so we created annual melt rate composites to improve signal to noise and increase total coverage for a given ~1- or ~2-year time interval. The methodology used to generate these composites is slightly different for the "initial pixel" and "along-flow distribution" approaches.

3.3.9.3.1 "Initial pixel" composites

We compute "stack median" melt rate products for each initial DEM(t_1). For the available 2008-2015 DEMs, this yields 117 unique DEM(t_1) stacks, with initial t_1 timestamps from 2008-2013 and ~2-year t_1-t_2 interval. With this approach, melt rates from each DEM(t_1)-DEM(t_2) combination were assigned to initial DEM(t_1) pixel locations, and median values for each pixel were computed assuming that local Dh/Dt remains constant for all t_1-t_2. This assumption, and also the accuracy of estimated particle paths, is validated by limited observed melt rate variance at each pixel in the final stack.

The "initial pixel" stack median products provide improved estimates for local melt rates, but are limited to the DEM(t_1) spatial extent. To overcome this, we generate mosaics of these "stack median" products using "reverse" time order, so melt rate estimates from the last DEM(t_1) timestamp are mosaicked on top for each year, respectively (Figure 3-11). This approach preserves local melt rate distribution within each stack, but provides coverage over as much of the shelf as possible, with limited time offset between spatially adjacent observations.

3.3.9.3.2 "Along-flow distribution" composites

We also generate weighted average melt rate mosaics from individual "along-flow distribution" melt rate products (usually ~15-60 input products over the full shelf with appropriate center timestamps for a given ~2-year period). This provides melt rate grids centered on January 1 for

the ~2-year interval products, and grids centered on July 1 for the ~1-year interval products. For each grid cell in the output mosaics, the weighted averaging approach favors pixels near the center of input products rather than pixels near edges. Maps of melt rate standard deviation are also produced, offering a spatially variable uncertainty estimate for each mosaic. The annual mosaics are then used to generate a weighted average melt rate mosaic for the entire 2008-2015 period (Figure 3-11).

3.3.10 *Mass budget analysis*

We performed an annual mass budget analysis [e.g., *Rignot et al.*, 2013] using the interpolated DEM and velocity time series described in Sections 3.3.5 and 3.3.4. Four flux gates were defined for the main PIG shelf with 500-m node spacing: ~1 km upstream of the 2011 grounding line (GL) position, ~10 km downstream of the GL, ~30 km downstream of the GL (where ice thickness approaches ~500 m), and ~1 km upstream of the 2011 rift that led to the 2013 calving event.

These gates bound three inter-gate areas: GL, Inner shelf, and Outer shelf (Table 3-5). Another set of gates was defined for the North and South PIG shelves: ~1 km upstream of the 2011 grounding line and ~1 km upstream of the shelf front (or lateral shear margin of main shelf). All gates were defined with identical start and end points to avoid leakage, and where possible, gates were drawn along flightlines with quality-controlled MCoRDS ice thickness measurements.

For each gate, thickness H over grounded ice was estimated using interpolated surface elevation and the bed described in Section 3.3.6. Over floating ice, freeboard thickness was estimated as described in Section 3.3.8.1. The magnitude of surface velocity normal to each gate segment was computed from the interpolated velocity time series. Total discharge Q through each gate with total length L was then computed by integrating across all gate segments of length dl:

$$Q = \int_0^L (H \cdot \|\mathbf{u} \cdot \hat{\mathbf{n}}\|) dl \tag{3.13}$$

Estimates for Eulerian dH/dt and average annualized monthly SMB were integrated over the volumes between flux gates for the specified time interval (e.g., 1 or 2 years). If these products covered >95% of the inter-gate area, then any residual data gaps were filled using a ~2.8 km Gaussian kernel, and the resulting sum was used for the mass budget analysis.

For each inter-gate area, total mass budget melt rates (B) were estimated from observed discharge across the upstream flux gate (Q_{in}), discharge across the downstream flux gate (Q_{out}), area-integrated SMB, and area-integrated thickness change:

$$B = (Q_{in} - Q_{out}) + \iint \dot{a} - \iint dH/dt \quad (3.14)$$

These estimates were then compared with integrated "along-flow distribution" Lagrangian Dh/Dt melt rates for the same inter-gate areas. Totals for the main shelf were calculated for years with spatially continuous coverage over all three inter-gate areas.

3.3.11 *Uncertainty*

Systematic elevation uncertainty over the PIG shelf includes errors due to the geoid (~0.1-0.4 m) and mean dynamic topography (~0.2 m), with additional variable uncertainty from the tide/IBE correction (~0.1 m). For simplicity, we assumed a spatially and temporally constant firn air content of 12 m, and we estimate uncertainty of ~2 m associated with local spatial variability. The depth-averaged density for ice is assumed to be 917 +/-5 kg/m^3 and 1026 +/-5 kg/m^3 for underlying ocean water. We assume that these densities are constant in both space and time. Uncertainties for mass budget estimates were calculated assuming uncorrelated errors of 1 m for surface elevation, 50 m for bed elevation, 30 m/yr for velocity (for ~37.5° look angle and +/-0.5 m tide) [*Joughin*, 2002] and 28% for SMB [*Depoorter et al.*, 2013].

Uncertainty for elevation change and melt rate products depends on time interval. For example, assuming that errors are uncorrelated, a 1-m absolute error in surface elevation should result in ~1.4 m root-mean-square error in elevation change. Associated Dh/Dt error is then ~1.4 m/yr for a 1-year interval or ~0.7 m/yr for a 2-year interval. This estimate does not, however, include vertical offsets due to cumulative horizontal displacement error, which will increase for longer time intervals. It is challenging to quantify this Dh/Dt uncertainty contribution in a forward sense, as multiple sources (e.g., cumulative displacement error, DEM resampling, DEM co-registration) can lead to slope- and aspect-dependent errors.

These formal error estimates do not include reduced uncertainty from the temporal and spatial "stacking" used to derive the final composite products described in Section 3.3.9.3. Some metric of final uncertainty can be obtained from observed mosaic variance, although spatial and temporal sampling is not constant. Uncertainty for area-integrated mass budget Dh/Dt melt rates was

estimated using the mean of observed mosaic standard deviation. Some of the observed variance is related to Dh/Dt melt rate error, but some is also due to real change in the magnitude and spatial distribution of melt rates during the time period, and/or advection of local melt rates associated with ridges/channels.

We do not update the grounding line mask for melt rate calculations, and note that some of the persistent high and low melt rate values <1 km downstream of the grounding line may be the result of incorrect grounding line position and insufficient masking over grounded ice. In addition, melt rates over main shelf shear margins and near the ice front display increased errors in velocity divergence. These locations can also display anomalously large Dh/Dt values (+/-20–40 m) over advecting icebergs, rifts and near the shelf front due to large surface gradients and increased sensitivity to cumulative velocity error.

3.4 RESULTS

3.4.1 *Long-term Eulerian dh/dt trends*

Figure 3-9 shows long-term Eulerian elevation change for the PIG study area. From ~2003-2010, thinning rates ~1-30 km upstream of the grounding line are ~5–10 m/yr, while those farther upstream over the catchment are ~1 m/yr. From ~2010-2015, thinning rates near the grounding line decrease to ~0-1 m/yr, with increased thinning of ~1-2 m/yr over the catchment. We also note significantly increased ~2010-2015 thinning rates (~3-4 m/yr) over upstream shear margins within ~60 km of the grounding line, especially the north shear margin.

A series of "crescent-shaped band" elevation anomalies with orientation approximately transverse to flow is apparent over the catchment ~40-100 km from the ~2011 grounding line (Figure 3-9D). At distances of ~60-100 km, these features appear concave relative to flow direction, while they appear convex at distances of ~30-60 km. These features are related to dense collections of arcuate surface crevasses [e.g., *Scott et al.*, 2010] that formed over and/or advected past these locations during the 2010-2015 period. Individual DEMs show elevation differences of ~0.5 m between these bands of crevasses and inter-band surfaces.

We observe dh/dt signals with spatial scales of ~10-15 km over the PIG shelf that are not related to advection of km-scale surface features. Over the main shelf, we observe a robust ~2010-2015 thickening signal of ~1-2 m/yr downstream of grounding line on the north side of the shelf (Figure

3-9D) and a thinning signal of ~1 m/yr over the south side of the outer shelf. The South PIG shelf shows <1 m/yr thinning from 2010-2015, with ~3 m/yr thinning over upstream ice within ~10 km of the grounding line. The north shelf shows little elevation change with <0.5-1 m/yr thinning over upstream tributaries.

3.4.2 *Interannual Eulerian dh/dt*

Figure 3-8 and Figure 3-12 and show significant interannual elevation change from 2008-2015. The 1-year and 2-year Eulerian dh/dt products show spatial patterns associated with advecting surface ridge/trough features, but also robust spatial patterns of Eulerian elevation change over ~5-10 km length scales.

Over the inner shelf, the maps show localized thinning rates of ~5-10 m/yr over the "ice plain" between 2008-2010. Elevation profiles from early altimetry data (Figure 3-13) show >60 m thinning over this location from 2003-2009, with limited elevation change after 2010.

Both the dh/dt and "Eulerian DEM anomaly" products document the propagation of a broad ~10-km-wide positive ice thickness anomaly and a set of ~km-scale anomalies along the main shelf centerline between 2008-2015. The dh/dt maps show the distinct negative-upstream/positive-downstream pattern of an advecting thickness anomaly.

The northern half of the inner shelf displays a thickening signal in 2010-2011, 2009-2011 and 2010-2012 dh/dt maps (Figure 3-8), and a propagating thickness anomaly is observed over this region in the DEM anomaly maps after ~2010 (Figure 3-8).

We note a significant decrease in thinning rates over grounded ice <20 km upstream of the main shelf grounding line (Figure 3-12). Upstream thinning rates of ~5-10 m/yr are observed from 2008-2010, with thinning rates of <1–3 m/yr by 2010-2012, and ~0-1 m/yr in subsequent years. The notable exception to this general pattern is enhanced thinning over the north shear margin. The 2-year Eulerian dh/dt maps also reveal a localized positive elevation change signal of +5-6 m/yr (significantly greater than the maximum tidal signal) over the northern portion of the main shelf grounding line from 2012-2014 and 2013-2015 (Figure 3-12), and a corresponding advance of the ~150 m contour visible in the 2015 DEM mosaic (Figure 3-8).

The 2008 DEM anomaly map (Figure 3-8) shows an approximately -30 m elevation anomaly associated with a longitudinal surface trough near the shelf centerline, ~15 km downstream of the 2011 grounding line. This feature advects downstream and displays reduced relief from 2008-

2012, with no evidence for a similar feature in this location during later years. However, the DEM anomaly maps document the formation and persistence of new longitudinal surface troughs in different locations. These include a deep, relatively wide longitudinal surface trough on the south side of the inner shelf, and a trough near the northern shear margin, with negative relief of approximately ~15-20 m and ~10-15 m over these features by 2015, respectively.

3.4.3 *Basal melt rate spatial distribution*

Figure 3-2 and Figure 3-11 show mean 2-year Dh/Dt melt rate products for the 2008-2015 period. Total melt rate for the full shelf is ~82 Gt/yr for "initial pixel" and ~93 Gt/yr for "along-flow distribution" composite 2-year Dh/Dt melt rate products (Table 3-5).

Melt rates are >150-200 m/yr near the main shelf grounding line, with highest rates along the north side of the grounding line. Melt rates are generally ~50-100 m/yr over the main shelf inner cavity, where ice thickness exceeds ~600-700 m, and ~10-20 m/yr over most of the outer shelf, where ice thickness is typically ~300-500 m. Melt rates show significant anisotropy, with general longitudinal correlation over lengths scales of ~20 km and significant ~km-scale transverse variability in both "initial pixel" and "along-flow distribution" products (Figure 3-11). The northern third of the outer main shelf (red arrow in Figure 3-2) displays ~3-4 longitudinal features with elevated melt rates of ~30-40 m/yr. Upstream of these features, a broad (~10 km wide x 20 km long) region of low-relief transverse ridges/troughs (green arrow in Figure 3-2) displays reduced melt rates of ~5-10 m/yr.

Melt rates are ~0-10 m/yr over the South shelf and ~0-5 m/yr over the North shelf (Figure 3-2C). Increased rates of ~60-90 m/yr are observed near the relatively deep (~900 m) grounding line of the fast-flowing (~700-1000 m/yr) South shelf tributary (Figure 3-2C). Elevated melt rates of ~20-50 m/yr are also apparent within large channels on the south shelf (blue arrow in Figure 3-2).

Figure 3-14 shows the relationship between km-scale surface features and melt rates. The highest melt rates are associated with longitudinal surface ridges within ~3-4 km of the grounding line. Between ~4-10 km from the grounding line, elevated melt rates are associated with longitudinal surface troughs. At greater distances from the grounding line and over the outer shelf, elevated melt rates are correlated with surface ridges, with decreased melt in troughs. Figure 3-14 shows that beyond ~25-30 km of the grounding line, elevated melt rates of ~10-20 m/yr are associated

with the ~50-70 km-long centerline ridges, while ~0 m/yr melt rates are observed within adjacent longitudinal troughs. One prominent centerline ridge displays elevated rates of ~30-40 m/yr (black arrow in Figure 3-2).

3.4.4 *Basal melt rate temporal evolution*

Both the magnitude and spatial distribution of basal melt evolved during the 2008-2015 period. We focus our discussion on the main shelf, with emphasis on the inner shelf, as temporal coverage is limited over the North and South shelves, and do not appear to show significant change.

Table 3-6 and Figure 3-12 shows that mean, maximum and total area-integrated melt rates for 2008-2010 appear significantly higher than those observed during all subsequent 2-year time periods. Minimum melt rates occurred from 2010-2012. While the 2009-2011 melt rate products do not cover the entire shelf, they suggest that much of the observed melt rate decrease occurred between the 2008-2010 and 2009-2011 time periods. Melt rates appear to increase during 2011-2013 and 2013-2015, but are still less than those from 2008-2010. Figure 3-8 shows maps of melt rate change for these time periods.

During 2008-2010, local melt rates of >250-300 m/yr are observed near the north main shelf grounding line, with rates of >200 m/yr observed >8 km downstream of the grounding line – well beyond the expected transition to hydrostatic equilibrium. The 2008-2010 melt rates show ~150-200 m/yr melt rates within a surface trough downstream of the "ice plain" anomaly near the centerline of the inner shelf (Figure 3-14). Melt rates decrease significantly where surface elevation of this downstream trough decreases below ~60-70 m. Laterally-adjacent melt rates on either side of the "ice plain" anomaly and downstream trough are <0-10 m/yr during this period.

The 2010-2012 products show a different spatial pattern, with significantly reduced melt rates over the former "ice plain" anomaly, and increased rates over the laterally-adjacent surfaces. We note that melt rates of ~120-160 m/yr are observed within the trough just north (left) of a notable positive surface anomaly. By 2011-2013, melt rates over the "ice plain" region display increase to ~60-120 m/yr, with significantly less spatial variability (Table 3-6).

We observe spatially coherent melt-rate variability over north side of the outer main shelf (green arrow in Figure 3-2) between 2008-2015. Melt rates are ~15-25 m/yr for 2008-2010, with apparent decrease to ~0 m/yr in 2009-2011 and 2010-2012 products, and a return to ~15-25 m/yr in 2012-2014 and 2013-2015 products.

We also note the evolution of melt rates over transverse rifts and surface depressions near the centerline of the outer shelf (e.g., Figure 3-14C). These features become more pronounced after ~2014 as these rifts open and surface depressions grow, with corresponding ~10-15 km long, transverse linear patterns of ~30-40 m/yr melt rates observed in the 2012-2014 and 2013-2015 products. Increased melt rates appear focused within ~1 km of transverse rift centerlines and over the upstream side of transverse surface depressions [*Shean et al.*, 2016c].

3.4.5 *Comparison with in situ measurements*

Basal melt rates were measured within a channel on the outer shelf during a 35-day field campaign from December 2012 to January 2013 [*Stanton et al.*, 2013]. Annualized basal melt rates from an upward-looking coherent acoustic profiler, phase-sensitive radar (pRES) surveys, and ocean flux package measurements near this site were ~14.2–24.5 m/yr. These measurements also document seaward currents within ~2-3 m of the channel ice base.

Figure 3-15 shows sampled "along-flow distribution" 2-year DEM Dh/Dt melt rates of ~15-25 m/yr for this location. Limited apparent interannual variability at this site is within uncertainty. The estimated Lagrangian Dh/Dt melt rates also show good agreement with *in situ* Dh/Dt observations for GPS receivers installed on the South shelf from January 2008 to January 2010 (PIG2, ~4 m/yr) and the outer main shelf from January 2012 to December 2013 (BOAR, ~10–15 m/yr) [*Shean et al.*, 2016c] (Figure 3-15).

3.4.6 *Melt rate vs. depth parameterization*

The right column of Figure 3-16 shows plots of inner shelf melt rate vs. depth calculated from freeboard thickness. We use these plots to evaluate the Joughin et al. [2010b] and Favier et al. [2014] piecewise linear parameterizations, and offer a new linear fit for each time period constrained with 0 m/yr melt rate intercept at 400 m depth.

In general, all periods show an approximately linear relationship between melt rates and depth, with increasing spread at depth. Anomalous clusters at depth can be correlated with individual channels and keels, which appear to display higher and lower melt rates, respectively. Anomalously low melt rates below ~800 m depth can be correlated with ephemerally-grounded keels that display positive Dh/Dt.

These plots show a significant shift in the melt rate distribution from 2008-2010 to 2010-2012, with decreased magnitude and spread. Constrained linear fits display slopes of ~21 m/yr melt increase per 100 m depth (m/yr/hm) from 2008-2010, and only ~16 m/yr/hm from 2010-2012. The 2011-2013 and 2013-2015 distributions show a slight increase of ~17-18 m/yr/hm, but reduced spread at all depths, which is consistent with reduced spatial variability observed in the melt rate maps.

Figure 3-17 shows maps of expected melt rates for the three piecewise linear models, with integrated values over the inner shelf presented in Table 3-7. The Joughin et al. [2010b] parameterization offers a reasonable fit for 2008-2010 melt rates, especially near the grounding line, but overestimates melt in later years. The Favier et al. [2014] parameterization consistently underestimates high melt rates near the grounding line, but offers a better overall fit for reduced melt rates and spatial variability from 2010-2015. Our constrained linear fits for each time period offer a compromise between the two models but fail to capture elevated rates near the grounding line and ~km-scale spatial variability.

3.4.7 *Mass budget analysis*

Figure 3-18 shows that discharge across the main shelf grounding line increases from ~110 Gt/yr to ~117 Gt/yr between 2008 and 2010. Discharge decreases slightly from 2011-2014, falling to ~114 Gt/yr, with an apparent increase from 2014-2015 to ~115 Gt/yr. These results are consistent with other recent mass budget analyses [*Medley et al.*, 2014; *Mouginot et al.*, 2014].

Discharge near the shelf front remains relatively constant at ~50-54 Gt/yr over the 2008-2015 period (Figure 3-18A). We note an apparent increase in discharge across the gate ~30 km downstream of the grounding line, which is consistent with spatial patterns of shelf thickening observed in Eulerian dh/dt and DEM anomaly products (Figure 3-8).

The RACMO SMB estimates from 2008-2015 are ~3-4 Gt/yr and ~1-1.5 Gt/yr over the full shelf and main shelf (Table 3-5), respectively, with negligible interannual variability. Estimates for Eulerian dH/dt over the main shelf are -15 Gt/yr for 2008-2010, and -7 to +4 Gt/yr in subsequent years.

We observe good agreement between the mass budget and integrated “along-flow distribution” DEM Dh/Dt melt rates (Figure 3-18). Total area-integrated main shelf melt rates are ~60-80 Gt/yr between 2008-2015. The two approaches show the same general temporal evolution, with a

significant decrease between 2008-2010 and 2010-2012 and a limited increase in melt rates from 2010-2012 and 2013-2015. The regions with valid 2009 DEM coverage show that much of this decrease appears to occurs between 2008-2010 and 2009-2011.

These results show that ~80-85% of main shelf melt occurs within the inner cavity, with limited melt rates of only ~11-12 Gt/yr over the outer shelf. Further partitioning the inner shelf melt shows that ~40-50% of total main shelf melt occurs within ~10 km of the main grounding line.

Table 3-5 summarizes mass budget results for the North and South shelves from 2008-2015. The South shelf shows discharge of ~14-15 Gt/yr, primarily due to the relatively thick, fast-flowing tributary (Figure 3-2). Discharge for the North shelf remains relatively steady at ~3 Gt/yr. Integrated Dh/Dt melt rates over the North and South shelves are ~4-5 and ~10 Gt/yr, respectively.

3.5 DISCUSSION

3.5.1 *Grounding history*

Much of the 2008-2015 grounding history for the PIG shelf is outlined in Joughin et al. [2016]. We include a brief summary of this evolution, with additional observations relevant for interpretation of melt rate results.

A portion of the PIG "ice plain" was likely grounded (or had ungrounded <6 months earlier) in early March 2008 (Figure 3-8, Figure 3-13). The 2008 DEM anomaly maps also suggest that a ~5 km long and ~1-1.5 km wide ridge/keel near the shelf centerline appears to be grounded ~15-20 km downstream of the main grounding line (Figure 3-8). While the 2009 DEM coverage is limited, the DInSAR results from February-March 2009 show that the ice plain is no longer grounded, and this ~5 km feature appears grounded, producing the ephemeral, "bicycle seat" shape observed in 2009 grounding line maps.

Subsequent years show the progressive advection and regrounding of at least 2-3 keels near the shelf centerline. These features appear to be the same features that were initially grounded over the "ice plain" in early 2008. As these features advect at a rate of ~4 km/yr over underlying bathymetry, they display elevation increases of >30 m and subsequent decreases of >30 m in the DEM anomaly and Eulerian dh/dt maps (Figure 3-8, Figure 3-13).

While the bathymetry is poorly constrained, estimates for the total area (~10-20 km^2) and volume (~0.5-1 km^3) above floatation for these features increase from 2010-2013, and then decrease from

2013-2015. We suggest that much of the observed 2012-2014 velocity variability (~2-3%) during this period [*Christianson et al.*, 2016] is related to evolving basal drag from the grounding/ungrounding of these keels. The shelf also experiences a northward rotation during this period [*Christianson et al.*, 2016; *Jeong et al.*, 2016], and we suggest that some if not all of this rotation is related to the regrounding of these keels on northward-sloping bathymetry (Figure 3-13B).

The localized positive elevation change over the north side of the main grounding line from 2012-2013 and 2013-2015 (Section 3.4.2, Figure 3-8) appears to be related to increased ice thickness and re-advance of the main shelf grounding line. This is potentially related to significant reduction in melt rates downstream of this location (Figure 3-12). While the impact of this apparent grounding line advance on ice stream dynamics is negligible, it represents a departure from monotonic retreat observed in recent decades [e.g., *Park et al.*, 2013; *Rignot et al.*, 2014].

3.5.2 *Melt rate spatial distribution*

The bifurcated spatial distribution of high melt rates near the grounding line is likely a function of modern (post-2006) cavity geometry (Figure 3-7). Mass conserving bed reconstruction for the 1990s shows a large longitudinal seabed ridge (~4 wide x 30 km long) near the centerline of the inner cavity [*Rignot et al.*, 2014]. High melt rates are observed within the deep areas near the grounding line on either side of this ridge. Highest melt rates of >250-300 m/yr on the north side, where warm water circulating through the inner cavity is expected to first reach the grounding line [e.g., *Dutrieux et al.*, 2014b].

We note that the enhanced ~30-40 m/yr melt rates over the northern portion of the outer shelf (red arrow in Figure 3-2) are located just downstream of the transverse seabed ridge. Both the Autosub observations and ocean GCM simulations show increased ocean current velocity near this location [*Dutrieux et al.*, 2014b], suggesting that this local high in melt rates could be related to local circulation patterns and/or upwelling near the transverse seabed ridge. This is one of the expected pathways for warm CDW inflow into the inner cavity [e.g., *St-Laurent et al.*, 2015], and we suggest that as this water flows over the transverse seabed ridge, it could lead to enhanced melting at this location.

3.5.3 *Melt rate temporal evolution*

The Lagrangian Dh/Dt melt rate products document significant changes in melt rate magnitude and spatial variability over the inner shelf. We performed several additional experiments to confirm this result, including Dh/Dt melt rate calculations with: 1) input DEMs without least-squares "tilt" correction, 2) a DEM stack including only LVIS/ATM and WorldView/GeoEye DEMs (i.e., no SPIRIT DEMs), 3) advection path estimates from a time-invariant, 2006-2016 median velocity grid, and 4) IMAU-FDM [*Ligtenberg et al.*, 2011] estimates of surface elevation change due to surface processes and firn compaction. We obtain the same general results for each of these cases, which confirms the efficacy of the noise-reduction approaches outlined in Section 3.3.9.

Our analysis suggests that the observed melt rate temporal change is related to significant changes in ice thickness and evolving cavity geometry. The largest changes appear to be related to the 2008-2009 ungrounding events over the "ice plain" and progressive advection, and grounding/ungrounding of deep keels. These deep keels were located in the deep inner cavity during 2008-2010, where they were exposed to the warmest ocean water. In subsequent years, keel depths in the inner cavity were significantly reduced.

In addition, profiles of ice thickness and bathymmetry suggest that keels could potentially block much of the north-south (cross-shelf) transport within the inner cavity. The formation of new transverse channels immediately upstream of grounded keels (Figure 3-16) supports this interpretation. These changes in inner cavity geometry should have a significant impact on circulation, potentially interrupting the circulation patterns responsible for higher melt rates observed before 2010.

We expect that major changes in circulation would significantly alter melt rate spatial distribution, which would lead to further changes in channel and cavity geometry. This potentially leads to a series of complex positive feedbacks, with initial perturbations related to grounding line evolution and the presence of deep keels within the inner cavity. This potentially provides a mechanism for the shift from focused melt within a large channel near the inner shelf centerline in 2008 to a large channel on south side of main shelf by 2015 (Figure 3-8).

The coherent spatial pattern of melt variability over north side of main shelf (green arrow in Figure 3-2) warrants further attention. The relief of transverse surface ridges/troughs over this region appears significantly reduced compared with transverse ridges/troughs closer to the grounding line

and over the southern portion of the main shelf (Figure 3-14). Some of this variability could be related to localized artifacts in the SPIRIT DEMs, potentially related to differences in image sun elevation and correlation quality for DEM generation. Indeed, these ridges appear relatively low in the January 3, 2009 DEM when compared to SPIRIT DEMs from March 3, 2008. However, variability over this region is also observed in melt rates derived exclusively from LVIS and WorldView/GeoEye DEMs, which display improved absolute and relative accuracy.

We suggest that some of the observed changes in Dh/Dt over the north side of the main shelf were related to surface and/or ocean processes. An evaluation of the Landsat archive and SPOT5 images (5 m/px) shows some redistribution of surface snow in these areas on ~1 to 2-year timescales. We also note elevation variability of +/-1.0 m in annual airborne altimetry data over the adjacent slope of the Evans Knoll peninsula. The Evans Knoll automated weather station (AWS) (74.85°S, -100.404°W) indicates that winds are consistently blowing across the shelf toward this slope, and we might expect enhanced localized accumulation of wind-blown snow within troughs. We note, however, that this portion of the shelf overlies the expected path of inflow over the transverse bathymetric ridge and into the inner cavity [e.g., Figure 9 of *St-Laurent et al.*, 2015]. We might expect warmer water moving over the bathymetric ridge to interact with the ice shelf base in this region. If this interpretation is correct, local melt rates near this location could potentially be used as a proxy to detect changes in the hydrographic properties of water entering the inner cavity.

3.5.4 *Channel-scale melt*

Our results confirm past conclusions about the importance of channel-scale geometry for basal melt [*Rignot and Steffen*, 2008; *Gladish et al.*, 2012; *Dutrieux et al.*, 2013, 2014a; *Millgate et al.*, 2013]. We observed increased total melt, increased maximum melt rates, and increased spatial variability during 2008-2010, when a few large, deep channels are present over the inner cavity. By 2013-2015, the number and relative depth of channels within the inner cavity decreases, with a corresponding decrease in these metrics. While many factors/feedbacks may be involved, the dramatic change in melt spatial pattern suggests that the deep channel/keel morphology is of primary importance.

In addition to the transverse channels that appear to form immediately upstream of the ephemerally-grounded locations between 2011-2015 (Figure 3-8), we observe the formation of transverse channels that appear to carve “notches” across large existing longitudinal keels. These

features likely initiate due to positive feedbacks involving enhanced circulation velocities and melting over initially minor keel depth perturbations, with further enhancement due to extensional "necking" processes [e.g., *Bassis and Ma*, 2015].

We observe enhanced melting in channels adjacent to grounded keels (Figure 3-8). The grounded keels display positive Dh/Dt for the 2-year time period, which translates to an apparent -5 to -30 m/yr melt rate. This confirms that these particular keels remain grounded (or become "more" grounded, with increased height above floatation) as they advect downstream during the 2-year time period. Thus, the observed negative Dh/Dt over adjacent channels cannot simply be attributed to a reduction in local bridging stresses that might be expected if these keels were to unground. In fact, we expect the opposite behavior as these features become "more" grounded – surface elevations over adjacent channels should increase due to enhanced bridging, and inferred Dh/Dt melt rates will decrease.

Our analysis confirms past interpretations [e.g., *Dutrieux et al.*, 2013] suggesting that increased melt is generally associated with deep channels closer to the grounding line, and keels over the outer shelf. However, increased coverage over the full shelf shows that this relationship is complex, with significant spatial and temporal variability (Figure 3-14). We note that the transverse surface ridges/troughs on the south side of the main shelf (both inner and outer shelf) display much greater relief than those along the north side of the shelf, with correspondingly higher melt rates over keels.

We also note apparent enhanced melting on the south sides of the longitudinal channels near the shelf centerline (Figure 3-14), which are less susceptible to cumulative displacement error than transverse channels. This is consistent with expectations for the Coriolis effect on seaward transport along these ~60-80 km long features. Based on these observations, we suggest that the relative position of high-resolution "initial pixel" melt rates within channels can potentially be used to infer and map the direction of sub-shelf ocean currents.

Our results support the conclusion that "irregularities imprinted on the ice by bedrock are preferentially amplified by ocean melting" [*Gladish et al.*, 2012]. We expect that surface elevation immediately upstream, over, and a few km downstream of the grounding line will be sensitive to ~km-scale bed topography.

For example, a ~km-wide, ~200-m high bed obstacle near the grounding line of a ~1 km thick ice stream should produce a smoothed, positive ~10-20 m surface elevation anomaly with ~2-4 km

width, centered ~200-400 m upstream of the obstacle. Local ice thickness directly over the obstacle, however, will be reduced by the full obstacle height (minus the surface anomaly, which is relatively small). Surface elevations over laterally-adjacent ice will appear similar to those over the obstacle, despite significantly greater ice thickness. Relevant surface anomaly length scales, dimensions, and magnitude will vary with bed obstacle dimensions, ice thickness, basal slipperiness, and other fundamental dynamic factors [*Gudmundsson*, 2003]. Regardless, as this column of thinner ice moves downstream of the grounding line obstacle, local surface elevations will evolve as the ice approaches hydrostatic equilibrium. Surface elevations over the thinner ice downstream of the obstacle will display a relative elevation decrease compared to elevations over adjacent thicker ice, forming surface troughs and ridges, respectively. Thus, an initially positive longitudinal surface ridge over an obstacle near the grounding line would form a longitudinal surface trough downstream, independent of basal melt. The relevant time and spatial scales for this relaxation will depend on a number of factors, including ice thickness and advection velocity.

This can potentially explain the observed relative surface topography downstream of the 2008 "ice plain" anomaly (Figure 3-8), and the observed 2008-2010 transverse variability in melt rate magnitude over the inner shelf (Figure 3-16). Some melt rates within ~1–2 km of the grounding line are potentially overestimated due to this effect. However, we also expect localized melting near the grounding line to be highest within these "pre-initiated" channels due to their steep slopes and increased availability of warm water.

This "inversion" of surface topography across the grounding line will also affect local snow redistribution by wind, with a shift in the expected location of sources and sinks. The magnitude of associated elevation changes, however, is likely small compared to observed Dh/Dt of ~20-30 m/yr near the PIG grounding line.

Finally, we note that the Dh/Dt results cannot unambiguously distinguish sub-shelf melting due to ocean water from that due to subglacial discharge entering the inner cavity near the grounding line. Estimates for total subglacial melt over the grounded catchment are ~1.7 km^3/yr [*Joughin et al.*, 2009], and remote sensing observations document repeat subglacial lake drainage events <30 km upstream of the grounding line during the 2008-2015 time period [*Joughin et al.*, 2016]. This is likely an important contribution to channel evolution for the inner shelf, although the timing and relative duration of these events is poorly constrained.

3.5.5 *Comparison with past melt rate assessments*

The local melt rates observed within channels near the grounding line (>200 m/yr) are significantly higher than past estimates of ~100 m/yr [*Payne et al.*, 2007; *Bindschadler et al.*, 2011; *Dutrieux et al.*, 2013]. They are more consistent with the [*Payne et al.*, 2007] flux divergence estimates, which show high rates of ~200-300 m/yr near the mid-1990s grounding line.

Our integrated melt rates from the full-shelf DEM Dh/Dt (~82-93 Gt/yr) are less than past estimates of ~95-101 Gt/yr for the 2003-2008 period [*Depoorter et al.*, 2013; *Rignot et al.*, 2013]. While this may represent a true decrease in shelf-wide melt from 2003-2008 to 2008-2015, we suggest that it can also be attributed to methodological differences.

For example, these past studies mixed observations from different periods over an unusually dynamic period, with dh/dt from 2003-2008 ICESat-1 data, velocities from a 2007-2008 InSAR mosaic [*Rignot et al.*, 2011b], and average SMB from 1979-2010. We also note differences in shelf area, gate placement, and the measurement resolution (10 km).

Much of the discrepancy with previous estimates also could be related to interpolation of sparse ICESat-1 Eulerian dh/dt thinning rates over the entire PIG shelf. We document robust ~10-km-scale spatial variability, with some regions thickening (e.g. north inner shelf) and other regions thinning (e.g., south outer main shelf) (Figure 3-9). However, the 1-year and 2-year Eulerian DEM dh/dt products also highlight issues related to advecting ridges and troughs. Aliasing of these signals can lead to significant errors in thinning rates inferred from smoothed ICESat-1 repeat tracks (e.g. Figure 13 of [*Sergienko*, 2013]), especially after converting elevation change to freeboard thickness change.

We note that smoothing surface elevations at ~10 km spatial scales (e.g. ICESat-1 or radar altimetery) removes the surface expression of km-scale channels/keels and anomalies associated with regrounding keels, which can significantly affect melt rates. We would still expect to see general temporal variability in melt rates and shelf thickness at lower resolution, but would lose the ability to identify the mechanisms responsible for the observed change.

The GLAS spot size was ~30-70 m in diameter with ~170 m along-track spacing and ~20 km cross-track spacing of repeat observations (e.g., Figure 3 of [*Pritchard et al.*, 2009]). Limited measurements are available to estimate local slopes sampled by repeat ICESat-1 tracks over the PIG shelf. While this may not be relevant for flat, smooth ice shelves like the Ross and Ronne-Filchner ice shelves [*Moholdt et al.*, 2014], this simple fact limits the accuracy of the sparse

ICESat-1 dh/dt measurements over the PIG shelf. Smoothing over ~10 km and interpolating these measurements for shelf-wide dH/dt estimates will compound these errors. Rignot et al. [2013] estimate shelf-wide 2003-2008 dH/dt of -5.32 +/- 0.3 m/yr or -33.2 +/- 2 Gt/yr. Our analysis suggests that this method overestimates dH/dt and published uncertainty estimates are likely too low. Thus, we cannot rule out the possibility that melt rates show no significant long-term change from ~2003-2008 to ~2008-2015.

3.5.6 *Model melt rate evaluation*

While the piecewise linear parameterizations discussed in Section 3.4.6 characterize general melt rate vs. depth relationships, they are unable to fully capture the observed evolution of cavity geometry and resulting melt rate spatial variability. Recent experiments with evolving cavity geometry in coupled ice-ocean models suggest that these linear parameterizations can significantly overestimate mass loss [*De Rydt and Gudmundsson*, 2016].

We note that ocean GCM simulations for the PIG cavity [*Schodlok et al.*, 2012; *Seroussi et al.*, 2014], however, show poor agreement with the observed magnitude and spatial distribution of Lagrangian Dh/Dt melt rates. This disconnect emphasizes the importance of accurate bathymetry, evolving cavity geometry, and fine (<0.5 km) spatial resolution for ocean GCM simulations. We suggest that relying exclusively on ocean GCM melt rates can also lead to unrealistic results in prognostic models, especially for longer ~50-100 year simulations. Considerable uncertainty in sub-shelf bathymetry (Figure 3-7) and the observed temporal/spatial variability in shelf thickness will lead to increased uncertainty in ocean GCM output.

The high-resolution DEM observations presented here could be used to calibrate and validate coupled ice-ocean models with evolving cavity geometry and ocean circulation. As these models become more sophisticated, they can be used in place of linear parameterizations in prognostic simulations to further constrain future PIG evolution and mass loss.

3.5.7 *Implications for ice-ocean sensitivity*

Our results have implications for the timescales and complexity of connections between ocean forcing, cavity geometry, and ice dynamics. Basal melt rates are expected to increase linearly to quadratically with increasing ocean temperature [*Holland et al.*, 2008]. However, recent modeling results show that warming ocean temperatures by a few tenths of a degree does not necessarily

lead to increased melting near the grounding line [Gladish et al., 2012]. Entrainment of this warmer water is slope-dependent, and efficiency is expected to decrease with increasing temperature [*Little et al.*, 2009].

Our results do not show the 50% decrease in melt inferred from hydrographic observations in Pine Island Bay between 2010 to 2012 [*Dutrieux et al.*, 2014b]. We observe a decrease of ~30% (53 Gt/yr to 36 Gt/yr) in total DEM Dh/Dt melt over the inner cavity, and a ~15-25% decrease in total main shelf melt between 2008-2010 and 2010-2012. Ocean temperature records from Pine Island Bay [*Christianson et al.*, 2016] show limited change during this time period (Figure 3-19). The estimated melt rate decrease occurs *before* observed temperatures decrease in mooring records between late 2011 to early 2012, and then from mid-2012 to early 2013 [*Christianson et al.*, 2016]. This disconnect is observed for melt rates estimated using both DEM and *in situ* GPS [*Shean et al.*, 2016c] Dh/Dt records during these periods.

These results raise important questions about the strength and timing of the connection between hydrographic observations in Pine Island Bay and sub-shelf processes >100 km upstream, within the inner cavity. The mooring records are positioned near the expected path for meltwater outflow, but the sensitivity of these observations to circulation in the outer cavity and/or Pine Island Bay is poorly constrained.

We note that the 2012 CTD sampling was relatively sparse (e.g., Figure S4 of Dutrieux et al. [2014b]) and ~20-30 km farther from the shelf front than sampling in previous years [*Dutrieux et al.*, 2014b]. Observed ocean temperature change is greatest from ~300-600 m depth, with limited change below these depths (only ~0.1-0.2°C below ~700 m between 2010 and 2012). While significant uncertainty remains in the sub-shelf bathymetry, our comparisons show local bed elevation minima along the transverse seabed ridge at >700-750 m depth (Figure 3-7). Thus, it is feasible that warmer water below ~600 m depth could continuously enter the inner cavity throughout the 2008-2015 period, resulting in relatively constant heat content near the grounding line. It has been suggested that only 20-50% of sub-shelf heat is used for melting [*Little et al.*, 2009]. Thus, it is possible that the PIG cavity always contains significant ocean heat content, which supports the interpretation that melt rates may be more sensitive to sub-shelf geometry and circulation.

Recent bathymetric and CTD surveys in West Greenland fjords suggest that ice retreat was not correlated with the presence of warm Atlantic water near the ice front [*Rignot et al.*, 2016]. While

a direct comparison of these outlet glaciers with PIG is not appropriate, these results are consistent with our general conclusion that sensitivity of melt rates to ocean forcing may be more limited than previously reported.

3.5.8 *Implications for past and present stability*

Grounding line retreat through ~2009 (Figure 3-13) is primarily responsible for the strong interannual thinning observed upstream of the grounding line [*Joughin et al.*, 2010b] (Figure 3-12). Our results document the end of this rapid retreat between ~2008-2009, with limited regrouding over the seabed ridge and decreased thinning rates upstream of the grounding line in the following years. The increased thinning rates over upstream shear margins (Figure 3-9) can also be attributed to this evolution, as sustained thinning rates of >5-10 m/yr over the main trunk prior to ~2009 led to significant increase in slopes and transverse driving stress across shear margins.

The observed velocity and elevation data are consistent with model simulations [*Joughin et al.*, 2010b] that show reduced speedup and thinning near the grounding line as retreat slows. This suggests that the current grounding line position is relatively "stable" and PIG may be entering another period during which ocean forcing will have greater influence over sub-shelf melt rates and the initiation of subsequent retreat [e.g., *Christianson et al.*, 2016]. Continued high-resolution DEM and velocity observations can be used to test this hypothesis, for the Pine Island Glacier and other Antarctic ice shelves.

3.6 SUMMARY AND CONCLUSIONS

We generated a new high-resolution DEM record from WorldView/GeoEye satellite stereo imagery, and integrated with available 2002-2015 DEM/altimetry data over the PIG ice shelf. We developed novel Lagrangian Dh/Dt methodology and combined with annual mass budget analysis to estimate basal melt. This analysis reveals the complex spatial/temporal evolution and interconnection of grounding zones, sub-shelf cavity geometry, basal melt rates, and upstream dynamics over grounded ice.

We document significant main shelf grounding line retreat between 2008-2009, and the ephemeral regrounding of ~2-3 deep keels as a positive shelf thickness anomaly advects over a seabed ridge. Eulerian dh/dt rates upstream of the grounding line decrease from ~5-10 m/yr in 2008-2010 to ~0 m/yr by ~2012-2014, with a small grounding line advance observed from 2012-2015.

Mean 2008-2015 basal melt rates for the full shelf are ~80-90 Gt/yr. Local melt rates of ~200-250 m/yr within large channels near the grounding line, ~10-30 m/yr over the main shelf, and ~0-10 m/yr over the North and South shelves, with notable exception of ~50-100 m/yr near the grounding line of a fast-flowing tributary on the South shelf. The Lagrangian Dh/Dt melt rates show excellent agreement with, and provide spatial/temporal context for, *in situ* melt rate observations [*Stanton et al.*, 2013; *Shean et al.*, 2016c].

Melt rates were highest for the 2008-2010 period, with significant (~20-30%) decrease by 2010-2012 and gradual increase from 2010-2012 to 2013-2015 (but remaining less than 2008-2010 rates). The inner shelf shows a ~1-2 m/yr thickening signal after ~2010, and we document the propagation of a broad positive thickness anomaly across the inner shelf between ~2010 and 2015 that likely originated due to some combination of ungrounding, increased discharge, and reduced melt rates.

Melt rates vary significantly across ~km-scale ice shelf thickness variations, with focused melting in basal channels near the grounding line and keels over the outer shelf. We suggest that these features alter sub-shelf circulation, leading to positive feedbacks that can influence regrounding and upstream ice dynamics. Sparse observational data from satellite altimetry and ocean circulation models may not capture these details, potentially leading to incorrect conclusions about mechanisms driving observed change.

The PIG shelf displays a positive linear relationship between melt rate and depth, with increasing melt rate magnitude and variability at depth. The slope of and spread about this linear relationship varies over time. Existing piecewise melt rate parameterizations in prognostic ice flow models provide reasonable approximations for this relationship, but fail to capture km-scale variability.

Our analysis does not show the ~50% decrease in melt rates between 2010 and 2012 inferred from hydrographic observations in Pine Island Bay [*Dutrieux et al.*, 2014b], and we do not observe significant melt rate variability associated with observed ~2012 ocean cooling in mooring records [*Christianson et al.*, 2016]. This suggests that PIG melt rates were not directly correlated with observed ocean heat content in Pine Island Bay during these periods.

Our results suggest that observed ice shelf melt and upstream dynamics were more sensitive to grounding evolution, channel-scale circulation, and internal instabilities than oceanographic forcing. These findings have important implications for diagnostic/prognostic flow modeling efforts used for projections of 21st century sea level rise.

ACKNOWLEDGEMENTS

D. Shean was supported by a NASA NESSF fellowship (NNX12AN36H). I. Joughin (#), B. Smith (#), P. Dutrieux (#). We acknowledge Claire Porter, Paul Morin, and others at the Polar Geospatial Center (National Science Foundation ANT-1043681) who managed tasking, ordering, and distribution of the WorldView/GeoEye stereo imagery. We thank Oleg Alexandrov and Zack Moratto for development and support of the Ames Stereo Pipeline, with support from the NASA Cryosphere program. We thank Stefan Ligtenberg and Peter Kuipers Munneke for providing RACMO SMB and FDM products.

Resources supporting this work were provided by the NASA High-End Computing (HEC) Program through the NASA Advanced Supercomputing (NAS) Division at Ames Research Center. SPOT-5 DEMs and imagery were provided at no cost by the French Space Agency (CNES) through the SPIRIT International Polar Year project [Korona et al., 2009]**.**

TABLES

Convergence angle	10-60°
Time between images	<2 days
Minimum intersection area	100 km^2
Minimum relative image area for intersection	30%

Table 3-1: Cross-track stereo pair criteria.

	Stereo		Mono		Combined	
Count	343		25		368	
Mean offset before/after co-reg (m)	-3.06	-0.01	-4.03	0.02	-3.12	-0.01
Mean RMSE before/after (m)	3.29	0.44	5.24	0.73	3.42	0.46
Mean NMAD before/after (m)	0.36	0.36	0.63	0.63	0.38	0.38

Table 3-2: Statistics before and after DEM co-registration for PIG catchment

Minimum n	4
Minimum total dt	1.5 years
Minimum elevation (EGM2008)	10 m
Maximum absolute dh/dt	2.0 m/yr
Maximum detrended std	3.0 m

Table 3-3: Criteria to identify dynamic control surfaces for least-squares correction.

	Mean (m)		Median (m)	
	Std.	Detr. Std.	Std.	Detr. Std.
Original	2.45	2.11	2.49	2.08
Co-registered	1.29	0.78	0.94	0.56
Co-registered and LS “tilt” correction	1.14	0.41	0.73	0.22

Table 3-4: Results of least-squares DEM correction. Statistics computed for 2010-2015 WorldView/GeoEye DEMs and ATM/LVIS altimetry data over dynamic control surfaces (n=4–44 at each pixel, sample of ~6.1×10^5 pixels, covering ~4×10^4 km^2). All metrics show decreased spread after correction, with median values less prone to outliers.

Region (gates)	Area (km^2)	Q_{in} (Gt/yr)	Q_{out} (Gt/yr)	Qdiv (Gt/yr)	SMB (Gt/yr)	dH/dt (Gt/yr)	B (Gt/yr)	"Along-flow" Dh/Dt Melt (Gt/yr)	"Initial pixel" Dh/Dt Melt (Gt/yr)
Main Shelf (GL, Rift)	1717	114.9	52.7	63.0	1.3	-4.8	69.1	69.0	57.8
GL (GL, GL+10)	247	114.9	86.7	28.9	0.2	-1.7	30.7	29.4	24.7
Inner (GL+10, GL+30)	536	86.7	60.3	26.8	0.4	1.5	25.7	26.7	21.1
Outer (GL+30, Rift)	928	60.3	52.7	7.3	0.7	-3.3	11.4	12.6	11.9
Subtotal	1711	--	--	63.0	1.3	-3.5	67.8		
2003-2008[1]	2577	--	--	--	--	--	63	--	--
South shelf	1065							10.5	10.7
S (GL, Edge)									
North shelf	1345							5.0	5.6
N (GL, Edge)									
Subtotal	4127							85.8	75.3
Full shelf*	5420							93.8	82.2
2003-2008[1]	5920	126.4+/-6	62.3+/-5		4.6+/-0.9	-33.2+/-2	101.2+/-8	--	--
2003-2008[2]		110+/-11	50+/-8		4+/-1	-30+/-2	95+/-14	--	--

Table 3-5: Mean 2008-2015 mass budget results and integrated Dh/Dt melt rates. Estimates from 2003-2008 from [1]Rignot et al. [2013] and [2]Depoorter et al [2013]. Note that integrated Dh/Dt melt rate estimates for main, North and South shelves do not include shear margins, while Full shelf estimates do include shear margins and additional transient area near calving front.

Period	Total melt (Gt/yr)		Mean melt rate (m/yr)		Std melt rate (m/yr)		Med melt rate (m/yr)		MAD melt rate (m/yr)	
	IP	AFD	IP	AFD	IP	AFD	IP	AFD	IP	AFD
2008-2010	48.1	57.0	98.1	116.5	59.9	56.6	87.4	105.7	54.3	50.0
2010-2012	33.8	43.2	69.2	88.3	47.3	45.0	64.4	82.9	45.3	44.1
2011-2013	37.4	44.6	76.2	91.2	46.8	48.7	68.9	83.1	42.1	45.6
2013-2015	39.5	46.6	81.2	95.3	42.0	43.3	73.6	88.2	38.5	41.9

Table 3-6: Temporal evolution of high-resolution Dh/Dt melt rates for inner shelf. Columns list statistics for "initial pixel" (IP) and "along-flow distribution" (AFD) melt rate estimates for ~533 km^2 inner shelf.

Period	Observed (Gt/yr)	Fit (Gt/yr)	Joughin et al., 2010 (Gt/yr)	Favier et al., 2013 (Gt/yr)
2008-2010	48.1	45.6	53.0	40.2
2010-2012	33.8	32.7	48.1	39.5
2011-2013	37.4	35.9	50.4	40.9
2013-2015	39.5	37.9	49.8	41.0

Table 3-7: Comparison of observed and parameterized melt rates for inner shelf. Observed "initial pixel" melt and piecewise linear melt vs. depth models for the ~533 km^2 inner shelf.

FIGURES

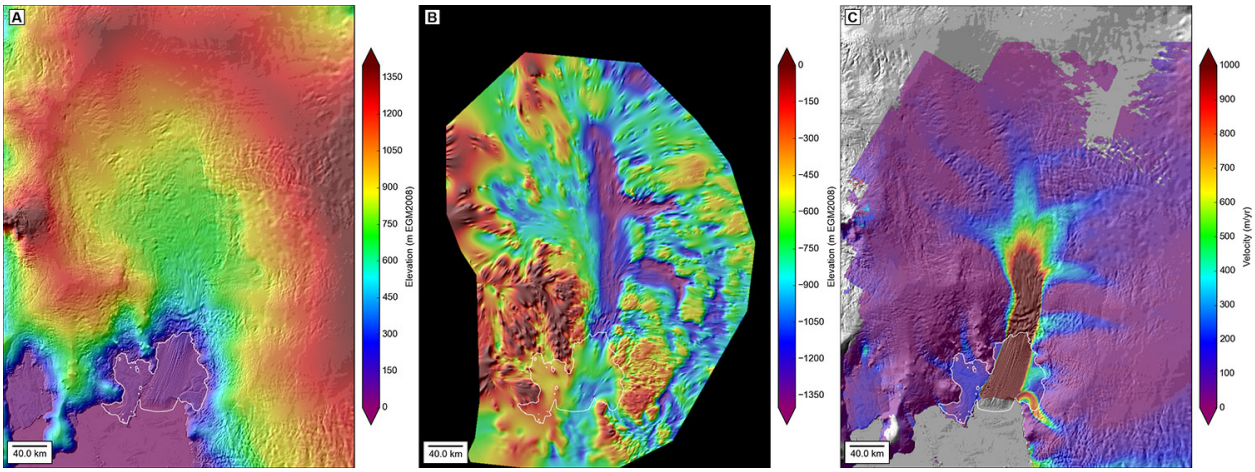

Figure 3-1: Context for Pine Island Glacier catchment: A) Surface elevation, WorldView/GeoEye DEM mosaic embedded in Bedmap2. B) Bed topography from anisotropic interpolation. Note deep channel beneath main trunk and tributaries. C) Median 2006-2016 surface velocity magnitude with color scale saturated at 1 km/yr to show detail over tributaries. White outline shows PIG ice shelf and ~2011 grounding line.

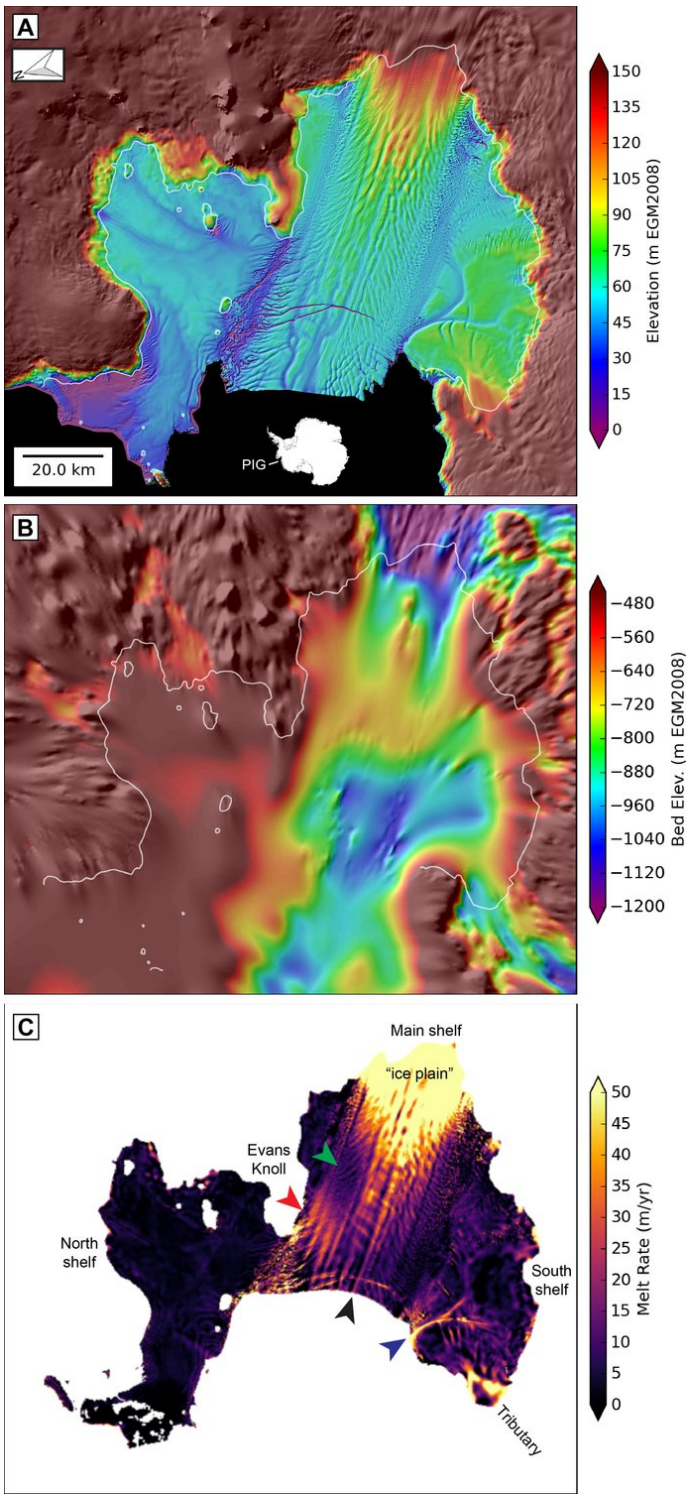

Figure 3-2: Context for Pine Island Glacier ice shelf. A) Surface elevation from October-December 2012 WorldView DEMs, B) Composite bed elevation over PIG cavity. Note transverse seabed ridge separating inner and outer cavities, longitudinal seabed ridge splitting inner cavity and increased seafloor depth near main shelf grounding line. C) Mean 2008-2015

"initial pixel" basal melt rate. Note high values over inner shelf and tributary on south shelf (lower right). Colored arrows show features discussed in text.

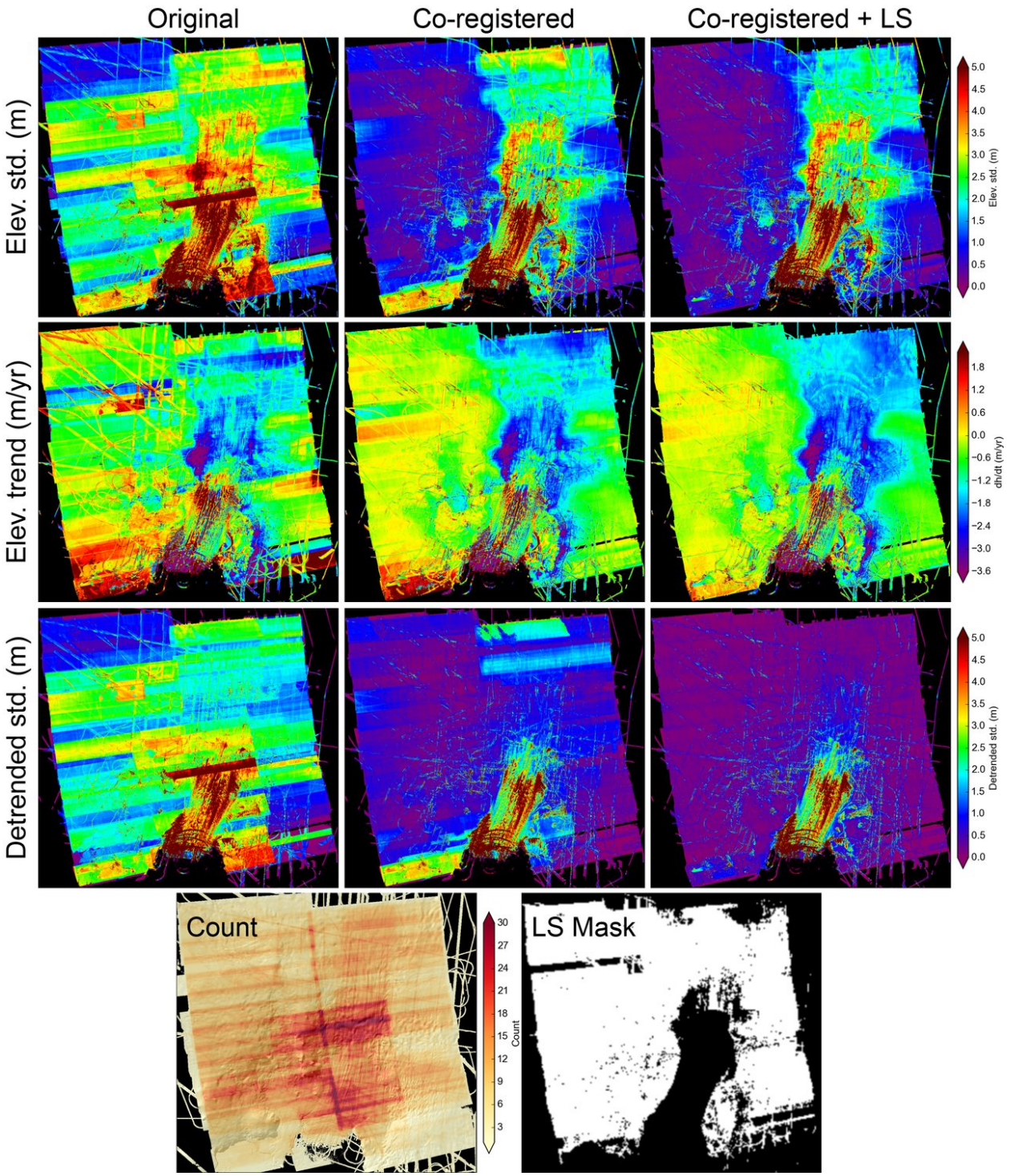

Figure 3-3: Statistics for PIG WorldView/GeoEye DEM correction. Statistics for 2010-2015 WorldView/GeoEye DEMs and available 2009-2015 ATM/LVIS altimetry data over the PIG

study area. Top row shows maps of elevation standard deviation, second row shows linear trend, and third row shows standard deviation of residuals from linear fit at every pixel. Left column ("Original") shows values for original products before correction, center column ("Co-registered") after ICP co-registration to filtered altimetry data, and right column ("Co-registered + LS") after least-squares "tilt" correction. Note overall improvement of final correction (right column). Bottom row shows count and dynamic control surfaces (white) used during least-squares correction, as defined by criteria in Table 3-3.

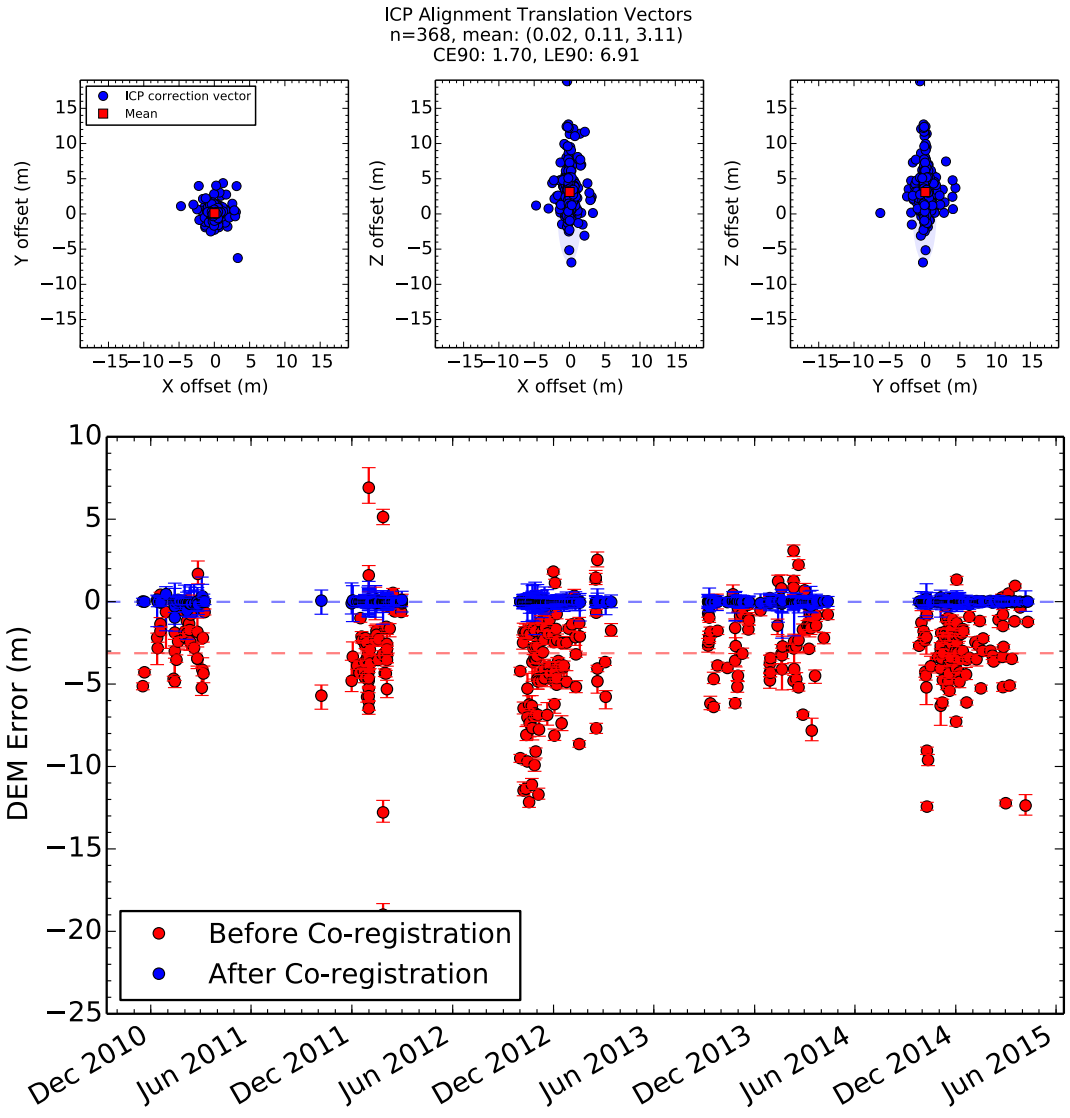

Figure 3-4: PIG WorldView/GeoEye DEM co-registration results. A) ICP translation vector components needed to co-register each DEM with filtered altimetry data. B) Median DEM error

(DEM - GCP) with 16-84% spread, before (red) and after (blue) co-registration (see Shean et al. [2016a] for details). Includes 2010-2015 along-track stereo DEMs and 2011/2012 "cross-track" stereo DEMs, which display larger errors before co-registration. Most DEMs display bias of ~0 m with <0.5–1 m spread after co-registration, as summarized in Table 3-2.

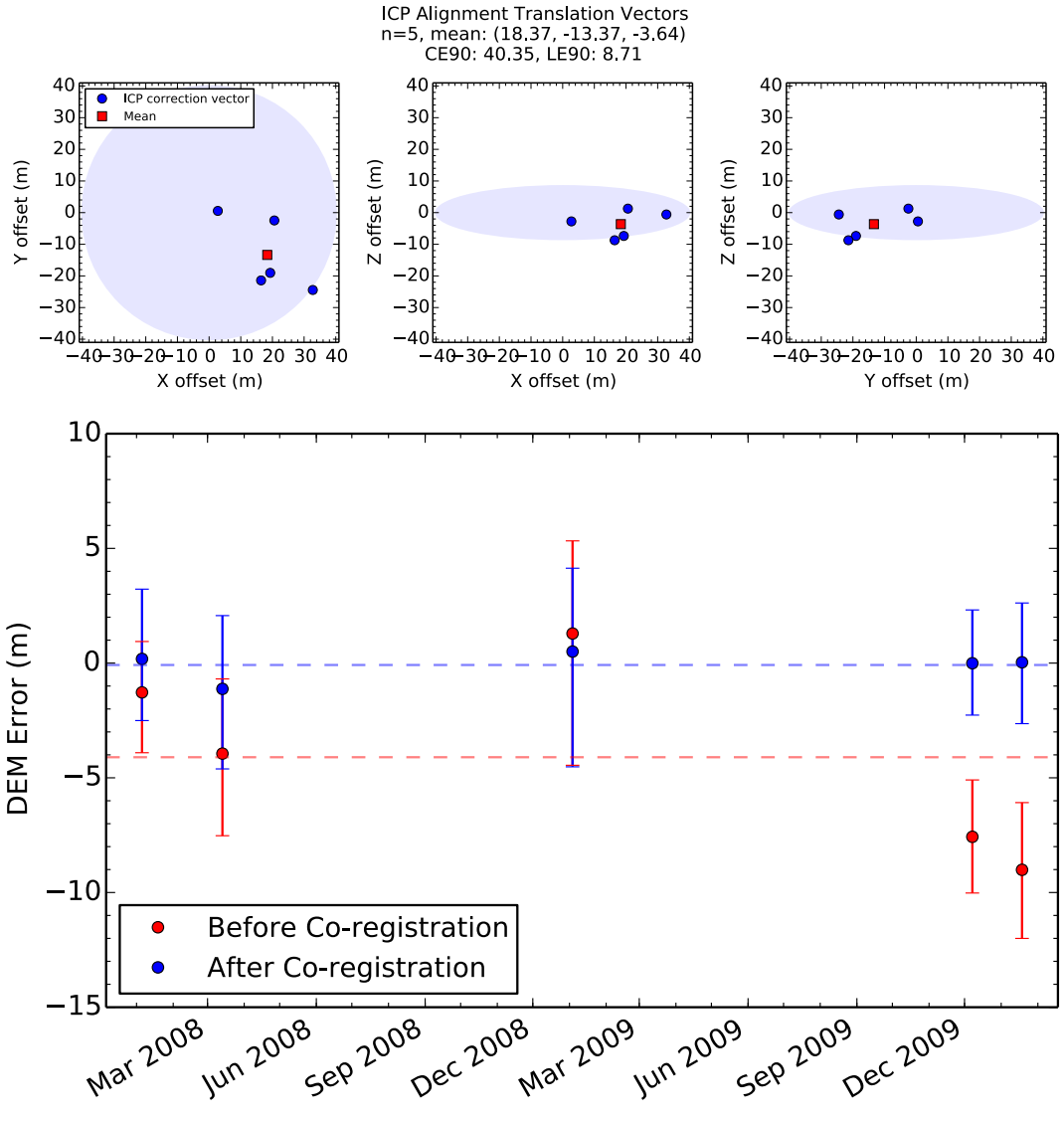

Figure 3-5: PIG SPIRIT DEM co-registration results.

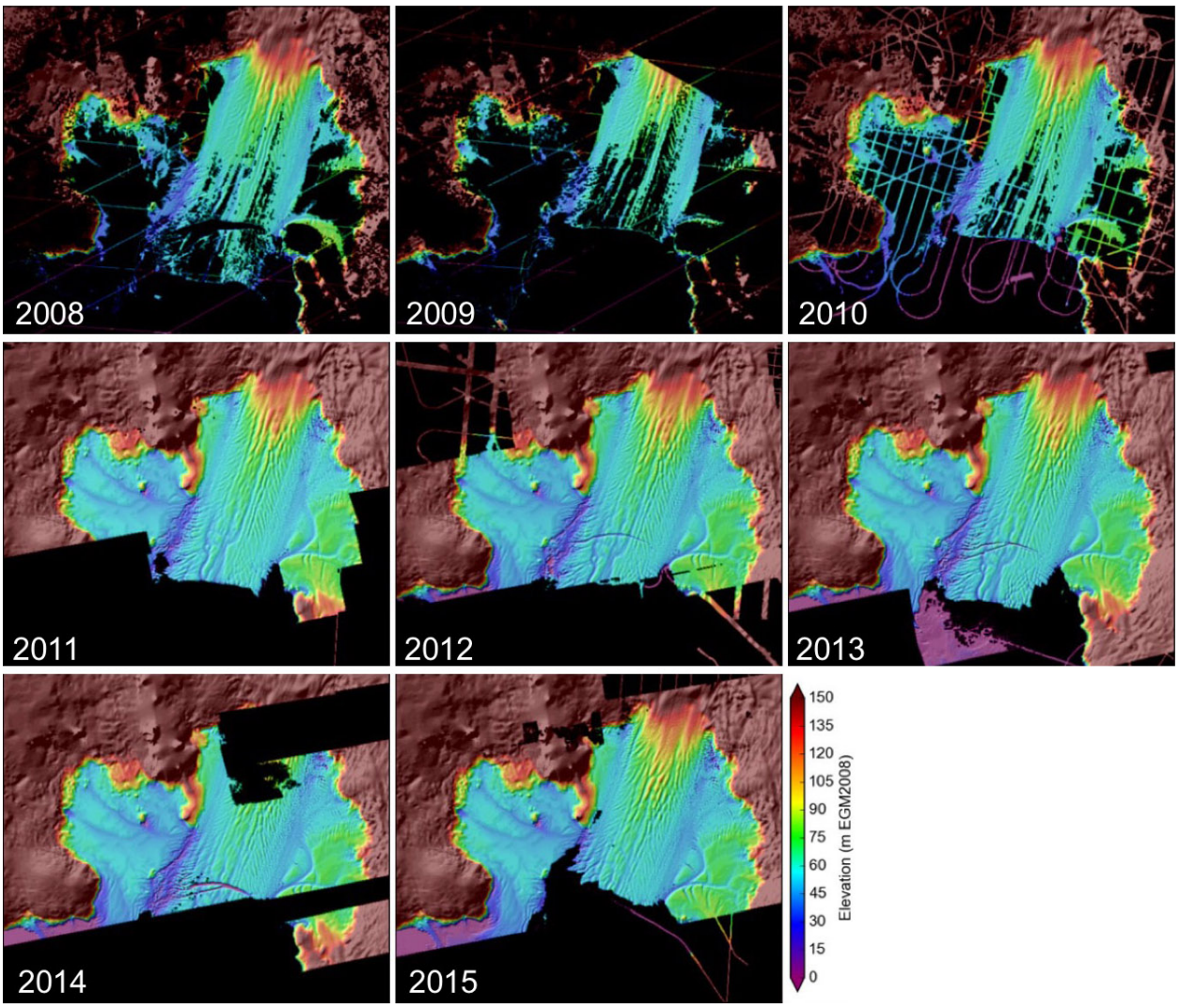

Figure 3-6: Annual DEM mosaics for the PIG shelf using all available elevation data. Primary DEM sources are SPIRIT (top row), and WorldView/GeoEye (middle and bottom rows).

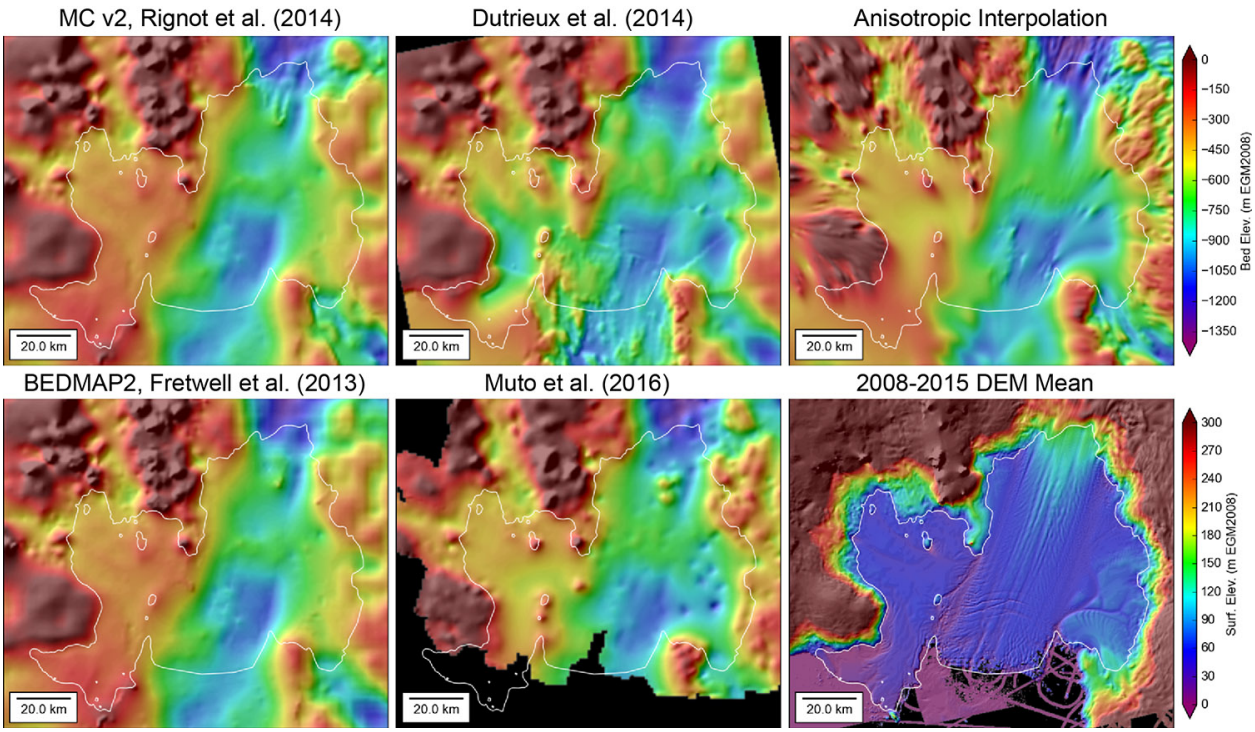

Figure 3-7: Comparison of available bed datasets for PIG. Note significant variability over the inner cavity.

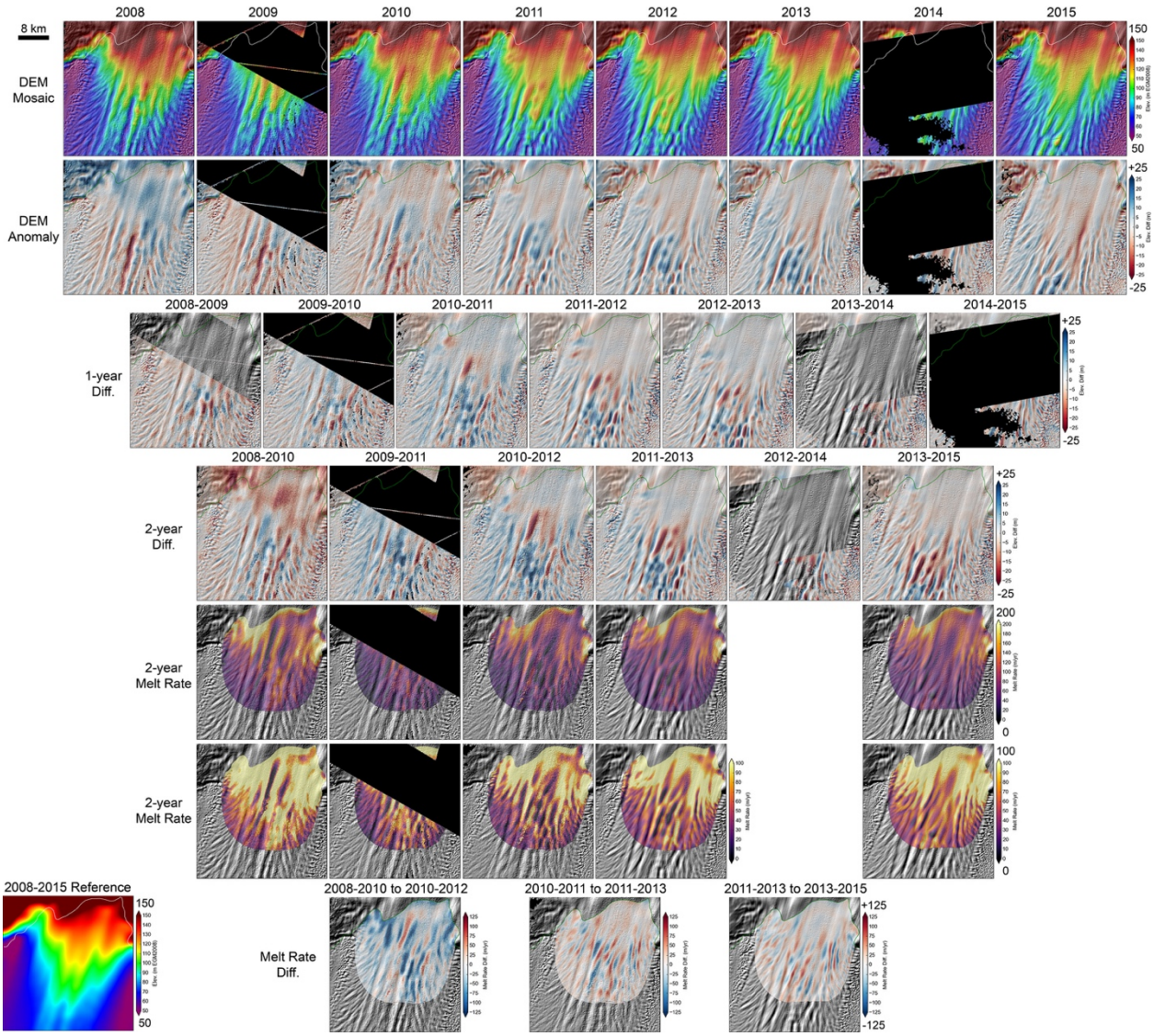

Figure 3-8: DEM mosaics and elevation change products for the inner PIG shelf. Top row shows annual DEM mosaics. Second row shows Eulerian DEM anomaly computed as the difference between DEM mosaic and a smoothed 2008-2015 average elevation (lower left inset). Third row shows 1-year Eulerian DEM difference maps. Fourth row shows 2-year Eulerian DEM difference maps. Fifth and sixth rows show 2-year "initial pixel" Lagrangian Dh/Dt melt rates with different contrast stretch. Final row shows melt rate change for the indicated time periods.

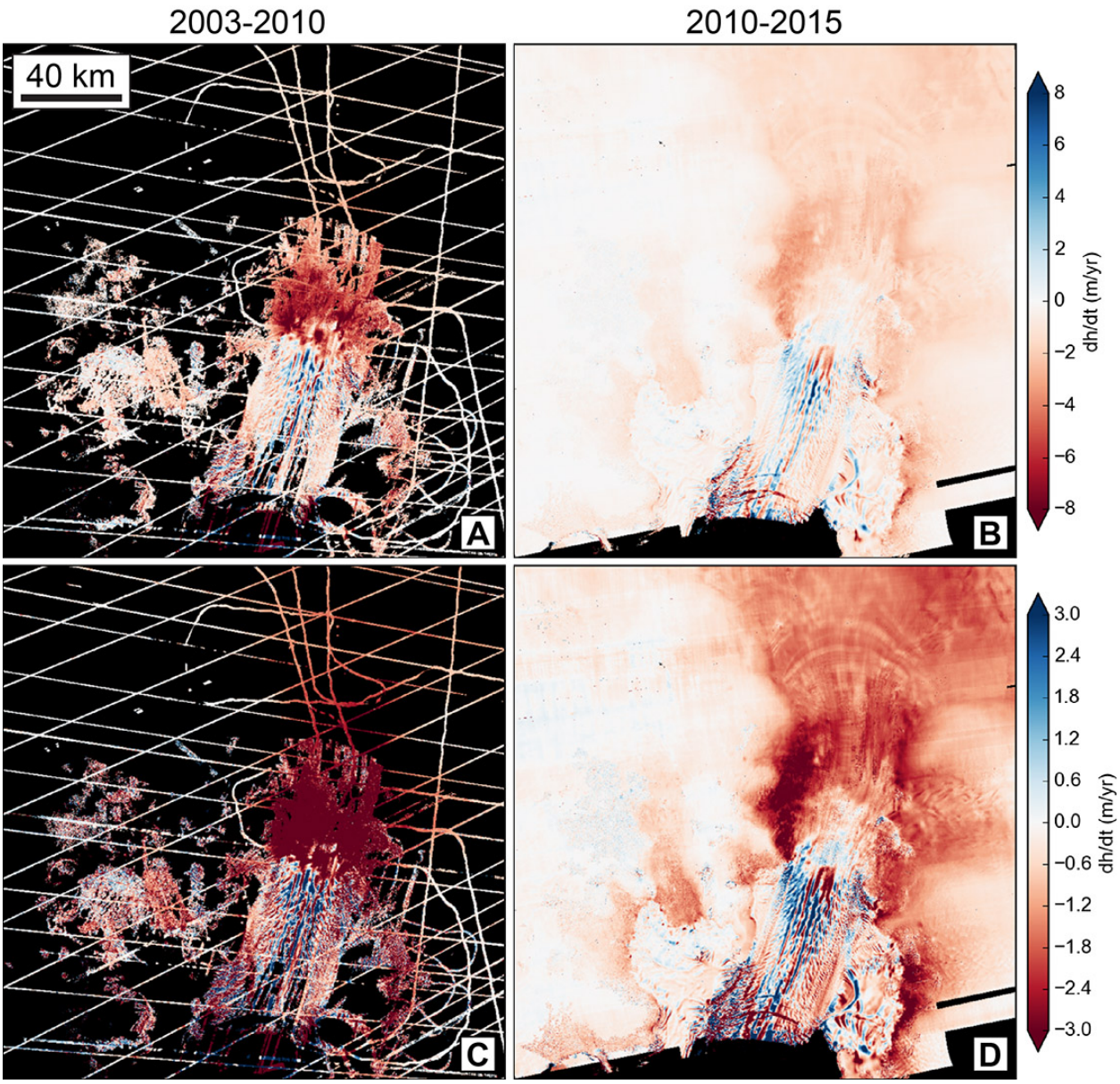

Figure 3-9: Long-term dh/dt trends for the PIG shelf and lower catchment. A) 2003-2010 dh/dt from ICESat, airborne altimetry and SPIRIT DEMs. B) 2010-2015 dh/dt from WorldView/GeoEye DEMs, SPIRIT DEMs and airborne altimetry. C+D) Same data as in A+B, but with enhanced contrast stretch.

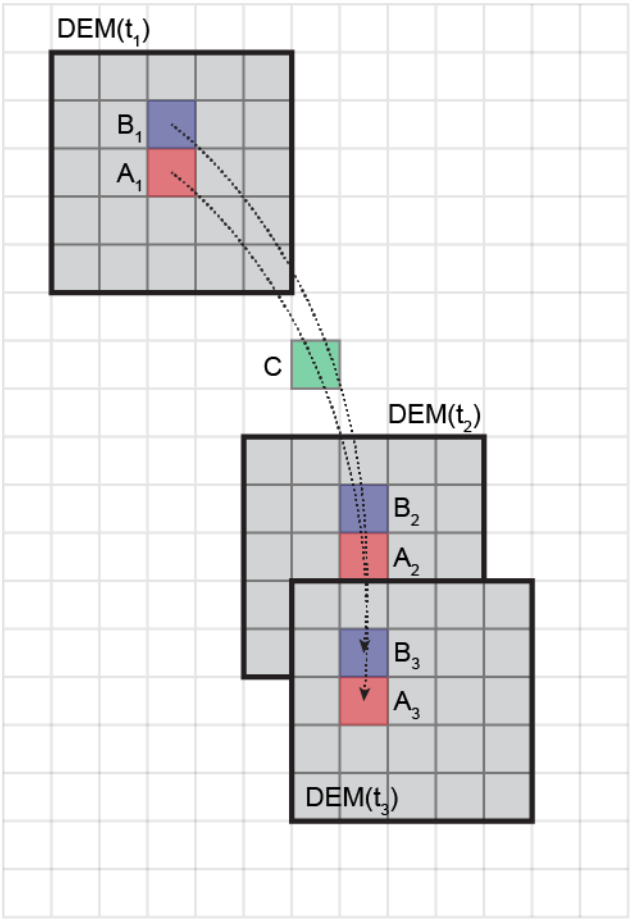

Figure 3-10: Schematic showing framework for Lagrangian Dh/Dt calculation. A global Eulerian grid (light gray) is defined and all DEMs are resampled on this grid. The relative positions of three DEMs acquired at times t_1, t_2, and t_3 are shown, with the same "features" A and B indicated as colored pixels. The position history for A and B is estimated using independent velocities, with paths indicated by dotted lines. Lagrangian Dh/Dt is calculated for $(A_1-A_2)/(t_1-t_2)$, $(A_1-A_3)/(t_1-t_3)$, $(B_1-B_2)/(t_1-t_2)$, $(B_1-B_3)/(t_1-t_3)$, etc. for all pixels and DEM combinations. The "initial pixel" melt rate value is computed from $(B_1-B_2)/(t_1-t_2)$ and $(B_1-B_3)/(t_1-t_3)$ and assigned to B_1. The "along-flow distribution" melt rate is computed from all pixel paths that cross C.

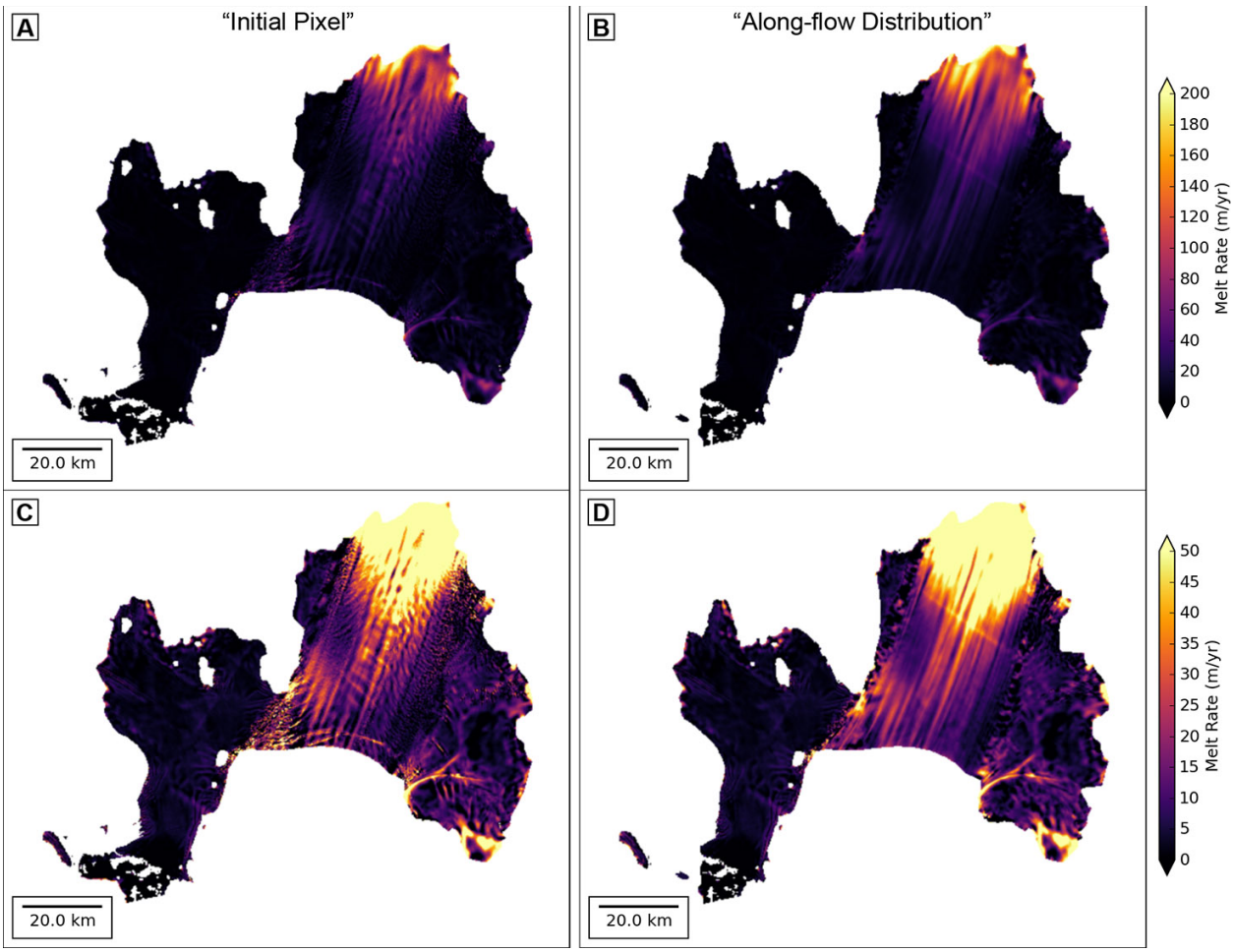

Figure 3-11: Comparison of mean 2008-2015 Dh/Dt melt rate composite products using: A+C) 2-year "initial pixel" and B+D) 2-year "along-flow distribution" methods. Top row shows 0-200 m/yr stretch, bottom row shows 0-50 m/yr stretch.

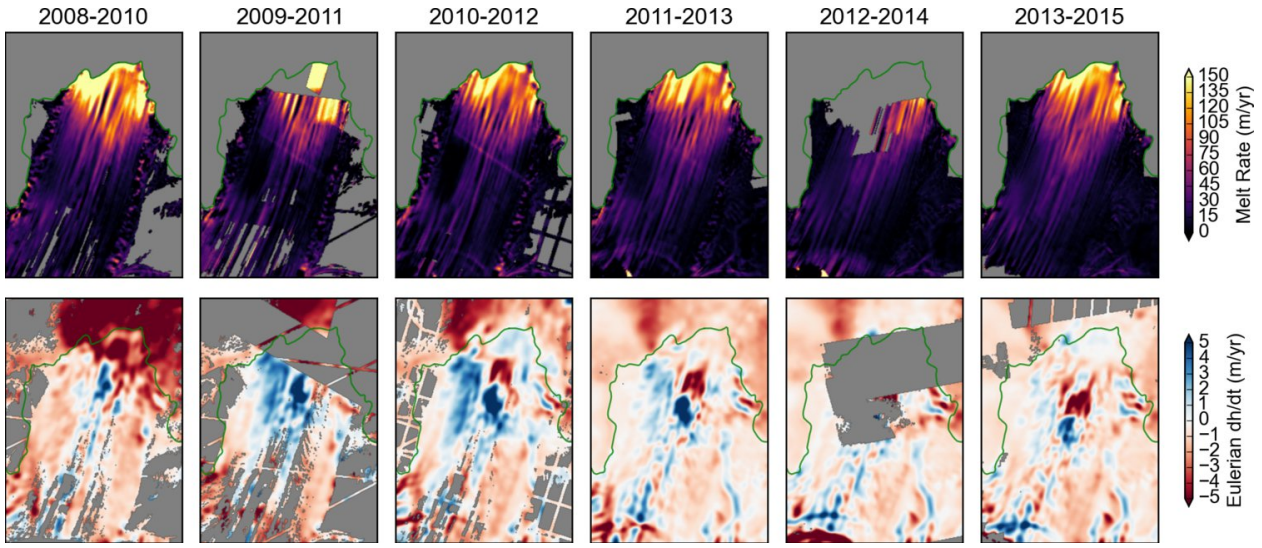

Figure 3-12: Temporal evolution of 2-year Dh/Dt melt rates and Eulerian dh/dt, with "along-flow distribution" 2-year Lagrangian Dh/Dt melt rates (top row) and smoothed (5-km Gaussian kernel, 0.8-km sigma) Eulerian dh/dt (bottom row) for the main PIG shelf. Note melt rate decrease from 2008-2010 to 2010-2012 and melt variability over North (left) side of shelf. Also note thickening of shelf (especially for 2009-2011 and 2010-2012), propagation of ungrounding/grounding signal (red/blue) and significant decrease in thinning upstream of the grounding line.

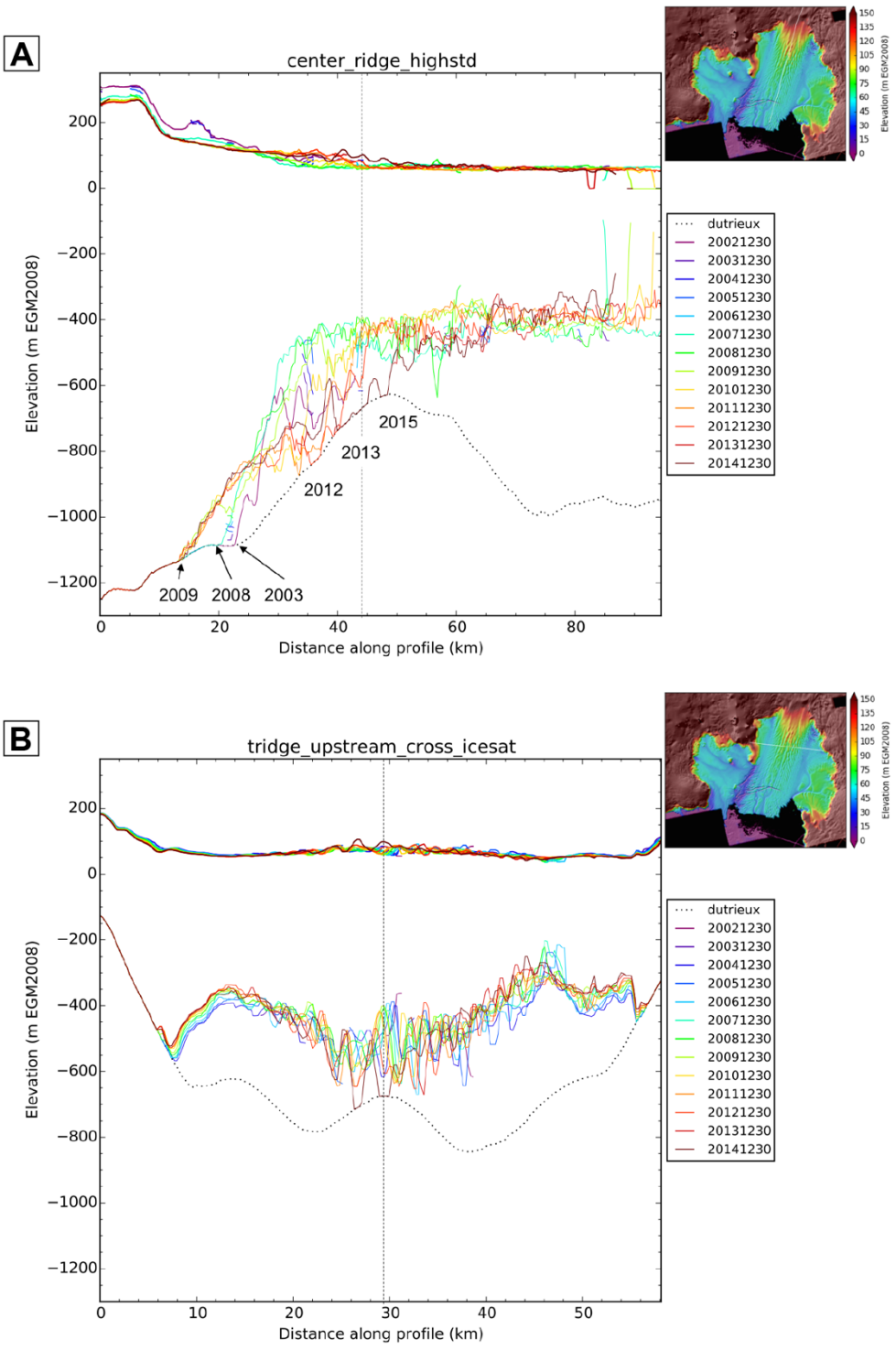

Figure 3-13: Annual surface elevation and freeboard thickness profiles from DEM mosaics. A) Longitudinal profile along PIG shelf centerline. Dotted black line shows Dutrieux et al. [2014b] bed. Thickness is truncated at the bed, providing an estimate for grounding line position. Vertical dashed line shows intersection with profile in B. White line on inset map shows

approximate profile location. Note surface elevation over ice plain from 2003-2005 (purple to blue profiles), in 2008 (cyan), and subsequent years. Also note change in 2011-2015 surface elevation over seabed ridge as deep keels reground. B) Transverse surface elevation profile across inner shelf showing long-term shelf thinning and apparent regrounding of keels.

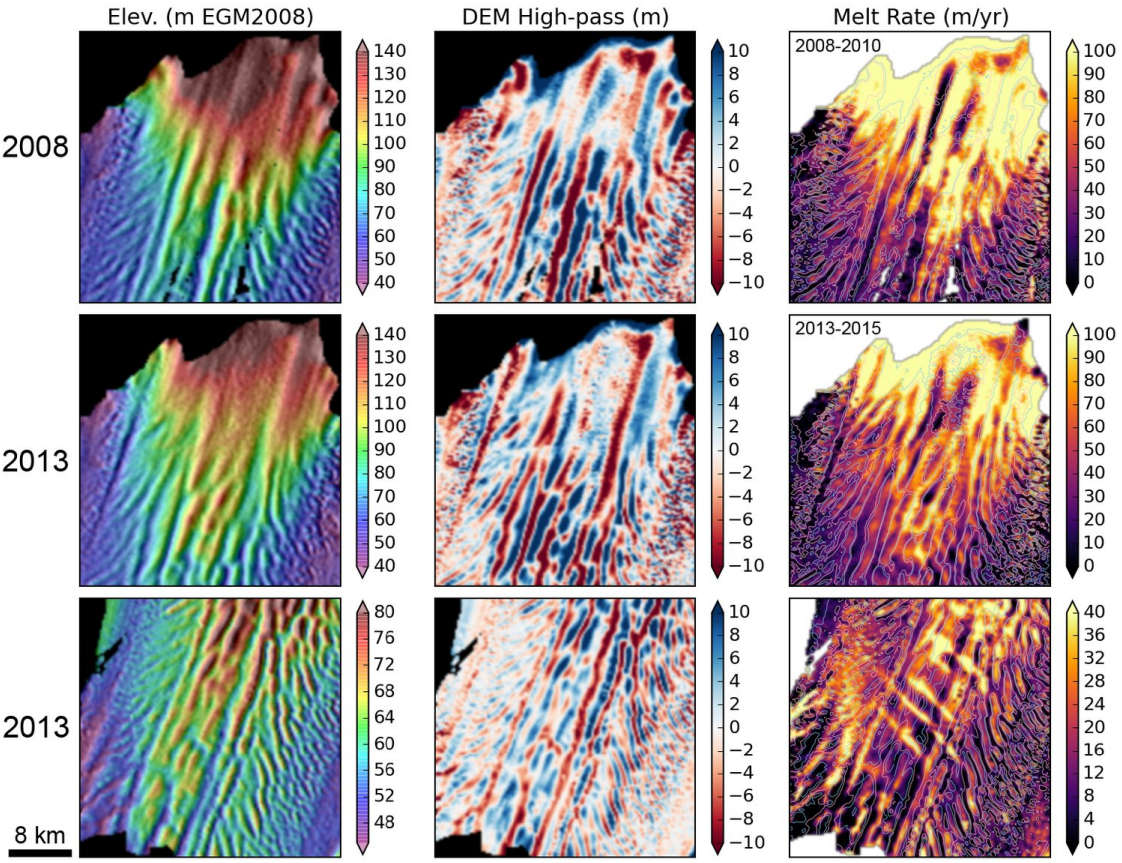

Figure 3-14: Relationship between km-scale ridge/trough features and melt rates over inner (top and middle rows) and outer shelf (bottom row, with enhanced stretch) for specified year. Left column shows 256-m DEM mosaic, center column shows km-scale surface anomalies after high-pass filter (5-km Gaussian kernel, 0.8-km sigma), and right column shows 2-year "initial pixel" Dh/Dt melt rates. Contours show -2 m (light red) and +2 m (light blue) surface elevation anomalies. Note high melt rates over longitudinal surface troughs (basal channels) and low melt rates over surface ridges (basal keels) at distances of ~4-15 km from the grounding line. Farther from the grounding line, higher melt rates are observed over transverse/longitudinal ridges, with reduced melt rates over troughs.

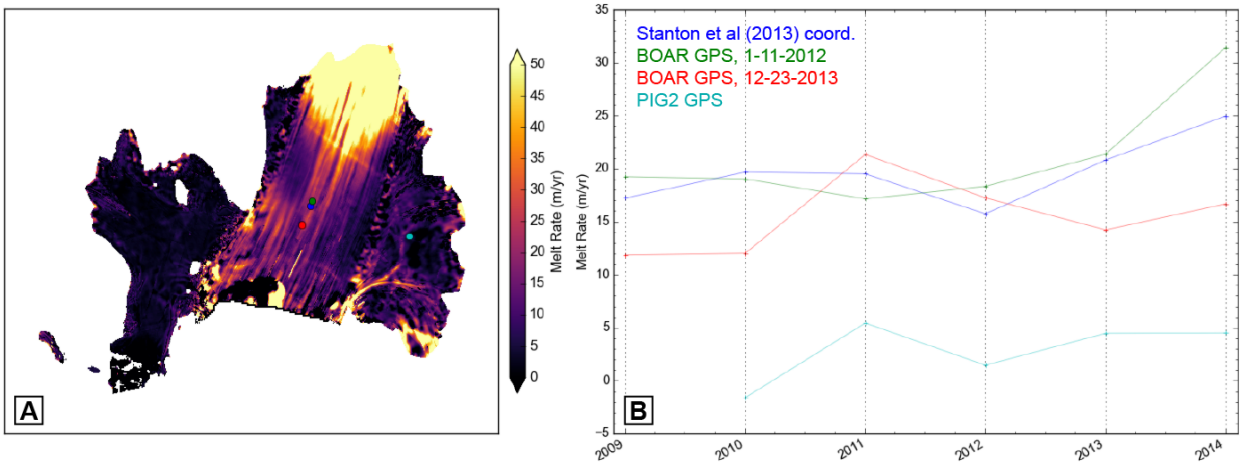

Figure 3-15: Samples of Dh/Dt melt rate for *in situ* measurement sites, including Stanton et al. [2013] borehole site and GPS receiver locations [*Christianson et al.*, 2016; *Shean et al.*, 2016c]. A) Context map showing sample locations. B) Sampled 2-year "along-flow distribution" Dh/Dt melt rate products showing excellent agreement with *in situ* measurements at the Stanton site (~15-25 m/yr) and GPS Dh/Dt melt rate estimates (BOAR ~10-15 m/yr; PIG2 ~4 m/yr).

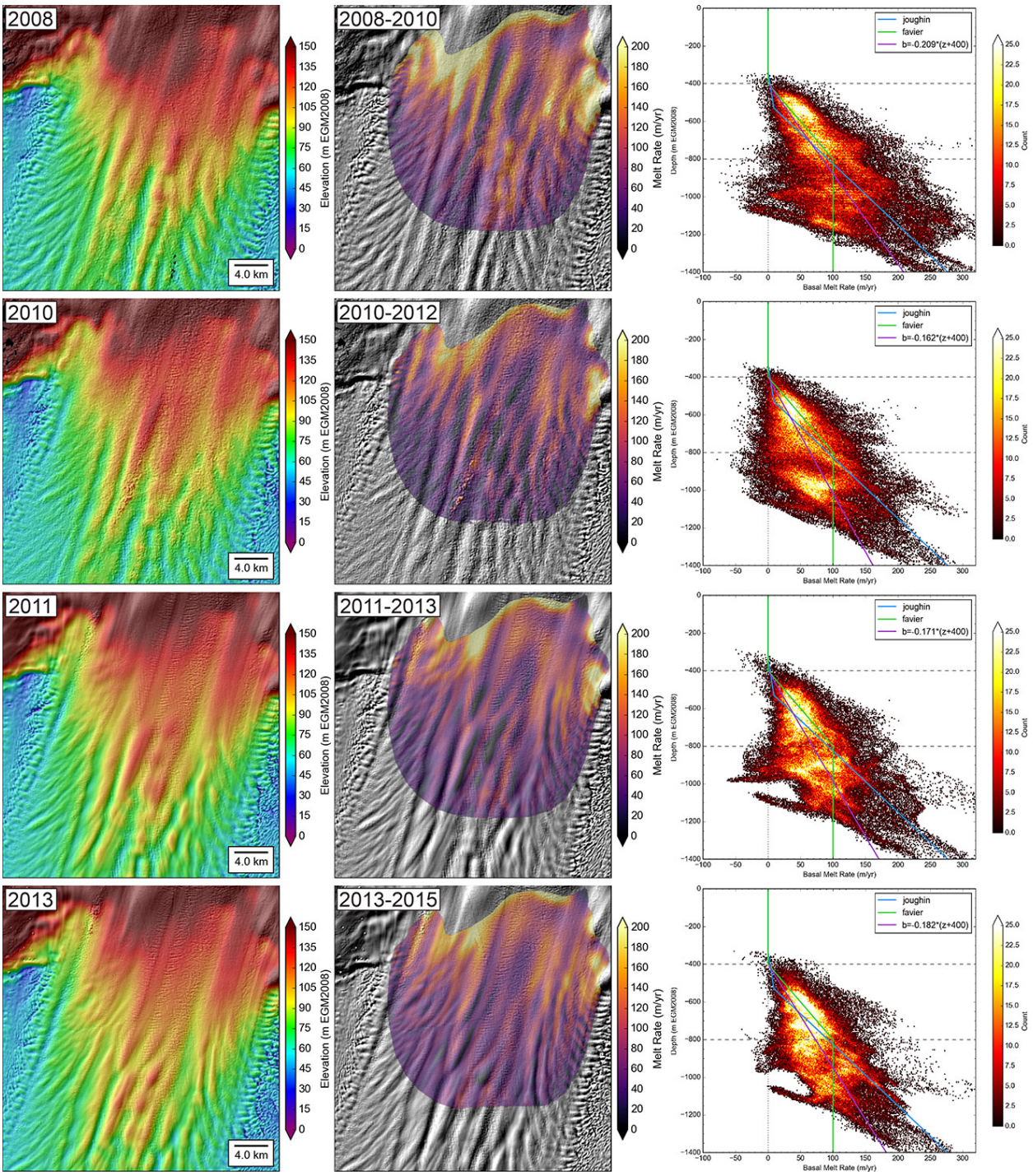

Figure 3-16: Results of high-resolution melt rate vs. depth analysis for inner shelf. Left column shows mosaics of surface elevation for indicated year, center column shows mosaics of corresponding "initial pixel" 2-year melt rate products and right column shows plots of melt rate vs. depth, with linear fit (purple) and piecewise linear models of Joughin et al. [2010b] (blue) and Favier et al. [2014] (green). The color ramp indicates pixel count within each ~5 m depth by

1 m/yr melt rate bin (total sample of ~1.3×10^5 64-m pixels over the ~535 km^2 area). Dashed horizontal lines show -400 and -800 m depth contours.

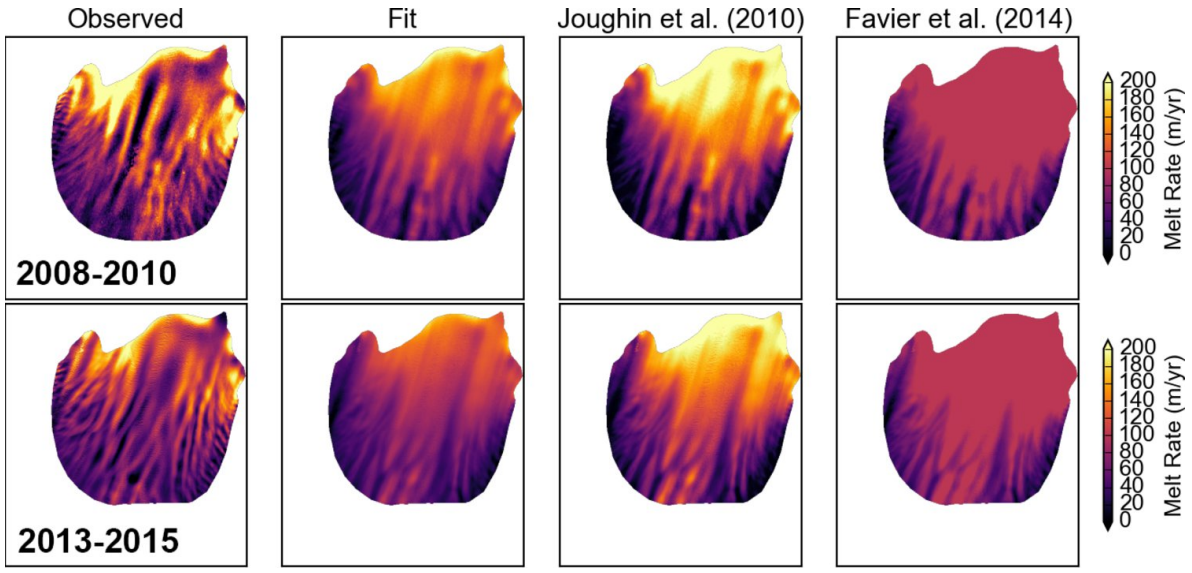

Figure 3-17: Maps of observed and parameterized melt rates calculated using piecewise linear parameterizations shown in Figure 3-16.

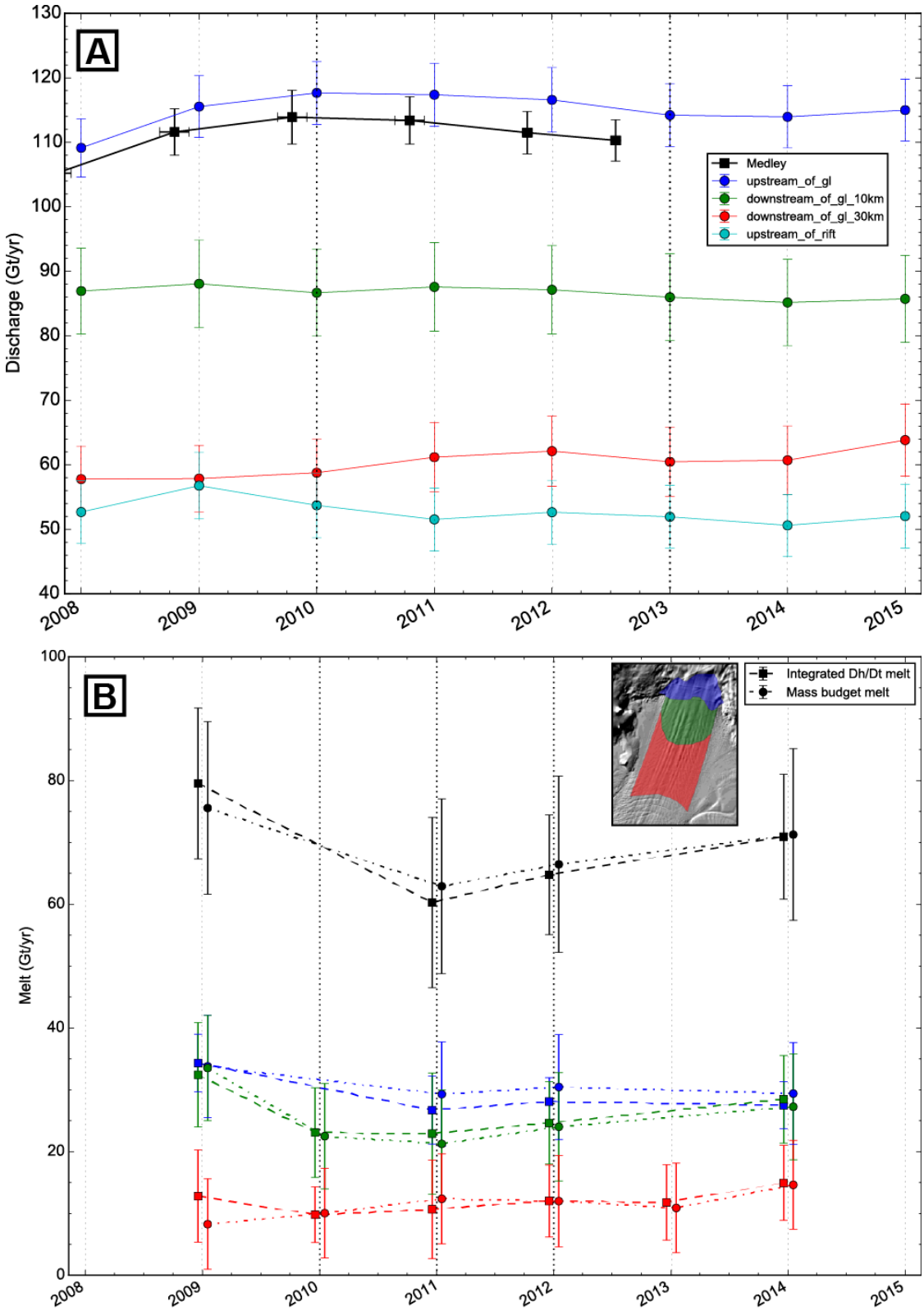

Figure 3-18: Annual mass budget discharge and comparison with Dh/Dt melt rates. A) Annual discharge through four main shelf flux gates: ~1 km upstream of grounding line (blue),

~10 km downstream of GL (green), ~30 km downstream of GL (red) and ~1 km upstream of 2011 rift position (cyan). Main shelf discharge estimates from Medley et al. [2014] (black) are plotted for comparison. B) Two-year interval melt rates calculated from mass budget analysis and integrated "along-flow distribution" Dh/Dt products for each of the colored regions in inset figure. Black points show total melt rate for years with complete coverage over all three areas. Time offset (15 days) between mass budget and integrated Dh/Dt points is for visualization purposes.

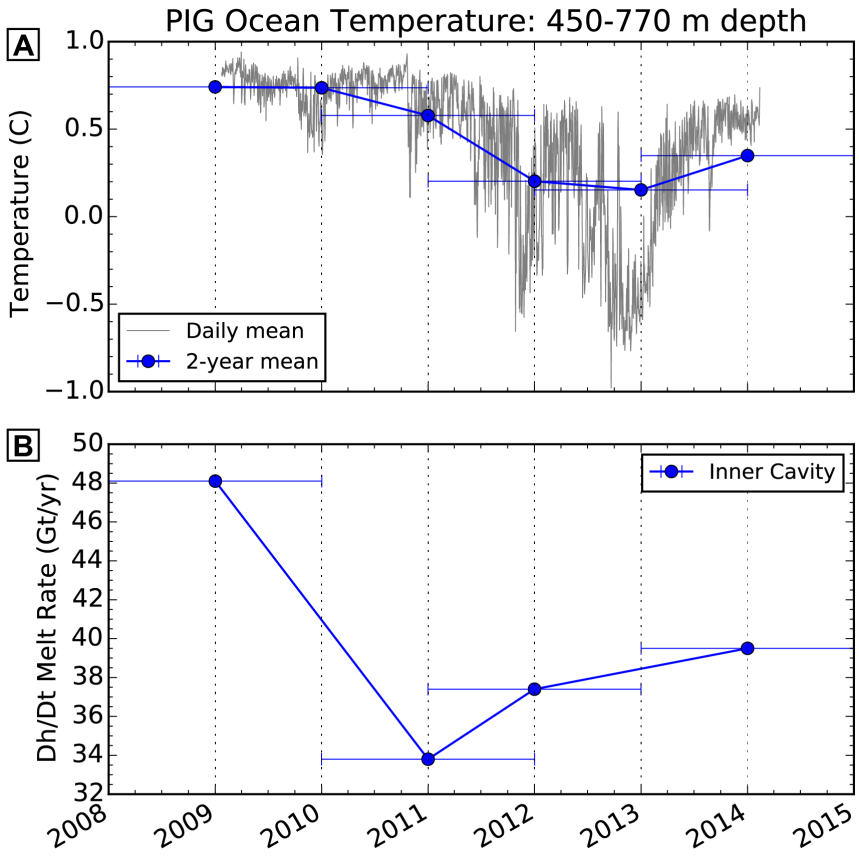

Figure 3-19: Comparison of inner cavity melt rates and ocean mooring temperatures. A) Mean daily water temperature from 450-770 m in Pine Island Bay [*Christianson et al.*, 2016] (gray). Mean of 2-year time periods (blue) is overlaid for comparison with Dh/Dt melt rates. Note that daily values vary between +1 and -1°C, but 2-year mean values only vary from ~0.75°C to ~0.20°C. B) Integrated 2-year "initial pixel" melt rate over 535 km^2 inner shelf. Note apparent decrease in melt rates between 2008-2010 and 2010-2012 periods, which precedes the decrease in ocean temperatures.

Chapter 4. IN SITU GPS RECORDS OF SURFACE MASS BALANCE, STRAIN RATES, AND BASAL MELT RATES FOR PINE ISLAND GLACIER, ANTARCTICA

ABSTRACT

In recent decades, Pine Island Glacier (PIG) has experienced marked retreat, speedup and thinning due to some combination of increased ice-shelf basal melt and internal instability. In an effort to constrain recent dynamics and evaluate potential causes, we analyzed 2008-2010 and 2012-2014 GPS records for the PIG shelf. We computed multi-path antenna heights, horizontal velocities, strain rates, cm-accuracy surface elevation and Lagrangian Dh/Dt elevation change. These data provide validation for complementary high-resolution WorldView stereo DEM records, with sampled DEM error of ~0.7 m.

The GPS antenna height records document a relative surface increase of ~0.7-1.0 m/yr, which is consistent with estimated RACMO2.3 surface mass balance (SMB) of ~0.7-0.9 m.w.e./yr and firn compaction rates from the IMAU-FDM dynamic firn model. An abrupt ~0.2-0.3 m surface elevation decrease due to surface melt and/or greater near-surface firn compaction is observed during a period of warmer atmospheric temperatures from December 2012 to January 2013.

Observed surface Dh/Dt for all PIG shelf sites is highly linear with trends of -1 to -4 m/yr and <0.4 m residuals. Similar Dh/Dt estimates with reduced variability are obtained after removing expected downward GPS pole base velocity from observed GPS antenna Dh/Dt. Estimated Dh/Dt basal melt rates are ~10 to 40 m/yr for the outer PIG shelf and ~4 m/yr for the South shelf. These melt rates are similar to those derived from complementary instrument and high-resolution stereo DEM records. The GPS/DEM records document higher melt rates within and near transverse surface depressions/rifts associated with longitudinal extension.

Basal melt rates for the 2012-2014 period show limited temporal variability, despite significant change in ocean heat content. This suggests that sub-shelf melt rates are less sensitive to ocean heat content than previously reported, at least for these locations and time periods.

4.1 INTRODUCTION

Remote-sensing observations provide measurements of ice-sheet surface elevation and velocity with excellent spatial coverage, but often relatively poor accuracy and limited temporal sampling. By contrast, *in-situ* geodetic GPS observations provide sparse point measurements of position and velocity with near-continuous temporal coverage and cm-scale accuracy. These two methods are highly complementary and can be combined to characterize ice dynamics over a broad range of spatial and temporal scales.

Surface mass balance and associated firn compaction rates are poorly constrained for the Amundsen Sea Embayment (ASE) region of the West Antarctic Ice Sheet. This adds uncertainty to estimates of ice-shelf basal melt rates derived from surface elevation change. With repeat radar observations of internal layers over time, it is possible to unambiguously determine firn-compaction rates [*Jenkins et al.*, 2006; *Medley et al.*, 2015]. These studies show that firn-compaction rates in the ASE region are consistent with those inferred from assumed steady-state density profiles. In the absence of radar observations, reanalysis and firn models can provide estimates of SMB and firn-compaction rates. Here, we constrain these processes for Pine Island Glacier, Antarctica using *in situ* GPS records.

4.1.1 *Pine Island Glacier*

Pine Island Glacier is one of the largest and most dynamic ice streams in West Antarctica, with present-day surface velocities of ~4 km/yr and annual discharge of ~130 Gt/yr [*Medley et al.*, 2014; *Mouginot et al.*, 2014; *Shean et al.*, 2016b] (Figure 4-1). The main ice stream terminates in a large ice shelf with ~25 km width, ~100 km length, and ~1–1.5 km ice thickness across the main grounding line. Basal melting accounts for ~60-80% of mass loss from the ice shelf, with estimated melt rates of ~95-101 Gt/yr [*Depoorter et al.*, 2013; *Rignot et al.*, 2013]. The fast-flowing region of this shelf is characterized by km-scale ridges and troughs that correspond to basal keels and channels, respectively [*Bindschadler et al.*, 2011; *Vaughan et al.*, 2012]. A series of longitudinal ridges and troughs are present along the shelf centerline, with transverse ridges and troughs along the lateral margins (Figure 4-1). Melting occurs preferentially over inner shelf channels and outer shelf keels [*Dutrieux et al.*, 2013].

Hydrographic observations beyond the PIG calving front in Pine Island Bay suggest a ~50% decrease in sub-shelf melt occurred between 2010 and 2012 [*Dutrieux et al.*, 2014b]. Long-term 2009-2015 mooring records beyond the south calving front show a significant decrease in ocean temperature over ~450-770 m depths from late 2011 to early 2012, and then again from mid-2012 to early 2013 [*Christianson et al.*, 2016]. These observations suggest ocean heat content beneath the PIG shelf varies considerably over ~annual timescales.

4.1.2 *PIG GPS sites*

Two GPS stations continuously collected data from January 2008 to January 2010 – one on the South PIG shelf (PIG2) and one over grounded ice south of the fast-flowing ice stream (PIG1) (Figure 4-1). A ~2x2 km array (Figure 4-2) of five additional stations (SOW1-4, BOAR) was installed from January 2012 to late December 2013 near the centerline of the outer main shelf (Figure 4-1), ~45 km downstream of the grounding line (~25 km from the 2012 ice front).

The GPS stations included dual-frequency Trimble NetR9 GPS receivers and Trimble Zephyr Geodetic 2 antennas mounted on 12-foot (3.66 m) poles driven into the snow by hand. Initial antenna heights were not recorded, but pole bases were likely set ~0.5-1.0 m beneath the surface [*Truffer*, personal communication, 2016].

High-resolution image and DEM data (Figure 4-2) over the 2012-2014 sites show that SOW1, BOAR, and SOW3 were oriented approximately along a flowline within a longitudinal surface trough (Figure 4-3) that overlies a longitudinal basal channel [*Stanton et al.*, 2013]. Transverse ice-penetrating radar profiles across this channel provide ice thickness estimates of ~460 m near the apex and ~540 m over adjacent keels [*Stanton et al.*, 2013].

Phase-sensitive radio-echo sounder (pRES) measurements and a borehole-mounted, upward-facing bottom altimeter provided estimated basal melt rate of ~14-25 m/yr within the channel [*Stanton et al.*, 2013].

The DEM data show several transverse depressions near the 2012-2014 GPS array (Figure 4-2). The largest of these depressions is located immediately downstream of SOW3 and SOW4, where local surface slopes are ~0.6-0.9°. A smaller depression is located immediately upstream of BOAR, where local surface slopes are negligible (~0.1°). Finally, a notable linear depression located approximately 1 km upstream of SOW1 (arrow in Figure 4-2) opened as a rift in ~2014 and was the site of a large iceberg calving event around July 2015 [*Jeong et al.*, 2016]. While the

apparently fortuitous placement of the 2012-2014 GPS array near these features complicates interpretation of GPS position and velocity records, it provides new constraints on the spatiotemporal evolution of longitudinal strain and rift formation on the PIG shelf.

4.2 DATA AND METHODS

4.2.1 *GPS position/velocity processing*

As described in Christianson et al. [2016], GPS data were processed using differential-carrier-phase positioning relative to a bedrock GPS site approximately 60 km away (Backer Island, BACK) with epoch-by-epoch zenith tropospheric delay estimation. Daily-averaged positions of the Backer Island base station were calculated using GAMIT and stabilized relative to a fixed circum-Antarctic reference frame using a Kalman filter (GLOBK). Geodetic GPS positions relative to WGS84 ellipsoid were calculated every 30 seconds, and we analyze a subset of these positions sampled at 10-minute intervals. All position data were converted to orthometric height above the EGM2008 geoid [*Pavlis et al.*, 2012] and a local Cartesian horizontal coordinate system to minimize distortion introduced from standard polar stereographic projections (~1% for EPSG:3031 at ~75°S) and. GPS positions with uncertainty >8 cm were removed. The BOAR record was curtailed on April 29, 2013 (1.31 years) due to an abrupt 1.87 m elevation decrease and horizontal offset, apparently related to a fallen antenna.

Horizontal velocities for each GPS station were computed from daily mean positions. Relative distances between stations were used to calculate strain, with linear fits to estimate strain rates.

4.2.2 *GPS elevation correction*

Vertical tidal displacement was estimated for all GPS positions using the CATS2008A model [*Padman et al.*, 2002]. Mean sea-level pressure was extracted from the 0.75°-grid-cell ERA-Interim reanalysis products with 6-hour interval [*Dee et al.*, 2011]. Estimated vertical displacement due to the inverse barometer effect (IBE) [e.g., *Padman et al.*, 2003] was calculated by removing the 2002-2016 median (985.21 hPa) from sea level pressure and scaling residuals by ~1 cm/hPa. Tidal amplitudes for these locations range from approximately -0.9 to +1.3 m and IBE amplitudes range from -0.3 to +0.3 m (Figure 4-4). These signals were removed from the GPS antenna phase center elevations, and residual high-frequency noise was removed with a 1.5-day

low-pass filter, providing smoothed time series for further analysis (Figure 4-4). The constant 3.66 m pole length and 5.32 cm antenna phase center offset was removed from filtered GPS antenna phase center elevation (h_a) records to estimate corresponding pole base elevation (h_{pb}) relative to the EGM2008 geoid (Figure 4-5).

4.2.3 *GPS relative antenna height*

We computed mean daily antenna height (z_a) above the surface from L1C multi-path surface reflections using the methodology outlined in Larson et al. [2015] (Figure 4-5). Elevation angles were limited to ~5-25°, which should sample surfaces within ~10-100 m of the antenna. Local surface slopes at each site are negligible, eliminating the need for azimuthal correction. Reflector height precision is ~0.01 m [*Larson et al.*, 2015].

Initial surface reflector height was used to estimate initial pole base depth at each site. Reflector heights were removed from filtered GPS antenna phase center elevations to obtain daily records of surface elevation (i.e., firn-air interface) for all sites. These elevations are directly comparable with satellite/airborne altimetry data and stereo DEM products.

4.2.4 *Surface mass balance (SMB)*

We analyzed records of 1979-2015 monthly and 2010-2013 daily surface mass balance for three 27-km grid cells over the PIG shelf from the Regional Atmospheric Climate Model (RACMO) v2.3 [*Van Meijgaard et al.*, 2008; *Ettema et al.*, 2009; *Lenaerts et al.*, 2012; *Van Wessem et al.*, 2014]. The grid cell closest to the 2012-2014 GPS array (-75.066°N, -100.798°E, Figure 4-1) displays average 1979-2015 SMB ($\bar{a}$) of ~0.913 m.w.e./yr. We note that values for adjacent 27-km grid points are 0.744 m.w.e./yr near the grounding line of the main shelf (-75.15°N, -99.88°E) and 0.841 m.w.e./yr over the south shelf (-75.30°N, -101.14°E). These values are consistent with estimates of ~0.5-1.0 m.w.e./yr from observed compaction rates in CReSIS Snow Radar data upstream of the PIG grounding line [*Medley et al.*, 2014].

We also analyzed meteorological data from the Evans Knoll automated weather station (AWS), located at an elevation of 188 m (height above WGS84 ellipsoid) on a bedrock outcrop approximately 40 km north of the 2012-2014 GPS array (Figure 4-1). To provide historical context, we extracted 2-m and skin temperature from the 1979-2015, 0.75°-grid-cell ERA-Interim reanalysis products with 6-hour interval [*Dee et al.*, 2011].

4.2.5 *Firn densification model*

Model output from RACMO2.3 SMB data (-75.066°N, -100.798°E) were used to force the semi-empirical 1-D IMAU-FDM firn model [*Ligtenberg et al.*, 2011; *van Wessem et al.*, 2016] with 2-day time steps. Velocities across the firn-ice transition (defined as the layer with 910 kg/m^3 density) were assumed to be in equilibrium with average 1979-2015 SMB. Vertical velocity components for surface accumulation, surface sublimation, surface snow drift erosion, surface melt, dry firn compaction (v_{fc}), and a vertical mass difference buoyancy correction (assuming ocean density of 1027 kg/m^3) were computed for the 2008-2010 and 2012-2014 periods. These estimates were combined to provide time series of expected surface elevations (IMAU-FDM "zs") and pole base elevations for each GPS station.

Similar IMAU-FDM output shows good agreement with CReSIS Snow Radar data for sites ~300-400 km from the PIG shelf [*Medley et al.*, 2014, 2015; *Ligtenberg et al.*, 2015]. These comparisons offer limited validation, although we note that increased SMB variability is expected near coastal topography.

4.2.6 *High-resolution stereo DEMs*

The GPS data provide validation for high-resolution WorldView/GeoEye commercial stereo DEMs over the PIG shelf [*Shean et al.*, 2016a, 2016b], while the DEMs provide spatial context for the continuous GPS time series. A total of 7 WorldView DEMs with 32-m posting intersected the GPS positions between 2012-2014. We sampled DEM surface elevation at GPS positions with matching timestamps and compared with surface elevation (as described in Section 4.2.3).

High-resolution Lagrangian Dh/Dt elevation-change maps were computed for valid 32-m DEM combinations using the "initial pixel" methodology outlined in [*Shean et al.*, 2016b]. Products with 0.5-2.5-year time interval were aggregated for initial DEM timestamps of February 2, 2012 and October 23, 2012, and median Dh/Dt was computed for all initial DEM pixel locations. Unfortunately, the 2008-2010 GPS positions do not intersect any valid pixels in the available SPIRIT DEMs or altimetry data from that time period.

4.2.7 *Basal melt rate*

Mass conservation for a column of ice with thickness H (after firn-air correction) relates Lagrangian ice thickness change (DH/Dt) with dynamic thinning/thickening due to local velocity divergence, surface mass balance $\dot{a}$ (meters ice equivalent), and basal mass balance $\dot{b}$ (ice equivalent, defined as positive for melt):

$$\frac{DH}{Dt} = -H(\nabla \cdot \mathbf{u}) + \dot{a} - \dot{b} \tag{4.1}$$

Assuming hydrostatic equilibrium and constant density for sea water (ρ_w=1026 kg/m^3) and ice (ρ_i= 917 kg/m^3), we compute ice-equivalent thickness from freeboard surface elevation $h_f = h - d$ (after removing firn-air content d with negligible density):

$$H \approx h_f \left(\frac{\rho_w}{\rho_w - \rho_i}\right) \tag{4.2}$$

and substitute for ice thickness H:

$$\frac{Dh_f}{Dt} = -h_f(\nabla \cdot \mathbf{u}) + \left(\dot{a} - \dot{b}\right)\left(\frac{\rho_w - \rho_i}{\rho_w}\right) \tag{4.3}$$

Rearranging, we obtain a relationship for basal melt rate:

$$\dot{b} = -\left(\frac{Dh_f}{Dt} + h_f(\nabla \cdot \mathbf{u})\right)\left(\frac{\rho_w}{\rho_w - \rho_i}\right) + \dot{a} \tag{4.4}$$

The effects of surface processes (e.g., accumulation, melting) are significantly dampened below the upper ~1-2 meters of the firn column. The elevation change of the pole base (Dh_{pb}/Dt) is more sensitive to long-term average compaction rates within the underlying firn. If the compaction rates from the firn-ice transition to the pole base are known, then the expected downward velocity of the pole can be removed from observed Dh_{pb}/Dt. Assuming that the velocity across the firn-ice transition is equal to the long-term (~1979-2015) average SMB ($\bar{a}$), and the local downward velocity due to firn compaction v_{fc} varies as a function of pole base depth z_{pb} within the firn column, we can estimate:

$$\frac{Dh_{pb}}{Dt} = -H(\nabla \cdot \mathbf{u}) + \left(\bar{a} - \dot{b}\right)\left(\frac{\rho_w - \rho_i}{\rho_w}\right) + v_{fc} \tag{4.5}$$

We then solve for basal melt rate using the pole base elevation change:

$$\dot{b} = -\left(\frac{Dh_{pb}}{Dt} + H(\nabla \cdot \mathbf{u}) - v_{fc}\right)\left(\frac{\rho_w}{\rho_w - \rho_i}\right) + \bar{a} \tag{4.6}$$

If pole base velocities estimated from SMB and firn-model compaction rates are correct, then melt rates computed from Dh/Dt and Dh_{pb}/Dt should be similar.

We neglect the slight reduction in total ice thickness at the pole base vs. surface, as $z_{pb} \ll H$. For the local flux divergence term, we use H from radar measurements [*Stanton et al.*, 2013] or local freeboard thickness. We note that over floating ice, inferred basal melt rates are ~9 times more sensitive to pole base elevation change and local v_{fc} than long-term SMB $\bar{a}$. Uncertainty is estimated as ~0.15 m/yr for downward firn-compaction velocity, ~0.1 m/yr for combined local flux divergence and downslope flow, ~5 kg/m^3 for ice and ~5 kg/m^3 for ocean density.

4.3 RESULTS

4.3.1 *Velocity*

Figure 4-6 shows that the surface velocity at PIG2 increases from ~355 m/yr to ~380 m/yr during 2008-2010, with increased speedup in late 2008. Velocities at PIG1 show a steady velocity increase from ~420 m/yr to ~460 m/yr as the station moves toward the fast-flowing PIG trunk (Figure 1).

The 2012-2014 GPS velocities at SOW1, SOW2, BOAR, SOW3, and SOW4 range from ~3830-4040 m/yr [*Christianson et al.*, 2016] (Figure 4-6). Velocities at SOW1, BOAR, and SOW3 are similar, while SOW4 (closer to shelf centerline) is consistently moving ~20 m/yr faster than these three sites, and SOW2 is consistently moving ~15 m/yr slower. Thus, there appears to be ~30-40 m/yr dextral (right-handed) shear across the ~2.4 km distance between SOW4 and SOW2. This subtle transverse velocity gradient is also apparent in velocity mosaics [e.g., *Christianson et al.*, 2016].

The 2012-2014 velocity records show ~2-3% temporal variability, as described in detail by [*Christianson et al.*, 2016]. In general, all five stations display similar relative velocity evolution. Several abrupt >10-20 cm/day velocity changes are observed (Figure 4-6), with an increase around June 15, 2012, decrease around August 19, 2012, decrease around April 11, 2013, increase around November 20, 2013 and increase around December 17, 2013.

4.3.2 *Strain rates*

For this analysis, we assume that SOW1, BOAR, and SOW3 GPS stations are oriented approximately along a flowline, and observed displacements represent longitudinal strain. Figure 4-7 shows that observed cumulative displacement between SOW1 and SOW3 (initial distance 2073.0 m) is ~6.7 m (~3.4 m/yr), with extensional strain rates of ~0.0017 yr^{-1}. Observed strain rates between SOW1 and BOAR (~2.1 m/yr over 1045.2 m, 0.0020 yr^{-1}) are greater than those between BOAR and SOW3 (~1.5 m/yr over 1029.1 m, 0.0014 yr^{-1}). Transverse strain rates are relatively low between BOAR and SOW2 are compressional (-0.0004 yr^{-1}, while those between BOAR and SOW4 are extensional at 0.0007 yr^{-1}.

For measured ice thickness of ~460 m [*Stanton et al.*, 2013] or from estimated local freeboard thickness of ~430-500 m, these longitudinal strain rates correspond to shelf thinning rates of ~0.5-0.9 m/yr and limited expected surface Dh/Dt (<0.07-0.13 m/yr).

Subtle changes in strain rates between SOW1 and SOW3 are observed from 2012-2014. These changes appear to occur around the same time as abrupt changes in the GPS velocity records (Figure 4-7). In general, increased (decreased) extensional strain rates are observed between SOW1 and SOW3 following an increase (decrease) in absolute GPS array velocity.

4.3.3 *Downslope flow*

In addition to elevation change associated with strain rates and corresponding local flux divergence, some component of the observed Dh/Dt is related to deformation due to local driving stress gradients. Over grounded ice, the vertical component of this motion (V_0) can be estimated with observed horizontal GPS displacement and local surface gradients from an independent DEM [e.g., *Larson et al.*, 2015]. For a floating ice shelf like PIG, however, nearly all of the observed horizontal displacement is due to advection, and a different approach must be used.

To estimate an upper bound for this deformation, we again consider relative horizontal displacements within the 2012-2014 GPS array. Local surface slopes near SOW1, SOW2 and BOAR are negligible (<0.2°), so we assume $V_0 = 0$ for these stations. If all of the observed ~3.4 m/yr relative displacement between SOW1 and SOW3 is due to flow down ~0.6° surface slopes at SOW3, the associated V_0 would only be ~0.03 m/yr, which is negligible compared to the observed 5.2 m/yr Dh/Dt. Considering that much of the observed relative displacement appears

to be related to longitudinal extension (Section 4.3.2), we assume that vertical Dh/Dt associated with flow down local slopes is negligible for these locations.

4.3.4 *GPS antenna and surface Dh/Dt*

Figure 4-8 and Figure 4-9 show relative GPS antenna elevation records over the PIG shelf. These results show negative, highly linear (R^2 0.98-1.00) Dh/Dt for their respective time periods (Table 4-1), with rates -1.6 to -2.1 m/yr at SOW1, SOW2, and BOAR, and higher rates of -5.2 m/yr and -3.8 m/yr at SOW3 and SOW4, respectively. The record from PIG1 over grounded ice displays Dh/Dt of -7.6 m/yr with apparent concave-downward curvature.

The PIG2 site shows limited surface elevation change from 2008-2010 (Figure 4-10). By contrast, surface elevations decrease at all 2012-2014 sites, with rates of -0.9 to -1.3 m/yr for SOW1, SOW2 and BOAR, and rates of -3.0 to -4.1 m/yr at SOW4 and SOW4. Residuals are typically <0.3 m about these linear fits (Figure 4-10).

Figure 4-10 shows residuals from linear Dh/Dt fits. Residuals at all sites show seasonal to annual variability with magnitude <0.2 m, as well as short-period (~days-weeks) elevation anomalies that are observed across all stations in the 2012-2014 array (e.g. June 2012).

4.3.5 *Reflector heights*

The initial relative antenna heights above the surface (z_a in Figure 4-5, Section 4.2.3) range from ~2.5 to 3.1 m. These records indicate that pole bases were initially ~0.6 to 1.2 m below the surface (Figure 4-9). Antenna heights at all sites decreased over time (Figure 4-9), with annual rates of ~1.0 m/yr for 2008-2010 sites and ~0.7-0.8 m/yr for 2012-2014 sites (with SOW3 at ~1.0 m/yr) (Figure 4-10).

Assuming that the pole base remains within its original firn layer, any observed decrease in relative antenna height above the surface can be attributed to surface accumulation (e.g, snowfall, deposition of snow by wind). Conversely, an increase in relative antenna height above the surface can be attributed to surface ablation (e.g., melt, removal of snow by wind) and compaction of snow/firn above the pole base.

Both PIG1 and PIG2 show periods of relatively rapid reflector height increase (e.g., from May–August 2008), followed by a steady decrease (e.g., August 2008–February 2009). The 2012-2014

records show similar periods with abrupt increase and steady decrease. All records show an abrupt reflector height decrease (~0.2-0.3 m) between December 2012 and January 2013.

4.3.6 *High-resolution DEMs*

Table 4-2 shows statistics for the sampled DEM elevation compared with GPS surface elevation (Figure 4-9). In general, we observe good agreement between the two. The limited DEM sample (n=7) for this location and time period displays RMSE of 0.72 m and NMAD of 0.57 m. The DEMs appear to be biased slightly high (+0.43 m) relative to the GPS surface elevation.

Observed DEM Dh/Dt trends are generally consistent with GPS surface Dh/Dt trends, with increased error observed for DEM Dh/Dt at stations with shorter DEM dt intervals (e.g., SOW1, BOAR). Comparisons show that the January 14, 2012 WorldView DEM is anomalously high, which biases DEM Dh/Dt trends with limited sample count (Figure 4-9).

The Lagrangian DEM Dh/Dt maps (Figure 4-11) provide context for the GPS Dh/Dt estimates. We observe good agreement between the observed GPS Dh/Dt and Lagrangian DEM Dh/Dt, with values of -1 to -2 m/yr near SOW1, SOW2 and BOAR and -4 to -5 m/yr near SOW3 and SOW4. The DEM Dh/Dt maps also reveal the spatial distribution of observed local elevation change, with little or no Dh/Dt over longitudinal ridges, and enhanced thinning within and near transverse depressions. It appears that enhanced thinning over length scales of ~0.5-1.0 km is concentrated on the upstream side of the transverse depressions. The Dh/Dt products relative to the October 23, 2012 DEM (Figure 4-11D) also show the pattern of thinning associated with the rift that opened upstream of SOW1 in ~2014.

4.3.7 *Surface mass balance*

The 1979-2015 RACMO average SMB over the central PIG shelf is ~0.9 m.w.e./yr. Monthly SMB climatology shows low accumulation rates of ~0.01-0.04 m.w.e./month over the PIG shelf during the austral summer (November to February), and high accumulation rates of ~0.08-0.1 m.w.e./month during austral winter (March to October) (Figure 4-10F). Daily SMB products show periods of days to weeks with increased accumulation that can be correlated with abrupt increases in surface reflector height (e.g., March 2013). In contrast, the reflector height records show a steady decrease during extended periods with little/no accumulation.

The ~4 weeks from December 2012 to January 2013 display anomalously warm atmospheric temperatures of ~1-5°C, at least in the ~4 year AWS record. Surface elevations decreased by ~0.2-0.3 m across the entire GPS array (Figure 4-10A), which is consistent with significant surface melting and/or enhanced near-surface firn compaction. No change is recorded in the pole-base GPS elevations, suggesting that the processes responsible for observed surface change were limited to the upper ~1.5 m.

4.3.8 *Firn model results*

Estimated downward velocity due to firn compaction near the GPS pole base are ~0.7–0.75 m/yr (Figure 4-8, Table 4-1) with similar values for a range of initial pole depths from 2008–2010 and 2012–2014. A slight decrease in the compaction rate is observed over time, but the curves appear linear (Figure 4-8).

Figure 4-10B shows the expected relative surface elevation change (IMAU-FDM zs) due to modeled surface mass balance and firn compaction is -0.1 to +0.4 m from 2008–2010 and -0.2 to +0.2 m from 2012–2014. These rates are slightly higher than previous estimates for 2003-2008 dh/dt from firn compaction of <0.05–0.12 m/yr over the PIG shelf [*Pritchard et al.*, 2012]. We note that the modeled IMAU-FDM zs appears to show a ~0.17 m/yr increase over the ~2 year period from 2008-2010, with no significant trend from 2012-2014.

The magnitude and timing of IMAU-FDM zs variability is consistent with the detrended reflector height and detrended surface elevation change (Figure 4-10C). The observed large negative surface elevation Dh/Dt (-1 to -4 m/yr) (Figure 4-10B), however, cannot be explained by modeled elevation change due to SMB and firn.

4.3.9 *Basal melt rates*

We computed basal melt rates from surface Dh/Dt and pole base Dh_{pb}/Dt using Equations 4.4 and 4.6, respectively. The resulting values for basal melt rates range from 3.6 +/- 1.7 m/yr at PIG2 to 42.3 +/- 3.2 m/yr at SOW3, with good agreement between the surface and pole base elevation change (Table 1).

The 2012-2014 GPS Dh/Dt melt rate estimates show significant spatial variability. The three upstream stations (SOW1, SOW2 and BOAR) show limited melt rates of ~8-13 m/yr, while the

downstream stations near the transverse depression (SOW3 and SOW4) have increased rates of ~29-42 m/yr for the same time period. In general, we see (Table 1).

4.4 DISCUSSION

4.4.1 *Assumptions*

4.4.1.1 SMB spatial variability

We used modeled SMB from a single RACMO grid cell to drive a dynamic firn model, and applied the result to all GPS stations. We expect these parameters to display spatial variability due to local environmental conditions (e.g. PIG2 is >400 m higher than stations on the shelf) and local surface topography (e.g., ridges, troughs). These factors will affect near-surface winds and the redistribution of snow. The increased reflector heights (a proxy for surface accumulation) at SOW3 could be indicative of enhanced local accumulation within the transverse depression. However, we note that the 2008-2010 and the remaining 2012-2014 stations all display similar reflector height evolution, suggesting comparable SMB and firn compaction for these periods. Future reanalysis products with improved resolution may provide further constraints on spatial variability at ~5-10 km scale, although observational constraints for these simulations are sparse over ASE.

4.4.1.2 Pole base settling

Some of the reflector height increase and/or observed negative Dh/Dt could be related to poles settling within the firn. We assume that the poles froze in place shortly after installation, and the contact area (~1200 cm^2 for a ~1 meter section with ~3.8 cm diameter) with surrounding snow/firn should be sufficient to counter the downward gravitational force. Thus, the Dh/Dt recorded by the antenna pole should represent rates at the base of the pole, rather than an overlying layer.

A related consideration involves heating of the pole during summer, which might decouple with surrounding snow/firn and lead to additional penetration. However, we do not see any indication of this during the December 2012 to January 2013 melt period; the surface elevation decreases by ~20-30 cm while the pole base shows little elevation change. This also suggests that meltwater formed at the surface during this period does not percolate below the upper ~1-2 m.

4.4.1.3 Strain rate length scales

As discussed in Section 4.3.2, the expected Dh/Dt from local flux divergence is <0.1 m/yr, assuming that observed ~1.5 m/yr relative displacement is evenly distributed across the ~1 km distance between GPS stations (BOAR and SOW3). If this strain is concentrated over a shorter distance, say ~200 m, then this contribution increases to <0.5 m/yr, which is still significantly less than the ~3-4 m/yr Dh/Dt signals. Interestingly, despite similar GPS strain rate estimates for SOW1-BOAR (2.0 m/yr) and BOAR-SOW3 (1.5 m/yr), we note large differences in local Dh/Dt values between these stations in the Lagrangian DEM analysis (Figure 4-10). This supports the assumption that local flux divergence for these sites is a minor component of observed Dh/Dt, and consequently, basal melt rate.

4.4.2 *Long-term SMB and firn compaction*

The observed reflector height increase of ~0.7-1.0 m/yr at all GPS sites appears consistent with long-term SMB of ~0.7-0.9 m.w.e./yr and downward near-surface velocity of ~0.7 m/yr due to firn compaction. The limited variability in surface elevation at PIG2 (Figure 4-10B) suggests that the observed 2008-2010 accumulation was approximately in balance with ongoing firn compaction and basal melt. The 2012-2014 sites show significant trend, but limited residuals.

The fact that we observe similar trends for surface Dh/Dt and pole base Dh/Dt (Table 4-1) also supports the interpretation that 2008-2010 and 2012-2014 SMB is consistent with long-term 1979-2015 SMB and firn-compaction rates. Computing basal melt rates from 1- or 2-year interval surface elevation data (altimetry or DEMs) should provide similar results.

Expected IMAU-FDM surface elevation change (zs) variability is <0.5 m/yr for all GPS sites. While the IMAU-FDM long-term trend uncertainty is ~2-5 cm/yr, we only consider relative elevation change over ~2 year periods. The 2012-2014 zs trend is consistent with long-term SMB, while the observed ~0.17 m/yr trend from 2008-2010 is potentially related to above-average accumulation during this period.

4.4.3 *Residual Dh/Dt variability*

A comparison of surface records suggests that the pole base elevation variability cannot be attributed to seasonal accumulation influencing near-surface compaction rates. We considered several possible sources for the systematic sub-annual variability in the surface and pole base

records, including the ocean (currents, sea surface height), atmospheric (pressure, temperature), and dynamic processes (resistive stress from sea ice, mélange in shear margins).

Some of the short-term (days-weeks) variability observed across all five 2012-2014 stations (Figure 4-10D) (e.g. June 2012) could be related to insufficient or incorrect IBE correction. The magnitude of these changes, however, is significant, and we suggest that these systematic anomalies could be related to grounding/ungrounding events.

4.4.4 *Strain rate history and grounding evolution*

The lateral shear across the GPS array is related to increased longitudinal extension closer to the PIG centerline, likely due to locally-enhanced ductile deformation ("necking" [*Bassis and Ma*, 2015]) across transverse depressions, and/or expansion of basal/surface crevasses and rifts. A slight acceleration in negative elevation change is apparent at SOW3, potentially due to increasing extension or downslope motion.

The fact that the rift immediately upstream of SOW1 ultimately became the site of the 2015 calving event [*Jeong et al.*, 2016] suggests that the velocities observed at the GPS array are not necessarily representative of the velocities near the grounding line at PIG. An upstream regrounding event would slow upstream ice, initially resulting in increased extensional strain rates across these features, followed by a slight velocity decrease over the GPS array. Similarly, an upstream ungrounding event would initially decrease strain rates across rifts/depressions, followed by increased GPS velocities.

We suggest that an upstream regrounding event in ~June 2012 could be responsible for increased strain rates across the GPS array (Figure 4-7). Similarly, an ungrounding event in ~April 2013 followed by a grounding event in ~November 2013 could explain the decrease and subsequent increase in strain rates.

Both SOW3 and SOW4 display an abrupt ~10-20 cm pole base elevation decrease in late 2013, near the end of the record (Figure 4-10D). This is not observed at other sites and does not appear to be related to site servicing. This is consistent with relatively abrupt local extension at these sites but not upstream sites.

4.4.5 *Comparison with* in situ *basal melt rate observations*

The precise locations of January–February 2012 borehole altimeter (~14.7 m/yr) and pRES (~15-25 m/yr) melt rate estimates [*Stanton et al.*, 2013] relative to the GPS array are not well documented. Presumably, the altimeter borehole was located near the BOAR GPS station, which displayed local melt rates of ~8-10 m/yr for the 2012-2014 period. The altimeter sampled a ~5 cm diameter spot approximately 30-40 cm from the edge of the 20 cm borehole, with unknown upstream/downstream orientation. Aside from local melt variability due to turbulent flow near the altimeter pole or borehole, the altimeter provided a small sample, and it may be imprudent to compare directly with inferred GPS Dh/Dt melt rate, which is sensitive to changes in a column of ice with much larger footprint (likely 10s to 100s of meters).

4.4.6 *Melt rate spatial variability*

The GPS records at SOW1, SOW2 and BOAR show similar Dh/Dt rates and residuals, which is consistent with their apparent orientation on the same "block" between transverse extensional features (rifts, depressions). They are also located over the same set of longitudinal basal channels, and should be exposed to similar sub-shelf circulation. The DEM Dh/Dt maps show enhanced rates on the north side (left side in Figure 4-11) of channels and on the upstream side of transverse depressions.

The SOW3 and SOW4 site are located on the upstream side of a transverse depression and they display higher Dh/Dt. It is possible that accumulation rates, and thus firn-compaction rates, are higher near the depression margins, but this is not apparent in reflector height records. Instead, these elevated Dh/Dt rates are consistent with increased melt rates on the upstream slope of the depression. This is potentially related to enhanced buoyant flow over increased basal slopes and/or turbulence as water within the upstream meltwater channel first enters the "cavern" of the transverse depression. We also suggest that the transverse depressions may serve as conduits connecting flow between the longitudinal channels, potentially leading to increased circulation velocity and higher melt rates within the transverse depressions.

4.4.7 *Sensitivity to ocean variability*

The 2012-2014 GPS data reveal subtle (~2-3%) velocity changes that were attributed to observed variations in ocean temperature records from moorings in Pine Island Bay [*Christianson et al.*, 2016]. Our analysis suggest that these velocity variations are likely related to upstream grounding evolution [e.g., *Joughin et al.*, 2016], and extension across a series of transverse depressions.

Both the GPS pole base and surface Dh/Dt fits are highly linear, with no significant variation in inferred basal melt rates for this 2-year time period. If melt rates had decreased by ~50%, we would expect to see a significant change in Dh/Dt. This suggests that melt rates at these sites are not significantly affected by observed ocean temperature variability.

This finding suggests that either: 1) these sites are not representative of melt rates for the greater shelf (e.g., those near the grounding line), 2) the oceanographic measurements are not representative of water circulating beneath these sites, 3) local melt rates are less sensitive to the observed oceanographic changes than previously assumed.

4.4.8 *Future work*

High-resolution velocity maps derived from sub-meter WorldView images could potentially constrain local velocity divergence and length scales for observed strain between GPS receivers. In addition, seismic data from stations deployed near the GPS array and regional sites could help constrain timing and location of rift propagation and grounding/ungrounding events.

It may be possible to further constrain firn-compaction rates, and thus long-term SMB, using relative layer thicknesses observed in CReSIS snow radar measurements [*Medley et al.*, 2015] or *in situ* pRES observations described in [*Stanton et al.*, 2013]. However, the airborne radar data will suffer from clutter due to km-scale topography and crevasses, while the available pRES records are of limited duration (~3 weeks) and lack the resolution to detect small changes in firn layer thickness. These limitations highlight the value of GPS reflector height records to constrain surface evolution where observations are sparse and model results are poorly constrained.

4.5 SUMMARY AND CONCLUSIONS

We analyzed 2008-2010 and 2012-2014 GPS records for PIG. These data provide validation for surface elevation and Dh/Dt derived from high-resolution WorldView stereo DEM records, with sampled DEM RMSE of ~0.72 m.

The GPS antenna height records document a relative surface increase of ~0.7-1.0 m/yr, which is consistent with long-term RACMO SMB of ~0.7-0.9 m.w.e./yr and expected firn compaction rates. An abrupt ~0.2-0.3 m surface elevation decrease due to surface melt and/or greater near-surface firn compaction is observed during a period of warmer atmospheric temperatures from December 2012 to January 2013. Estimated IMAU-FDM surface elevation change due to SMB and firn compaction is <0.5 m for these periods. Observed longitudinal strain rates for the 2012-2014 GPS array are ~0.001-0.002 1/yr, with negligible associated surface elevation change.

Observed surface Dh/Dt for all PIG shelf sites are linear, with values of -1 to -4 m/yr and <0.4 m residuals. Similar Dh/Dt estimates are obtained after removing expected downward GPS pole base velocity from observed GPS antenna elevation records, with reduced residual variability. Estimated Dh/Dt basal melt rates are ~10 to 40 m/yr for the outer PIG shelf and ~4 m/yr for the South shelf. These melt rates are similar to those derived from complementary instrument records and high-resolution stereo DEMs.

Both GPS and DEM records show higher melt rates within/near transverse surface depressions and rifts associated with longitudinal extension. Basal melt rates for the 2012-2014 period show limited temporal variability, despite significant changes in sub-shelf ocean heat content. This suggests that sub-shelf melt, at least at these locations, is less sensitive to ocean heat content than previously reported.

ACKNOWLEDGEMENTS

D. Shean was supported by a NASA NESSF fellowship (NNX12AN36H) and NSF OPP grant ANT-0424589. We acknowledge P. Kuipers Munneke and M. van den Broeke for providing RACMO SMB products. The AWS data are available from the University of Wisconsin-Madison Automatic Weather Station Program (NSF ANT-1245663). We acknowledge GPS data collection and archiving provided by the UNAVCO Facility with support NSF and NASA under NSF Cooperative Agreement No. EAR-0735156.

TABLES

Site	Time period	Days	h_0 (m)	z_{pb0} (m)	GPS antenna Dh_a/Dt (m/yr)	v_{fcpb} (m/yr)	Surf. Dh/Dt (m/yr)	Pole base Dh_{pb}/Dt (m/yr)	Surf. $\dot{b}$ (m/yr)	Pole base $\dot{b}$ (m/yr)
PIG1	2008-1-13, 2009-9-4	601	484.3	0.71	-7.60	-0.75	-6.76		--	--
PIG2	2008-1-10, 2010-1-27	747	76.1	0.78	-1.17	-0.74	-0.13	-0.38	1.9 +/-1.0	4.3 +/-1.7
SOW1	2012-2-10, 2013-12-23	714	67.7	0.61	-1.81	-0.75	-1.13	-1.06	11.4 +/-1.2	10.7 +/-1.8
SOW2	2012-2-10, 2013-12-23	714	64.5	0.89	-2.07	-0.74	-1.33	-1.34	13.3 +/-1.3	13.4 +/-1.9
BOAR	2012-2-10, 2013-4-29	476	66.3	0.82	-1.56	-0.77	-0.91	-0.81	9.3 +/-1.1	8.4 +/-1.8
SOW4	2012-2-10, 2013-12-24	714	69.7	1.08	-3.75	-0.73	-3.00	-3.03	29.0 +/-2.1	29.3 +/-2.5
SOW3	2012-2-9, 2013-12-24	716	63.3	1.16	-5.22	-0.72	-4.10	-4.50	39.4 +/-2.7	43.1 +/-3.2

Table 4-1: GPS station data, Dh/Dt, and melt rate estimates. Fields include initial height h_0 (meters above EGM2008 geoid), initial pole base depth z_{pb0}, linear GPS antenna Dh_a/Dt, estimated downward vertical velocity due to firn compaction at pole base v_{fcpb}, observed surface Dh/Dt, and pole base Dh_{pb}/Dt after removing v_{fcpb}. Corresponding ice-equivalent basal melt rates $\dot{b}$ computed assuming hydrostatic equilibrium and including long-term surface mass balance of ~1.0 m/yr.

Site	DEM n	DEM dt (days)	DEM Dh/Dt (m/yr)	DEM RMSE (m)	GPS-DEM mean (m)	GPS-DEM std (m)
SOW1	5	302*	-2.30	0.69	-0.26	0.64
SOW2	5	619	-2.03	0.76	-0.46	0.60
BOAR	4	302*	-1.69	0.86	-0.55	0.66
SOW4	5	368*	-3.35	0.75	-0.61	0.44
SOW3	6	619	-4.32	0.54	-0.30	0.45

Table 4-2: WorldView DEM accuracy from measured GPS surface elevation. Asterisks identify records with shorter DEM Dh/Dt time intervals.

FIGURES

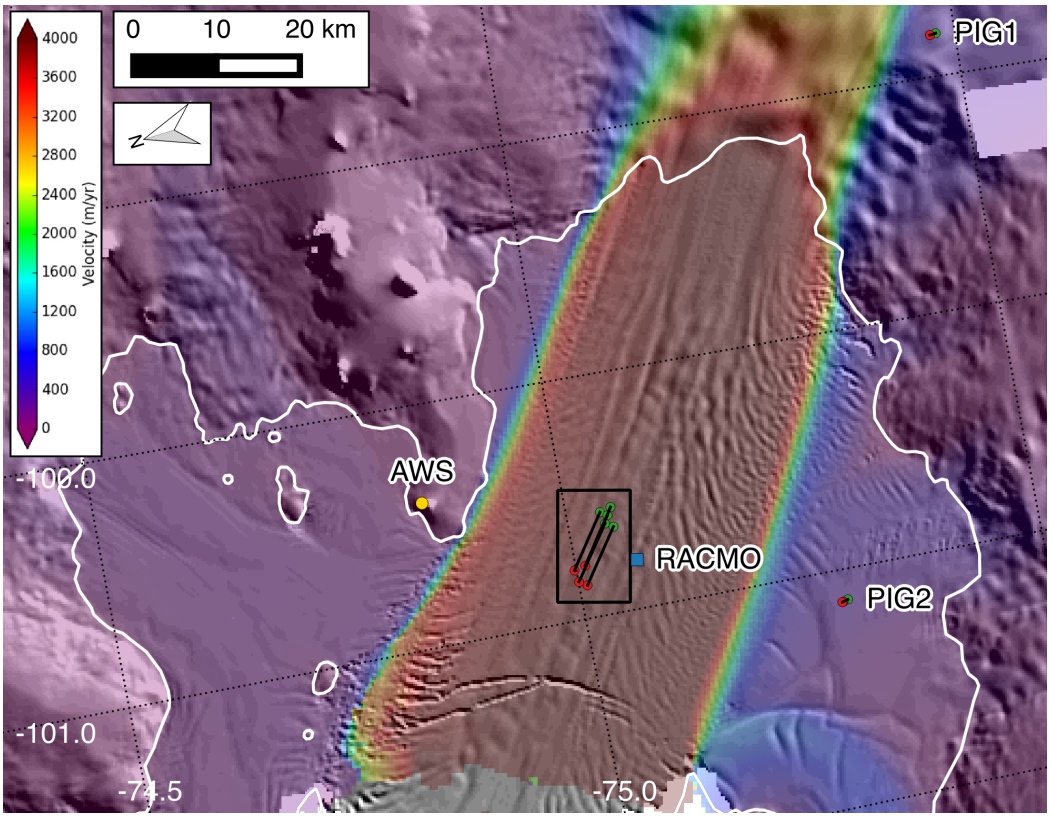

Figure 4-1: Context for Pine Island Glacier ice shelf, with 2006-2016 median surface velocity over 2012/2013 DEM mosaic shaded relief map. Points show initial (green) and final (red) GPS station locations, Evan's Knoll AWS (yellow dot) and RACMO grid cell (blue square, -75.07°N, -100.80°E) used during analysis. White line shows approximate 2011 grounding line. Black rectangle shows location of Figure 4-2.

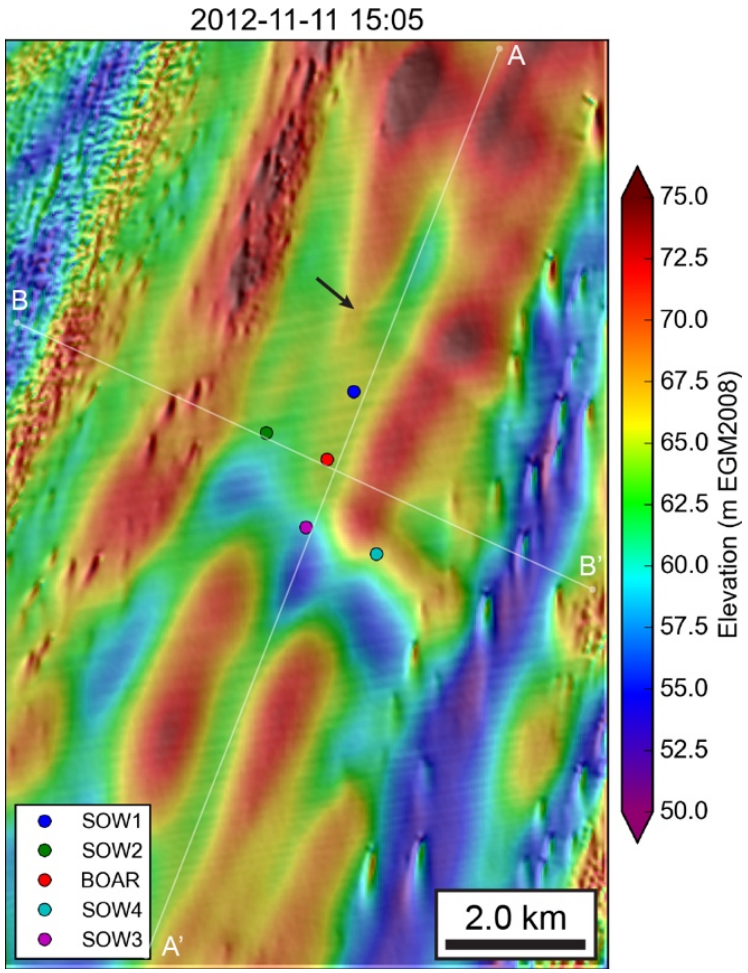

Figure 4-2: WorldView DEM context for 2012-2014 GPS array. Note positions of GPS stations relative to transverse depressions and location of rift associated with 2015 calving event (arrow). White lines show locations of profiles in Figure 4-3.

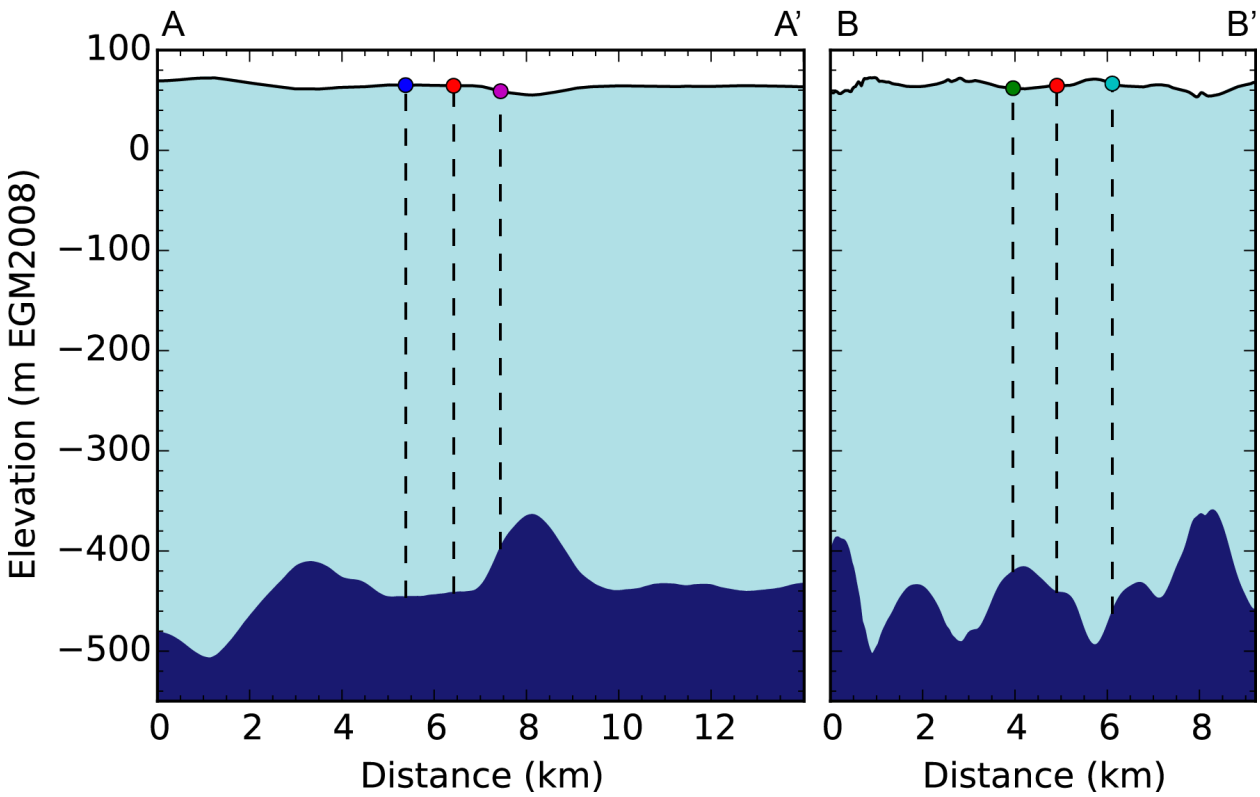

Figure 4-3: Longitudinal and transverse profiles across the 2012-2014 GPS array. Surface elevation from October 23, 2012 and smoothed (~0.5 km kernel, ~1H) freeboard thickness are plotted. Profile intersection is near BOAR (red point). Vertical exaggeration is 22x.

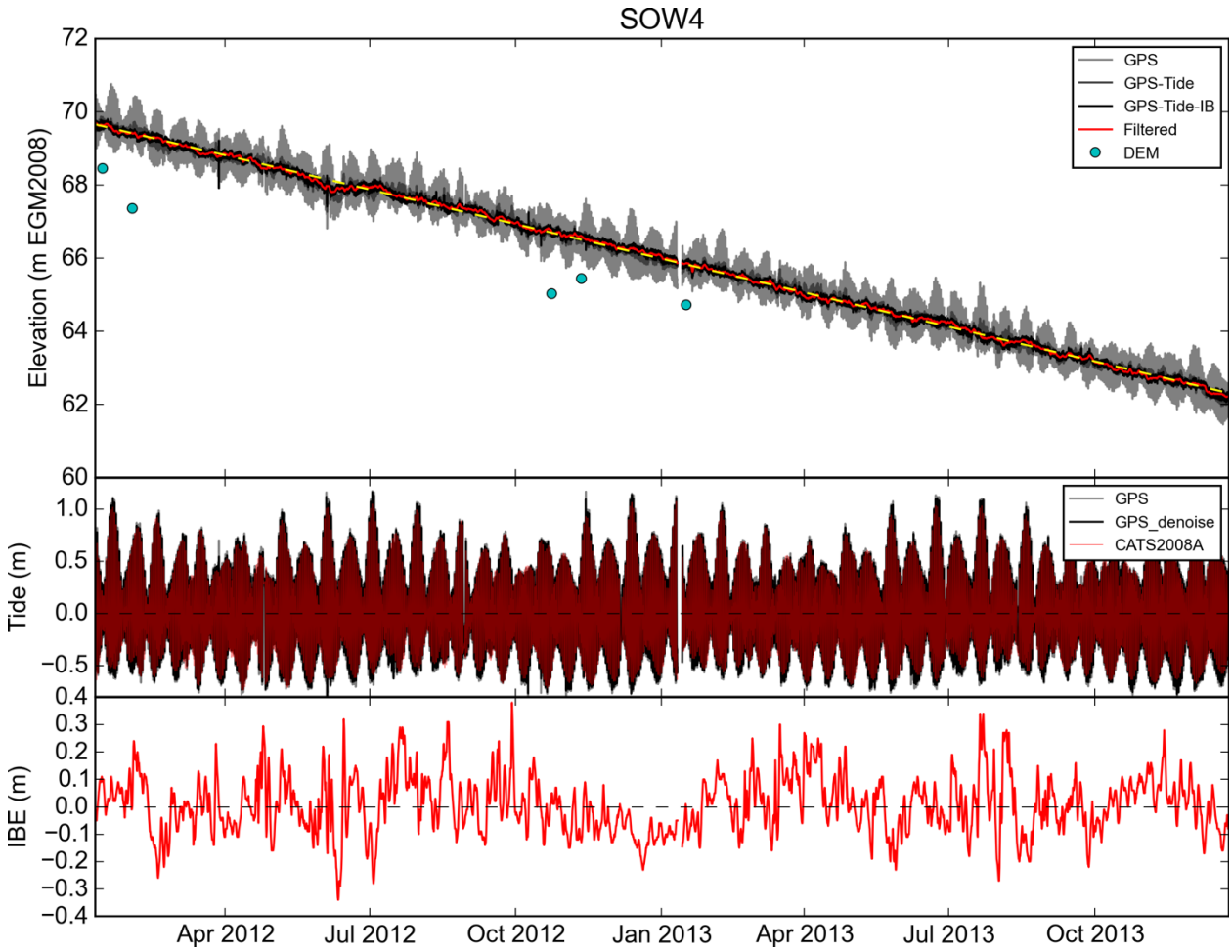

Figure 4-4: SOW4 GPS record with tide and IBE correctionA) original GPS record (light gray), tidally-corrected record (mid-gray), and tidally- and IBE-corrected record (black). Red line shows smoothed time series and yellow dashed line is linear fit (-3.76 m/yr). Sampled DEM elevations represent surface elevation, while plotted GPS elevations represent antenna heights. B) High-frequency (<1.5 days) component of GPS record compared with CATS2008A tide model prediction, showing excellent agreement. C) Estimated IBE magnitude.

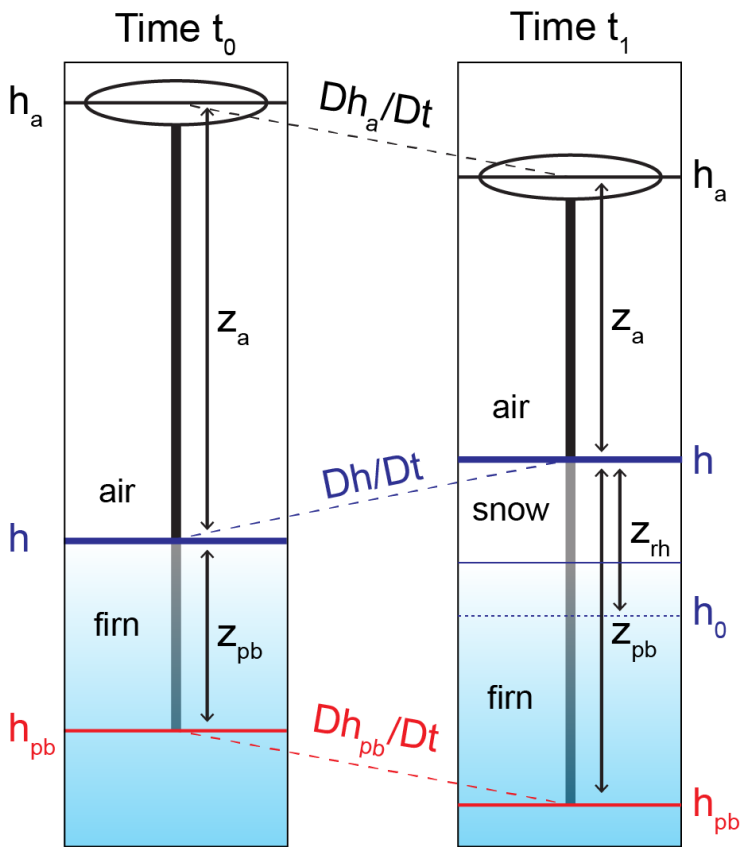

Figure 4-5: Schematic showing GPS station geometry over time. Measured quantities are GPS height above EGM2008 geoid (h_a, black line) and multi-path antenna height above surface (z_a). These are used to infer surface elevation (h), pole base depth below the initial surface (z_{pb}), and pole base elevation (h_{pb}, red line). At time t_1 (right panel), the GPS antenna and pole have moved downward due to firn compaction at the pole base, but the surface has experienced a relative increase in elevation due to ongoing accumulation. Reflector height (z_{rh}) is measured relative to the initial surface h_0 (dotted blue line), while the thin blue line shows the surface elevation prior to fresh snow accumulation.

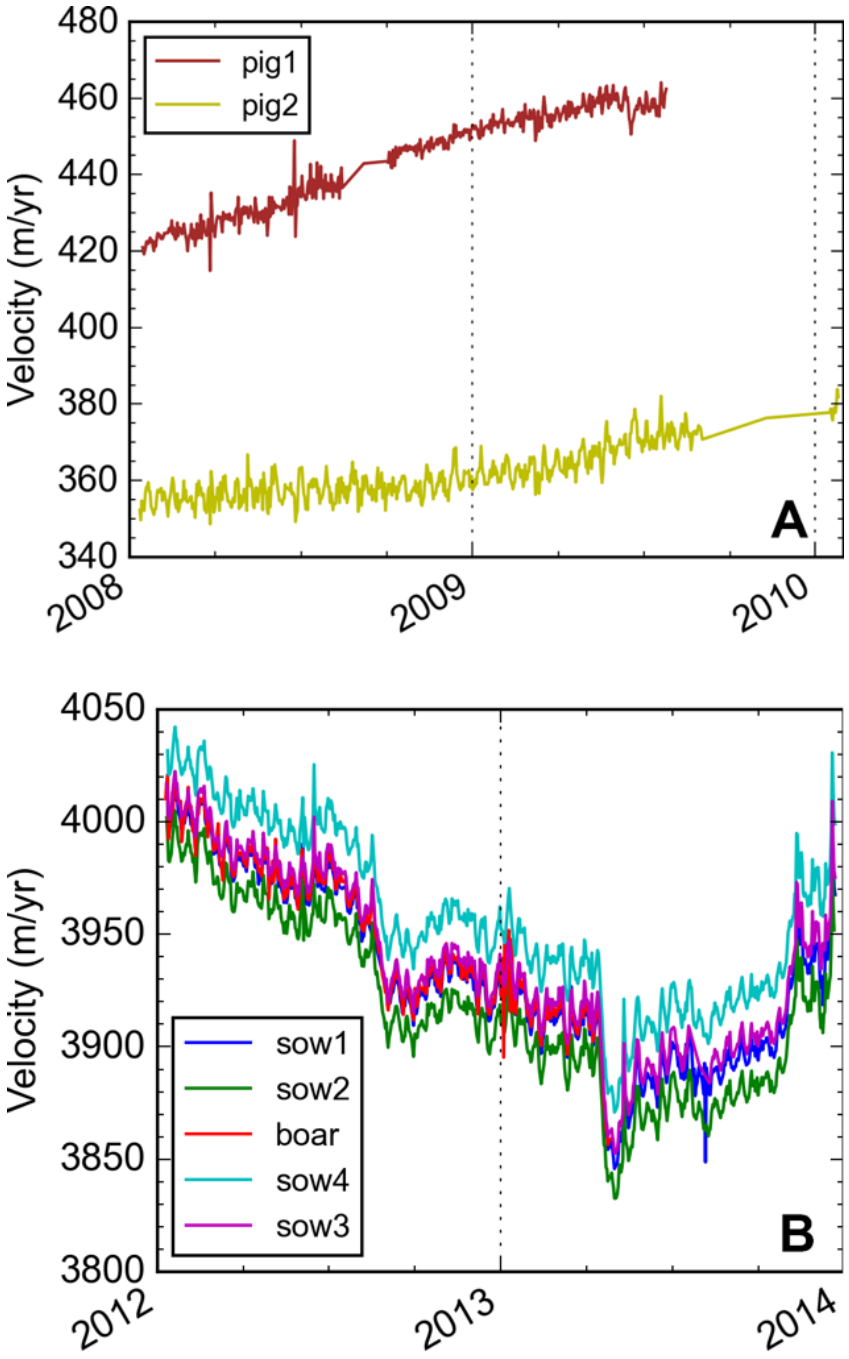

Figure 4-6: GPS velocities derived from daily mean positions. A) 2008-2010 GPS sites, and B) 2012-2014 GPS sites. Note offset between SOW2 and SOW4, indicative of lateral shear across the ~2 km wide array, with greater extension near the center of the PIG shelf.

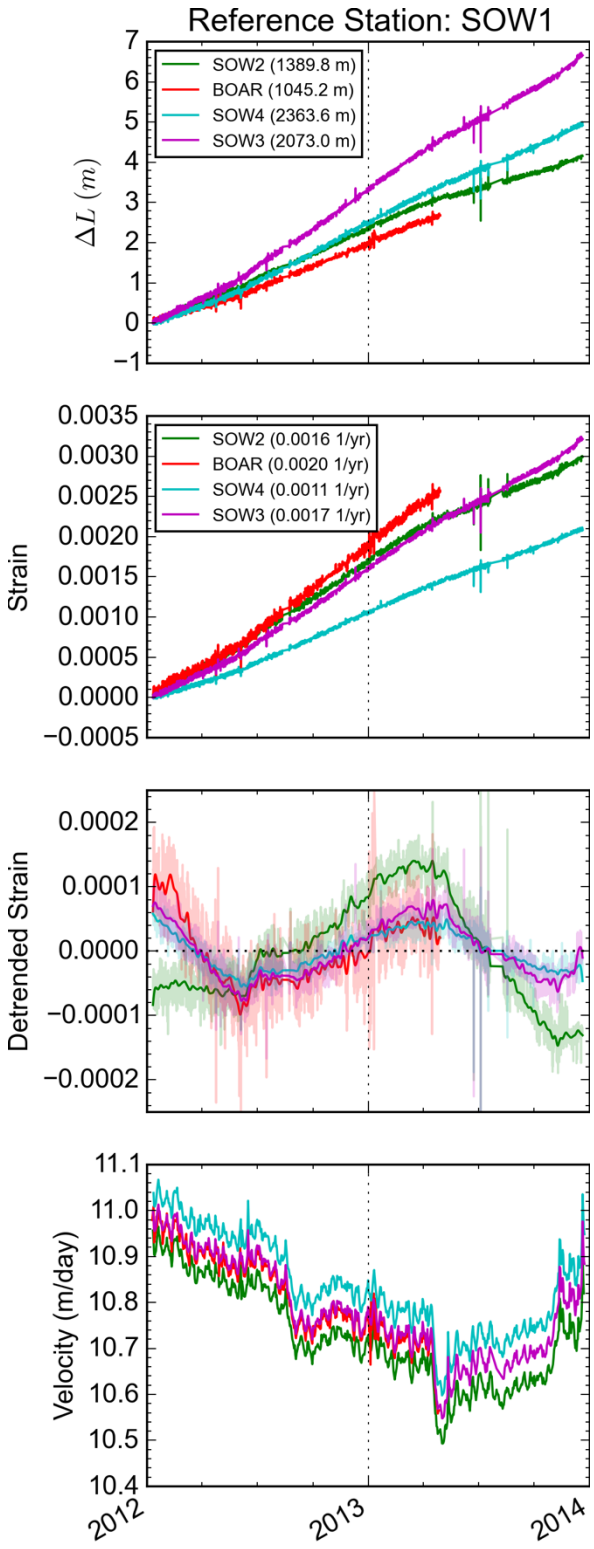

Figure 4-7: Strain between SOW1 and other 2012-2014 stations. A) Observed cumulative displacement. Legend lists initial distances. B) Observed cumulative strain, with best fit strain rate listed in legend. C) Smoothed residuals from linear fit, highlighting subtle variations and

inflections in strain rates. D) Daily GPS velocity. Note timing of abrupt absolute velocity changes observed at all sites and inflection points in observed strain across the array.

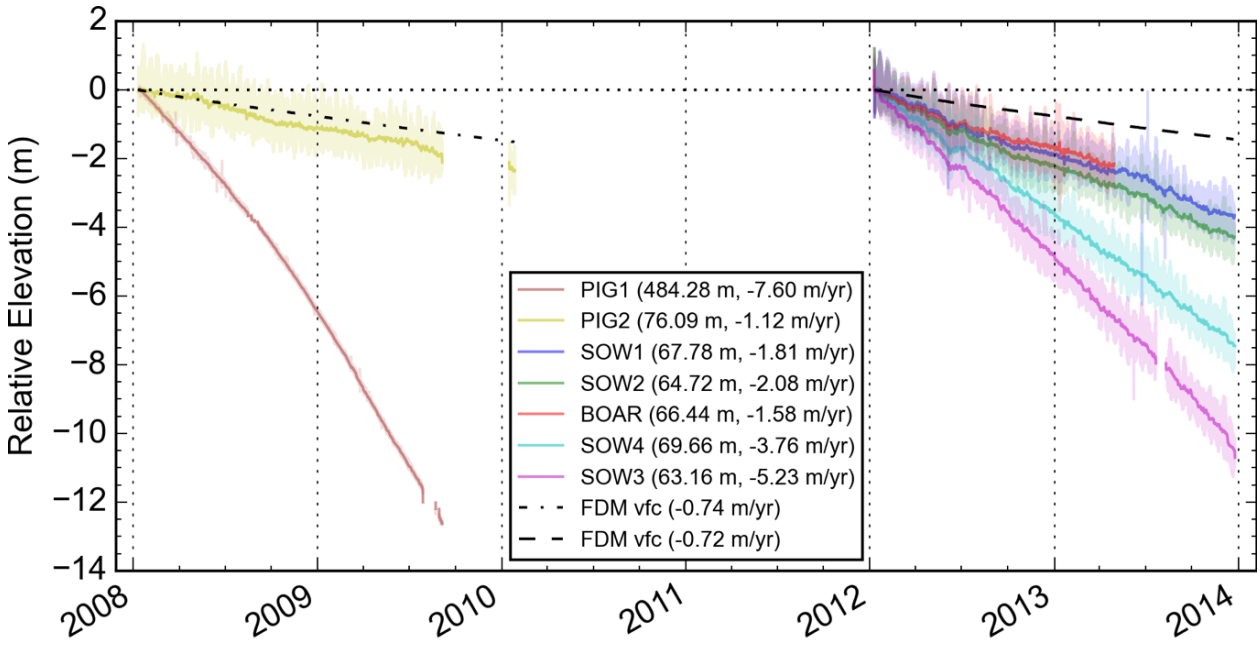

Figure 4-8: Original and filtered relative GPS antenna elevation for all sites. Legend lists initial elevation and linear Dh/Dt fit to filtered elevations. Dashed black lines show IMAU-FDM estimated downward velocity due to firn compaction at the pole base.

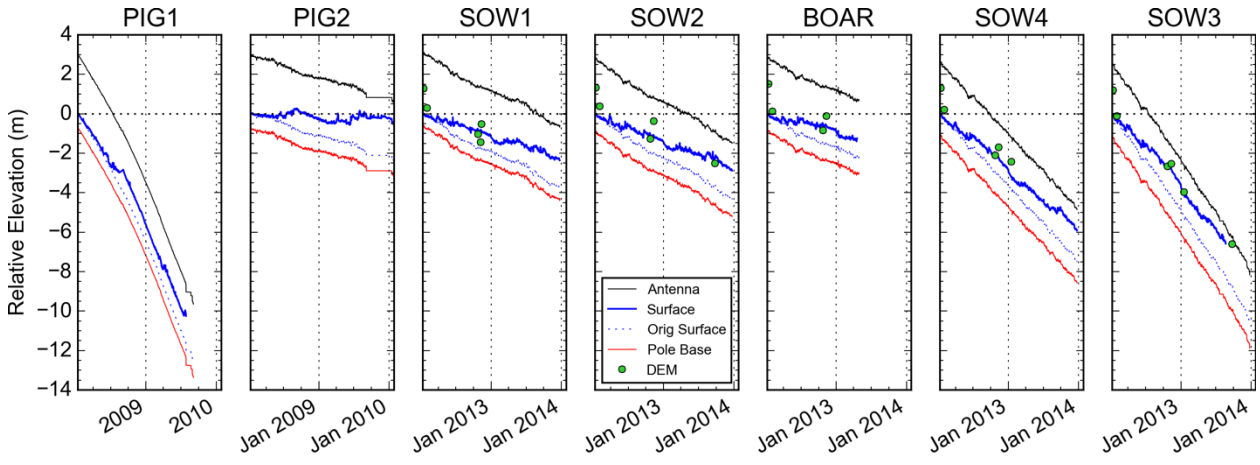

Figure 4-9: Comparison of GPS and WorldView DEM surface elevation. Antenna elevation data (black), pole base anchor elevation (red), surface elevation obtained by removing reflector height from antenna elevation (thick blue), and tracer for initial surface (dotted blue line), all relative to initial GPS surface elevation. See Figure 4-5 for reference. Points show sampled 32-m

WorldView DEM elevations at each site, with good agreement between DEM and GPS surface elevation records. The PIG2 surface shows little change, while all others show surface elevation decrease over their respective ~2-year periods.

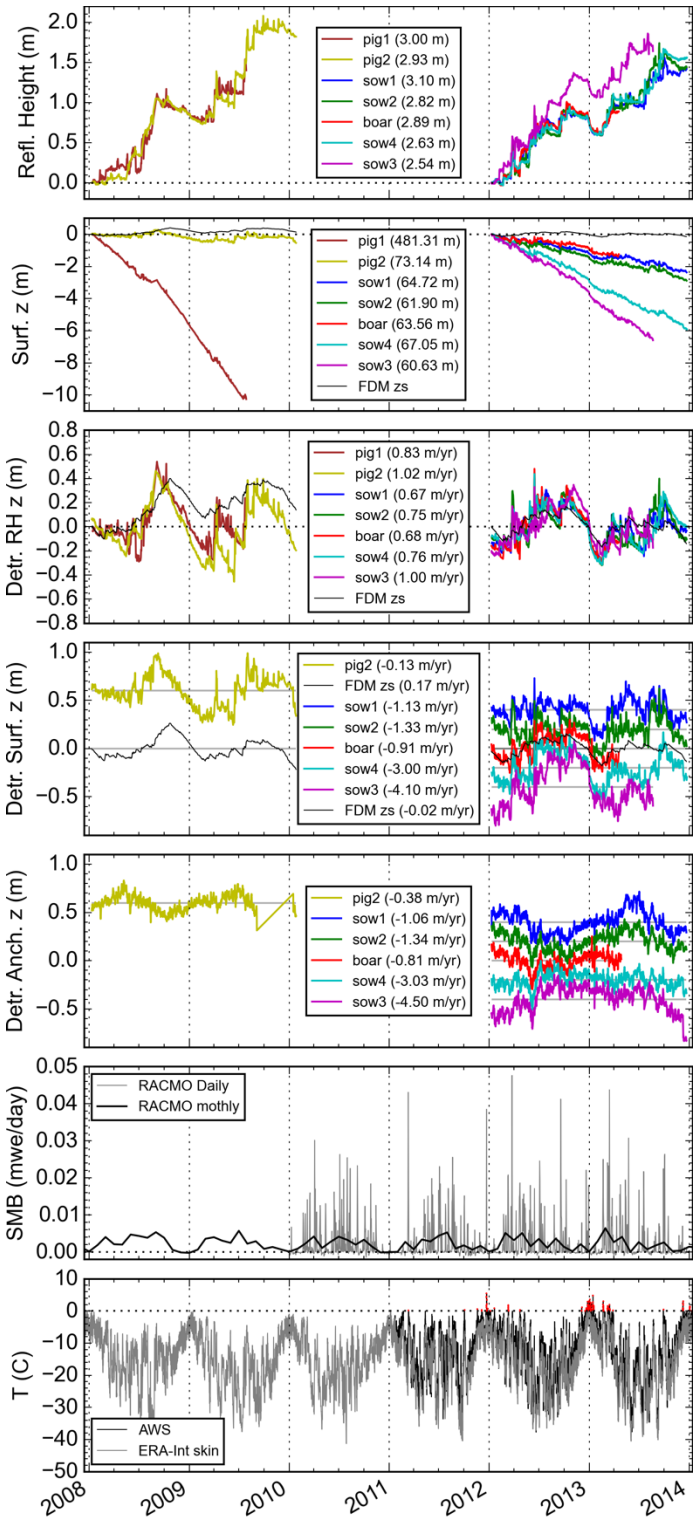

Figure 4-10: Comparison of detrended GPS records, SMB, and air temperature. A) Reflector height relative to initial surface, positive values indicate surface height increase relative to GPS antenna. Legend indicates initial antenna height above surface. Note ~20-30 cm surface decrease

from December 2012 to January 2013. B) Surface elevation from combined GPS positions and reflector heights. Legend indicates initial surface height (m above EGM2008 geoid). Black lines show expected surface elevation from the IMAU-FDM firn compaction model with same scale. C) Detrended reflector height and IMAU-FDM surface elevation. Legend lists linear fit to reflector height change. D) Detrended GPS surface and Detrended IMAU-FDM surface elevation, with arbitrary y-axis offset. Legend lists linear fit. E) Detrended GPS pole base elevation after removing expected downward velocity due to firn compaction (see Figure 4-8), with arbitrary y-axis offset. Note reduced residual magnitude and dampened ~seasonal signal compared to detrended surface records. Unlike surface records, no significant change is observed from December 2012 to January 2013. F) Daily and monthly RACMO2.3 SMB. G) Observed AWS and ERA-Interim temperature records for PIG shelf, with above-zero AWS temperatures plotted in red. Note period of extended warm temperatures in December 2012 to January 2013, which corresponds to ~0.2-0.3 m decrease in reflector height.

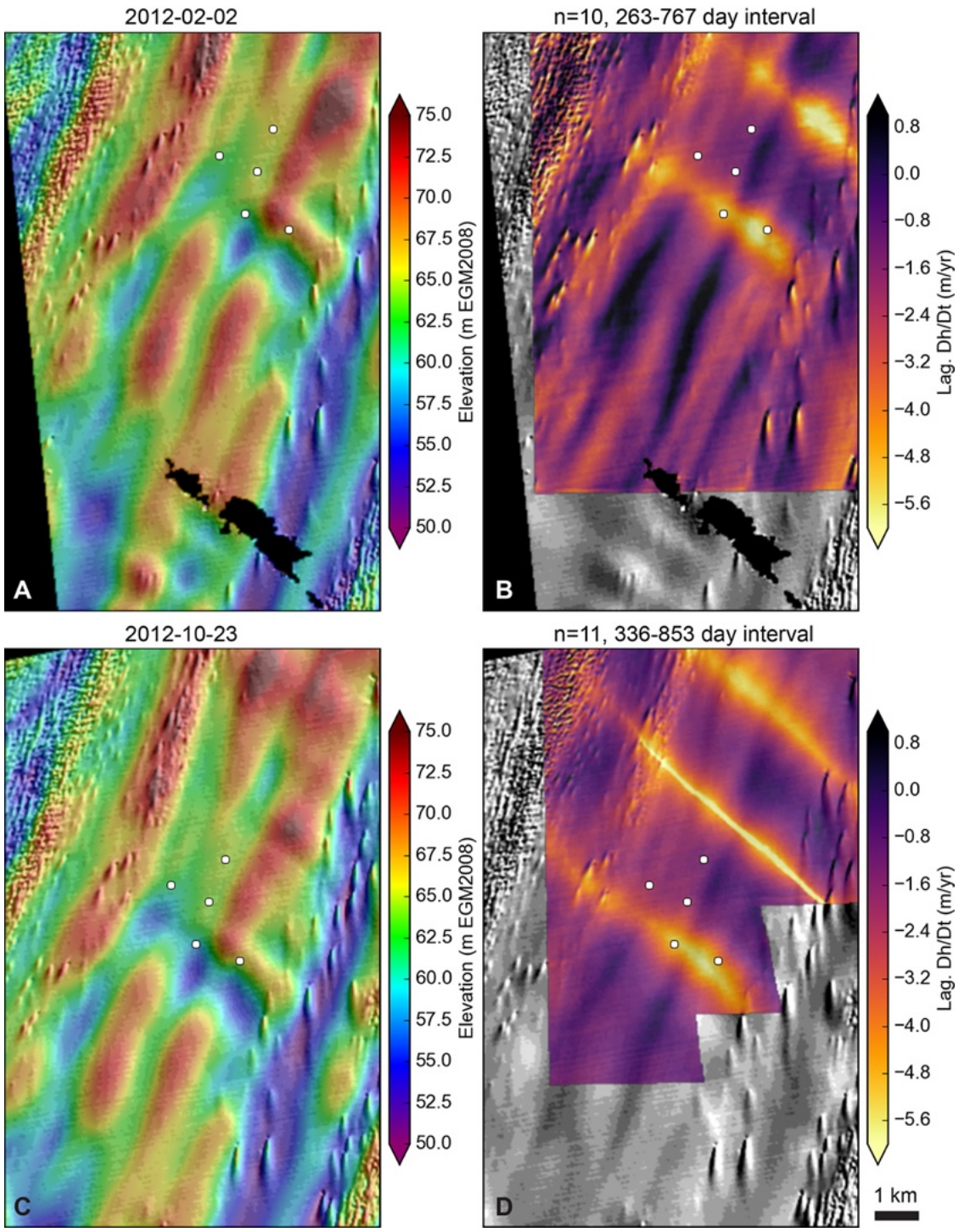

Figure 4-11: WorldView DEMs and composite Lagrangian Dh/Dt products. A-B) Initial DEM from February 2, 2012, and C-D) initial DEM from October 23, 2012. Note enhanced thinning observed within transverse depressions and rift upstream of GPS array. The Dh/Dt maps provide

a proxy for local basal melt rates, with scaling factor of ~9 (e.g., ~1.0 m/yr Dh/Dt = ~9-10 m/yr melt rate).

REFERENCES

Abdalati, W. et al. (2010), The ICESat-2 Laser Altimetry Mission, *Proc. IEEE*, *98*(5), 735–751, doi:10.1109/JPROC.2009.2034765.

Aguilar, M. A., M. del M. Saldaña, and F. J. Aguilar (2013), Assessing geometric accuracy of the orthorectification process from GeoEye-1 and WorldView-2 panchromatic images, *Int. J. Appl. Earth Obs. Geoinformation*, *21*, 427–435, doi:10.1016/j.jag.2012.06.004.

Aguilar, M. A., M. del Mar Saldana, and F. J. Aguilar (2014), Generation and Quality Assessment of Stereo-Extracted DSM From GeoEye-1 and WorldView-2 Imagery, *IEEE Trans. Geosci. Remote Sens.*, *52*(2), 1259–1271, doi:10.1109/TGRS.2013.2249521.

Allstadt, K. E., D. E. Shean, A. Campbell, M. Fahnestock, and S. D. Malone (2015), Observations of seasonal and diurnal glacier velocities at Mount Rainier, Washington, using terrestrial radar interferometry, *The Cryosphere*, *9*(6), 2219–2235, doi:10.5194/tc-9-2219-2015.

Andersen, O. B., and P. Knudsen (2009), DNSC08 mean sea surface and mean dynamic topography models, *J. Geophys. Res.*, *114*(C11), doi:10.1029/2008JC005179.

Anderson, J. A. (2008), ISIS Camera Model Design, in *39th Lunar and Planetary Science Conference Abstracts*, vol. 39, p. 2159.

Bamber, J. L., R. E. M. Riva, B. L. A. Vermeersen, and A. M. LeBrocq (2009), Reassessment of the Potential Sea-Level Rise from a Collapse of the West Antarctic Ice Sheet, *Science*, *324*(5929), 901–903, doi:10.1126/science.1169335.

Bassis, J. N., and Y. Ma (2015), Evolution of basal crevasses links ice shelf stability to ocean forcing, *Earth Planet. Sci. Lett.*, *409*, 203–211, doi:10.1016/j.epsl.2014.11.003.

Becker, K. J., B. A. Archinal, T. M. Hare, R. L. Kirk, E. Howington-Kraus, M. S. Robinson, and M. R. Rosiek (2015), Criteria for Automated Identification of Stereo Image Pairs, in *46th Lunar and Planetary Science Conference Abstracts*, p. 2703.

Berthier, E., Y. Arnaud, R. Kumar, S. Ahmad, P. Wagnon, and P. Chevallier (2007), Remote sensing estimates of glacier mass balances in the Himachal Pradesh (Western Himalaya, India), *Remote Sens. Environ.*, *108*(3), 327–338, doi:10.1016/j.rse.2006.11.017.

Beyer, R. A. et al. (2010), LROC Stereo Data — Results of Initial Analysis, in *41st Lunar and Planetary Science Conference Abstracts*, vol. 41, p. 2678.

Bindschadler, R., D. G. Vaughan, and P. Vornberger (2011), Variability of basal melt beneath the Pine Island Glacier ice shelf, West Antarctica, *J. Glaciol.*, *57*(204), 581–595.

Bindschadler, R. A. (2002), History of lower Pine Island Glacier, West Antarctica, from Landsat imagery, *J. Glaciol.*, *48*(163), 536–544.

Blair, J. B., D. L. Rabine, and M. A. Hofton (1999), The Laser Vegetation Imaging Sensor: a medium-altitude, digitisation-only, airborne laser altimeter for mapping vegetation and topography, *ISPRS J. Photogramm. Remote Sens.*, *54*(2), 115–122.

Bouillon, A., M. Bernard, P. Gigord, A. Orsoni, V. Rudowski, and A. Baudoin (2006), SPOT 5 HRS geometric performances: Using block adjustment as a key issue to improve quality of DEM generation, *ISPRS J. Photogramm. Remote Sens.*, *60*(3), 134–146, doi:10.1016/j.isprsjprs.2006.03.002.

Broxton, M. J., and L. J. Edwards (2008), The Ames Stereo Pipeline: Automated 3D Surface Reconstruction from Orbital Imagery, in *39th Lunar and Planetary Science Conference Abstracts*, vol. 39, p. 2419.

Broxton, M. J., A. V. Nefian, Z. Moratto, T. Kim, M. Lundy, and A. V. Segal (2009), 3D Lunar Terrain Reconstruction from Apollo Images, in *Advances in Visual Computing*, pp. 710–719, Springer.

Brunt, K. M., H. A. Fricker, L. Padman, T. A. Scambos, and S. O'Neel (2010), Mapping the grounding zone of the Ross Ice Shelf, Antarctica, using ICESat laser altimetry, *Ann. Glaciol.*, *51*(55), 71–79.

Cheng, P., and C. Chaapel (2008), DigitalGlobe's WorldView-1 Satellite: Increased Image Collection Opportunities, *Geoinformatics*, (April/May), 16–21.

Christianson, K., P. Dutrieux, D. M. Holland, and I. R. Joughin (2016), Sensitivity of Pine Island Glacier to observed ocean forcing, *Nat. Geosci.*, *submitted*.

Church, J. A. et al. (2013), *Sea Level Change*, Climate Change 2013: The Physical Science Basis. Contribution of Working Group I to the Fifth Assessment Report of the Intergovernmental Panel on Climate Change.

Csatho, B. M., A. F. Schenk, C. J. van der Veen, G. Babonis, K. Duncan, S. Rezvanbehbahani, M. R. van den Broeke, S. B. Simonsen, S. Nagarajan, and J. H. van Angelen (2014), Laser altimetry reveals complex pattern of Greenland Ice Sheet dynamics, *Proc. Natl. Acad. Sci.*, 201411680, doi:10.1073/pnas.1411680112.

Czimczik, C. (2014), *Climate data Thule airport; Collaborative Research: Environmental changes alter the carbon cycle of High Arctic ecosystems: shifts in the ages and sources of CO2 and DOC, https://www.aoncadis.org/dataset/THU_climate.html*, ACADIS Gateway.

De Rydt, J., and G. H. Gudmundsson (2016), Coupled ice shelf-ocean modeling and complex grounding line retreat from a seabed ridge, *J. Geophys. Res. Earth Surf.*, doi:10.1002/2015JF003791.

De Rydt, J., P. R. Holland, P. Dutrieux, and A. Jenkins (2014), Geometric and oceanographic controls on melting beneath Pine Island Glacier, *J. Geophys. Res. Oceans*, *119*(4), 2420–2438, doi:10.1002/2013JC009513.

Dee, D. P. et al. (2011), The ERA-Interim reanalysis: configuration and performance of the data assimilation system, *Q. J. R. Meteorol. Soc.*, *137*(656), 553–597, doi:10.1002/qj.828.

Deilami, K., and M. Hashim (2011), Very high resolution optical satellites for DEM generation: a review, *Eur. J. Sci. Res.*, *49*(4), 542–554.

Depoorter, M. A., J. L. Bamber, J. A. Griggs, J. T. M. Lenaerts, S. R. M. Ligtenberg, M. R. van den Broeke, and G. Moholdt (2013), Calving fluxes and basal melt rates of Antarctic ice shelves, *Nature*, doi:10.1038/nature12567.

DigitalGlobe (2014), *Geolocation Accuracy of WorldView Products*, White Paper.

Dolloff, J., and R. Settergren (2010), An Assessment of WorldView-1 Positional Accuracy based on Fifty Contiguous Stereo Pairs of Imagery, *Photogramm. Eng. Remote Sens.*, *76*(8), 935–943, doi:10.14358/PERS.76.8.935.

Dolloff, J. T., and H. J. Theiss (2012), Temporal Correlation of Metadata Errors for Commercial Satellite Images: Representation and Effects of Stereo Extraction Accuracy, in *ISPRS XXII Congress*, pp. 215–223.

Drews, R. (2015), Evolution of ice-shelf channels in Antarctic ice shelves, *The Cryosphere*, *9*(3), 1169–1181, doi:10.5194/tc-9-1169-2015.

Drews, R., J. Brown, K. Matsuoka, E. Witrant, M. Philippe, B. Hubbard, and F. Pattyn (2016), Constraining variable density of ice shelves using wide-angle radar measurements, *The Cryosphere*, *10*(2), 811–823, doi:10.5194/tc-10-811-2016.

Dupont, T. K. (2005), Assessment of the importance of ice-shelf buttressing to ice-sheet flow, *Geophys. Res. Lett.*, *32*(4), doi:10.1029/2004GL022024.

Dutrieux, P., D. G. Vaughan, H. F. J. Corr, A. Jenkins, P. R. Holland, I. Joughin, and A. H. Fleming (2013), Pine Island glacier ice shelf melt distributed at kilometre scales, *The Cryosphere*, *7*(5), 1543–1555, doi:10.5194/tc-7-1543-2013.

Dutrieux, P., C. Stewart, A. Jenkins, K. W. Nicholls, H. F. J. Corr, E. Rignot, and K. Steffen (2014a), Basal terraces on melting ice shelves, *Geophys. Res. Lett.*, n/a-n/a, doi:10.1002/2014GL060618.

Dutrieux, P., J. De Rydt, A. Jenkins, P. R. Holland, H. K. Ha, S. H. Lee, E. J. Steig, Q. Ding, E. P. Abrahamsen, and M. Schroder (2014b), Strong Sensitivity of Pine Island Ice-Shelf Melting to Climatic Variability, *Science*, *343*(6167), 174–178, doi:10.1126/science.1244341.

Ettema, J., M. R. van den Broeke, E. van Meijgaard, W. J. van de Berg, J. L. Bamber, J. E. Box, and R. C. Bales (2009), Higher surface mass balance of the Greenland ice sheet revealed by high-resolution climate modeling, *Geophys. Res. Lett.*, *36*(12), doi:10.1029/2009GL038110.

Fassett, C. I. (2016), Topographic Observations of Mercury using High-Resolution Digital Terrain Models created with the Ames Stereo Pipeline, *Icarus*, in press.

Favier, L., G. Durand, S. L. Cornford, G. H. Gudmundsson, O. Gagliardini, F. Gillet-Chaulet, T. Zwinger, A. J. Payne, and A. M. Le Brocq (2014), Retreat of Pine Island Glacier controlled by marine ice-sheet instability, *Nat. Clim. Change*, doi:10.1038/nclimate2094.

Federal Geographic Data Committee (1998), *Geospatial Positioning Accuracy Standards Part 3: National Standard for Spatial Data Accuracy*.

Fretwell, P. et al. (2013), Bedmap2: improved ice bed, surface and thickness datasets for Antarctica, *The Cryosphere*, *7*(1), 375–393, doi:10.5194/tc-7-375-2013.

Gesch, D., M. Oimoen, S. Greenlee, C. Nelson, M. Steuck, and D. Tyler (2002), The National Elevation Dataset, *Photogramm. Eng. Remote Sens.*, *68*(1), 5–32.

Gladish, C. V., D. M. Holland, P. R. Holland, and S. F. Price (2012), Ice-shelf basal channels in a coupled ice/ocean model, *J. Glaciol.*, *58*(212), 1227–1244, doi:10.3189/2012JoG12J003.

Griggs, J. A., and J. L. Bamber (2011), Antarctic ice-shelf thickness from satellite radar altimetry, *J. Glaciol.*, *57*(203), 485.

Grodechi, J., and G. Dial (2003), Block adjustment of high-resolution satellite images described by rational polynomials, *Photogramm. Eng. Remote Sens.*, *69*(1), 59–68.

Groh, A., H. Ewert, M. Scheinert, M. Fritsche, A. Rülke, A. Richter, R. Rosenau, and R. Dietrich (2012), An investigation of Glacial Isostatic Adjustment over the Amundsen Sea sector, West Antarctica, *Glob. Planet. Change*, *98–99*, 45–53, doi:10.1016/j.gloplacha.2012.08.001.

Gudmundsson, G. H. (2003), Transmission of basal variability to a glacier surface, *J. Geophys. Res.*, *108*(B5), doi:10.1029/2002JB002107.

Gunter, B. C., O. Didova, R. E. M. Riva, S. R. M. Ligtenberg, J. T. M. Lenaerts, M. A. King, M. R. van den Broeke, and T. Urban (2014), Empirical estimation of present-day Antarctic glacial isostatic adjustment and ice mass change, *The Cryosphere*, *8*(2), 743–760, doi:10.5194/tc-8-743-2014.

Heid, T., and A. Kääb (2012), Evaluation of existing image matching methods for deriving glacier surface displacements globally from optical satellite imagery, *Remote Sens. Environ.*, *118*, 339–355, doi:10.1016/j.rse.2011.11.024.

Hofton, M. A., J. B. Blair, S. B. Luthcke, and D. L. Rabine (2008), Assessing the performance of 20–25 m footprint waveform lidar data collected in ICESat data corridors in Greenland, *Geophys. Res. Lett.*, *35*(24), doi:10.1029/2008GL035774.

Höhle, J., and M. Höhle (2009), Accuracy assessment of digital elevation models by means of robust statistical methods, *ISPRS J. Photogramm. Remote Sens.*, *64*(4), 398–406, doi:10.1016/j.isprsjprs.2009.02.003.

Holland, P. R., A. Jenkins, and D. M. Holland (2008), The Response of Ice Shelf Basal Melting to Variations in Ocean Temperature, *J. Clim.*, *21*(11), 2558–2572, doi:10.1175/2007JCLI1909.1.

Holland, P. R., H. F. J. Corr, H. D. Pritchard, D. G. Vaughan, R. J. Arthern, A. Jenkins, and M. Tedesco (2011), The air content of Larsen Ice Shelf, *Geophys. Res. Lett.*, *38*(10), n/a-n/a, doi:10.1029/2011GL047245.

Howat, I. M., A. Negrete, and B. E. Smith (2014a), The Greenland Ice Mapping Project (GIMP) land classification and surface elevation data sets, *The Cryosphere*, *8*(4), 1509–1518, doi:10.5194/tc-8-1509-2014.

Howat, I. M., A. Negrete, and B. E. Smith (2014b), The Greenland Ice Mapping Project (GIMP) land classification and surface elevation datasets, *Cryosphere Discuss.*, *8*(1), 453–478, doi:10.5194/tcd-8-453-2014.

Jacobs, S., A. Jenkins, H. Hellmer, C. Giulivi, F. Nitsche, B. Huber, and R. Guerrero (2012), The Amundsen Sea and the Antarctic Ice Sheet, *Oceanography*, *25*(3), 154–163, doi:10.5670/oceanog.2012.90.

Jacobs, S. S., H. H. Hellmer, and A. Jenkins (1996), Antarctic ice sheet melting in the Southeast Pacific, *Geophys. Res. Lett.*, *23*(9), 957–960.

Jacobs, S. S., A. Jenkins, C. F. Giulivi, and P. Dutrieux (2011), Stronger ocean circulation and increased melting under Pine Island Glacier ice shelf, *Nat. Geosci.*, *4*(8), 519–523, doi:10.1038/ngeo1188.

Jakobsson, M., J. B. Anderson, F. O. Nitsche, R. Gyllencreutz, A. E. Kirshner, N. Kirchner, M. O'Regan, R. Mohammad, and B. Eriksson (2012), Ice sheet retreat dynamics inferred from glacial morphology of the central Pine Island Bay Trough, West Antarctica, *Quat. Sci. Rev.*, *38*, 1–10, doi:10.1016/j.quascirev.2011.12.017.

Jenkins, A., D. G. Vaughan, S. S. Jacobs, H. H. Hellmer, and J. Keys R. (1997), Glaciological and oceanographic evidence of high melt rates beneath Pine Island Glacier, West Antarctica, *J. Glaciol.*, *43*(143), 114–121.

Jenkins, A., H. F. Corr, K. W. Nicholls, C. L. Stewart, and C. S. Doake (2006), Interactions between ice and ocean observed with phase-sensitive radar near an Antarctic ice-shelf grounding line, *J. Glaciol.*, *52*(178), 325–346.

Jenkins, A., P. Dutrieux, S. S. Jacobs, S. D. McPhail, J. R. Perrett, A. T. Webb, and D. White (2010), Observations beneath Pine Island Glacier in West Antarctica and implications for its retreat, *Nat. Geosci.*, *3*(7), 468–472, doi:10.1038/ngeo890.

Jeong, S., I. M. Howat, and J. Bassis (2016), Accelerated ice shelf rifting and retreat at Pine Island Glacier, West Antarctica, , *Nature Geoscience*(submitted).

Joughin, I. (2002), Ice-sheet velocity mapping: a combined interferometric and speckle-tracking approach, *Ann. Glaciol.*, *34*(1), 195–201.

Joughin, I., and R. B. Alley (2011), Stability of the West Antarctic ice sheet in a warming world, *Nat. Geosci.*, *4*, 506–513, doi:10.1038/ngeo1194.

Joughin, I., and L. Padman (2003), Melting and freezing beneath Filchner-Ronne Ice Shelf, Antarctica, *Geophys Res Lett*, *30*(9), 1477, doi:10.1029/2003GL016941.

Joughin, I., E. Rignot, C. E. Rosanova, B. K. Lucchitta, and J. Bohlander (2003), Timing of Recent Accelerations of Pine Island Glacier, Antarctica, *Geophys. Res. Lett.*, *30*(13), doi:10.1029/2003GL017609.

Joughin, I., S. Tulaczyk, J. L. Bamber, D. Blankenship, J. W. Holt, T. Scambos, and D. G. Vaughan (2009), Basal conditions for Pine Island and Thwaites Glaciers, West Antarctica, determined using satellite and airborne data, *J. Glaciol.*, *55*(190), 245–257.

Joughin, I., B. E. Smith, I. M. Howat, T. Scambos, and T. Moon (2010a), Greenland flow variability from ice-sheet-wide velocity mapping, *J. Glaciol.*, *56*(197), 415–430.

Joughin, I., B. E. Smith, and D. M. Holland (2010b), Sensitivity of 21st century sea level to ocean-induced thinning of Pine Island Glacier, Antarctica, *Geophys. Res. Lett.*, *37*(20), n/a-n/a, doi:10.1029/2010GL044819.

Joughin, I., R. B. Alley, and D. M. Holland (2012), Ice-sheet response to oceanic forcing, *Science*, *338*(6111), 1172–1176.

Joughin, I., B. E. Smith, D. E. Shean, and D. Floricioiu (2014a), Brief Communication: Further summer speedup of Jakobshavn Isbræ, *The Cryosphere*, *8*(1), 209–214, doi:10.5194/tc-8-209-2014.

Joughin, I., B. E. Smith, and B. Medley (2014b), Marine Ice Sheet Collapse Potentially Under Way for the Thwaites Glacier Basin, West Antarctica, *Science*, *344*(6185), 735–738, doi:10.1126/science.1249055.

Joughin, I. R., D. E. Shean, B. E. Smith, and P. Dutrieux (2016), Short-term Grounding Line Variability and Subglacial Lake Drainage on Pine Island Glacier, Antarctica, *Prep*.

Kääb, A., and S. Leprince (2014), Motion detection using near-simultaneous satellite acquisitions, *Remote Sens. Environ.*, *154*, 164–179, doi:10.1016/j.rse.2014.08.015.

Kehrl, L., I. R. Joughin, B. E. Smith, D. E. Shean, D. Floricioiu, and L. Krieger (2016), Seasonal to multiyear variability in ice-front position, glacier speed, and surface elevation at Helheim and Kangerdlugssuaq Glaciers, SE Greenland, from 2008-2016, *J. Geophys. Res. Earth Surf.*, *in prep*.

Kim, I., D. Hahm, T. S. Rhee, T. W. Kim, C.-S. Kim, and S. Lee (2016), The distribution of glacial meltwater in the Amundsen Sea, Antarctica, revealed by dissolved helium and neon, *J. Geophys. Res. Oceans*, n/a-n/a, doi:10.1002/2015JC011211.

Kirshner, A. E., J. B. Anderson, M. Jakobsson, M. O'Regan, W. Majewski, and F. O. Nitsche (2012), Post-LGM deglaciation in Pine Island Bay, West Antarctica, *Quat. Sci. Rev.*, *38*, 11–26, doi:10.1016/j.quascirev.2012.01.017.

Kobs, S., D. M. Holland, V. Zagorodnov, A. Stern, and S. W. Tyler (2014), Novel monitoring of Antarctic ice shelf basal melting using a fiber-optic distributed temperature sensing mooring: Novel monitoring of Antarctic ice shelf, *Geophys. Res. Lett.*, n/a-n/a, doi:10.1002/2014GL061155.

Korona, J., E. Berthier, M. Bernard, F. Rémy, and E. Thouvenot (2009), SPIRIT. SPOT 5 stereoscopic survey of polar ice: Reference images and topographies during the fourth international polar year (2007-2009), *ISPRS J. Photogramm. Remote Sens.*, *64*(2), 204–212.

Krabill, W. B., W. Abdalati, E. B. Frederick, S. S. Manizade, C. F. Martin, J. G. Sonntag, R. N. Swift, R. H. Thomas, and J. G. Yungel (2002), Aircraft laser altimetry measurement of elevation changes of the Greenland ice sheet: Technique and accuracy assessment, *J. Geodyn.*, *34*(3), 357–376.

Langley, K., A. von Deschwanden, J. Kohler, A. Sinisalo, K. Matsuoka, T. Hattermann, A. Humbert, O. A. Nøst, and E. Isaksson (2014a), Complex network of channels beneath an Antarctic ice shelf, *Geophys. Res. Lett.*, n/a-n/a, doi:10.1002/2013GL058947.

Langley, K., J. Kohler, A. Sinisalo, M. J. Øyan, S. E. Hamran, T. Hattermann, K. Matsuoka, O. A. Nøst, and E. Isaksson (2014b), Low melt rates with seasonal variability at the base of Fimbul Ice Shelf, East Antarctica, revealed by in situ interferometric radar measurements, *Geophys. Res. Lett.*, n/a-n/a, doi:10.1002/2014GL061782.

Larson, K. M., J. Wahr, and P. Kuipers Munneke (2015), Constraints on snow accumulation and firn density in Greenland using GPS receivers, *J. Glaciol.*, *61*(225), 101–114, doi:10.3189/2015JoG14J130.

Lenaerts, J. T. M., M. R. van den Broeke, W. J. van de Berg, E. van Meijgaard, and P. Kuipers Munneke (2012), A new, high-resolution surface mass balance map of Antarctica (1979-2010) based on regional atmospheric climate modeling, *Geophys. Res. Lett.*, *39*(4), n/a-n/a, doi:10.1029/2011GL050713.

Leprince, S., P. Muse, and J.-P. Avouac (2008), In-Flight CCD Distortion Calibration for Pushbroom Satellites Based on Subpixel Correlation, *IEEE Trans. Geosci. Remote Sens.*, *46*, 2675–2683, doi:10.1109/TGRS.2008.918649.

Ligtenberg, S. R. M., M. M. Helsen, and M. R. van den Broeke (2011), An improved semi-empirical model for the densification of Antarctic firn, *The Cryosphere*, *5*(4), 809–819, doi:10.5194/tc-5-809-2011.

Ligtenberg, S. R. M., B. Medley, M. R. Van Den Broeke, and P. K. Munneke (2015), Antarctic firn compaction rates from repeat-track airborne radar data: II. Firn model evaluation, *Ann. Glaciol.*, *56*(70), 167–174, doi:10.3189/2015AoG70A204.

Little, C. M., A. Gnanadesikan, and M. Oppenheimer (2009), How ice shelf morphology controls basal melting, *J. Geophys. Res.*, *114*(C12), doi:10.1029/2008JC005197.

Logan, L., G. Catania, L. Lavier, and E. Choi (2013), A novel method for predicting fracture in floating ice, *J. Glaciol.*, *59*(216), 750–758, doi:10.3189/2013JoG12J210.

Marsh, O. J., H. A. Fricker, M. R. Siegfried, K. Christianson, K. W. Nicholls, H. F. J. Corr, and G. Catania (2015), High basal melting forming a channel at the grounding line of Ross Ice Shelf, Antarctica, *Geophys. Res. Lett.*, n/a-n/a, doi:10.1002/2015GL066612.

Martin, C. F., W. B. Krabill, S. S. Manizade, R. L. Russell, J. G. Sonntag, R. N. Swift, and J. K. Yungel (2012), *Airborne topographic mapper calibration procedures and accuracy assessment*, Technical Memorandum, National Aeronautics and Space Administration, Goddard Space Flight Center.

Mattson, S., A. Boyd, R. L. Kirk, D. A. Cook, and E. Howington-Kraus (2009), HiJACK: Correcting spacecraft jitter in HiRISE images of Mars, in *European Planetary Science Congress Abstracts*, vol. 4, p. EPSC2009-604-1.

McEwen, A. S. et al. (2007), Mars Reconnaissance Orbiter's High Resolution Imaging Science Experiment (HiRISE), *J. Geophys. Res.*, *112*(E5), doi:10.1029/2005JE002605.

Medley, B. et al. (2014), Constraining the recent mass balance of Pine Island and Thwaites glaciers, West Antarctica, with airborne observations of snow accumulation, *The Cryosphere*, *8*(4), 1375–1392, doi:10.5194/tc-8-1375-2014.

Medley, B., S. R. M. Ligtenberg, I. Joughin, M. R. Van Den Broeke, S. Gogineni, and S. Nowicki (2015), Antarctic firn compaction rates from repeat-track airborne radar data: I. Methods, *Ann. Glaciol.*, *56*(70), 155–166, doi:10.3189/2015AoG70A203.

Millgate, T., P. R. Holland, A. Jenkins, and H. L. Johnson (2013), The effect of basal channels on oceanic ice-shelf melting, *J. Geophys. Res. Oceans*, n/a-n/a, doi:10.1002/2013JC009402.

Moholdt, G., L. Padman, and H. A. Fricker (2014), Basal mass budget of Ross and Filchner-Ronne ice shelves, Antarctica, derived from Lagrangian analysis of ICESat altimetry: Ice shelf basal melting from altimetry, *J. Geophys. Res. Earth Surf.*, n/a-n/a, doi:10.1002/2014JF003171.

Moon, T., I. Joughin, B. Smith, and I. Howat (2012), 21st-Century Evolution of Greenland Outlet Glacier Velocities, *Science*, *336*(6081), 576–578, doi:10.1126/science.1219985.

Moratto, Z. M., M. J. Broxton, R. A. Beyer, M. Lundy, and K. Husmann (2010), Ames Stereo Pipeline, NASA's Open Source Automated Stereogrammetry Software, in *41st Lunar and Planetary Science Conference Abstracts*, vol. 41, p. 2364.

Morlighem, M., E. Rignot, H. Seroussi, E. Larour, H. B. Dhia, and D. Aubry (2011), A mass conservation approach for mapping glacier ice thickness, *Geophys. Res. Lett.*, *38*(19), L19503.

Mouginot, J., E. Rignot, and B. Scheuchl (2014), Sustained increase in ice discharge from the Amundsen Sea Embayment, West Antarctica, from 1973 to 2013, *Geophys. Res. Lett.*, *41*(5), 1576–1584, doi:10.1002/2013GL059069.

Müller, J., I. Gärtner-Roer, P. Thee, and C. Ginzler (2014), Accuracy assessment of airborne photogrammetrically derived high-resolution digital elevation models in a high mountain environment, *ISPRS J. Photogramm. Remote Sens.*, *98*, 58–69, doi:10.1016/j.isprsjprs.2014.09.015.

Muto, A., L. E. Peters, K. Gohl, I. Sasgen, R. B. Alley, S. Anandakrishnan, and K. L. Riverman (2016), Subglacial bathymetry and sediment distribution beneath Pine Island Glacier ice shelf modeled using aerogravity and in situ geophysical data: New results, *Earth Planet. Sci. Lett.*, *433*, 63–75, doi:10.1016/j.epsl.2015.10.037.

Nefian, A. V., K. Husmann, M. Broxton, V. To, M. Lundy, and M. D. Hancher (2009), A Bayesian formulation for sub-pixel refinement in stereo orbital imagery, in *2009 16th IEEE International Conference on Image Processing (ICIP)*, pp. 2361–2364.

Neigh, C. S., J. G. Masek, and J. E. Nickeson (2013), High-Resolution Satellite Data Open for Government Research, *Eos Trans. Am. Geophys. Union*, *94*(13), 121–123.

Noh, M.-J., and I. M. Howat (2014), Automated Coregistration of Repeat Digital Elevation Models for Surface Elevation Change Measurement Using Geometric Constraints, *IEEE Trans. Geosci. Remote Sens.*, *52*(4), 2247–2260, doi:10.1109/TGRS.2013.2258928.

Nuth, C., and A. Kääb (2011), Co-registration and bias corrections of satellite elevation data sets for quantifying glacier thickness change, *The Cryosphere*, *5*(1), 271–290, doi:10.5194/tc-5-271-2011.

Padman, L., H. A. Fricker, R. Coleman, S. Howard, and L. Erofeeva (2002), A new tide model for the Antarctic ice shelves and seas, *Ann. Glaciol.*, *34*(1), 247–254.

Padman, L., M. King, D. Goring, H. Corr, and R. Coleman (2003), Ice-shelf elevation changes due to atmospheric pressure variations, *J. Glaciol.*, *49*(167), 521–526, doi:10.3189/172756503781830386.

Paolo, F. S., H. A. Fricker, and L. Padman (2015), Volume loss from Antarctic ice shelves is accelerating, *Science*, *348*(6232), 327–331, doi:10.1126/science.aaa0940.

Park, J. W., N. Gourmelen, A. Shepherd, S. W. Kim, D. G. Vaughan, and D. J. Wingham (2013), Sustained retreat of the Pine Island Glacier, *Geophys. Res. Lett.*, n/a-n/a, doi:10.1002/grl.50379.

Pavlis, N. K., S. A. Holmes, S. C. Kenyon, and J. K. Factor (2012), The development and evaluation of the Earth Gravitational Model 2008 (EGM2008), *J. Geophys. Res.*, *117*(B4), doi:10.1029/2011JB008916.

Payne, A. J., P. R. Holland, A. P. Shepherd, I. C. Rutt, A. Jenkins, and I. Joughin (2007), Numerical modeling of ocean-ice interactions under Pine Island Bay's ice shelf, *J. Geophys. Res.*, *112*(C10), doi:10.1029/2006JC003733.

Pomerleau, F., F. Colas, R. Siegwart, and S. Magnenat (2013), Comparing ICP variants on real-world data sets: Open-source library and experimental protocol, *Auton. Robots*, *34*(3), 133–148, doi:10.1007/s10514-013-9327-2.

Pope, A., T. A. Scambos, M. Moussavi, M. Tedesco, M. Willis, D. Shean, and S. Grigsby (2015), Estimating supraglacial lake depth in western Greenland using Landsat 8 and comparison with other multispectral methods, *The Cryosphere*, *9*(3), 3257–3292, doi:10.5194/tcd-9-3257-2015.

Pritchard, H. D., R. J. Arthern, D. G. Vaughan, and L. A. Edwards (2009), Extensive dynamic thinning on the margins of the Greenland and Antarctic ice sheets, *Nature*, *461*(7266), 971–975, doi:10.1038/nature08471.

Pritchard, H. D., S. R. M. Ligtenberg, H. A. Fricker, D. G. Vaughan, M. R. van den Broeke, and L. Padman (2012), Antarctic ice-sheet loss driven by basal melting of ice shelves, *Nature*, *484*(7395), 502–505, doi:10.1038/nature10968.

Re, C., G. Cremonese, E. Dall'Asta, G. Forlani, G. Naletto, and R. Roncella (2012), Performance evaluation of DTM area-based matching reconstruction of Moon and Mars, in *Image and Signal Processing for Remote Sensing XVIII, Proc. of SPIE*, vol. 8573, edited by L. Bruzzone, p. 85370V.

Rietbroek, R., S.-E. Brunnabend, J. Kusche, J. Schröter, and C. Dahle (2016), Revisiting the contemporary sea-level budget on global and regional scales, *Proc. Natl. Acad. Sci.*, 201519132.

Rignot, E. (2008), Changes in West Antarctic ice stream dynamics observed with ALOS PALSAR data, *Geophys Res Lett*, *35*(12), L12505, doi:10.1029/2008GL033365.

Rignot, E., and S. Jacobs (2002), Rapid Bottom Melting Widespread near Antarctic Ice Sheet Grounding Lines, *Science*, *296*(5575), 2020–2023, doi:10.1126/science.1070942.

Rignot, E., and K. Steffen (2008), Channelized bottom melting and stability of floating ice shelves, *Geophys. Res. Lett.*, *35*(2), doi:10.1029/2007GL031765.

Rignot, E., G. Casassa, P. Gogineni, W. Krabill, A. Rivera, and R. Thomas (2004), Accelerated ice discharge from the Antarctic Peninsula following the collapse of Larsen B ice shelf, *Geophys Res Lett*, *31*(18), L18401.

Rignot, E., J. Mouginot, and B. Scheuchl (2011a), Antarctic grounding line mapping from differential satellite radar interferometry, *Geophys Res Lett*, *38*, L10504.

Rignot, E., J. Mouginot, and B. Scheuchl (2011b), Ice Flow of the Antarctic Ice Sheet, *Science*, *333*(6048), 1427–1430, doi:10.1126/science.1208336.

Rignot, E., S. Jacobs, J. Mouginot, and B. Scheuchl (2013), Ice-Shelf Melting Around Antarctica, *Science*, *341*(6143), 266–270, doi:10.1126/science.1235798.

Rignot, E., J. Mouginot, M. Morlighem, H. Seroussi, and B. Scheuchl (2014), Widespread, rapid grounding line retreat of Pine Island, Thwaites, Smith, and Kohler glaciers, West Antarctica, from 1992 to 2011, *Geophys. Res. Lett.*, *41*(10), 3502–3509, doi:10.1002/2014GL060140.

Rignot, E., I. Fenty, Y. Xu, C. Cai, I. Velicogna, C. ó Cofaigh, J. A. Dowdeswell, W. Weinrebe, G. Catania, and D. Duncan (2016), Bathymetry data reveal glaciers vulnerable to ice-ocean interaction in Uummannaq and Vaigat glacial fjords, West Greenland, *Geophys. Res. Lett.*, n/a-n/a, doi:10.1002/2016GL067832.

Scambos, T. A. (2004), Glacier acceleration and thinning after ice shelf collapse in the Larsen B embayment, Antarctica, *Geophys. Res. Lett.*, *31*(18), doi:10.1029/2004GL020670.

Schenk, T., and B. Csatho (2012), A New Methodology for Detecting Ice Sheet Surface Elevation Changes From Laser Altimetry Data, *IEEE Trans. Geosci. Remote Sens.*, *50*(9), 3302–3316, doi:10.1109/TGRS.2011.2182357.

Schmidtko, S., K. J. Heywood, A. F. Thompson, and S. Aoki (2014), Multidecadal warming of Antarctic waters, *Science*, *346*(6214), 1227–1231, doi:10.1126/science.1256117.

Schodlok, M. P., D. Menemenlis, E. Rignot, and M. Studinger (2012), Sensitivity of the ice-shelf/ocean system to the sub-ice-shelf cavity shape measured by NASA IceBridge in Pine Island Glacier, West Antarctica, *Ann. Glaciol.*, *53*(60), 156–162, doi:10.3189/2012AoG60A073.

Schoof, C. (2007), Ice sheet grounding line dynamics: Steady states, stability, and hysteresis, *J Geophys Res*, *112*(10.1029).

Schutz, B. E., H. J. Zwally, C. A. Shuman, D. Hancock, and J. P. DiMarzio (2005), Overview of the ICESat Mission, *Geophys. Res. Lett.*, *32*(21), doi:10.1029/2005GL024009.

Scott, J. B., A. M. Smith, R. G. Bingham, and D. G. Vaughan (2010), Crevasses triggered on Pine Island Glacier, West Antarctica, by drilling through an exceptional melt layer, *Ann. Glaciol.*, *51*(55), 65–70.

Sergienko, O. V. (2013), Basal channels on ice shelves, *J. Geophys. Res. Earth Surf.*, *118*(3), 1342–1355, doi:10.1002/jgrf.20105.

Seroussi, H., M. Morlighem, E. Rignot, J. Mouginot, E. Larour, M. Schodlok, and A. Khazendar (2014), Sensitivity of the dynamics of Pine Island Glacier, West Antarctica, to climate forcing for the next 50 years, *The Cryosphere*, *8*(5), 1699–1710, doi:10.5194/tc-8-1699-2014.

Shabtaie, S., and C. R. Bentley (1982), Tabular icebergs: implications from geophysical studies of ice shelves, *J. Glaciol.*, *28*(100).

Shean, D., I. Joughin, D. Floricioiu, B. Smith, Z. Moratto, O. Alexandrov, P. Morin, and C. Porter (2014), A 2008-2013 Time Series of TanDEM-X & WorldView-1/2 Stereo DEMs for Jakobshavn Isbrae, Greenland, in *International Geoscience and Remote Sensing Symposium: Technical Program*, p. 3553.

Shean, D. E., J. Fahle, M. C. Malin, L. J. Edwards, and L. Posiolova (2011), MRO CTX Stereo Image Processing and Preliminary DEM Quality Assessment, in *42nd Lunar and Planetary Science Conference Abstracts*, vol. 42, p. 2646.

Shean, D. E., O. Alexandrov, Z. M. Moratto, B. E. Smith, I. R. Joughin, C. Porter, and P. Morin (2016a), An automated, open-source pipeline for mass production of digital elevation models (DEMs) from very-high-resolution commercial stereo satellite imagery, *ISPRS J. Photogramm. Remote Sens.*, *116*, 101–117, doi:10.1016/j.isprsjprs.2016.03.012.

Shean, D. E., I. R. Joughin, B. E. Smith, P. Dutrieux, and E. Berthier (2016b), Ice shelf melt and inland response of the Pine Island Glacier, West Antarctica from a 2008-2015 high-resolution DEM record, , *in prep*.

Shean, D. E., K. Christianson, K. M. Larson, S. R. M. Ligtenberg, I. R. Joughin, and B. E. Smith (2016c), In-situ GPS measurements of surface mass balance, firn compaction, and basal melt rates for the Pine Island Glacer Ice Shelf, Antarctica, , *in prep*.

Shean, D. E., I. R. Joughin, B. E. Smith, and D. Floricioiu (2016d), Seasonal and interannual evolution of Jakobshavn Isbrae, Greenland from a high-resolution DEM and Velocity time series, , *in prep*.

Shepherd, A., D. Wingham, and E. Rignot (2004), Warm ocean is eroding West Antarctic ice sheet, *Geophys Res Lett*, *31*(23), L23404.

Shepherd, A., D. Wingham, D. Wallis, K. Giles, S. Laxon, and A. V. Sundal (2010), Recent loss of floating ice and the consequent sea level contribution, *Geophys. Res. Lett.*, *37*(13), n/a-n/a, doi:10.1029/2010GL042496.

Shepherd, A. et al. (2012), A Reconciled Estimate of Ice-Sheet Mass Balance, *Science*, *338*(6111), 1183–1189, doi:10.1126/science.1228102.

Shimizu, M., and M. Okutomi (2002), Precise subpixel estimation on area-based matching, *Syst. Comput. Jpn.*, *33*(7), 1409–1418.

Siegfried, M. R., R. L. Hawley, and J. F. Burkhart (2011), High-Resolution Ground-Based GPS Measurements Show Intercampaign Bias in ICESat Elevation Data Near Summit, Greenland, *IEEE Trans. Geosci. Remote Sens.*, *49*(6), 3393–3400, doi:10.1109/TGRS.2011.2127483.

Stanton, T. P., W. J. Shaw, M. Truffer, H. F. J. Corr, L. E. Peters, K. L. Riverman, R. Bindschadler, D. M. Holland, and S. Anandakrishnan (2013), Channelized Ice Melting in the Ocean Boundary Layer Beneath Pine Island Glacier, Antarctica, *Science*, *341*(6151), 1236–1239, doi:10.1126/science.1239373.

Steig, E. J., Q. Ding, D. S. Battisti, and A. Jenkins (2012), Tropical forcing of Circumpolar Deep Water Inflow and outlet glacier thinning in the Amundsen Sea Embayment, West Antarctica, *Ann. Glaciol.*, *53*(60), 19–28, doi:10.3189/2012AoG60A110.

Stein, A. N., A. Huertas, and L. Matthies (2006), Attenuating stereo pixel-locking via affine window adaptation, in *Proceedings IEEE International Conference on Robotics and Automation*, pp. 914–921.

Stevens, L. A., M. D. Behn, J. J. McGuire, S. B. Das, I. Joughin, T. Herring, D. E. Shean, and M. A. King (2015), Greenland supraglacial lake drainages triggered by hydrologically induced basal slip, *Nature*, *522*(7554), 73–76, doi:10.1038/nature14480.

St-Laurent, P., J. M. Klinck, and M. S. Dinniman (2015), Impact of local winter cooling on the melt of Pine Island Glacier, Antarctica, *J. Geophys. Res. Oceans*, n/a-n/a, doi:10.1002/2015JC010709.

Sutterley, T. C., I. Velicogna, E. Rignot, J. Mouginot, T. Flament, M. R. van den Broeke, J. M. van Wessem, and C. H. Reijmer (2014), Mass loss of the Amundsen Sea Embayment of West Antarctica from four independent techniques, *Geophys. Res. Lett.*, *41*(23), 8421–8428, doi:10.1002/2014GL061940.

Thoma, M., A. Jenkins, D. Holland, and S. Jacobs (2008), Modelling circumpolar deep water intrusions on the Amundsen Sea continental shelf, Antarctica, *Geophys. Res. Lett.*, *35*(18).

Thomas, R., E. Rignot, P. Kanagaratnam, W. Krabill, and G. Casassa (2004), Force-perturbation analysis of Pine Island Glacier, Antarctica, suggests cause for recent acceleration, *Ann. Glaciol.*, *39*(1), 133–138.

Updike, T., and C. Comp (2010), *Radiometric Use of WorldView-2 Imagery*, DigitalGlobe Technical Note.

Van Meijgaard, E., L. H. Van Ulft, W. J. Van de Berg, F. C. Bosveld, B. Van den Hurk, G. Lenderink, and A. P. Siebesma (2008), *The KNMI regional atmospheric climate model RACMO version 2.1*, Koninklijk Nederlands Meteorologisch Instituut.

Van Wessem, J. M. et al. (2014), Improved representation of East Antarctic surface mass balance in a regional atmospheric climate model, *J. Glaciol.*, *60*(222), 761–770, doi:10.3189/2014JoG14J051.

van Wessem, J. M. et al. (2016), The modelled surface mass balance of the Antarctic Peninsula at 5.5 km horizontal resolution, *The Cryosphere*, *10*(1), 271–285, doi:10.5194/tc-10-271-2016.

Vaughan, D. G., H. F. J. Corr, R. A. Bindschadler, P. Dutrieux, G. H. Gudmundsson, A. Jenkins, T. Newman, P. Vornberger, and D. J. Wingham (2012), Subglacial melt channels and fracture in the floating part of Pine Island Glacier, Antarctica, *J. Geophys. Res.*, *117*(F3), doi:10.1029/2012JF002360.

Vaughan, D. G. et al. (2014), Observations: Cryosphere, in *Climate Change 2013: The Physical Science Basis. Contribution of Working Group I to the Fifth Assessment Report of the Intergovernmental Panel on Climate Change*, edited by Intergovernmental Panel on Climate Change, pp. 317–382, Cambridge University Press, Cambridge.

Velicogna, I., T. C. Sutterley, and M. R. van den Broeke (2014), Regional acceleration in ice mass loss from Greenland and Antarctica using GRACE time-variable gravity data, *Geophys. Res. Lett.*, n/a-n/a, doi:10.1002/2014GL061052.

Walker, R. T., T. K. Dupont, B. R. Parizek, and R. B. Alley (2008), Effects of basal-melting distribution on the retreat of ice-shelf grounding lines, *Geophys Res Lett*, *35*(17), L17503, doi:10.1029/2008GL034947.

Watters, W. A., L. M. Geiger, M. Fendrock, and R. Gibson (2015), Morphometry of small recent impact craters on Mars: Size and terrain dependence, short-term modification, *J. Geophys. Res. Planets*, *120*(2), 226–254, doi:10.1002/2014JE004630.

Weertman, J. (1974), Stability of the junction of an ice sheet and an ice shelf, *J. Glaciol.*, *13*, 3–11.

Willis, M. J., B. G. Herried, M. G. Bevis, and R. E. Bell (2015), Recharge of a subglacial lake by surface meltwater in northeast Greenland, *Nature*, doi:10.1038/nature14116.

Zwally, H. J., B. Schutz, W. Abdalati, J. Abshire, C. Bentley, A. Brenner, J. Bufton, J. Dezio, D. Hancock, and D. Harding (2002), ICESat's laser measurements of polar ice, atmosphere, ocean, and land, *J. Geodyn.*, *34*(3), 405–445.

APPENDIX A

FIRN AIR CONTENT

Altimetry and stereo DEM data measure surface elevation, which can be used to estimate the thickness of floating ice if the ice is in hydrostatic equilibrium. To make such estimates, we need to account for the reduced density of air in the firn column [*Shabtaie and Bentley*, 1982; *Pritchard et al.*, 2012]. Firn density measurements are rare, but it is possible to estimate the total air content of the firn column from SMB/firn model output [e.g., *Ligtenberg et al.*, 2011] and/or a combination of altimetry and ice-penetrating radar data [*Holland et al.*, 2011]. This firn air correction provides an estimate of expected surface elevation for thickness with bulk density of ice, which is more useful for estimates of ice discharge and mass change.

This correction is irrelevant for surface elevation change (Dh/Dt) measurements, assuming that spatial/temporal variability in the firn air content is small for the advection length scales. However, it must be considered when computing ice thickness for mass budget analysis and the flux divergence term in the mass conservation equations.

Firn air content estimated from RACMO SMB and FDM dynamic firn model [*Ligtenberg et al.*, 2011] is ~18-21 m over the PIG shelf. While the RACMO grid cell spacing is coarse (27 km), interpolated results suggest a spatial pattern with increased firn air thickness over the South shelf and decreased thickness over the North shelf. Previously reported estimates of firn air content for the PIG shelf range from ~10-14 m [*Bindschadler et al.*, 2011]. To help resolve the uncertainty of these estimates, we attempt to constrain the spatial distribution of firn air content using airborne radar data.

All available Center for Remote Sensing of Ice Sheets (CReSIS) Multichannel Coherent Radar Depth Sounder (MCoRDS) level 2 (L2) ice thickness data were compiled for PIG. This includes data from 2002, 2004, 2009, 2010, 2011, 2012 and 2014 flights, with excellent coverage over the shelf in 2009. These points were linked with contemporaneous Airborne Topographic Mapper (ATM) LiDAR measurements of surface elevation. All ATM elevations were tide-corrected and converted to orthometric height above the EGM2008 geoid.

We compute freeboard thickness from ATM elevations with no firn air correction, assuming hydrostatic equilibrium for a column of ice with density 917 kg/m^3 and ocean water with density

1028 kg/m^3. These freeboard thickness estimates appear much larger than CReSIS L2 thickness estimates over the shelf.

The CReSIS L2 thickness estimates are derived from the two-way travel time of a manually-identified reflector assuming a uniform dielectric constant of 3.15 for ice. We convert this thickness estimate (H) to original two-way travel time:

$$T = \frac{2H}{v_i} \tag{A.1}$$

where v_i is the corresponding radar velocity in ice (0.169 m/ns). We use the model of Holland et al. [2011] to solve for the firn air content given the two-way travel time T and measured ATM surface elevation h, assuming hydrostatic equilibrium and no liquid water in the firn:

$$A = \left[\frac{\frac{cT}{2} + n_i \left(\frac{\rho_w}{\rho_i - \rho_w} \right) h}{n_a + n_i \left(\frac{\rho_w - \rho_a}{\rho_i - \rho_w} \right)} \right] \tag{A.2}$$

where ρ_a is the density of air (2.0 kg/m^3), c is the speed of light (3x10^8 m/s), n_i is the refractive index of ice (1.78) and n_a is the refractive index of air (1.0).

The assumption of a dry firn is reasonable for relative timing of radar measurements (typically October–November), when there should be no surface melting at PIG. We mask points where computed floatation thickness is negative, the CReSIS thickness exceeds ATM floatation thickness with no firn air correction, or the computed firn air content is >20 m. This effectively excludes points over grounded ice and questionable radar reflector picks (e.g. tops of basal crevasses). Basal crevasses with heights of ~20-200 m and widths of ~50-200 m are observed near the apices of channels in dense airborne radar data [*Vaughan et al.*, 2012] and autonomous submersible sonar data [*Dutrieux et al.*, 2014a] over the PIG shelf.

We note spatial variability in apparent firn air content along individual flightlines that cross alternating surface ridges and troughs. This spatial variability could be related to differences in firn column thickness, firn column density, and/or density differences associated with surface/basal crevasses. High-resolution images show that snow and firn are not evenly distributed across the shelf, with wind-blown snow within troughs, and exposed ice with dense surface crevasses over ridge surfaces. The air content within these crevasses is significant – likely on the order of ~10 m. In addition, firn density is likely ~5% greater in troughs than adjacent surfaces

[*Shabtaie and Bentley*, 1982; *Drews et al.*, 2016]. On some level, the physical causes for short-wavelength spatial variability in firn air content are irrelevant, as long as it is accurately estimated. We computed median firn air of filtered points within 256-m bins and applied a rolling 21-pixel (~5.3 km) median filter and subsequent 11-pixel (~2.8 km) Gaussian smoothing filter. The size of these filters was chosen to smooth ridge/trough variability and interpolate over ~2-3 flighlines, providing a continuous, smoothed grid with reduced spatial resolution.

The results show that firn air content over the main shelf is in typically ~10-12 m, with reduced values over thinner shear margins. Firn air content appears significantly higher over the south shelf (~16 m) and the periphery of the north shelf. Significantly lower values are observed near the grounding line of the north shelf (~2-4 m), which is consistent with optical image data that show refrozen meltwater ponds in these locations.

HYDROSTATIC EQUILIBRIUM

The assumption of hydrostatic equilibrium is invalid for grounded ice, and within a few ice thicknesses of grounded areas [*Brunt et al.*, 2010; *Griggs and Bamber*, 2011]. It is also potentially invalid for large thickness gradients over small distances (e.g. closely-spaced ridges, troughs), where lateral bridging stresses become more important. Surface elevations over a ridge supported by adjacent ice will appear higher, resulting in an overestimate of freeboard thickness compared to true thickness; the opposite is true for troughs [*Shabtaie and Bentley*, 1982; *Vaughan et al.*, 2012]. Experiments with a high-resolution ice-flow model show that wider channels tend to be near equilibrium, with increasing bridging stresses for narrow channels [*Drews*, 2015].

The assumption of hydrostatic equilibrium is also invalid near any ephemeral grounded spots over the shelf. Ephemeral regrounding of keels will yield increased surface elevations and larger apparent freeboard thickness values. This may also lead to localized ice deformation and non-zero vertical strain rates that are inconsistent with the assumption that surface velocity equals the column-average velocity.

Previous studies using airborne ice-penetrating radar data have noted that most of the PIG shelf is generally near hydrostatic equilibrium [*Bindschadler et al.*, 2011; *Vaughan et al.*, 2012]. Detailed studies with ground-based radar, however, reveal shelf-bottom channels and other features that are not apparent in surface topography [*Vaughan et al.*, 2012; *Langley et al.*, 2014a]. Basal crevasses of varying size are likely present over the PIG shelf [*Vaughan et al.*, 2012; *Logan et al.*, 2013;

Bassis and Ma, 2015]. These crevasses could be filled with relatively dense seawater or relatively buoyant melt water, which would tend to decrease and increase observed surface elevations, respectively. In addition, basal crevasses should widen over time due to ductile failure (necking) [*Bassis and Ma*, 2015], which would bring surface elevations closer to hydrostatic equilibrium.

We note that freeboard thickness estimates are sensitive to systematic errors in geoid and mean dynamic topography corrections, which are poorly constrained near the Antarctic-coastline. More importantly, freeboard thickness estimates are highly sensitive to the choice of ice and ocean density, which must be included in uncertainty assessments.

We use consistent methodology for full 2008-2015 study time period, which increases confidence in observed temporal change. While issues associated with shelf-wide hydrostatic equilibrium may impact results in an absolute sense, the effects on relative measurements (e.g., Dh/Dt) should be similar for all time periods.

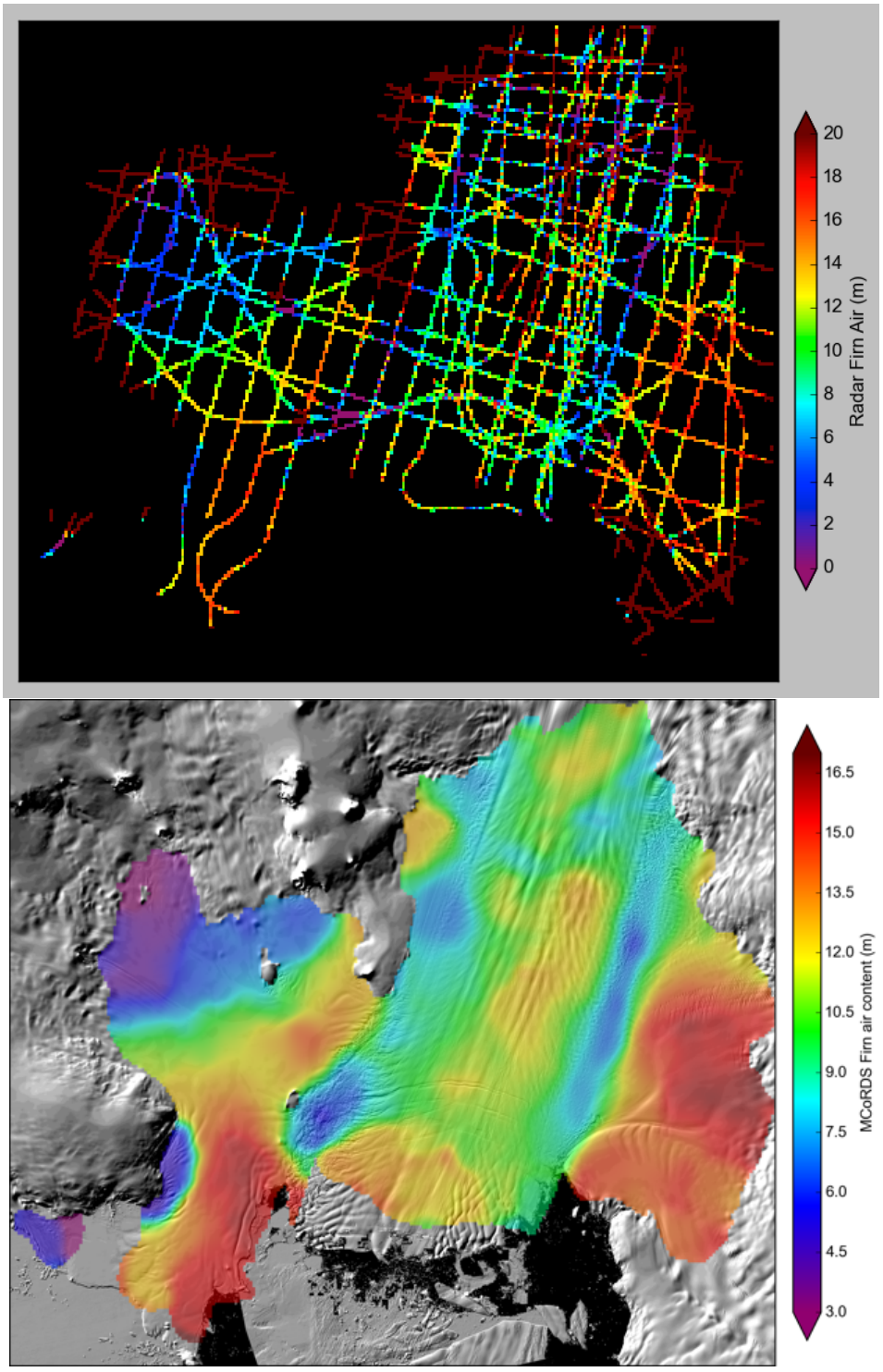

Figure A-1: Firn air content calculated from 2002-2014 airborne radar measurements. A) Median of firn air content estimates within 256-m bins. Estmates >20 m correspond to grounded ice and/or bad radar picks. B) Filtered, smoothed interpolation over floating ice. Note significantly higher values on S shelf and low values near grounding line on N shelf.

VITA

David Shean received his Sc.B. in Geology-Physics/Mathematics (2004) and Sc.M. in Geology (2006) from Brown University. While at Brown, he performed experiments on NASA's microgravity research aircraft and conducted geophysical surveys on glaciers in the Transantarctic Mountains. His early research involved documenting past glaciation and evidence for climate change on Mars. In 2006, he worked in Yellowstone National Park, doing field work and procesing/analyzing historical aerial photographs to study dynamic hydrothermal features. David then worked in the Dept. of Earth Sciences at Boston University, where he performed additional fieldwork in the Transantarctic Mountains. From 2007-2011, David was a member of the Mars Reconnaissance Orbiter CTX/MARCI science operations team while working for Malin Space Science Systems, Inc in San Diego, CA. His current research relies on satellite/airborne/UAS remote sensing observations to study ice dynamics and mass balance in Antarctica, Greenland, and the Pacific Northwest.